The Development and Application of Biological Models for Evaluation of Direct Nose-to-Brain Drug Delivery Systems

Alpesh Mistry

MPharm(Hns), MRPharmS

Thesis submitted to the University of Nottingham

for the degree of Doctor of Philosophy

August 2008

ABSTRACT

The olfactory neuroepithelium is the only part of the central nervous system that is exposed directly to the external environment. Therefore, it is the only non-invasive drug delivery route to the brain. Surface modification of PS nanoparticles with chitosan (C-PS), polysorbate 80 (P80-PS) and polysorbate 80+FCS (P80-FCS-PS) changed the toxicity and distribution of these nanoparticles in olfactory mucosae. In addition, a reduction in nanoparticle diameter from 200nm to 20nm increased nanoparticle mucosal penetration and possibly also their cellular toxicity.

In vitro vertical Franz diffusion chamber and *in vivo* mouse models were adapted to investigate the transport of nanoparticles via the olfactory system. For the *in vitro* model, preliminary studies found that olfactory epithelium lined the caudal portion of the dorsal nasal turbinate in the porcine nasal cavity. To ensure the scientific validity of the diffusion chamber studies, it was necessary to prove that the experimental procedures themselves (without the addition of nanoparticles) had no effect on the mounted tissue. Therefore, viability and cellular morphology of the dissected olfactory epithelia were assessed prior to application of nanoparticles to tissues. Alamar Blue™ viability and histological findings showed that the diffusion chamber experiment did not affect the olfactory tissue when compared to samples that were not mounted on the apparatus. Citrate buffer (pH6.0) had significantly reduced the viability (PD, I_{sc} and Alamar Blue™) of the porcine olfactory epithelium compared to SNS buffer (pH7.4) but it did not kill it. Citrate buffer may have depleted the mucosal pH gradient in the epithelium. Overall both SNS buffered and citrate buffered porcine olfactory epithelia were suitable for nanoparticle transport studies in the vertical Franz diffusion cell.

The *in vitro* and *in vivo* biological models showed surface modification had changed the distribution of nanoparticles within the epithelia. There was good agreement between particle losses from donor chamber, fluorescence microscopy images and stereology results that C-PS particles adhered to extracellular mucus to a greater extent compared to PS and P80-FCS-PS. P80-PS nanoparticles were taken into the nasal epithelial cells to a greater extent than C-PS. Nanoparticles were not transported to the receiver chamber *in vitro* or the olfactory bulbs *in vivo*. The size of the nanoparticles was also important. Fluorescence microscopy and stereology showed that greater numbers of 100nm PS and 100nm P80-FCS-PS were taken up into mouse olfactory epithelial cells compared to 200nm diameter equivalents. Larger particles may not have penetrated mucus as effectively as smaller ones.

Bright field microscopy images of olfactory epithelia dismounted from the diffusion chamber apparatus after transport study with C-PS nanoparticles showed that these particles caused the greatest amount of cellular damage compared to PS, P80-PS and P80-FCS-PS systems. Greater damage was observed for progressively smaller particles. For example, 20nm C-PS may have accessed subcellular organelles such as mitochondria to cause cell death by oxidative stress. However, similar findings in the mouse model were not observed. It was hypothesised that, unlike the *in vitro* model, the mouse model may have been able to maintain a pH gradient across the mucous layer by neutralising the acidity from the citrate buffer using blood borne HCO_3^- ions. This would protect the epithelial cells by causing C-PS to aggregate in the mucus thereby preventing them from accessing the epithelial cells.

ACKNOWLEDGMENTS

I would like to thank my PhD supervisors Prof. Lisbeth Illum and Dr. Snjezana Stolnik for their guidance and knowledge.

The Division of Drug Delivery & Tissue Engineering (School of Pharmacy, University of Nottingham) and technical support staff (in particular Mrs. Christine Grainger-Boultby and Mrs. Teresa Marshall) are also credited for their contribution. Sys Glud Zoffman (University of Aarhus, Denmark) is thanked for the histological and stereological work that was undertaken and for her constructive comments during the *in vivo* study. Fredrick Dagnaes-Hansen (University of Aarhus, Denmark) is acknowledged for supervision of animals during the *in vivo* study. John Corbett (Sutton Bonnington Campus, University of Nottingham, UK) is thanked for procurement of animals used in the *in vitro* study. I am also grateful to the Engineering and Physical Sciences Research Council (EPSRC) and The School of Pharmacy, Nottingham, UK for funding the project.

Finally, I express my sincerest gratitude to my family for giving me the strength to follow my dreams.

“What will tell in the end will be character and not a knowledge of letters.”

Mohandas Karamchand Gandhi

(b. Porbandar, 2 Oct. 1869; d. Delhi 30 Jan. 1948)

ABBREVIATIONS

ApoE	Apolipoprotein E
C-PS	Chitosan-coated polystyrene (C-PS) nanoparticles
%DA	% Degree of deacetylation
Direct N-B	Direct nose-to-brain
FCS	Foetal Calf Serum
I_{sc}	Short Circuit Current
MW	Molecular Weight
NALT	Nasopharynx-associated lymphoid tissue
P80-FCS-PS	FCS adsorbed P80-PS (P80-FCS-PS) nanoparticles
P80-PS	Polysorbate 80-coated polystyrene (P80-PS) nanoparticles
PD	Potential Difference
PEG	Polyethylene glycol
P-gp	P-glycoprotein
PS	Polystyrene (PS) nanoparticles
R_m	Transepithelial Electrical Resistance
ROS	Reactive oxygen species

1. INTRODUCTION AND OVERVIEW

1.1 INTRODUCTION

Diseases of the Central Nervous System (CNS) that require drug treatments are numerous; schizophrenia, meningitis, migraine, obesity, Parkinson's disease and Alzheimer's disease and are all such examples. Drug delivery to the brain, however, remains problematic because of poor bioavailability from the blood due to the impervious nature of the endothelial membrane separating the systemic circulation and central interstitial fluid, termed the Blood Brain Barrier (BBB) (Pardridge 1999). This is a major impeding factor to progress in the field. Hence, many potent therapeutic agents may have been abandoned because sufficient drug levels in the brain can not be achieved via the blood.

A well described strategy to promote BBB penetration is to derivatise small molecular weight drugs into pro-drug analogues which are more lipophilic and so allow passive diffusion of the pro-drugs across the BBB. These are later converted by enzymes to the native form (Krishnamoorthy & Mitra 1998). This approach however creates a new chemical entity which itself requires additional safety assessment for regulatory approval; therefore it can be an undesirable strategy. In any case, macromolecular drugs such as peptides and proteins, termed 'biologics,' are too large and too hydrophilic to penetrate the BBB from the systemic circulation and are rapidly cleared by gastrointestinal enzymes (if taken orally) or the liver cytochromes. In addition, non-invasive therapy is also desirable for patients particularly for diseases that require chronic dosing such as those related to dementia. Therefore, it is beneficial to develop a non-invasive technique that circumvents the need to overcome the BBB.

In recent years it has been shown in the literature from animal and human investigations that transport of exogenous materials directly from nose-to-brain is a potential route for by-passing the BBB (Illum 2000). This route, termed direct nose-to-brain (N-B) drug delivery, involves the olfactory or trigeminal nerve systems which initiate in the brain and terminate at the olfactory neuroepithelium or respiratory epithelium (respectively) in the nasal cavity. It is the only externally exposed portion of the CNS and therefore represents the most direct method of non-invasive entry into the brain. The system is not currently used therapeutically and no product is licensed specifically via this route.

Moreover, the strategy of applying drugs that are encapsulated into particulate vectors (such as synthetic nanoparticles) to the olfactory epithelium could improve non-invasive and direct CNS delivery of drugs - including biologics. If drugs could reach the CNS by this route then it would not only regenerate interest in previously abandoned drug compounds but also enable an entirely novel approach to CNS drug delivery. However, before it is possible to contemplate aspects of N-B drug delivery one must have a reasonable understanding of nasal anatomy and physiology relating to the field.

1.2 NASAL ANATOMY AND PHYSIOLOGY

This section describes the rationale for nasal drug delivery in general and the nasal anatomy and physiology relating to N-B drug delivery. A more detailed discussion of the nasal physiology and anatomy can be found elsewhere (De Lorenzo 1970; Mygind 1979; Mygind & Dahl 1998; Lledo et al 2005).

Currently, the nasal route is exploited to deliver drugs either locally (e.g. decongestants) or systemically (e.g. the ‘triptans’ for migraine). The nasal route offers many benefits

over traditional routes: (i) the process is non-invasive and rapid; (ii) the rich vasculature underlying the nasal mucosa can be used to greatly enhance the potential for systemic absorption; (iii) the enzymatic degradation of peptides is reduced compared to oral delivery; (iv) avoidance of first-pass metabolism has the potential to considerably improve bioavailability; and (v) it may improve bioavailability where symptom related factors reduce systemic uptake (e.g. oral anti-emetics).

The disadvantages of the nasal route are that: (i) the nasal mucosa usually favours the passive diffusion of a combination of low molecular weight drugs (Sakane et al 1995), lipophilic (Sakane et al 1991) and unionized molecules (Sakane et al 1994), (ii) the nasal mucosa retains some enzymatic activity compared to other mucosae which can degrade the active compounds however, the capacity for degradation is less than for other absorptive tissues (Graff & Pollack 2003); (iii) nasal congestion due to allergy or minor infection could effect the bioavailabilty of the product considerably (Mygind & Dahl 1998); and (iv) local irritation (Charlton et al 2007).

With specific reference to N-B delivery, drawbacks compared to systemic delivery include: (i) toxicity to the olfactory and trigeminal systems particularly since toxicity in chronic dosing to these areas is yet to be evaluated; (v) access to and targeting of the olfactory mucosa may be difficult considering its relatively inaccessible location at the roof of the nasal cavity in man since it lies away from the usual route taken by inhaled air (Gizurarson 1990; Ugwoke et al 2001).

1.2.1 The External Nose and the Nasal Cavity

The main functions of the nose are the sense of smell, the regulation of humidity and temperature of inhaled air, and the removal of large particulates from the inhaled air. In

humans, the total surface area and total volume of both nasal cavities was derived from computed tomography (CT) scans as 150.4cm^2 (made possible by three protusions or 'turbinates' within the cavity) and 13.0ml, respectively (Menache et al 1997).

The filtering of particulates from the inhaled air starts where the nose opens to the external environment (nasal vestibule). The nasal hairs (*vibrissae*) filter large air-borne particles. Approximately 1.5 cm from the bottom of the nasal vestibule is the nasal valve (or internal ostium). This is the narrowest portion of the upper respiratory tract and thus accounts for the 50% of the total airway resistance from nostril to alveoli (Mygind & Dahl 1998).

During rest the air is drawn into the nasal cavity in a laminar fashion at low flow rates. It is then directed into the medial and inferior meatuses (Figure 1.1). The medial meatus connects to the maxillary sinus through a 2-5mm opening (ostium). The maxillary sinus helps to warm and humidify inhaled air. After passing through the main nasal passage (cross-section B Figure 1.1), the inspired air then passes through the nasopharynx (cross-section C Figure 1.1) and onwards to the bronchi and lungs.

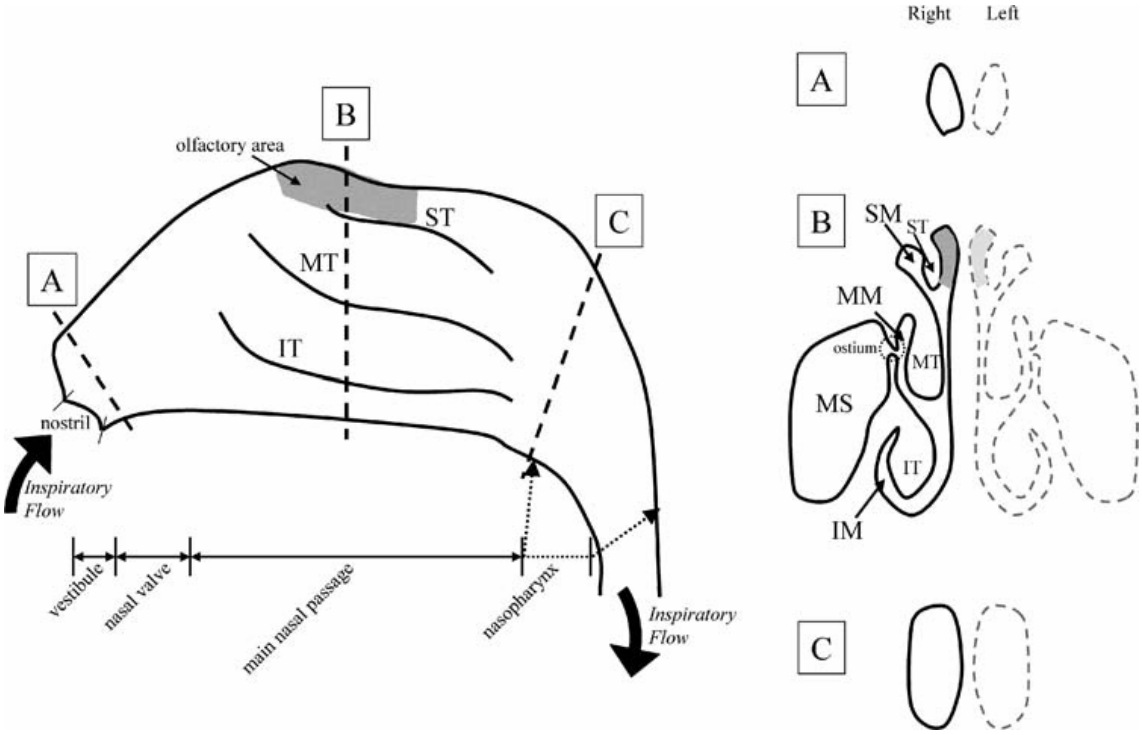

Figure 1.1 Schematic diagram showing the gross anatomy (in sagittal [left] and frontal [right] planes) of the human nasal cavities. IT, MT, and ST refer to inferior, middle, and superior turbinates. IM, MM, and SM refer to inferior, middle, and superior meatuses. MS refers to the maxillary sinus. Taken from (Croce et al 2006).

The olfactory epithelium is located high in the nasal cavity in man (Figure 1.1). It partly overlies the cribriform plate, a bony structure that contains many pores that allow the passage of neuronal bundles from the olfactory epithelium to pass into the CNS (Figure 1.6). Olfactory epithelium may also lie partly on the nasal septum and on the superior turbinate. It is above the normal path of the airflow which means that odorant molecules normally reach the sensitive receptors by diffusion. The act of sniffing enhances the diffusional process by increasing the airflow rate and changing it from continuous to pulsatile in nature. This behaviour increases the turbulence within the nasal cavity and therefore allows greater interaction of the inspired air with the olfactory region at the roof of the nasal cavity.

Figure 1.2 shows a CT scan image (Figure 1.2) of air passing through a plastinised model of the human nasal cavity (Croce et al 2006). Vortices appear at high airflow (231ml/s) in the nasal cavity in the olfactory region and at the head of the inferior turbinate. The CT scan shows that the vortex in the olfactory region had a low velocity magnitude (0.4m/s). The low velocity may aid odorants to interact with the olfactory neuroepithelium by allowing sufficient residence time for the interaction to take place.

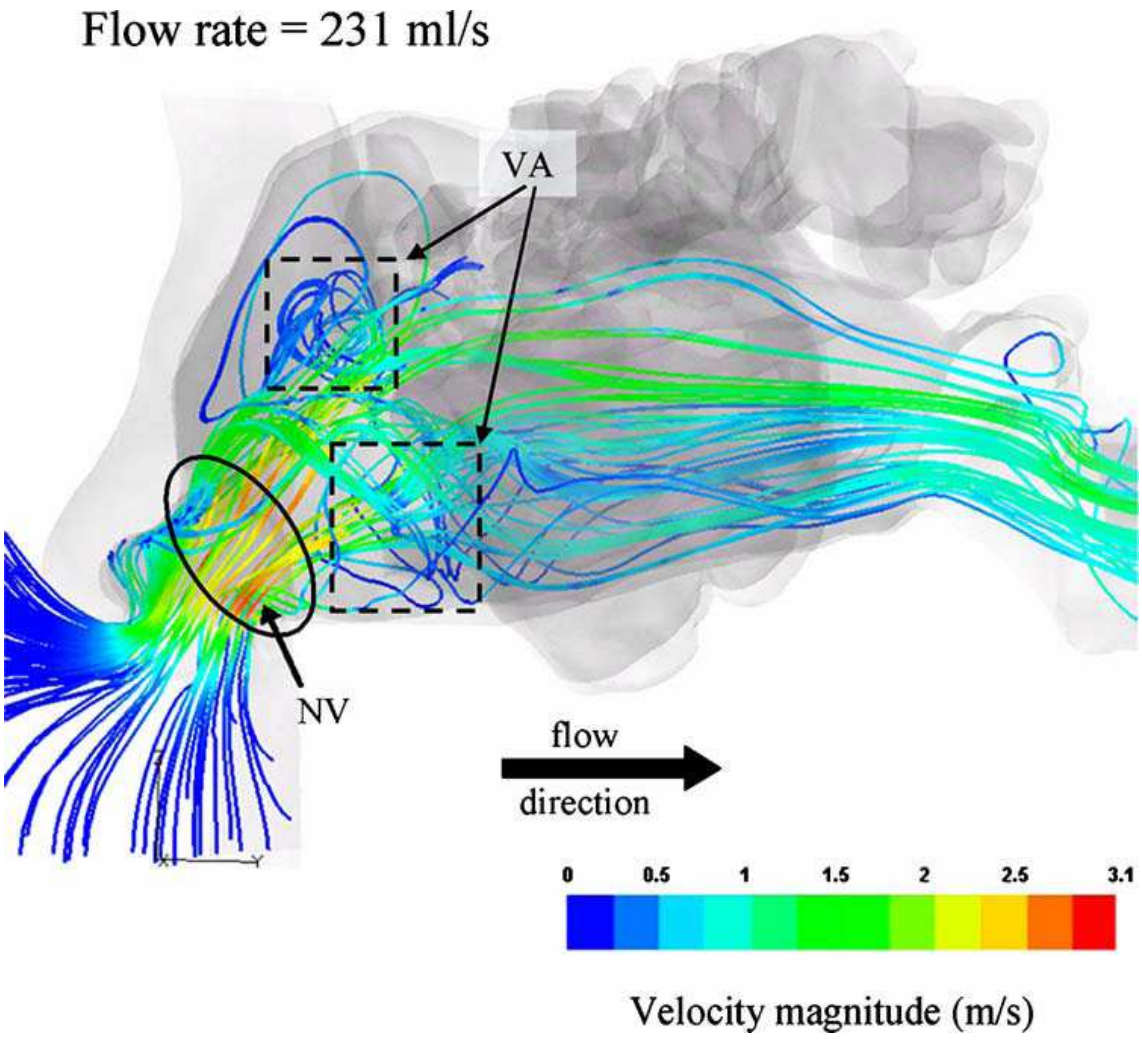

Figure 1.2 CT scan of high airflow through a plastinated model of the human nasal cavity. NV=Nasal Vestibule. VA= Vortex Area. Taken from (Croce et al 2006).

However, the laminar airflow used in this experiment did not simulate the pulsatile nature of sniffing. By pulsating the airflow, future studies may provide a clearer

aerodynamic understanding within the nasal cavity during the act of sniffing and therefore its significance to olfaction.

1.2.2 The Structure of Nasal Epithelia

There are two physiologically important epithelia in the nasal cavity relating to drug delivery, 'respiratory' and 'olfactory'. From a drug delivery perspective the respiratory epithelium, which has a rich submucosal blood supply, is particularly important for systemic drug absorption. Certain regions of the respiratory epithelium also contain microfold (M) cells whose function it is to present antigens found in the mucus to underlying nasaopharynx-associated lymphoid tissue (NALT) structure in the *lamina propria*. This initiates an immunological cascade involving T cells and B cells that ultimately ends in both systemic and local immune responses (e.g. mucosal IgA antibody secretion). This immunological cascade may be useful for the development of nasal vaccines. In contrast, the olfactory epithelium (which has a surface area of 3% (~4.5cm^2) of the total nasal epithelium and is placed in the roof of the nasal cavity in man (Morrison & Costanzo 1990)) contains olfactory neurones that ultimately reach the brain via a number of connections (Mygind 1979; Mygind & Dahl 1998).

There are three structural morphologies of epithelia in the human nasal cavity: (i) keratinised stratified squamous found in the nasal vestibule; (ii) pseudostratified columnar located caudally (distal to the nasal vestibule); or (iii) stratified cuboidal situated between the previous two types (Mygind 1979; Mygind & Dahl 1998).

The nomenclature is described in terms of the shape of the individual cells and the overall structure of the epithelium. Squamous cells are flat and have an irregular shape (Figure 1.3). They may produce keratin which is a tough insoluble protein that helps to

protect the underlying tissue from mechanical damage and/or dedydration. Stratified describes cells that appear in layers of which the superficial layers have lost contact with the basement membrane. (The basement membrane, or *basal lamina*, is an extracellular condensation of mucopolysaccharide and proteins that consists of a dense filamentous sheet measuring 50-100nm in thickness).

Pseudostratified columnar cells form the respiratory epithelium. Columnar cells are tall and rectangular such that the height exceeds the width of the cell (Figure 1.3). It is thought that the shape of the columnar cell helps to maintain its 'polarised' function (Wright & Alison 1984). For example, columnar cells contain a higher density of mitochondria at the apical region of the cell presumably to facilitate the functions of active transport and/or cilia motility. Nasal pseudostratified epithelia appear to form different cell layers above the basement membrane but careful examination reveals that both basal cells and columnar cells maintain their attachment to it. The olfactory epithelium is a modified pseudostratified columnar epithelium as described in detail later (1.2.4 Olfactory Epithelium and Neuronal Supply).

Cuboidal cells are so called since the height of each component cell is similar to its width. Cuboidal cells have a stratified layer organisation (Figure 1.3).

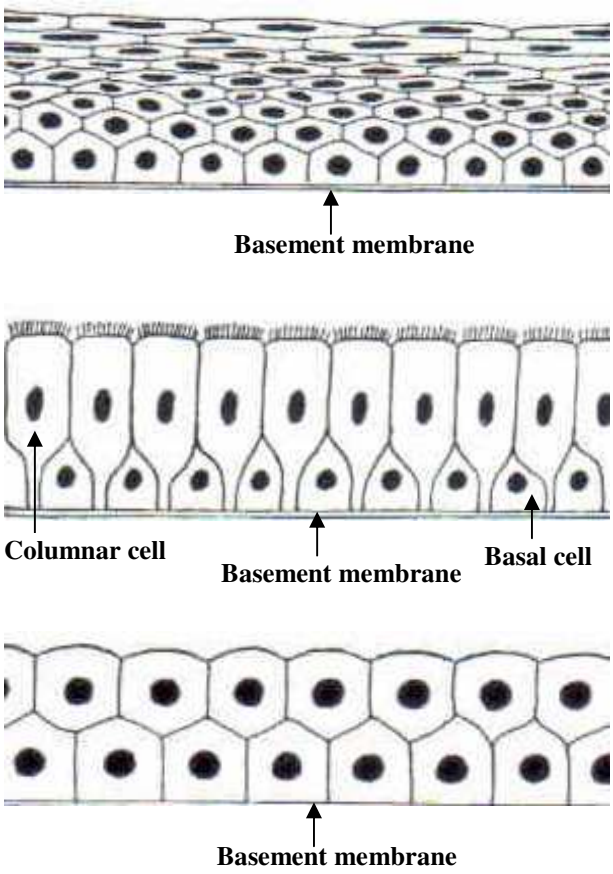

(a) Stratified squamous epithelium – cells are flat with irregular shapes

(b) Pseudostratified columnar epithelium – columnar cells are tall and narrow with a regular shape. Basal cells give the epithelium a stratified appearance; however, all cells are attached to the basement membrane so the epithelium is described as 'pseudostratified.'

(c) Stratified cuboidal epithelium – a layered cellular organisation whereby the height of each component cell is similar to its width

Figure 1.3 Schematic representations of different epithelia found in the human nasal cavity (illustrations adapted from (Freeman & Bracegirdle 1976))

In some mammals, including humans, there are also transitional areas at the boundaries between different morphological regions where these distinctions are gradually blurred.

1.2.3 Respiratory Epithelium and Mucocillary Clearance

The respiratory epithelium is composed of four types of cells, namely, non-ciliated and ciliated columnar cells, basal cells and goblet cells (Figure 1.4). All columnar cells express around 300 microvilli per cell that increase the surface area at the apical surface (Ugwoke et al 2001). These features probably facilitate active transport processes such as the exchange of water and ions between cells and motility of cilia (where applicable). They may also serve to prevent drying of the mucosa by trapping moisture.

The ciliated and non-ciliated columnar cells contain a high density of mitochondria particularly near the apical surface (Matulionis & Parks 1973). This implies that these cells are heavily involved in active transport processes in this region. Columnar cells may be responsible for the transport of drug from the environment into the underlying blood supply either actively (for hydrophilic molecules) and/or passively (for lipophilc molecules). They are anchored to the neighbouring cells apically by junctional complexes (1.2.5 Junctional Complexes).

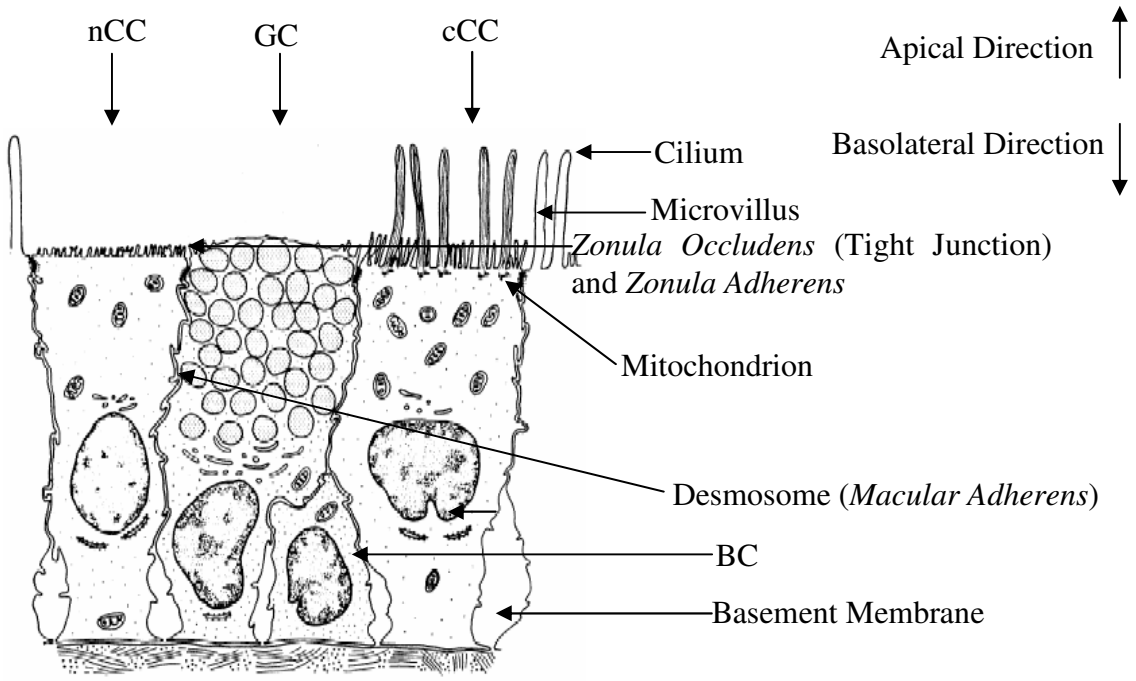

Figure 1.4 Diagram of the four cell types in the respiratory epithelium (from the left) non-ciliated columnar cell (nCC), goblet cell (GC), basal cell (BC) and ciliated columnar cell (cCC). Adapter from (Mygind & Dahl 1998).

Ciliated columnar cells also contain a mitochondria-rich apical region and these cells represent 15-20% of the respiratory epithelium (Matulionis & Parks 1973). Each ciliated cell contains around 100 cilia (Ugwoke et al 2001). They use energy from the mitochondria to facilitate the beating of cilia in an innate and synchronised fashion at a

frequency of 10-20Hz so as to clear the covering mucus layer at a rate of 6 mm/min towards the nasopharynx (Ugwoke et al 2001).

Mucus (or nasal secretion) is a complex mixture of materials. It is approximately 95% water, 2% mucin, 1% salts, 1% of other proteins such as albumin, immunoglobulins, lysozymes and lactoferrin, and <1% lipids (Kaliner et al 1984).

Mucus exists in two layers in order to facilitate mucociliary clearance; hence, a mucus 'blanket' (Figure 1.5c; 'gel layer', 2-4µm thickness) floats on a serous fluid (Figure 1.5e 'sol layer', 3-5µm thickness). The viscous gel layer is moved along by the hook shaped cilia termini during the energy-dependent 'effective stroke' phase of the ciliary motion (Figure 1.5a). Cilia are up to 7µm in length when fully extended but can fold to half this length during the recovery stroke. During the 'recovery stroke' the hook terminus detaches from the gel layer and moves in the opposite direction to the gel layer movement (Figure 1.5b). The cilia are immersed only in the sol layer during the recovery stroke and thus the gel layer moves only in one direction (Mygind 1979; Lenaerts & Gurny 1990).

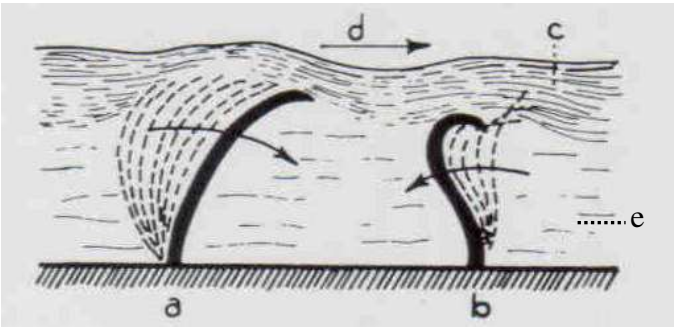

Figure 1.5 The relationship between ciliary motion and mucus layer composition that allows mucociliary clearance. (a) effective stroke, (b) recovery stroke, (c) gel layer (d) direction of gel layer movement, (e) sol layer. Adapted from (Proetz 1953).

In addition, it is well known that this mucocilary clearance rate is altered by the action of anaesthetics and this may complicate interpretation of *in vivo* experimental data since anaesthetics are usually required during *in vivo* studies (Van Der Baan 2000).

The third type of cell contained in the respiratory epithelium is the basal cell. These are the progenitors of the other cell types. They also provide mechanical stability to the epithelium since they are anchored to adjacent cells and the basement membrane and by desmosomes and hemidesmosomes, respectively (Mygind & Dahl 1998).

Finally, Goblet cells produce mucus and so the are densely packed with golgi apparatus which reflects their high secretory capacity. Goblet cells, however, may contribute less than the exocrine glands (Bowman's Glands) to the main production of nasal secretions over the olfactory epithelium (Getchell & Getchell 1992).

1.2.4 Olfactory Epithelium and Neuronal Supply

The olfactory epithelial layer predominantly contains three cell types; the olfactory cells, supporting (or sustentacular) cells and basal cells. Basal cells are progenitor cells (of supporting cells) that also provide mechanical support as described for the respiratory epithelium. Supporting cells are elongated non-ciliated columnar cells that contain microvilli. They provide mechanical support to the olfactory cell by surrounding them and forming junctional complexes with them (1.2.5 Junctional Complexes). Also, they may help to maintain a suitable extracellular potassium environment for the neurones to allow polarisation, priming them, ready for an action potential.

The third cell type is the olfactory axon. The axons are unmyelinated and interspaced between the supporting cells (Figure 1.6). They originate at the olfactory bulb in the CNS and terminate at the apical surface of the olfactory epithelium.

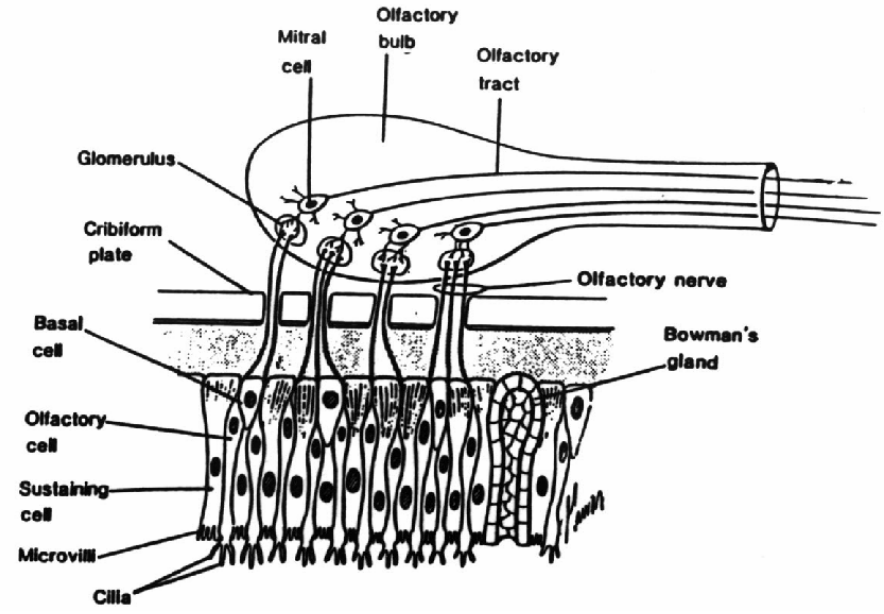

Figure 1.6 Diagram of the olfactory area showing the olfactory epithelium, bulb and tract. From (Adams et al 1989)

The olfactory knob (or vesicle) protrudes out from and above the apical surface of the olfactory epithelium (Figure 1.7). Approximately 10-23 cilia project from the basal bodies of the knob, each of length up to 200µm. The cilia contain chemical detectors that, once activated by odorants, initiate depolarisation of the receptor cell by either direct ion-gated channels or cAMP operated ion-channels (Gartner & Hiatt 2000). The cilia entangle with the thick brush-border of microvilli of the supporting cells at the air/mucus/tissue interface (Figure 1.7). The cilia are non-motile in the olfactory region (in contrast to respiratory tissue) since they lack the dynein arms which contain the Mg^{2+}-ATPase that generates the force for cilary motility (Moran et al 1982).

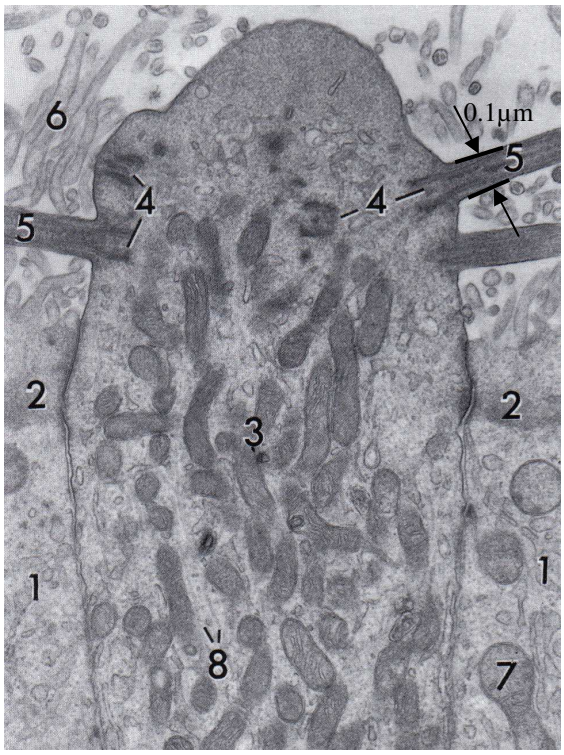

Figure 1.7 Electron microscope images of cat olfactory knob. (1) Neighbouring supporting cell; (2) tight junction; (3) mitochondrion in olfactory knob; (4) basal bodies; (5) olfactory cilia; (6) microvilli; (7) mitochondrion in supporting cell; (8) microtubules. From (Rhodin 1974).

The *lamina propria* of the olfactory epithelium, which is located beneath the epithelial layer(s), contains a blood supply, mucus secreting acinar glands (Bowman's glands), nasal lymphatics, and a neuronal supply that consists of olfactory axon bundles, autonomic nerve fibres and maxillary branch of the trigeminal nerve (Tucker 1971; Mygind 1979; Brand 2006; Brodbelt & Stoodley 2007). Bowman's glands are under the control of the parasympathetic nervous system. These acinar-type glands produce nasal secretions in the *lamina propria* and secrete them through a narrow tube-like opening into the luminal space.

Also in the *lamina propria* the olfactory neurones taper together and are ensheathed by glial cells (or Schwann cells). These processes are called *filia olfactoria*. De Lorenzo (1962) has described the *fila olfactoria* in detail. *Fila olfactoria* are unique features in the mammalian body in that around twenty axons are partitioned by the Schwann cell into fascicles. Five fascicles are shown in Figure 1.8. In this way a single Schwann cell

may ensheathe around a hundred or so axons. In contrast, single non-olfactory neurones are usually ensheathed by a one Schwann cell. This feature allows 10-15nm sized spaces between axons that act as ionic reservoirs for action potential propagation. Hence, perineuronal transport of molecules to the olfactory bulbs is limited by the size of these spaces. Mesaxons are pores in the *filia olfactoria* structure that allow passage of extracellular fluid into the neuronal bundle structure.

The average diameter, by electron microscopy, of olfactory axons in 2 month old rabbits is ~200nm, however, many of the axons have diameters of <100nm (De Lorenzo 1960). Theoretically therefore transcellular transport of up to 200nm diameter particles is possible in these animals. Other species show similar olfactory axonal diameters, for example, the African Clawed frog, various bird species and humans have diameters of 198±93nm, 210-260nm and 100-700nm, respectively (Burd 1991; Morrison & Costanzo 1992; Matsuzaki 1995).

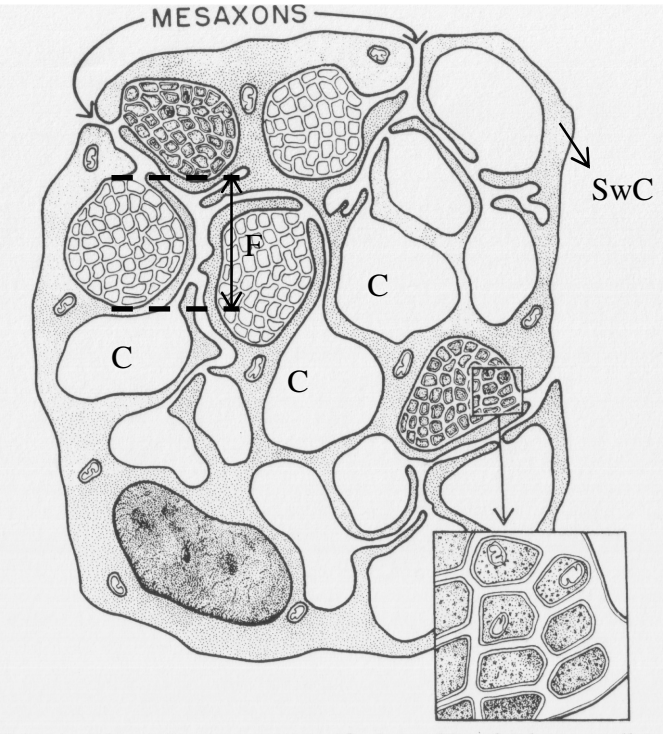

Figure 1.8 Schematic representation of *fila olfactoria*. The arrangement of neurones is unusual in that many (~20) neurones are isolated into fascicles (F). Here five such fascicles are ensheathed by a single Scwann Cell (SwC). In addition, the cavities in the structure (C) provide reservoirs for ions. This enables ion exchange between the axoplasm and the extracellular fluid. Mesaxons are pores in the structure that allow continuity between the extracellular fluid and the *filia olfactoria*. Adapted from De Lorenzo (De Lorenzo 1962).

The Schwann-sheathed axonal bundles then pass through the *lamina propria* and into the porous structure of the cribriform plate. They then synapse on a mitral cell or tufted cell in the glomeruli of the olfactory bulb. Around 1500 sensory neurones synapse on one mitral cell. The mitral and tufted cells are branched; they project one dendrite to each glomerulus. These neurones then pass through to the olfactory tubercle. From there, the third-order neuronal projections pass to the amygdala, prepyriform cortex, the anterior olfactory nucleus and the entorhinal cortex as well as the hippocampus, hypothalamus and thalamus (Lledo et al 2005).

1.2.5 Junctional Complexes

Junctional complexes are the cell-to-cell contact areas found between both respiratory and olfactory epithelial cells in the nasal cavity. Some consist of protein anchors that hold two adjacent cells closely together to maintain cell contiguity and strengthen the epithelial sheet (Shin et al 2006). There are three different types of these complexes (Figure 1.4); *macular adherens* (or desmosomes), *zonula adherens* and *zonula occludens* (tight junctions [Figure 1.7]). *Zonula occludens* are located closest to the luminal space. *Zonula adherens* are located close to the *zonula occludens* and *macular adherens* are situated basolaterally in relation to other two complexes. Thus, the transport of drugs between cells is largely determined by the integrity of these complexes for in tact epithelia.

Macular adherens are composed of dense attachment plaques between cells. Cells attach to these extracellular plaques by anchoring them to tonofilaments that loop out and back into the cell. *Macular adherens* are particularly well developed between stratified squamous epithelium. They are clearly observed as thin strands between cells

under the light microscope. Unlike the *macular adherens*, the *zonula adherens* do not possess a well-developed attachment plaque. They associate with the apical terminal web a meshwork of proteins found in the cytoplasm of cuboidal and columnar cells. *Zonula occludens* press tightly against each other (by contact of adjacent cell membranes) to seal the intercellular space between cells from the lumen. The pore size between the cells is largely determined by the claudin proteins in the *Zonula occludens* (Gumbiner 1987; Van Itallie & Anderson 2006).

The structure of junctional complexes is similar throughout the body since junctional complexes share similar protein compositions. For example, tight junctions are mainly composed of three transmembrane proteins; namely, claudins, occludins and junctional adhesion molecules. Therefore it can be assumed that variations in tight junction composition between cells in the olfactory and respiratory epithelia have little importance for paracellular transport of nanoparticles (Shin et al 2006).

1.2.6 Interspecies Variability of Nasal Anatomy

The histological features of the olfactory epithelium are similar between most mammals. The epithelium has been consistently observed to have a pseudostratified columnar morphology interspaced with olfactory cells (as described before) amongst many species in the class (e.g. humans (Morrison & Costanzo 1990; Moran et al 1992), pig (Booth et al 1981), mouse (Bannister & Dodson 1992), rat (Miller et al 1995), koala (Kratzing 1984), rabbit (De Lorenzo 1962)). In addition, the sialylated and sulphated acid mucin components of mucus has been shown to be similar in pigs and humans (Larochelle & Martineaudoize 1991). Thus, the similarities may go beyond physical appearance alone.

Nevertheless, some variation does exist. For example, rabbits and dogs have branching conchae instead of scrolls that are found in pigs and rodents (Gizurarson 1990). Such anatomical differences may restrict the access of formulations to the olfactory regions of rabbits and dogs compared to pigs and rodents depending on the exact location of the olfactory epithelium in each of these species.

Also, the surface area of olfactory epithelium in the human nasal cavity is up to 3% (Morrison & Costanzo 1990) of the total nasal epithelium; whereas in mouse it is 56% (Adams 1972). Therefore proportionally more drug molecules may be transported to the mouse brain via the olfactory route compared to humans. In addition, clearance half-life of mucus from the nasal cavity is 1 min in mice compared to 15 minutes in humans (Gizurarson 1990). Hence, higher concentrations of drug may appear in the CSF of mice than humans. Finally, the human brain (1500g) is larger than that of rat (2g) this makes penetration of drug molecules deep into the brain parenchyma more difficult in humans (Nieuwenhuys et al 1998).

Similar differences may exist between human and porcine nasal cavities; however, there is relative less information about nasal mucus clearance rates and percentage olfactory epithelium coverage in domestic pigs. Nevertheless, conclusions regarding the impact of the olfactory transfer of drugs in humans from other animals are difficult to make particularly since there is a lack of studies in man.

Species variation between rats and mice has been seen for direct N-B delivery of morphine solution (Westin et al 2005). [^{3}H]-morphine levels were found, by autoradiography and liquid scintillation analysis, to peak in the right olfactory bulb in

male Sprague-Dawley rats within 15 minutes of *i.n.* administration; however, it was 60 minutes in Balb/c mice.

In addition, morphine is metabolised in the periphery to pharmacologically active morphine-6-glucoronide and inactive morphine-3-glucoronide in humans (Westerling et al 1995) while only the inactive metabolite is formed in mice and rats (Kuo et al 1991). High levels of drug metabolising enzymes exist in the olfactory epithelium (Lazard et al 1991) which could produce similar variations in drug metabolism at the level of the nasal mucosa. This would also be relevant if a nanoparticle formulation was used to release drug at the olfactory mucosa.

Hence, these findings demonstrate that it may be difficult to extrapolate conclusions made from direct N-B drug delivery studies between mammalian species.

1.3 CELLULAR MECHANISMS FOR TRANSMUCOSAL DRUG DELIVERY

Two broad mechanisms of drug transport through the epithelial cell layer have been identified, namely, paracellular (between epithelial cells) or transcellular (apical to basolateral transport through epithelial cell).

The paracellular route comprises of a hydrophilic channel that allows only the smallest of drug molecules to pass through it due to the restrictive nature of the junctional complexes that link the epithelial cells. In nasal epithelia the largest molecular size for paracellular drug transport has been estimated as 1000Da (McMartin et al 1987). Hence, dopamine (Dahlin et al 2000; Dahlin et al 2001) and morphine (Westin et al 2005) are both believed to pass paracellular (as well as trancellularly) between olfactory epithelial cells. However, tight junctions are generally impermeable to molecules with a

hydrodynamic radius greater than 4-8Å (depending on the 'leakiness' of the epithelium) which restricts the movement of molecules larger than this to pass between neighbouring cells (McMartin et al 1987). Hence, nanoparticles are too large for this route to be of use. Therefore, since the main focus of this review is to evaluate the particulate delivery of drugs directly from nose-to-brain, the rest of this section will concentrate on the transcellular route.

The transcellular route is less well characterised than the paracellular route (Miaczynska & Stenmark 2008). However, novel spectroscopy and microscopy techniques such as electron energy loss spectroscopy and energy filtering transmission electron microscopy are providing new insights into this complex process (Rothen-Rutishauser et al 2006). Lipophilic, small molecular weight drugs are able to passively transport through the cell membrane and this is discussed later (1.6 The Transport of Drug Solutions Direct from Nose-to-Brain). The aim of this section, however, is to describe the different endocytic routes of transcellular uptake of drugs and nanoparticles by cells, and speculate how they may influence direct N-B drug delivery.

Endocytosis has been categorised by a number of different molecular mechanisms including macropinocytosis, clathrin-mediated, clathrin-independent, caveolin-mediated, caveolin-independent and phagocytosis (Conner & Schmid 2003) (Figure 1.9). Macropinocytosis is an endocytic mechanism where the action of actin filaments gives rise to curved 'ruffles' on the cell surface. Sealing of the aperture into discrete vacuoles forms the macropinosome (0.5-5µm diameter) which efficiently takes up extracellular fluid into the cell (Xiang et al 2006). Considerable volumes of dissolved molecules and particles can be taken up in this way. Macropinocytosis is generally

thought of as a constitutive process by which the cell can sample the extracellular environment and is not believed to be initiated by receptor activation at the cell surface (Xiang et al 2006).

Receptor-meditated endocytosis is a term used to describe a group of endocytic mechanisms where the 'cargo' is thought to stimulate the endocytic event by complementing a receptor on the cell membrane. Receptor-mediated endocytosis can involve either clathrin-dependent or independent mechanisms. The clathrin protein is endogenously expressed within mammalian cells in the form of a heavy chain and a light chain. The fusion of these chains results in the formation of a triskelion structure, a 3D array of which produces a clathrin coat (Edeling et al 2006). Recruitment of the coat to the cytosolic cell membrane gives rise to regions called 'coated pits' during the initial stages of receptor-mediated endocytosis. Invagination of the pit results in a clathrin-coated vesicle that is taken into the cytosol. These vesicles can take various shapes and sizes but are generally believed to be <150nm (Xiang et al 2006). Clathrin-dependent endocytosis is currently the best characterised endocytic mechanism; however, there is still debate over exactly how the cargo initiates the event (Sorkin 2004).

Clathrin-independent endocytosis may involve cholesterol-enriched microdomains in cell membranes called 'lipid-rafts'. Caveolae-mediated endocytosis is dependent on lipid rafts for its function. Caveolae are flask-shaped structures (50-80nm) that are rich in proteins and lipids such as cholesterol and sphingolipids and may be involved in signal transduction (Anderson 1998). Caveolae-independent lipid raft-dependent endocytosis also exists and has recently been identified to involve microdomains (40-

50nm) that contain a protein called flotillin (Frick et al 2007). But this mechanism is not yet fully understood.

A form of clathrin-independent endocytosis that does not involve the formation of lipid rafts is phagocytosis. This is a receptor-mediated uptake of exogenous materials by specialised phagocytic cells such as macrophage. This route of uptake leads to internalisation of relatively large (>1µm) patches of membrane (Mayor & Pagano 2007) and engulfment of the exogenous material into lysosomes either for destruction or antigen presentation. Hence, phagocytic cells act to destroy materials that may be harmful to other cells and also alert immune system cells to their prescence.

Phagocytic cells make up a minority of the total cell population in the nasal cavity and therefore are not thought to contribute to cellular uptake in therapeutic concentrations (Mygind & Dahl 1998). Furthermore, processing of drugs by the lytic enzymes and acidic pH conditions present in the lysosome may reduce drug potency. Consequently, other forms of endocytosis (macropinocytosis and clathrin-mediated endocytosis) represent more promising trancellular routes of drug uptake into cells that may allow therapeutic levels of drug to enter the body without substantial damage to the drug molecule.

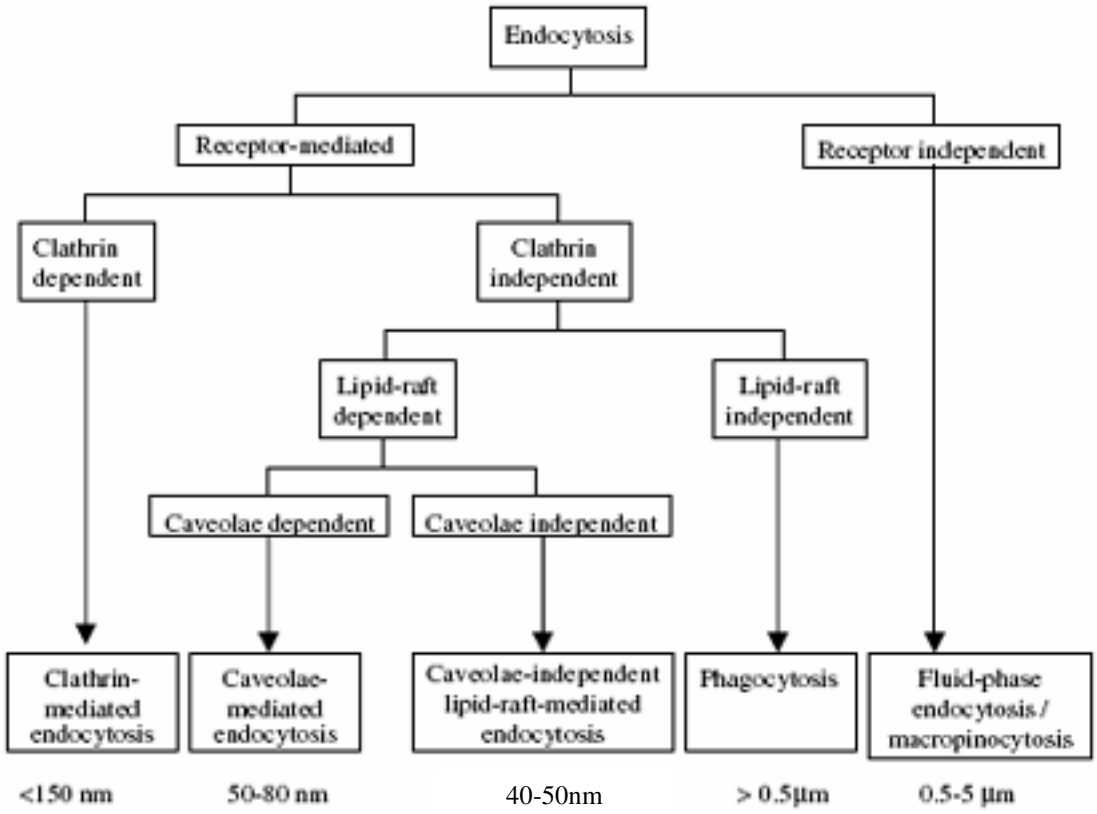

Figure 1.9 Cellular endocytic pathways (adapted from (Xiang et al 2006))

Overall, in many cases, it is not yet fully understood how substrates such as nanoparticles initiate the process of cellular internalisation. Moreover, some commentators have even questioned the existence of a 'cargo specific' mechanism of uptake (Sorkin 2004).

However, the lack of clear understanding of endocytic mechanisms should not dampen optimism. Knowledge from novel microscopic and spectroscopic techniques continually adds to the understanding of endocytosis (Gaidarov et al 1999). Phagocytosis may lead to damage of the drug molecule, however, other lipid raft-dependent mechanisms (which include caveolae or flotillins) form vesicles that could deliver very small nanoparticles (40-80nm diameter) into the cells. Moreover, clathrin-mediated and macropinocytosis vesicles are larger (<150nm and 0.5-5µm, respectively) and allow

passage of nanoparticles into cells in greater quantities which could be of therapeutic benefit. A better understanding of how these later two processes initiate could lead to the development of nanoparticles that can target these routes of uptake.

With respect to nose-to-brain drug delivery of nanoparticles it is clear that the delivery of different nano-sized particles may lead to uptake of the drug carriers into different endocytic pathways. The fate of the nanoparticles is dependent on one or more of these individual systems. Hence, altering nanoparticle size and composition could be useful approaches to improving their cellular uptake into olfactory epithelial cells.

1.4 EARLY NOSE-TO-BRAIN THERAPEUTICS

Intranasal administration of medicines and recreational therapeutics has been used throughout humanity. For example, ancient Tibetans used extracts of sandalwood and aloewood given nasally as anti-emetics (Rinpoche & Kunzang 1973). Today, cocaine, a highly addictive central nervous system stimulant extracted from the leaves of the coca plant (*Erythroxylon coca*) is administered intranasally for recreational use (Madge 2001). However, a fuller understanding of the transport pathways of drugs directly from N-B has only become available in recent times.

1.5 VIRAL PARTICLES AND ENVIRONMENTAL POLLUTANTS IN THE OLFACTORY SYSTEM

Workers in the heavy metals industry have shown symptoms of clinical pathologies that are associated with poisoning of the brain (Sunderman 2001). For example, workers with chronic exposure to methylmercury can show symptoms of impaired visual, auditory and/or gustatory sensations.

Moreover, when instilling solutions of heavy metal toxicants (e.g. mercury, zinc and cobalt) to the occluded nasal cavities of rats, the metal ions appeared in distal tissues such as the olfactory tract, bulb and cortex (Henriksson 1998; Persson et al 2003b; Persson et al 2003a). It is thought that they traversed the olfactory epithelium from where they navigated to the brain.

This interpretation concurs with that for viral particles whereby herpes simplex virus and mouse hepatitis virus are found in mice olfactory bulbs after intranasal inoculation (Barnett et al 1993).

These observations lead to the suggestion that an 'olfactory' pathway exists that can completely bypass the somewhat impenetrable BBB.

1.6 THE TRANSPORT OF DRUG SOLUTIONS DIRECT FROM NOSE-TO-BRAIN

Investigations of the transport pathways of drugs from the nasal cavity to the CNS have been a result of the observations made from traditional medicines, viral particles and heavy metal poisonings of the brain. The following summary highlights key experiments that have progressed the understanding of N-B drug delivery of solutions to date. Analyses of similar findings have previously been reviewed elsewhere (Illum 2000, 2004; Merkus & van den Berg 2007).

Physicochemical properties (logDC, pK_a and MW) of drug molecules can affect intranasal absorption into the brain. For example, the CSF and plasma drug concentrations obtained for four sulphonamides (with molecular weights of 173.2 to 278.3) were compared after *i.v.* and *i.n.* administration in Wister rats (Sakane et al 1991). The CSF concentration of drug at 60 minutes after dosing was positively related

to its partition coefficient. Hence, *i.n.* drug absorption increased with increasing drug lipophilicity using the nasal perfusion model (Hirai et al 1981). The bioavailability of these drugs into the CSF was ~0.1% of the administered dose 60 minutes after dosing.

The effect of drug ionisation was also studied using a similar nasal perfusion model by the same group (Sakane et al 1994). In order to change the degree of drug ionisation between samples, sulphisomidine (pK_a 7.5) was nasally perfused with different buffer solutions over the pH range 5.5-9.4. The CSF drug concentration was found to increase as the concentration of the unionised drug form increased. Bioavailability of sulphisomidine into the CSF was low (~0.1-2% of the administered dose) which was similar to that for sulphonamides that were previously studied (Sakane et al 1991).

To investigate the effect of molecular weight, fluorescently labelled dextrans up to 40kDa were used in a similar experiment as above (Sakane et al 1995). The largest molecular weight of detectable dextrans was 20kDa, therefore, molecules larger than this are not likely to pass into the CSF between the olfactory epithelial cells (paracellularly). The absorption of dextrans into the CSF decreased with increasing size (from 4kDa to 20kDa). Also, the CSF bioavailability of these compounds was 2-3 orders of magnitude lower than that for the sulphonamides (Sakane et al 1991; Sakane et al 1994). Therefore, drugs of molecular weight less than 4kDa are likely to absorb into the CSF more efficiently than larger ones. This is similar to findings by McMartin *et al.* (1987) as described earlier in this review.

Hence, it is thought that the transport of drugs through these different routes could be manipulated by changing the physicochemical properties of the drug. Thus, increasing

hydrophilicity and reducing molecular weight of drugs may increase paracellular uptake; whereas increasing lipophilicity and reducing degree of ionisation may increase trancellular uptake of drugs.

Unfortunately, increasing drug absorption into the CSF after *i.n.* administration may not be as simple as making physicochemical changes to the drug molecule. For example, one study used a series of antihistamines (hydroxyzine, chlorcyclizine, triprolidine and chlorpheniramine) to investigate the absorption of drugs from the nasal cavity into the CSF compared to plasma. Two of these drugs, hydroxyzine (MW375, 2.37 logDC) and chlorcyclizine (MW300, 2.91 logDC), were cationic in pH6.8 0.1M Sørensen's phosphate buffer, had similar molecular weights and similar logDC values. The nasal cavities of male Sprague-Dawley rats were isolated *in vivo* and drug solutions were applied intranasally. CSF samples and intra-arterial samples were analysed by HPLC for drug levels after 3 hours. Although the physicochemical properties of the drugs were similar, four times more hydroxyzine was found in the CSF compared to plasma; whereas, chlorcyclizine was not detectable in the CSF after *i.n.* administration (Chou & Donovan 1997). The different antihistamines may have been metabolised or effluxed by the nasal epithelium at different rates. Therefore, transport of drug directly into the CSF is determined by a combination of molecular and biological properties of the drug which are difficult to predict.

Nevertheless, an *in vitro* diffusion chamber experiment such as the one described in Chapter 2 can be used to investigate paracellular/transcellular drug transport routes through epithelia. Indeed, Jansson (2004) found that 1mg/ml [^{3}H]-dopamine was transported across the porcine olfactory mucosa both transcellularly (because this route

was saturated by the addition of 4mg/ml [^{3}H]-dopamine) and paracellularly (because permeability of [^{3}H]-dopamine to the epithelium was negatively correlated with the 'leakiness' of the epithelium as measured by the electrical resistance across the epithelium). This conclusion was strengthened by earlier (*in vivo*) observations made by Dahlin *et al.* (2000) (described later).

The *in vitro* diffusion chamber method can also be used to evaluate the effect of drug formulations on the morphological appearance of the epithelium after exposure of the formulation to the mucosal surface. For example, porcine nasal respiratory epithelium was exposed to varying concentrations of a non-ionic surfactant (polyethyleneoxide-8-lauryl ether) for 150 minutes at 37°C in Krebs Ringer Bicarbonate buffer solution (pH7.4) (Ekelund et al 2005). Transepithelial electrical resistance (R_m) was measured to determine the damage induced by the different concentrations of surfactant. Reductions in R_m were found as surfactant concentrations increased above 0.2mM. This correlated well with the assessment of damage to the epithelial cells after histological examination of the dismounted nasal mucosae (i.e. more cellular damage was found as R_m decreased).

Other drugs have also been shown to be transported directly to the brain after intranasal administration. [^{3}H]-morphine was found in the CSF surrounding the olfactory bulbs by autoradiography in male Sprague-Dawley rats within 5 minutes of *i.n.* administration (Westin et al 2005). After 60 minutes the morphine was found in the olfactory bulb ipsilaterally to the side of the nasal cavity that was administered with the dose. A gradient of radioactivity was observed in the brain at this time point where higher levels of morphine were found closer to the cribiform plate. This showed that the radioactivity

originated from the nasally cavity. The radioactivity in the olfactory bulb was cleared 240 minutes after dosing. However, no significant penetration of the radioactivity was detected in deeper brain regions.

A similar study using 5µCi [^{3}H]-dopamine in female NMRI mice showed that significantly more radioactivity was found in the olfactory bulb that was ipsilateral to the dosing side of the nasal cavity (Dahlin et al 2000). Two radioactivity peaks were observed in the olfactory bulbs; first at 30 minutes (the earliest sampling time point) and later at 4 hours. This indicated that the drug was passing through two alternative pathways. The earlier appearance of radioactivity was attributed to paracellular passage of drug between olfactory axons whereas the later peak was attributed to transcellular passage of drug through the axons. This was later confirmed by Jansson's (2004) *in vitro* method as described previously. However, in this experiment only 0.12% of the administered dose was detected in the olfactory bulbs 4 hours after dosing which was similar to that found by Sakane *et al.* for sulphonamides (1991a, 1991b).

Dahlin *et al.* (2001) conducted a similar experiment as described above but this time 50µCi [^{3}H]-dopamine was placed into the nasal cavity in order to investigate whether a higher radioactivity dose could enable detection of radioactivity in deeper brain regions after *i.n.* dosing. Indeed a significantly greater amount of radioactivity was detected after 30 minutes in the cerebellum and cerebrum of the mice after *i.n.* dosing compared to intravenously dosed animals (Dahlin et al 2001). However, despite this, bioavailability remained low since 0.1% of the nasally administered dose was detected by HPLC in the CSF 30 minutes after dosing. This may have been partly due to

dopamine metabolism to dihydroxyphenylacetic acid (DOPAC) that was shown to have occurred by TLC either during the transfer to or in the CSF.

Macromolecular transport has also been shown from N-B (Frey et al 1997; Dufes et al 2003). One detailed study followed the transport of [^{125}I]-IGF-I, a 7.65kDa protein neurotrophic factor, after *i.n.* or *i.v.* administration in Sprague-Dawley rats both in the olfactory system and trigeminal nerve (Thorne et al 2004). In this study, the animals were killed and transcardially perfused 29-30minutes after dosing with 1.25% glutaraldehyde/1% paraformaldehyde in 0.1M Sørenson's phosphate buffer. The key findings from this study were: (i) a 100-fold greater [^{125}I]-IGF-I concentration was found in most CNS areas after *i.n.* administration compared to *i.v.*; (ii) CNS levels peaked earlier after *i.n.* compared to *i.v.*; and (iii) highest concentrations appeared in rostral brain areas (olfactory bulb, motor cortex, anterior olfactory nucleus), caudal brain areas (medulla, cervical spinal cord) and in the trigeminal nerve. These observations were all consistent with the existence of a N-B pathway that involved both the olfactory system and the trigeminal nerve.

Nevertheless, despite these observations, there was no [^{125}I]-IGF-I found in the CSF. The authors' speculated that this could be a result of a direct connection between the brain interstitial fluid and the nasal lymphatic system that avoided the involvement of the CSF.

An alternative explanation, however, is that the supporting cells (or sustantacular cells) in the olfactory mucosa may play a role in the N-B uptake of [^{125}I]-IGF-I by transcellular uptake of the peptide and subsequent transport into the *lamina propria*

where it can access both the lymphatic system and the trigeminal nerves. This would account for both the lack of [^{125}I]-IGF-I in the CSF (because the 7.65kDa molecule was too large to be paracellularly transported) and the appearance of [^{125}I]-IGF-I in the olfactory system (by transcellular transport into the olfactory axons), trigeminal nerve (by uptake in the *lamina propria* after transcellular transport through the supporting cells) and the lymphatic system (by uptake into the nasal lymph vessels in the *lamina propria*).

To strengthen this hypothesis, Jansson found by fluorescence microscopy that FITC-labelled dextran (3kDa) was transported transcellularly in male Sprague-Dawley rats in both olfactory neurones and supporting cells after *i.n.* administration (Jansson 2004). However, the supporting cells only transported the dextran into certain parts of the olfactory epithelia. The reason for the uneven regional distribution of dextran amongst supporting cells was unclear. However, this does allow an important distinction to be made i.e that dextran appeared in the *lamina propria* only when it was transcellularly transported by supporting cells. If true, then transport of the 3kDa dextran to the *lamina propria* (and further to the lymphatics and trigeminal nerve) is regulated by uptake into the supporting cells.

However, this hypothesis has not yet been proven experimentally in terms of the exact mechanism by which substances such as [^{125}I]-IGF-I (Thorne et al 2004) or manganese (Fechter et al 2002) is transported by the trigeminal nerve.

The experiments that have been highlighted thus far have all used animal models. Relatively few studies have been performed on human subjects. These human studies do

not report absolute measurements of drug in the CSF or brain tissues since it would be unethical to do so. Nevertheless, a number of studies have demonstrated the pharmacological effects of drugs on the brain directly from the nasal cavity. Below are the findings of important direct N-B studies in humans. A more detailed review of human direct N-B studies can be found elsewhere (Illum 2000; Stockhorst & Pietrowsky 2004).

Pietrowsky *et al.* (1995) administered doses of 10µg *i.n.*, 0.25µg *i.v.* or 2.5µg *i.v.* cholecystokinin (CCK) (a neurologically active peptide hormone), or (*i.n./i.v.*) placebo to groups of five human subjects. Auditory event related potentials were recorded by an electroencephalogram to distinguish the effects of CCK via the different drug delivery routes. The area under the curve of the electroencephalogram P3 complex was used to determine the effect of the drug on each subject. Plasma CCK levels were measured by an antibody assay and were equivalent for the 10µg *i.n.* and 0.25µg *i.v.* groups; but higher for the 2.5µg *i.v.* group. P3 complexes were significantly larger for 10µg *i.n.* compared to *i.n.* placebo ($p<0.01$ ANOVA) and 0.25µg CCK *i.v.* ($p<0.05$ ANOVA). This showed that CCK produced a significantly greater pharmacological effect via the *i.n.* compared to *i.v.* route. In addition, the 2.5µg *i.v.* dose did not produce a greater pharmacological effect than 0.25µg *i.v.* which demonstrated that the *i.v.* route was saturated at the higher dose. These findings show strong evidence for an enhanced drug effect directly to the brain via the nasal cavity (Pietrowsky et al 1996a).

CCK was chosen as a model drug in this study since it is an endogenously expressed neuropeptide/neuromodulator whose release may be mimicked by *i.n.* administration. It is a hormone that, like other hormones, has the potential to complement a high density

of suitable receptors in the CNS. Nevertheless, the observed pharmacological effects may have resulted from axonal depolarisation due to receptor-ligand interaction at the level of the olfactory epithelium (or its accessory neuroepithelium, the vomeronasal organ) rather than a direct pharmacological effect in the brain parenchyma. This criticism may be extended to similar studies that use endogenous hormones (e.g. vasopressin (Pietrowsky et al 1996b) and insulin (Benedict et al 2008)). Hence, tracing radiolabelled drug would provide better evidence for direct N-B transport into the human brain interstitium.

An attempt has been made to trace radiolabelled diethylenetriamine penta-acetic acid (^{99}Tc-DTPA) through the olfactory epithelium after deposition of the drug solution onto the neuroepithelium via vinyl tubing (Okuyama 1997). A gamma camera was used to conclude that radioactivity had penetrated olfactory epithelium of a 67 year old anosmic woman. However, this result could neither be quantified (due to the limitations of the gamma camera) nor was it reproducible in a 60 year old healthy man. It was thought that inflammation of the olfactory epithelium that caused the anosmia could also have increased the neuroepithelial permeability to ^{99}Tc-DTPA. Nevertheless, this is a suitable method to reveal the fate of the radiolabelled drug after *i.n.* administration, especially, with the use of modern Positron Emission Tomography techniques that may accurately locate the radiolabelled product within the human cranium.

In conclusion, the direct N-B transport of numerous small molecular weight and macromolecular drugs have been proven in a variety of animal models. Indeed, intact peptide drugs have been shown to appear in brain parenchyma areas distal to the nasal cavity in rats (Thorne et al 2004). However, a similar body of evidence does not exist

for human subjects. Attempts have been made to evaluate the direct N-B pharmacological effects of various endogenous hormones. However, the transport of these molecules into the olfactory system has not been conclusively determined since it could not been excluded that they did not innervate the nasal neuroepithelia by receptor-ligand interactions (Stockhorst & Pietrowsky 2004). Future studies could combine behavioural investigations with radiolabelled drugs so that pharmacological effects and location of radioactivity may be correlated to provide stronger evidence of direct N-B drug delivery in humans.

1.7 NOSE-TO-BRAIN TRANSPORT OF SYNTHETIC PARTICLES

This section considers some of the key studies that have developed the understanding of N-B delivery of particles. To date fewer studies, than those published on N-B drug delivery of non-particulate drug formulations, have specifically examined the direct transfer of particles from the nasal cavity to the brain. Those that have mostly used basic particulate materials such as iron (II) oxide (Wang et al 2007), manganese oxide (Elder et al 2006), gold (De Lorenzo 1970), carbon-13 (Oberdorster et al 2004) and iridium-192 (Semmler et al 2004a). These particles have demonstrated a proof of concept (with varying degrees of success) for direct N-B transport of particulate matter. They were mostly carried out in relation to an evaluation of the toxicity to the CNS of environmental nanoparticles. The application of these basic materials for nanoparticle N-B drug delivery has a narrow scope (if at all) since they have no known targeting ability towards the olfactory system and their translocation has resulted in brain toxicity in some cases.

For example, drug delivery studies have shown statistically greater appearance of model drugs such as nimodipine in the olfactory bulb (Zhang et al 2006) or enhanced pharmacological activity of morphine (Betbeder et al 2000) when these small molecules were applied intranasally in combination with nanoparticles. However, the fate of the nanoparticles was not investigated in these studies therefore it is not clear whether the effects were caused by transport of the nanoparticles into the olfactory epithelial cells.

A study using Fe_2O_3 nanoparticles (280±80nm diameter) demonstrated the deep brain penetration of the metal oxide and its potential to disrupt cellular morphology in the hippocampus after nasal administration (Wang et al 2007). A dose of 40mg/kg was *i.n.* instilled into 4-week old male mice (20-22g). The brain samples were examined for iron by absorption spectroscopy 14 days after a single dose exposure. Olfactory bulbs and brain stems were indeed found to contain more iron than the control group which were exposed to an *i.n.* 1% sodium caroboxy methyl cellulose solution.

In addition, the hippocampus of the Fe-exposed group was also histologically dissimilar to that of the control group. These mice contained signs of toxicity since 'fatty degeneration' features were found in the hippocampus region. It was concluded that the iron was responsible for the toxicity. A direct passage of iron from nose to brain was hypothesised as the route of uptake possibly by the trigeminal nerve since the trigeminal nerve has shown to connect the nasal mucosa with the hind brain regions of the rat (1.6 The Transport of Drug Solutions Direct from Nose-to-Brain). The results showed that iron penetration to deep regions of the brain was possible by the intranasal route. An *i.v.* control group, however, was not included in this study therefore the observation may

have been due to systemic absorption of Fe from the nasal cavity and subsequent translocation to the deep brain regions via receptor-mediated uptake at the BBB.

In another study, poorly soluble (MnO, Mn_2O_3) salts of manganese were inhaled through the nose as aerosol by rats (200-250g body mass) (Elder et al 2006). The nanoparticles had a diameter of 30nm. Manganese was detected, after 6 and 12 days of inhalation exposure (these were repeated exposures of 6 hours/day, 5 days/week), in the olfactory bulbs and also in deep brain structures such as the cortex and cerebellum by using graphite absorption spectroscopy of microdissected brain structures (olfactory bulbs, striatum, trigeminal ganglions, midbrain, frontal cortex, and cerebellum). The manganese salts used in this study were poorly soluble and therefore the manganese was thought to have remained in the particulate form when transported into the brain. Unfortunately, images of the (30nm) nanoparticles in these brain regions were not shown in the publication therefore strong evidence of actual uptake of the manganese salt in particulate form was not presented.

In an important study, De Lorenzo (1970) visualised exogenous particulate matter (50nm colloidal gold particles) within the olfactory neurones by TEM. The gold was suggested to enter the receptor cells by an endocytic process into the axoplasm within 30 minutes. They were moved along the axon possibly by a mechanism related to microtubules in the cytoplasm. The velocity of this movement was estimated to be 2.5mm/hr (De Lorenzo 1970). This was inline with observations made of poliomyelitis virus in rhesus monkey sciatic nerve (2.4mm/hr) (Bodian & Howe 1941). Within 60 minutes of application to the nasal cavity the gold particles were seen in the *filia olfactoria* and olfactory glomerulus having crossed the (first-order) synapse to reach the

mitral cells. At this point (in the olfactory bulb) the particles were mostly located within mitochondria; the reason for this is unclear but it is evident that translocation of nanoparticles into the mitochondria can lead to cellular toxicity (Li et al 2003). Furthermore, the particles did not appear to travel extra-axonally.

In another experiment, 14 week old rats (mean body mass 284g) were twice exposed to (insoluble) ~36nm elemental ^{13}C nanoparticles (150-170µg/m^3) in an inhalation chamber for a total of 6 hours (Oberdorster et al 2004). Exposing the rats to the nanoparticles by inhalation chamber is thought to allow nanoparticles access to the rat nasal cavity since the animals are obligate nasal breathers. The results showed that there was a significant ($p<0.05$) and persistant increase of ^{13}C of 0.35µg/g to 0.43µg/g in the olfactory bulbs from day 1 to day 7. Also, deeper brain penetration of these particles into the cerebellum and cerebrum was not conclusive since a significant increase in radioactivity was not consistently observed during the full duration of the experiment. More repeated exposures may have increased the concentration of ^{13}C nanoparticles in the cerebrum and cerebellum.

Low levels of 20nm iridium-192 nanoparticles (insoluble) have also been observed over a 6 month period in the brain after inhalation of a single dose of particles via an intratracheal tube (Semmler et al 2004b). A peak number of particles were found in the rat brains 7 days after a 60-90 minute single exposure. This rate of transfer appears to be much slower than the movement of 50nm gold particles from the nasal cavity to the olfactory bulbs in rabbits as described earlier (De Lorenzo 1970). The differences between the rates of transport could have been due to the different time points at which

samples were taken in each case. Hence, a larger peak may have been expected if a measurement of iridium-192 particles were made after 60 minutes post application.

Enhancement of nimodipine delivery to the brain was seen when it was intranasally applied in methoxy-PEG-PLA (MPEG-PLA) nanoparticles (76.5nm diameter) compared to solution alone (Zhang et al 2004). Statistically more drug appeared in the CSF compared to the blood in rats. Furthermore, 1.6-3.3 times more drug was found in the CSF and olfactory bulb after administration of nanoparticles compared to the drug solution alone. The nanoparticles may have been taken into the cells and the drug released thereafter. However, from analysis of the available literature (Table 1.1), it is likely that the drug would also have been released from the nanoparticles in the mucous layer from where it would be absorbed paracellularly through the tight junctions between cells in the epithelium. The increased bioavailability conferred by nanoparticles may have been due to the protection of the encapsulated drug from: i) biological and/or chemical degradation, and/or ii) extracellular efflux by P-gp transporter proteins.

Nasally applied morphine only increased analgesia in mice when 60nm maltodextrin nanoparticles (Biovectors™) were mixed with [^{3}H]morphine compared to [^{3}H]morphine solution (Betbeder et al 2000). The effect was not due to increased levels of [^{3}H]morphine transported into the brain via the blood because an *s.c.* dose of morphine produced higher plasma levels but lower analgesia than the *i.n.* dose of morphine+Biovectors™. Also, *i.n.* morphine+Biovectors™ produced similar plasma levels as *i.n.* morphine solution which also did not explain the increased analgesia via the blood. Hence, another route was involved which was speculated as the direct N-B

pathway. The analgesic effect was reversed by naloxone, an opioid antagonist, which shows that the analgesia was opiod-induced.

Although this evidence showed that morphine may have transferred by the direct N-B route, the exact mechanism of morphine uptake was uncertain. For instance, the nanoparticles do not interact with the morphine *in vitro* and the analgesic effect is not enhanced by sodium deoxycholate, a tight junction modifier (or permeation enhancer), which was expected to increase the delivery of morphine to the brain by opening tight junctions.

An attempt has also been made to improve N-B transport of particles by conjugation of Wheat Germ Agglutinin (WGA) lectin to coumarin-loaded PEG-poly(lactic acid) (PEG-PLA) nanoparticles (85-90nm diameter) (Gao et al 2006). WGA binds to N-acetyl-D-glucosamine and sialic acid residues both of which are abundant in mucus. A 2-fold increase in coumarin was observed in the olfactory bulb, olfactory tract, cerebrum and cerebellum of rats within 15 hours of a single dose compared to unmodified nanoparticles without any evidence of ciliotoxicity. The enhanced uptake was, however, thought to be poorly selective for coumarin delivery directly to the brain since similar increases were also observed in the blood. This was probably due to poor selectivity of WGA binding to the olfactory mucosa. However, these particles were not designed to be selectivity transported into the olfactory mucosa.

A more recent investigation by the same group does provide evidence for successful targeting to the olfactory epithelium, which was suggested by visualisation of nanoparticle uptake in the olfactory epithelium, in rats (Gao et al 2007). The PEG-PLA

nanoparticles (111nm diameter) were conjugated to *Ulex europeus* agglutinin I (UEA I), a lectin that binds to an olfactory rich saccharide – L-fucose. Detection of coumarin (which was associated with the nanoparticles) in the different brain regions was 1.7 times increased after surface modification with the lectin compared to unmodified particles. In addition, fluorescence microscopy shows that the affinity was enhanced for UEA I-modified nanoparticles to the olfactory epithelium compared to the respiratory mucosa. Nevertheless, the visual evidence provided in the article showed a low magnification image of the nasal tissues. Higher magnification images could have enabled a detailed analysis of individual particles inside the olfactory epithelium as well as details of the morphological condition of the olfactory epithelium. This would have provided yet stronger evidence for the uptake of individual particles into undamaged olfactory neurones.

Recently, the literature has shown that nanoparticles are not inherently benign towards biological systems (Oberdorster et al 2005; Nel et al 2006). Nanoparticles may affect the biological behaviour of cells, subcellular organelles and proteins, to cause injurious responses. The oxidative stress paradigm best describes the toxic effects of inhaled nanoparticles. Under normal conditions reactive oxygen species (ROS) are generated in mitochondria which can be easily neutralised by antioxidants such as glutathione in cells. Oxidative stress occurs when glutathione is depleted by the ROS. Oxidative stress can be triggered by the presence of nanoparticles, possibly due to their large relative surface area and/or their greater ability to gain access into mitochondria, which can disrupt cellular function (Xia et al 2006). The formation of ROS can lead to tissue inflammation and cellular damage and damage to DNA and enzymes.

In summary, there is evidence to suggest that direct N-B transport of synthetic nanoparticles is possible and may be even to therapeutic levels of bioavailability. Nevertheless, it is still unclear whether whole particles can be selectively taken into the olfactory epithelial cells. The clearest evidence of uptake of synthetic particles into olfactory neurones remains with that published by De Lorenzo (De Lorenzo 1970). However, intracellular axonal transport may not be necessary since an analysis of the available literature tentatively suggests that targeting of different brain regions may be possible by altering the basic properties of the drug delivery system such as nanoparticle size or drug physicochemical properties (Table 1.1). It has also been suggested that nanoparticles may cause cellular and subcellular damage to biological systems. The challenge now is to improve the transfer efficiency of drug loaded particles from the olfactory epithelium to the brain in order to safely and successfully reach therapeutically relevant levels in the target brain regions.

Future studies could use fluorescently labelled nanoparticles composed of non-biodegradable polymer which could determine the route of these particles from the olfactory epithelium to the brain and possibly their further fate through clearance. Other information such as the transport rate of different sized nanoparticles to the brain and evaluating the effect of different surface modifications (or other formulation strategies) would provide useful information and progress in the field.

1.8 SUMMARY: DIRECT NOSE-TO-BRAIN TRANSPORT OF DRUG DELIVERY FORMULATIONS

Table 1.1 summarises the properties of drug formulations, their suggested route of transport and possible destinations into the CNS. The conclusions are based on the current anatomical knowledge of the connection between the nasal cavity and the brain

and the available evidence from drug transport studies that are detailed in sections 1.6 The Transport of Drug Solutions Direct from Nose-to-Brain and 1.7 Nose-to-Brain Transport of Synthetic Particles of this review.

In general, lipid soluble drugs are more likely to take the transcellular route to the brain. Water soluble drugs (<1000Da) may have rapid access to CSF compared to lipohilic molecules since they are less likely to be taken into the neuronal and supporting cells of the olfactory epithelium. Nanoparticles may be taken into the neurones and supporting cells by a number of endocytic mechanisms. However, nanoparticles larger than 100nm are thought to have a restricted access to the brain via the intra-axonal route because their diameters increasingly exceed that of the axons in the *filia olfactoria*.

Table 1.1 The influence of drug formulation on the cellular route of uptake and final CNS destinations of drugs after intranasal administration

Drug Formulation	Transport Route	Transport Pathway	Possible Drug Destinations in CNS	Reference
Solution (Drug Lipophilic)	Transcellular (Supporting Cells, Olfactory Axons)	Olfactory, trigeminal	Rostral brain, caudal brain	(Sakane et al 1991)
Solution (Drug MW<1000Da, Hydrophilic)	Transcellular (Supporting Cells, Olfactory Axons) by endocytosis (Phagocytic, Macropinocytic, Clathrin-mediated, Caveolae-mediated, Caveolae-independent lipid raft). Paracellular.	CSF, Olfactory, trigeminal	Rostral brain, caudal brain. (Drug delivered to CSF may not penetrate the brain parenchyma before clearance)	(Dahlin et al 2000; Dahlin et al 2001; Westin et al 2005)
Solution (Drug MW>1000Da, Hydrophilic)	Olfactory Axons, Supporting Cells	Olfactory, trigeminal	Rostral brain, caudal brain	(Thorne et al 2004)
Nanoparticle (>150nm)	Endocytosis (Phagocytic, Macropinocytic)	Olfactory, trigeminal*	Rostral brain, caudal brain*	(Wang et al 2007)
Nanoparticle (<150nm)	Endocytosis (Phagocytic, Macropinocytic, Clathrin-mediated)	Olfactory, trigeminal	Rostral brain, caudal brain	(Gao et al 2007)
Nanoparticle (<80nm)	Endocytosis (Phagocytic, Macropinocytic, Clathrin-mediated, Caveolae-mediated)	Olfactory, trigeminal	Rostral brain, caudal brain	(De Lorenzo 1962, 1970; Zhang et al 2006)
Nanoparticle (<50nm)	Endocytosis (Phagocytic, Macropinocytic, Clathrin-mediated, Caveolae-mediated, Caveolae-independent lipid raft)	Olfactory, trigeminal	Rostral brain, caudal brain	(Oberdorster 2004; Semmler et al 2004b; Elder et al 2006)

* Bioavailability theoretically limited for nanoparticles with diameter >100nm due to diameter of olfactory axons in *filia olfactoria*

1.9 NANOPARTICLE FORMULATION STRATEGIES FOR ENHANCING NOSE-TO-BRAIN DRUG DELIVERY

Nanoparticles may offer a realistic transmucosal drug delivery strategy since they are able to protect the encapsulated drug from biological and/or chemical degradation, and extracellular transport by P-gp efflux proteins. Also, their high relative surface area means that these particles will release drug faster than larger particles; this would be desirable where acute management of pain is required. In addition, their small diameter may allow them to be transported transcellularly through olfactory neurones to the brain via the various endocytic pathways as described earlier (1.3 Cellular Mechanisms For Transmucosal Drug Delivery).

By using nanoparticles as a platform technology it may also be possible to deliver a number of different drugs using similar systems. One approach would be to surface modify nanoparticles so that the drug delivery properties of the formulation are determined by the interaction of the surface coating with the biological system. To the author's knowledge, however, there has currently been no published study that has clearly proven the pharmacological efficacy of nanoparticle formulations for direct N-B drug delivery. However, chitosan and polysorbate 80 are two materials that may modify transport of nanoparticles across the olfactory epithelium as discussed below.

1.9.1 Chitosan

Chitin is one of the most abundant polymers found in nature and is present in all crustaceans and insects - as well as some fungi, algae and yeast. Chitin is extracted from the shells of crabs, lobsters and shrimps once edible portions have been removed. Chitosan is a linear polysaccharide which is derived from naturally occurring chitin by

deacteylation, using enzymatic (chitindeacetylase [Figure 1.10]) or chemical methods. It has randomly distributed ß-(1-4)-linked D-glucosamine (deacetylated unit) and N-acetyl-D-glucosamine (acetylated unit). The proportion of deacetylated units to acetylated units is reported as the degree of deacetylation (%DA).

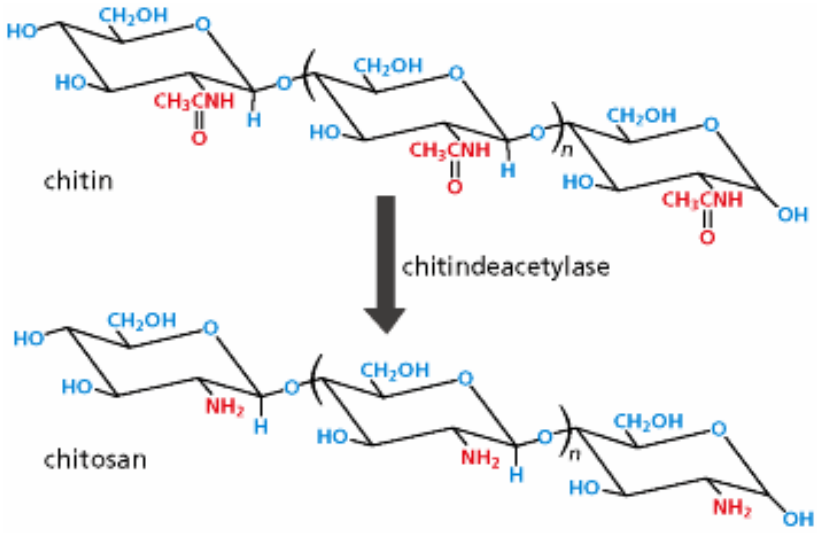

Figure 1.10 The conversion of chitin to chitosan via enzymatic deacetylation.

Chitosan has a long history of use in the drug delivery field. It has been used as an excipient in direct compression and wet granulation, in emulsions, and in gels and its uses have been reviewed numerous times. Singla *et al.* have written one such broad review (Singla & Chawla 2001).

Chitosan may also be a useful material for direct N-B drug delivery. It has mucoadhesive properties (Kawashima et al 2000) that may increase the particle residence time over the target olfactory epithelium. The positive charges on the protonated amine groups allow interaction with negatively charged sialic acid groups on mucin (Kawashima et al 2000). This benefits transmucosal drug delivery by allowing increased residence time over the target cells (possibly by altering the viscoelastic

properties of the mucus (Aspden et al 1997)), and therefore permits a greater delivery opportunity.

As a result of the general electrostatic nature of chitosan interaction with mucus it is not expected that chitosan formulation used for N-B drug delivery would selectively interact with olfactory mucosa compared to respiratory mucosa. Therefore, for optimal performance it would be advantageous for a drug delivery device to deposit a chitosan-based nanoparticle formulation over the olfactory epithelium; otherwise, drug absorption may occur through non-olfactory regions which could lead to local or systemic side effects of the delivered drug.

A recent study has compared the targeting ability of a 1% chitosan glutamate (MW 200-600kDa, 75-90%DA) in saline-acetate buffer (pH4.5) in both nasal drop and nasal spray formulations (Charlton et al 2007). Nasal drops were administered in the supine position with the head tilted back so that the formulation could drain to the olfactory epithelium at the roof of the nasal cavity. The nasal spray was administered in the upright position. It was found by nasendoscopy that nasal drops delivered the chitosan formulation over the olfactory mucosa better than the spray formulation in human volunteers. In addition, the chitosan formulation increased the olfactory residence time over the olfactory epithelium compared to saline-acetate buffer (pH4.5) control from 1.33 minutes to 12.6 minutes. This shows that chitosan can increase the residence time of formulations over the olfactory epithelium. Also, combining this with a delivery device that can target the olfactory epithelium could be a useful approach in the future.

Chitosan has also been shown to affect the permeability of epithelial membranes by its interaction with the junctional complexes between epithelial cells. It is thought that the positive charge can transiently open the tight junctions and therefore allow a paracellular passage of materials through the epithelial barrier. The exact mechanism of this is still not yet fully understood. The latest theories, however, include: (i) translocation of junctional proteins, ZO-1 and claudins, from the biomembrane to the cytosol; and (ii) functional alteration of a tight junction protein, ZO-1, by changes in protein kinase Cα (PKCα) activity (Smith et al 2004; Smith et al 2005).

Smith *et al.* (2004) used western blotting and immunofluorescence to identify protein association patterns after application of 0.5%w/v chitosan glutamate (MW128kDa, 85 DA%) buffered solution (Modified Eagles Medium pH6.3) to Caco-2 cells. They found that chitosan application could reduce the association of ZO-1 and occludins in the cell membrane and concurrently increase association of these proteins with the cell cytoskeleton. The tight junctions were opened during the application of the chitosan since significantly more Horse-Radish Peroxidase (40kDa) could pass through the cell monolayer after 60 minutes exposure ($p<0.01$) compared to buffer control (pH6.3). This was confirmed by measuring transepithelial electrical resistance (R_m). The R_m values were found to return to 80% of pre-treatment levels 24 hours after removal of chitosan.

Smith *et al.* (2005) also found, using the same materials and techniques, that chitosan increased the presence of PKCα in the Caco-2 cell membranes. This was related to ZO-1 depletion from cell membranes since a PKC inhibitor (Ro318220) reduced the chitosan-induced translocation of ZO-1 out of the cell membrane. PKC β and δ isozymes were excluded as the cause of the translocation by the same methods.

Recently, chitosan has been used as a nucleic acid delivery vehicle. Its pK_a (~6.5) allows a positive charge at acidic pHs (Howard et al 2006). This enables electrostatic interaction with nucleic acids to form polyplexes. Howard *et al.* found that siRNA-chitosan polyplexes could knockdown the green fluorescent protein signal (EGFP) both *in vitro* (human lung carcinoma cells) and *in vivo* (murine bronchiole epithelial cells) models. It was thought that chitosan allowed positively charged polyplexes to interact with negatively charged cell membranes, therefore enabling uptake into the cell.

Molecular weight, %DA and salt form of chitosan can affect its ability to interact with mucosa in the aforementioned ways. It has been found that 0.01%w/v pH6.2 solutions of different chitosan salt forms could reduce R_m reading across Caco-2 monolayers to 60% for chitosan aspartate, 53% for chitosan lactate, 43% for chitosan lactate, and 31% for chitosan HCl, of initial values (Opanasopit et al 2007). The same study showed that increasing molecular weight of the chitosan HCl could reduce R_m values across the Caco-2 cells compared to the initial values; 70% for 20kDa, 50% for 45kDa, 60% for 200kDa and 40% for 460kDa. Therefore, *in vitro*, high molecular weight chitosan HCl had the greatest effect on tight junction opening.

In addition, chitosan nanoparticles can be taken into A549 (human lung carcinoma) cells and this uptake is increased by increasing molecular weight (from 10kDa to 98kDa) and increasing %DA (from 46% to 88%) of chitosan acetate (Huang et al 2004). Also, the rate of uptake was saturated at concentration of chitosan above 0.8mg/ml which suggested that uptake was endocytic.

In summary, chitosan HCl of molecular weight >98kDa and DA% >88% may improve the uptake of chitosan containing nanoparticles across mucosal membranes. Alternatively, chitosan containing nanoparticles may improve paracellular transport of drugs that are released from the nanoparticles in the nasal mucus by opening the tight junctions. Both paracellular and transcellular transport could benefit from an increased residence time over the olfactory mucosa.

1.9.2 Polysorbate 80

Polysorbate 80 belongs to a group of non-ionic detergents called 'polysorbates'. Polysorbates are often used in cosmetics and food products as solubilising agents (Tadros 2005). They are derived from PEO sorbitan that are esterified with fatty acids. The numeric value after the 'polysorbate' refers to the fatty acid contained in each type of polysorbate.

Hence, polysorbate 80 (MW 1310) is a derivative of PEG-ylated sorbitan (MW 1073) and oleic acid (MW 237) (Figure 1.11); the two moieties composing the hydrophilic tail and hydrophobic head, respectively. In addition, like all surfactants, polysorbate 80 forms micelles in aqueous solution. Critical Micellar Concentration (CMC) polysorbate 80 in HBSS buffer (pH7.4) at 25°C has been measured at 65.5µg/ml (50µM) (Nerurkar et al 1997).

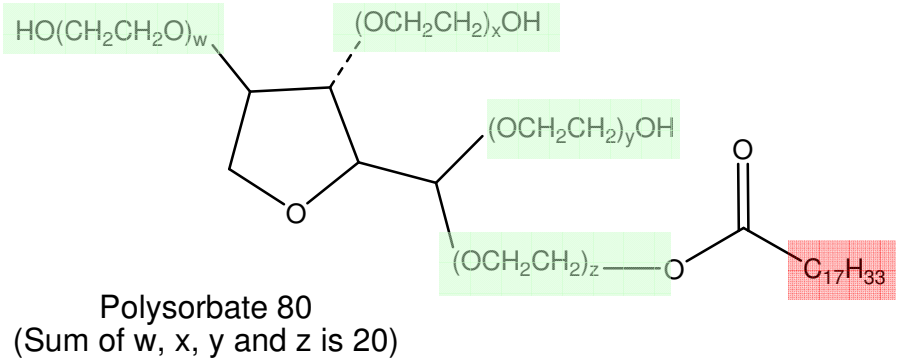

Figure 1.11 The chemical structure of polysorbate 80 containing ethylene glycol moieties (green highlight) and oleic acid (red highlight).

In biopharmaceutics, polysorbate 80 has been used in emollient eye drops (e.g. Refresh Endura, Allergan). It is regarded as an acceptable pharmaceutical excipient since it is found in the FDA GRAS list.

Polysorbate 80 may also be a useful P-gp efflux inhibitor. For example, it has been shown that efflux by Caco-2 cells of a model peptide $Acf(NMef)_2NH_2$ was effectively inhibited by polysorbate 80 (Nerurkar et al 1997). Therefore this may provide a better chance for drugs which are normally effluxed by cells to remain in the cell or be transported to its target (although the mechanism is not yet fully understood).

Polysorbate 80 has also been used as a surface modification material for particles. Its adsorption to polybutylcyanoacrylate (PBCA) particle surfaces is thought to enhance their uptake compared to the native form of the particle from the systemic circulation into the brain via the BBB (Kreuter 2001). It has been shown that polysorbate 80 achieves this by selectively adsorbing serum proteins (ApoE in particular) in cell culture which allows phagocytic uptake into the brain capillary endothelial cells (Ramge et al 2002).

In addition, the polysorbate 80-coated PBCA nanoparticles were overcoated with an analgesic hexapeptide (dalargin) and Apo E (Kreuter et al 2002). These particles were administered intravenously into mice. Analgesia was determined in these mice by tail flick test which showed that the dalargin could reach receptors in the brain in a pharmacologically active form. However, Apo E deficient mice (ApoEtm1Unc) did not show signs of analgesia. These results showed that the analgesic effect was derived from an Apo E receptor-mediated uptake of the hexapeptide.

It is thought that non-ionic surfactants alter the pattern of protein adsorption to charged particle surfaces (Muller et al 1997). Foetal Calf Serum (FCS) is a complex mixture of plasma proteins and other biological molecules. Differential adsorption of certain plasma proteins from FCS, such as Apo E, is thought to promote active uptake of polysorbate 80 coated PBCA particles into the cells as described above. It is speculated that similar mechanisms may exist that could promote the uptake of polysorbate 80-coated particles through the olfactory epithelium as well.

Polysorbate 80 can also reduce the overall zeta potential of a charged particle by sterically hindering the approach of counterions to the particle surface. This charge shielding effect may promote mucosal penetration of the coated particle, and allow access to underlying epithelial cells by reducing electrostatic repulsion between negatively charged particle and mucus (Lai et al 2007). For example, covalent modification of carboxylated PS nanoparticles with PEG (~2kDa) (a molecule similar in size and chemical composition to polysorbate 80) increased the particle transport rates of 100nm, 200nm and 500nm nanoparticles through human cervicovaginal mucus by factors of 100, 200, and 1100-fold, respectively. In my opinion, the reason for the

improved penetration is due to the steric repulsion resulting from a loss of conformational entropy of the bound PEG chains upon the approach of a mucus fibres and the low interfacial free energy of PEG in the hydrophilic water channel. If similar results were found for olfactory mucosa then this could increase transport of nanoparticles into the olfactory epithelial cells. Moreover, the authors of the study speculate that particles as large as 800nm could be transported through the mucus in this way.

Vila *et al.* (2004) investigated the effect of PLA (poly-lactic acid) particle size and particle PEG-ylation on nasal uptake into rat epithelial cells by confocal microscopy. First, 60µl (0.083%w/v in PBS) rhodamine-load PLA-PEG particles (186±11nm or 1412±200nm diameter) were intranasally administered to rats (n=4) over 30 minutes after which the animals were killed by cervical dislocation. The nasal epithelia were dissected, washed and fixed in Formalin 4% for 30 minutes. Then, the whole mucosa was observed directly by confocal microscopy. Quantitative analysis of particles could not be performed, however, visibly more nanoparticles than microparticles were observed at a depth of 10-20µm into the surface epithelial cells. Conversely, more microparticles than nanoparticles were found at the mucosal surface of the epithelium than inside cells. This result agrees with the observation by Lai et al. (2007) who concluded that larger particles penetrated mucus less successfully than smaller particles (as discussed previously).

Second, it was concluded that a PEG-coating was required to maintain the PLA colloidal stability at the nasal epithelium (Vila et al 2004). PLA (191±8nm diameter) or PEG-PLA (186±11nm) nanoparticles were administered into rat nasal cavities as

described before. It was found by confocal microscopy that fewer PLA-PEG nanoparticles aggregated at the epithelial mucosal surface compared to PLA nanoparticles. This allowed the smaller PEG-PLA nanoparticles to penetrate the mucus layer. Hence, visibly more PEG-PLA nanoparticles compared to PLA nanoparticles were found at a depth of 10-20µm into the epithelial cells. The author's speculated that lysozymes found in the mucus layer were responsible for the formation of PLA aggregates. Nevertheless, this study provides evidence that PEG-coating can improve nanoparticle transport into nasal epithelial cells *in vivo*.

1.10 PROJECT OUTLINE

The primary aims of the project are listed below.

(i) Design biological drug delivery models to investigate the physiological mechanisms that may allow the transport of nanoparticles directly from nose-to-brain

(ii) Formulate a number of novel non-biodegradable nanoparticulate systems and compare their relative abilities to transport into the olfactory system.

(iii) Monitor the affect of nanoparticle exposure to the viability and morphology of olfactory epithelia.

1.11 STUDY PLAN

Validation of the *in vitro* Franz diffusion cell method was performed in relation to viability of excised olfactory epithelium from the porcine nasal cavity. An electrophysiological method and a fluorometeric assay were used to determine metabolic activity of the dissected olfactory epithelium to ensure that the epithelium was alive during the experiments. The metabolic activity was statistically compared with samples that had been exposed to the metabolic inhibitor sodium azide. In addition, the physical condition of epithelia was examined after application of the samples in the diffusion chamber.

A number of fluorescently-labelled polystyrene-containing colloid formulations were surface modified with chitosan, polysorbate 80 or polysorbate 80+FCS. As well as the surface character, the nanoparticles were varied in diameter (20nm, 100nm and 200nm).

The transport of these fluorescently labelled nanoparticles was studied across the nasal mucosa. Transport was quantitatively and qualitatively assessed by the *in vitro* diffusion chamber and *in vivo* mouse models. In the *in vitro* system, transport of nanoparticles across the olfactory epithelium was detected by the appearance of the nanoparticles in the receiver chamber with the use of fluorescence spectroscopy. The olfactory epithelium was dismounted after the end of the experiment to examine the condition of the tissue and the association of the formulations with the mucosa. In the *in vivo* system, histological sections were taken of the mice heads after intranasal application of the test formulations. The distribution of nanoparticles in olfactory and non-olfactory samples were qualitatively assessed by fluorescence microscopy and quantitatively assessed by stereology.

2. *IN VITRO* EXPERIMENTAL SETUP AND METHOD VALIDATION

2.1 INTRODUCTION

The traditional Franz diffusion cell and the Ussing chamber methods have been used for measuring the transport of a variety of small molecular weight drugs across epithelia by applying drug formulation to the mucosal side of dissected epithelium and sampling buffer from the basolateral side (e.g. dopamine (Jansson 2004) and chlorcyclizine (Kandimalla & Donovan 2005b)).

In the present studies a modified *in vitro* approach involving the use of porcine olfactory epithelium mounted vertically in a Franz diffusion chamber was used to evaluate the transepithelial passage of nanoparticles. Advantages of this *in vitro* approach compared to an *in vivo* model are that: (i) drug transport across biological tissues can be determined in a time-related manner (ii) it is possible to demonstrate viability of the epithelium during the course of a vertical Franz diffusion cell experiment; (iii) the condition of the tissue after dismounting can be evaluated once the study is complete; (iv) it is possible to control the temperature, pH, oxygenation and composition of the buffering solutions as well as the concentration of particles applied to the mucosal surface of the olfactory epithelium; and (v) the experiments can be conducted on olfactory epithelium without the presence of respiratory epithelium.

However, it was necessary to complete a thorough method validation to ensure the scientific rigor of the model before commencing the nanoparticle transport studies (Chapter 4). Hence, it was necessary to prove that the experimental procedures had no effect on the tissue with respect to viability and cellular morphology. The aim of the work presented in this chapter is to describe the method validation of the vertical Franz

diffusion cell for its use with olfactory epithelium in the investigation of direct N-B drug delivery of nanoparticles.

First an excision protocol was established in order to ensure that the epithelium to be mounted in the diffusion chamber mounted was indeed olfactory. Second, an assessment procedure of tissue viability was developed to ensure that the mounted tissue was alive during the experiments. Finally, the morphological appearance of the olfactory epithelium before and after exposure to the experimental conditions was assessed (in the absence of nanoparticles on the apical surface).

Once this initial stage was complete, the application of nanoparticles to the olfactory epithelium could be reliably investigated (Chapter 4).

2.2 MATERIALS AND METHODS

2.2.1 Materials

2.2.1.1 Diffusion Chamber Experiments

Krebs Ringer Bicarbonate buffer from Sigma (Gillingham, UK), containing 1.5 mM NaH_2PO_4, 0.83 mM $NaHPO_4$, 1.67 mM Mg_2Cl_2, 4.56mM KCl, 119.78 mM NaCl and 10 mM D-glucose. $NaHCO_3$, $CaCl_2$, citric acid and all other chemicals were also obtained from Sigma (Gillingham, UK). 0_2(95%)/CO_2(5%) gas was obtained from BOC Special Gases (Guilford, UK).

2.2.1.2 Viability Assays

Alamar Blue™ (AbD Serotec Ltd., Oxford). Bisbenzimide Hoescht No. 33258, Papain, dibasic sodium phosphate, cysteine HCl, EDTA, saline sodium citrate, NaCl, Trizma

sodium azide and all other reagents and chemicals purchased from Sigma. Calf-thymus DNA was purchased from R&D systems (Abingdon, UK).

2.2.1.3 Microscopy Sample Preparation and Differential Stains

Glutaraldehyde, sodium cacodylate, propylene oxide, Araldite CY212, Agar 100 resin, DDSA and Dibutyl phthalate DMP 30 were purchased from Agar Scientific (Stanstead, UK). Glycine (Fisher Scientific, Loughborough, UK). IMS, osmium tetroxide (Sigma-Aldrich, Gillingham, UK). Glass knife (Thermometric Ltd, Northwich, UK). Diamond knife (Diatome, Biel, Switzerland).

2.2.2 Preparation of Physiological Buffering Solutions

Krebs Ringer Bicarbonate buffer was modified according to (Osth et al 2002a), with the addition of 15 mM $NaHCO_3$ and 1.2 mM $CaCl_2$ to make Simulated Nasal Solution (SNS). The osmolarity was adjusted to 300±5 mol/kg by the addition of NaCl and the pH was adjusted to 7.4 by adding 1M NaOH. The buffer was oxygenated using a mixture of 0_2(95%) and CO_2(5%).

Citrate buffer was identical to the SNS buffer but citric acid was used instead of NaH_2PO_4, $NaHPO_4$ and $NaHCO_3$ since these ingredients would interfere with the buffering ability of the citrate at pH 6.0. Isotonicity of the citrate buffer was maintained by the addition of NaCl as required.

2.2.3 Dissection of Nasal Epithelia from the Pig

The porcine tissue has been selected previously as suitable for *in vitro* diffusion chamber studies (Jansson 2004; Fransen et al 2007). The pig is a suitable model since (i) the olfactory epithelium is sufficiently large to obtain workable tissue pieces for loading into the diffusion cell apparatus, and (ii) gross morphology of the epithelium

and some compositional aspects of the mucus are similar between humans and pigs as described previously (Larochelle & Martineaudoize 1991).

The objectives for this section were: (i) to develop a protocol for the excision of olfactory epithelium from the head of a pig; (ii) to assess the morphology of fresh tissue samples from various parts of the porcine nasal cavity; and (iii) to confirm the location of olfactory epithelium in the porcine nasal cavity by bright field microscopy and Transmission Electron Microscopy (TEM).

For excision of porcine nasal mucosa, the tissue was isolated from 6 month old domesticated sows after slaughtering in the slaughterhouse (Sutton Bonnington Campus, University of Nottingham, UK). A health plan was in place and was agreed between a veterinary surgeon and the slaughterhouse personnel to ensure only healthy pigs were slaughtered. The animals were electrically stunned and then killed by exsanguination.

Thereafter, the head was removed and the nasal cavity exposed. To gain access to the various nasal regions a ventral incision (up to and including the hard palette) was made directly in front of the eyes (line (c)Figure 2.1) and then again ~5 cm rostrally (line (b) Figure 2.1); this gave Section C (Figure 2.1). A further cut was made ~6cm rostrally (line (a) Figure 2.1) to yield Sections B and A (Figure 2.1). This revealed the transverse profiles of the various turbinate structures as shown in Figure 2.2.

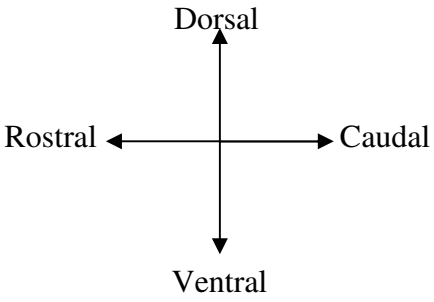

Figure 2.1 Schematics showing sections of the pig head for retrieval of porcine nasal mucosa.

Top, anatomical navigation terminology in relation to middle and bottom schema.

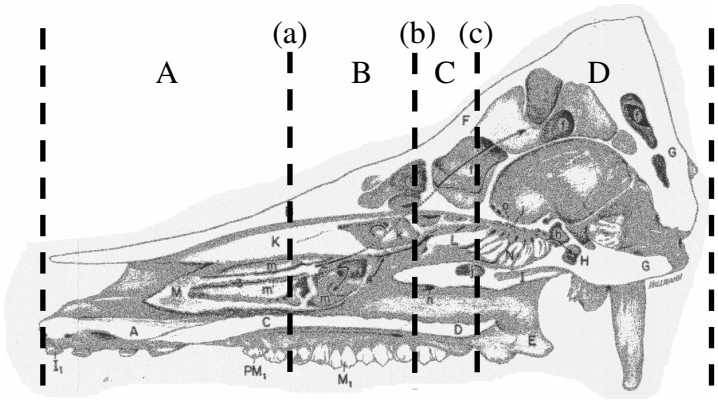

Right side of sagittal section of mature swine skull. Sections A, B, C and D. Adapted from (Getty 1975).

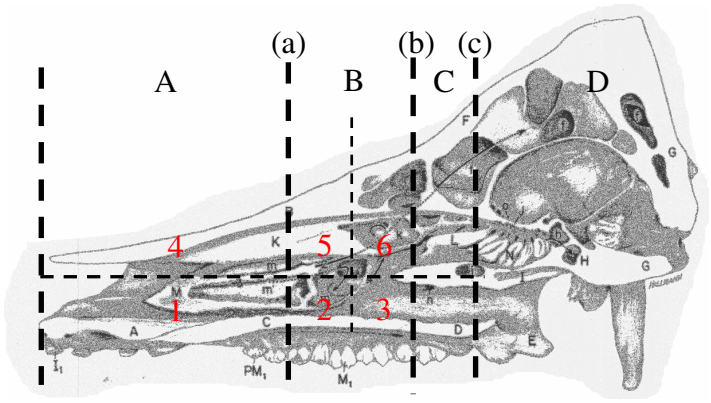

Right side of sagittal section of mature swine skull. Epithelium was retrieved from six different areas as shown. For reference, the regions are shown in relation to the sections taken above. Adapted from (Getty 1975).

Sections A, B and C were then sawn horizontally along the middle of the nasal cavity as shown in each Section by the straight dashed line (Figure 2.2). The required epithelium (labelled 1-6 in Figure 2.1) was then exposed and peeled away in the rostro-caudal direction from the underlying bone or cartilage with forceps and a haemostat. Region 5 was taken from the ventral turbinate. Arrangements were made to have quick access to the slaughtered pig so that the dissection could be performed within the shortest possible time (~15 minutes *post-mortem*).

Figure 2.2 Actual images of caudal faces of Sections A, B and C (taken at (a), (b) and (c) as per Figure 2.1). In addition, regions 1-6 from Figure 2.1 are cross referenced on each section.

Section A

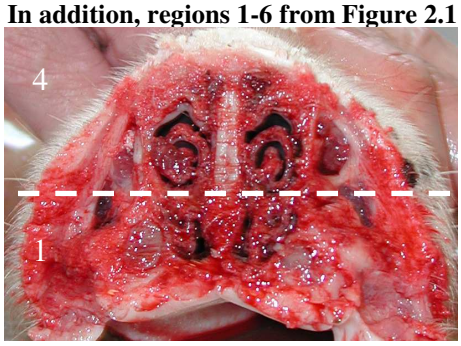

Section A demonstrates the scrolls of the turbinates. However, the mucosa lining this section lay too far anteriorly to be of the olfactory type.

Section B

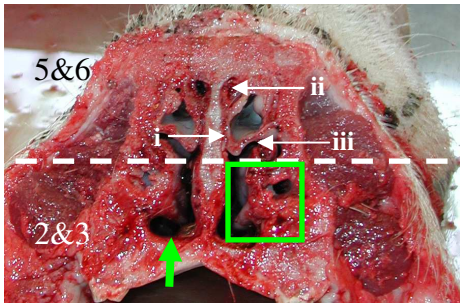

The epithelium of Section B between points (i), (ii) and (iii) was region 6. Epithelium taken from the ventral turbinate (solid line, green box) was region 5. Regions 2 and 3 were taken from the base of the nasal cavity (green arrow). Region 2 was directly rostral to region 3.

Section C

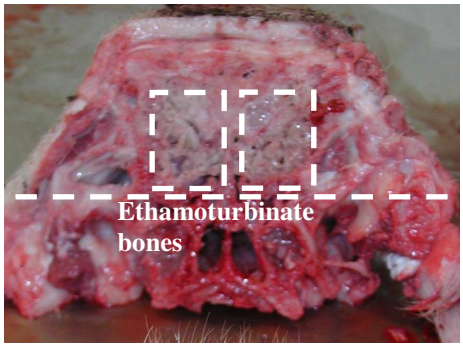

Section C was taken too close to the eyes in this animal since the ethamoturbinate bones are clearly visible and hence little olfactory epithelium was retrievable.

Each tissue sample was then processed for visualisation by microscopic techniques as described elsewhere (2.2.7 Preparation of Tissue Samples for Microscopy).

2.2.4 Vertical Franz Diffusion Chamber Studies

The olfactory epithelium (retrieved from Section B (Figure 2.2)) was easily distinguishable from the surrounding respiratory type by its yellowish appearance (due to the presence of olfactory pigment) compared to the pinkish colour of the respiratory mucosa. Within 20 minutes of slaughter, two pieces (2cm diameter) of olfactory epithelium (one from each side of the nasal cavity) were cut out with a cork borer (Figure 2.3). They were then transported to the laboratory on ice in 2 x 20ml vials containing the relevant pre-oxygenated (using O_2/CO_2 95:5 mix) buffer (0.5mM citrate buffer or SNS) to perform transport study.

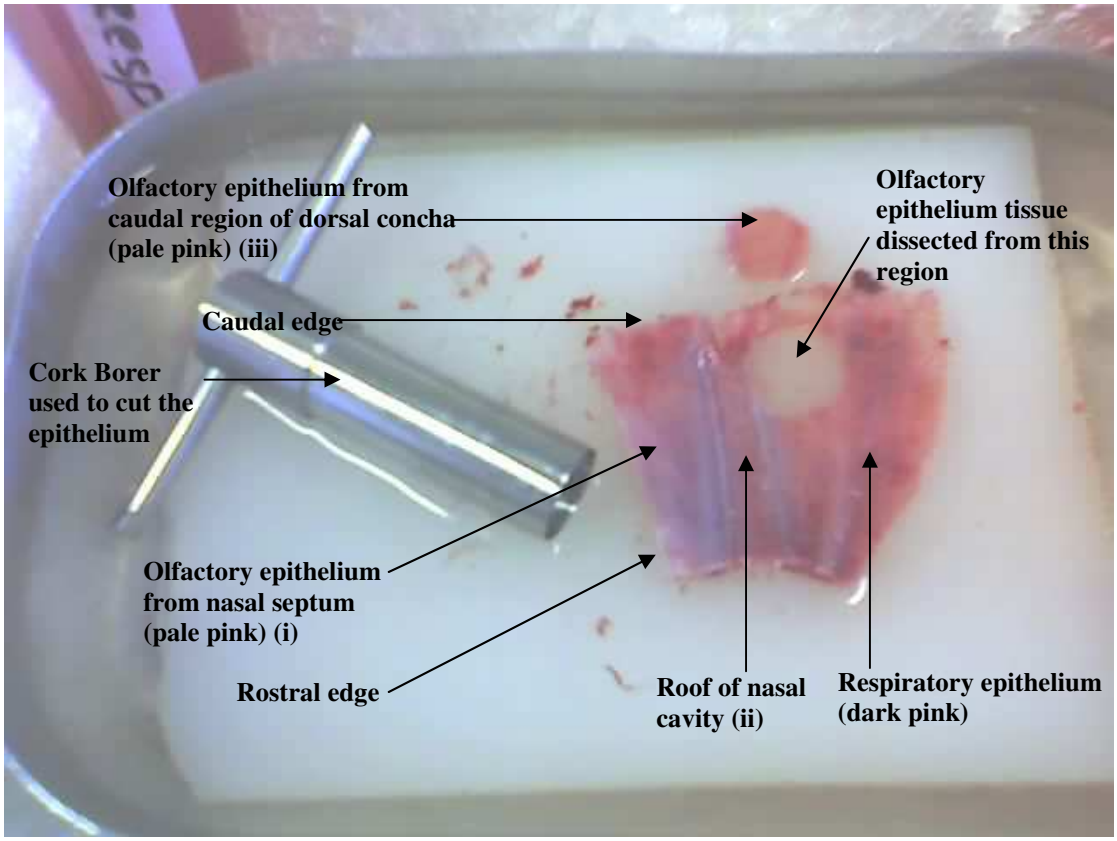

Figure 2.3 Epithelium extracted from one half of the roof of nasal cavity (Section B Figure 2.2) using the aforementioned dissection method. A clear distinction can be made between the lighter coloured olfactory epithelium and darker respiratory epithelium due to less vascularisation and presence of (yellowish) olfactory pigment of olfactory epithelium. The hole in the tissue shows the best area to retrieve enough olfactory epithelium to load onto one diffusion cell.

The tissue was removed from the cold buffer and loaded into the diffusion chamber apparatus using two cork-ring braces within ~1 hour of slaughter. The braces reduced the physical tension on the tissue during the experiment and therefore the likelihood of minor tears that are unobservable to the naked-eye. The epithelium was mounted vertically (mucosal side facing the donor chamber) as shown in Figure 2.4.

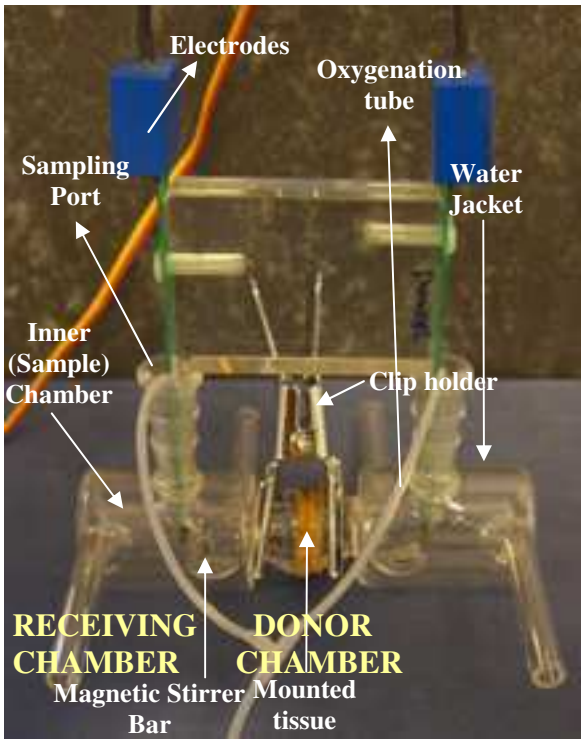

Figure 2.4 Vertical Franz diffusion chamber (Crown Glass Company, CA) apparatus was comprised of two symmetrical diffusion chambers. This equipment was used to investigate the transport of nanoparticles across olfactory epithelium. The tissue was mounted vertically between the chambers on cork supports; magnetic stirrer bars maintained homogeneity and water jacket kept chamber temperature at 29±1ºC.

The inner chambers were then filled with pre-oxygenated cold buffer solution to the collar of the sample port by syringe through these ports. The buffer was allowed to warm slowly by the heating effect of the insulating outer water jackets, which were filled using tubing connected to a water bath via a pump. The water bath was set to maintain the buffer temperature within the chambers at 29±1ºC. The epithelium was then allowed to equilibrate for 30 minutes (equilibration period) during which time electrophysiological measurements (2.2.1.2 Viability Assays) were taken every 5 minutes.

In the setup used here, magnetic stirrer bars maintained homogeneity of particles and oxygen, and the water jacket maintained chamber temperature at 29±1ºC. It has been suggested that a temperature setting of 37ºC may be too high since the temperature of the nasal mucosa is usually slightly above room temperature due to the cooling effect of the inspired air (Lehr 2002). Therefore, a more suitable range may be 28-30ºC; in fact,

time-related pattern of ciliary activity was more stable at 25ºC than 33ºC or 37ºC (Phillips et al 1990). In light of this, Cremaschi *et al.* carried out their experiments at 27 ºC (Cremaschi et al 1996). Some experiments have also been performed at room temperature (Hersey & Jackson 1987).

With regards to oxygenation of the buffer, it has been found that pre-sparging the buffer with O_2/CO_2 was more important than bubbling the gas during the experiment itself (Maitani et al 1997). The researchers used bubbling of gas as an agitator as well as for sparging during the diffusion chamber experiment. In the present experiments a combination of pre-sparging and the use of magnetic stirrer bars was selected.

The experimental parameters that needed to be controlled were pH, temperature, buffer oxygenation and experimental runtime. pH 7.4 was selected since the majority of similar *in vitro* experiments have used phosphate-based isotonic buffering solution at this pH (Osth 2002). However, in Chapter 3 the buffer pH was reduced to pH6.0 with the use of a citrate buffer in order to permit the stability of a chitosan-based colloidal system.

The experimental parameters used here were largely based on a studies by Osth *et al.* (2002a) and Jansson (2004), however, the following improvements were made in order to evaluate the physiological mechanisms responsible for any observed effects: (1) use of an improved viability methodology (based on Alamar Blue™); (2) use of varying sizes of nanoparticles placed in the donor cell with the epithelium; (3) measurement of donor cell particle reductions. Further improvements to the methodology involving

imaging of the dismounted tissue using fluorescence based microscopic techniques are described in Chapter 4.

After a 30 minute resting period (equilibration period), 200µL aliquots (~6% of the total chamber volume) were collected through the sampling port from the receiving chamber every 10 minutes for 90 minutes. This was replaced with fresh (pre-warmed and pre-oxygenated) buffer. Fresh pipette tips (Gilson Inc., Middleton, WI, USA) were used each time to prevent contamination of the inner chamber. The aliquots were pipetted into a 96 well plate (Co-Star, Schiphol-Rijk, The Netherlands). In addition, four evenly distributed electrophysiological measurements were taken at the 40, 60, 80 and 100 minute time points after mounting the tissue to the diffusion chambers.

Thereafter, electrophysiological measurements were taken again every 5 minutes for the last 30 minutes of the run and the transport run was terminated after a total of ~3½ hours post-mortem. Then, the epithelium was dismounted and used for the Alamar Blue™ assay and microscopy (2.2.5.2 Alamar Blue™ and 2.2.7 Preparation of Tissue Samples for Microscopy).

To summarise, Table 2.1 is a breakdown of events for the duration of the experiment.

Table 2.1 Summary of events during diffusion chamber studies

Post Mortem Time (minutes)	*Activity*
0-60	Slaughter, dissection, transport and initiation of experiment
60-90	Electrophysiological data and tissue equilibration
90-180	Diffusion chamber study (Electrophysiological data a 100, 120, 140 and 160 minutes)
180-210	Electrophysiological data
210	Tissue dismounted and cut up for Alamar Blue™ assay and histological analysis.

In addition, Alamar Blue™ assay was also performed on fresh olfactory epithelium samples directly upon arrival to the laboratory.

2.2.5 Sample Viability Measurements

It was necessary to ensure that the olfactory epithelium was alive during the experiment therefore viability measurements were performed using a standard electrophysiological technique for measuring viability of epithelia in diffusion chamber apparatus (2.2.5.1 Electrophysiological Viability Measurements) and also an Alamar Blue™ test (2.2.5.2 Alamar Blue™). Hence, the experiments had the following objectives: (i) to evaluate the viability of the olfactory epithelium during and after diffusion chamber studies; (ii) to reduce variability in Alamar Blue™ data by normalising it with DNA content; (iii) to compare the effect of sodium azide on olfactory epithelium R_m and viability; (iv) to compare the effect of both phosphate- and citrate- based buffering systems on olfactory epithelium R_m and viability; and (v) to establish viability acceptance criteria for further diffusion chamber studies.

In the olfactory tissue transport studies the single most important criterion was to demonstrate that the excised tissue was viable and undamaged during the experiments. Hence, the tissue viability was measured using two methods based on different scientific principles; the first method was based on electrophysiology and the second method was based on the rate of cell enzymatic activity.

To test the viability of the tissue by these methods, negative and positive controls were needed to be included in the experiments. Freshly dissected olfactory epithelium was selected as positive control since this would provide maximum values for viability.

Tissue that was metabolically inactivated by chemical means was chosen as the negative control. It was decided not to allow the tissue to die naturally (*ex vivo*) since increased enzymatic activity from bacterial growth on dead tissue would increase the viability signal from the Alamar Blue™ assay.

Sodium azide (300mM) was chosen as the tissue inhibitor since it reversibly blocks the same metabolic pathway as Alamar Blue™, i.e. the mitochondrial electron transport chain (Seifalian et al 2001). One of the products of metabolism is ATP which (amongst other functions) maintains the electrochemical gradient of ions over the epithelia and keeps tight junctions closed. These phenomena can be detected by the electrophysiological method.

2.2.5.1 Electrophysiological Viability Measurements

From the moment of animal slaughter, the integrity of the tight junctions between the epithelial cells slowly diminishes and hence the passage of materials through the membrane becomes less comparable to the situation when the tissue was in the live animal. The dead tissue may pass materials paracellularly due to the opening of tight junctions and pores may appear due to tissue degradation after cellular death.

Mannitol has been traditionally used as a paracellular marker since it is not readily transported across a membrane via the transcellular route (i.e. through cells). ^{14}C-labelled mannitol has been used to determine the 'leakiness' of the tight junctions across biological membranes in the past (Lehr 2002). Live tissue will resist the paracellular movement of mannitol compared to dead epithelium since dead epithelium has 'leakier' tight junctions.

It was decided, however, to employ the electrophysiological methods since it is simple and it is a standard method to measure the viability of epithelia that are mounted in diffusion cells. The technique can measure both passive and active ion transport properties of biological membranes. Passive properties can be observed as the 'leakiness' of the epithelium whereas active properties include the measurement of Na-pump and ion channel activities.

One way of measuring the active and passive transport properties of epithelia is to plot the potential difference across the epithelium when an external current is applied. The principle is based on Ohm's Law. A straight line relationship such as that in Figure 2.5 was observed when the potential difference was plotted against an applied current in these experiments. The resting membrane potential (PD) (i.e. the potential difference across the membrane when no current was applied) and the short circuit current (I_{sc}) (i.e. the current required to extinguish the resting membrane potential) can be calculated by applying simple arithmetic to the plotted values. In addition, the gradient of the straight line is proportional to the membrane electrical resistance (R_m). These three parameters can be compared between epithelia to evaluate overall trends.

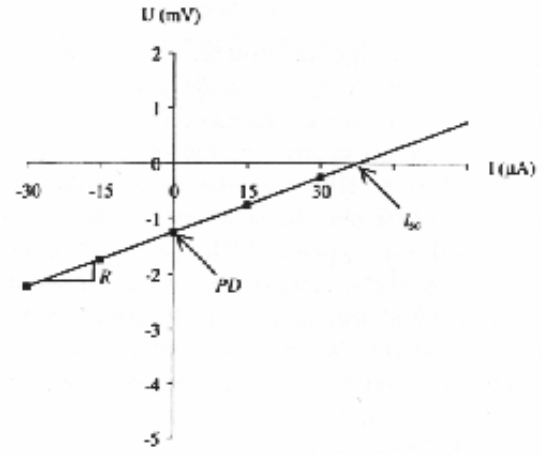

Figure 2.5 Explanation of the electrophysiological parameters used to determine tissue damage and viability. This plot is based on the Ohm's Law principle and is made for each time point in the experiment. PD (mV) is the natural potential in the resting state (when no external current is applied). I_{sc} ($\mu A/cm^2$) is the short-circuit current (the current that is applied across the epithelium necessary to extinguish the PD). The gradient R is proportional to the transepithelial electrical resistance (R_m) (R x 1000 = R_m (Ωcm^2)). Taken from (Osth 2002).

An EVOM (World Precision Instruments, Stevenage, UK) was used to determine the R_m (Ωcm^2), I_{sc}($\mu A/cm^2$) and PD (mV) (see Figure 2.5 for diagrammatic explanation of terms) by use of the following equations:

$R_m = (R_E - R_C)\ \pi r^2$

$PD = (PD_E - PD_C)$

$I_{sc} = (0\text{-}PD) / R_m$

Where:

PD_E = potential difference measurement during experiment (mV)

PD_C = background potential difference measurement (mV)

R_E = resistance measurement during experiment (Ω)

R_C = background resistance measurement (Ω)

r = radius of tissue sample under investigation (cm)

Background levels were taken without the presence of epithelium between the chambers both before and after mounting the tissue. The arithmetical mean of these two values were used as the background level for each experiment.

The following is an explanation of the electrophysiological basis for these parameters. An innate resting membrane potential (PD) is generated by the differential transport of ions across the epithelium. The exact nature of this differential depends on the ions present and the epithelium used. It can be measured experimental by manipulating the concentration of Na^+ and K^+ ions on either side of the membrane (Gizurarson et al

1991). Moreover, the differential transport of ions requires energy from cell metabolism and so it is understood that PD is proportional to epithelial viability/metabolic rate. The magnitude of PD depends on a combination of two factors; (a) the rate of ion-transport across the epithelium and (b) the 'leakiness' of the epithelium.

(I_{sc} is described as the externally applied current needed to extinguish the PD. Hence, PD and I_{sc} are electrophysiologically linked and so the previous explanation may be extended to I_{sc} as well as the given example for PD).

The equilibration (or bioelectrical stabilisation) period is the time required for the dissected tissue to return to a steady electrophysiological state after having been placed onto the diffusion chamber apparatus. Since the tissue samples are transported from the site of removal from the pig in buffer on ice, the epithelium uses some time to physically warm up and restart its temporarily dormant metabolic activities. This allows for tight junctions to become fully integral and for active ion transport pumps to form a resting membrane potential across the epithelium (Lehr 2002).

2.2.5.2 Alamar Blue™

The Alamar Blue™ viability assay incorporates a reduction-oxidation (REDOX) indicator that can be detected by fluorometric methods. It is easily interpreted, minimally toxic and stable. The manufacturer's literature suggests that the reagent, resazurin, is taken up by cells and reduced – predominantly in the electron transport chain (AbD Serotec Ltd 2004). The reduction mechanism depends on the ability of the reagent to substitute molecular oxygen for any of the oxioreductase enzymes. In this way, the non-fluorescent blue substrate (resazurin) is reduced to the red-fluorescent product (resorufin). Resorufin has excitation and emission maxima of 560nm and

590nm respectively (Figure 2.6). Hence, this assay gives a measure of cell metabolic activity and viability.

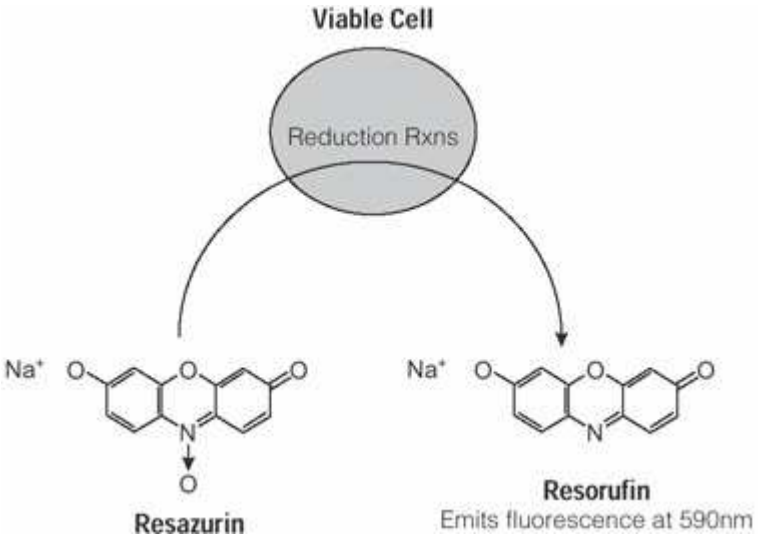

Figure 2.6 Biochemical basis of Alamar Blue™ assay. Taken from AbD Serotec Ltd 2004.

The Alamar Blue™ tests were performed on tissue samples that were collected directly after the transport study. To perform the Alamar Blue™ test a 10%v/v solution of Alamar Blue™ was made up from the manufacturer's stock solution in SNS. Next, 200µl of this working solution was placed in wells of a 96 well microtitre plate (Co-Star, Schiphol-Rijk, Netherlands). A 3mm diameter core of sample tissue was then placed into a well containing the solution. The samples were kept in the dark by wrapping foil around the well plate to prevent photobleaching of the fluorophore and left for 90 minutes at 37°C 95%O_2/5%CO_2 (80%) for colour to develop. The experiment was done in triplicate for each sample.

In addition, triplicate blanks were also analysed where the same procedure was followed, except with no tissue. This gave the background fluorescence values.

After incubation the microtitre plate was de-foiled and placed into a fluorometric plate reader (FluoroSkan Ascent, Thermo, Stone, UK) and analysed using excitation light at 530nm and emission light at 590nm. Subsequently, the blank values were subtracted from the sample readings to give the final result.

The tissue samples were then frozen (-20°C) and later quantified for DNA using the Hoechst methodology (2.2.5.3 Hoechst DNA Quantification). Thereafter, the viability data was normalised per mass DNA by dividing the Alamar Blue™ viability value by mg DNA per sample.

2.2.5.3 Hoechst DNA Quantification

The viability of the excised tissue may vary depending on the thickness of the epithelium. An attempt was made to normalise the Alamar Blue™ viability assay measurements by the unit mass of tissue in each sample using the Hoechst DNA quantification assay. It was thought that this may reduce the effect of variations in tissue thickness. The Hoechst assay is a method used to quantify the amount of DNA in tissue samples. The reagent, bisbenzamide, is a chemical that becomes fluorescently active (Ex/Em 365nm/480nm) when bound to adenine-thymine base pairings in DNA in solution. This fluorescence activity can be quantified and standardised using calibration plots. The method is particularly useful since, unlike protein content, the amount of DNA per sample is directly proportional to number of cells in the sample.

DNA quantification is more accurate than other measures of tissue mass. For example, measurement of tissue samples dry mass would require very sensitive weight balances that were not available in the laboratory. Protein content measurements would also be less accurate than DNA measurements since protein expression, for example of mucin,

can vary markedly between animals due to phenotypic differences, living conditions and weather.

Thus, variability in Alamar Blue™ measurements deriving from the variation in thickness of different tissue between samples should be reduced by combining the results of the Alamar Blue™ and the Hoechst assays.

The DNA measurements were performed in the following way. Frozen cores of porcine nasal epithelium (that had previously been evaluated for viability by the Alamar Blue™ assay) were allowed to thaw to room temperature. Next, they were individually digested in papain solution by placing each sample in an Eppendorf Tube and adding 1ml of papain solution. The Eppendorf tubes were then sealed using Parafilm and incubated at 60°C overnight in a water bath. Following this samples were filtered using 70μm^2 nylon BD Falcon™ cell strainers to remove undigested material and therefore reduce variability from light scatter artefacts in the fluorometer. Next, triplicate 200µl aliquots of each sample were added to a 24-well plate followed by 0.5 ml Hoechst buffer and 0.75 ml Hoechst working solution. The well plate was wrapped in foil and rested for 5 minutes at room temperature to allow for the reaction between DNA and bisbenzamide. Finally, fluorescent readings were carried out for each sample (FL600FA, Labtech Int. Ltd., Ringmer, UK). Fluorescent measurements were read at excitation wavelengths 360±12.5nm and emission wavelengths 460±20nm.

A standard curve was produced using calf thymus DNA to estimate the amount of DNA per sample. This was recommended by Hoechst manufacturer's literature since it is

cheap, easily purified and (being eukaryotic) has a low variation in adenine-thymine base content.

To produce a standard curve, seven 700µl concentrations of DNA solution were made up in Eppendorf tubes using papain solution (Table 2.2). These were sealed with Parafilm and immersed in 60°C water overnight. Samples were then filtered using 70µm^2 nylon BD Falcon™ cell strainers (BD BioSciences, Oxford, UK). This ensured that the calf DNA calibration samples underwent the exact same procedure as the epithelial samples.

Next, triplicate aliquots of 200µl of these varying concentrations of calf-thymus DNA solution (Table 2.2) were added to a 24-well plate followed by 0.5 ml Hoechst buffer and 0.75 ml Hoechst working solution, wrapped in foil, rested and measured for fluorescence as previously described.

Table 2.2 DNA calibration curve solutions for Hoechst DNA quantification

[DNA] mg/ml	*Vol. stock DNA (10µg/ml) (µl)*	*Vol. Papain solution (µl)*	*Total Vol. (µl)*
0.00	0	700.00	700
0.05	3.5	696.50	700
0.10	7.0	693.00	700
0.15	10.5	689.50	700
0.20	14.0	686.00	700
0.30	21.0	679.00	700
0.40	28.0	672.00	700

The composition of the buffers that were required during sample preparation for measuring DNA content of tissues are described in the Appendix.

2.2.6 Comparison of Olfactory and Respiratory Tissue Metabolism

To gain a better understanding of the rate of metabolism of olfactory epithelium in comparison to other tissues, the Alamar Blue™ method was used to compare the viability of olfactory to respiratory epithelia directly after excision from the pig nasal cavity.

Hence, epithelial cores were taken from the porcine nasal cavity (as described in 2.2.3 Dissection of Nasal Epithelia from the Pig) for respiratory and olfactory epithelia from regions 5 and 6, respectively. The samples were transported in 0.5mM citrate buffer pH6.0 and the Alamar Blue™ test was performed using the methods described earlier (2.2.1.2 Viability Assays).

Samples were taken from nine pigs on different days. Some samples were taken for epithelia from the same animal. The Alamar Blue™ viability scores of 3-7 tissue cores from one animal were averaged per pig. The mean scores were then used in an unpaired statistical analysis to compare the differences between mean viability scores.

2.2.7 Preparation of Tissue Samples for Microscopy

Morphological examination of the epithelia was required for two reasons; first, to confirm location of the olfactory epithelium; and second, to demonstrate the morphology of the olfactory epithelium after manipulation in the diffusion chamber apparatus.

Tissue samples were immediately placed in 3% glutaraldehyde for primary fixation. They remained in the fixative for at least 48 hours to allow for crosslinkage of cysteine

residues in the tissue, after which the fixative was disposed into 1M glycine using a plastic pipette. Then fresh (aldehyde-free) 0.1M cacodylate buffer was then added to the sample and was allowed to rest for 5 minutes. This rinsed away any excess glutaraldehyde which would chemically reduce the osmium tetroxide in the proceeding step.

The cacodylate buffer was then replaced with a 1%w/w osmium tetroxide solution for 1 hour. This high molecular weight metal salt had a dual purpose; (i) it chemically crosslinked fatty acids in the epithelial samples (termed secondary fixation); and (ii) its high electron density was used as a contrast medium for electron microscopy.

After the 1 hour osmium tetroxide treatment the osmium salt was replaced with distilled water for five minutes. This was repeated twice. Then, the samples were placed through a series of graded alcohols as follows; 2x15 minutes in each 50%, 70%, 90%, 100% IMS (in distilled). Next, the IMS was replaced by immersing for 2x15 minutes in propylene oxide (PO). The IMS dehydrated samples were not placed directly into resin since these reagents were immiscible. Therefore, PO was used as an intermediate reagent since it is miscible in both IMS and resin.

The embedding resin was made up by mixing 25ml Araldite CY212 resin, 15ml Agar 100 resin and 55ml DDSA with a wooden stick. Thereafter, 2ml Dibutyl phthalate and 1.5ml DMP 30 were added until the colour changed from red-orange to orange.

Next, a short series of graded resin in PO was used to bring the sample slowly to 100% resin as follows; 3:1 PO:resin for 2 hours, 1:1 PO:resin overnight, 1:3 PO:resin for 3 hours, 3x2 hours in 100% resin.

Finally the samples were placed in a flatbed mould that would hold the correct orientation for slicing the tissue. The moulds were placed in an oven for 48 hours at 60°C. This hardened the sample and the resin ready for cutting. An ultra-microtome was used to slice the samples. For light microscopy 500nm sections were cut using a glass knife. For TEM 70-90nm sections were cut using a diamond knife (TEM sections were cut by the Imaging Unit, Queens Medical Centre, University of Nottingham, Nottingham, UK).

2.2.8 Staining Samples for Light Microscopy

The samples were stained using toluidine blue to check that the gross tissue morphology and identify the region(s) of interest by applying the stain for a few moments then washing off with distilled water. If the sample was understained then the process was repeated until satisfactory staining was achieved.

Toluidine blue is a basic dye and therefore it has a higher affinity for negatively charged cell constituents (such as sulphated glycosaminoglycans and phosphated nucleic acids) compared to positively charged ones (such as proteins under acid conditions). This leads to a two-tone staining pattern in which cytoplasm contrasts with nuclei.

2.2.9 Staining Samples for TEM

TEM was also used to see the epithelia at high magnification. Heavy metal staining was employed using two complementary stains. Lead citrate (acidophilic) stains positively charged groups (e.g. mitochondria and cilia) in the epithelium whereas uranyl acetate (basophilic) stains negatively charged groups (e.g. nucleic acids). They are used in combination as a standard method to visualise differential staining patterns in electron microscopy.

To prepare the samples, regions of interest were isolated, cut to ~70-90nm using a diamond knife and placed on a small circular copper grid (diameter ~2mm). Then a drop of the uranyl acetate was placed on a Petri dish. The copper sample grids were inverted (sample face down) and placed on top of this drop for 10 minutes. They were then rinsed lightly with 50% (v/v) methanol in water then again in water alone. This was done by holding the grid between fine curve ended forceps and using the curved ends of the forceps to break the force of the liquid from a bottle. This reduced the likelihood of sample damage from the force of the jet. This was repeated for lead citrate solution. The samples were rinsed with water and methanol as before and guided off the forceps with filter paper onto more filter paper and allowed to air dry.

2.2.10 Statistical Analyses

All statistical analyses were performed by SPSS software version 15.0 (Chicago, USA).

2.2.10.1 Comparison between grouped continuous data

Datasets were analysed for normality using the Shapiro-Wilk test. Parametric datasets containing only 2 groups were analysed using a (paired/unpaired) Student's t-test; non-parametric datasets were analysed by Mann-Whitney test unpaired data. A non-

parametric test was used to determine significance in cases where one group was parametrically distributed and the other group was non-parametrically distributed. A one-way analysis of variables (ANOVA) with *post hoc* test was performed on datasets with more than 2 groups. Bonferroni *post hoc* test was performed on groups with equal variances and a Games-Howell *post-hoc* test was performed on groups with unequal variances. A value of $p<0.05$ was considered statistically significant.

2.2.10.2 Testing for correlation between continuous datasets

The Pearson product-moment correlation co-efficient, r, was calculated for parametric continuous datasets. For non-parametric continuous datasets the Spearman's Rank (ρ) correlation test was performed. This test used the same algorithm as the Pearson product-moment correlation; however, the values were ranked in ascending order and the algorithm was executed on the ranked values and the ranked means.

Correlation coefficients are dimensionless indices that range from -1.0 to 1.0 inclusive; they reflect the extent of a linear relationship between two data sets. A correlation of +1 means a perfect positive linear relationship between variables i.e. all the points lying exactly on a straight line of positive slope. Conversely, a correlation of -1 means a perfect negative linear relationship between variables. A correlation of 0 means there is no linear relationship between the two variables. In analytical practice, correlation values greater than 0.99 are usually required and values of less than 0.90 are uncommon (Miller 1993).

2.2.10.3 Relative Standard Deviation (RSD)

Relative Standard Deviation (%) is a measure of data variability that relates the spread of data in a dataset to the mean value. It is calculated as:

$$\%RSD = \frac{\bar{x}}{\sqrt{n}}$$

where $\bar{x}$ was the sample mean and n was the sample number.

It is a useful measure of variability when the absolute values (e.g. standard deviation) for two datasets are markedly different (e.g. Alamar Blue™ viability scores and Alamar Blue™ viability scores after adjustment for DNA content).

2.3 RESULTS

In this section the results are presented in relation to the chapter objectives: (i) the location of the olfactory epithelium in the porcine nasal cavity was determined by standard histological techniques and bright field microscopy; (ii) the viability of the vertical Franz diffusion cell loaded olfactory epithelia were determined in different physiological buffers (citrate pH6.0 and SNS pH7.4) in presence and absence of metabolic blockade with sodium azide; (iii) the histological appearance of citrate and SNS buffered olfactory epithelia were evaluated after the diffusion cell studies using bright field microscopy; (iv) an assessment of the bioelectrical equilibration period was made for the porcine olfactory epithelium using the current experimental conditions; (v) the viability of olfactory epithelium was compared to that of respiratory nasal epithelia; and (vi) the effect of correcting Alamar Blue™ viability data with DNA content was evaluated.

2.3.1 Morphological Features of Porcine Nasal Epithelia

Figure 2.7 to Figure 2.12 show the morphology under the bright field microscope of epithelia from Regions 1-6 of the nasal cavity (Figure 2.2). Region 1 (Figure 2.7) was extracted from the nasal vestibule. It showed a stratified squamous structure with a keratinised surface. The keratinised surface morphologically was anuclear. Its function is to protect the underlying cells from mechanical damage and dehydration (Figure 2.7(a)). The underlying cells were typical of stratified squamous epithelium. They were round in shape and layered in no definite formation. Intercellular connections, such as desmosomes, are clearly visible as strands between the cells (Figure 2.7(b)).

Figure 2.7 Histology of the porcine nasal vestibule.

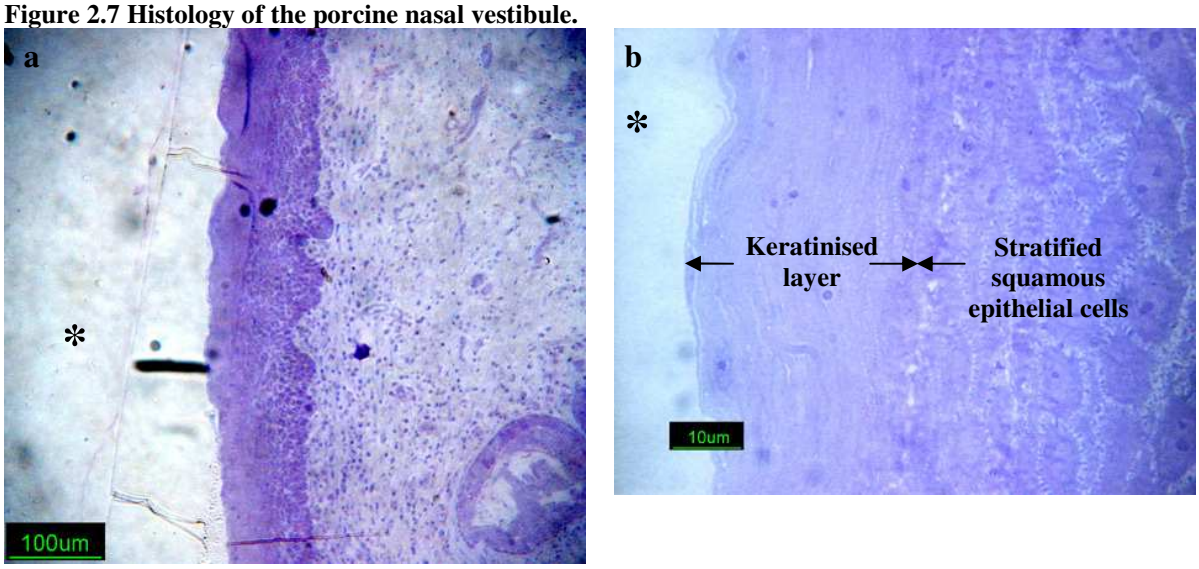

(a) Region 1: Keratinised stratified squamous epithelium (b) Region 1: Close-up of keratinised layer and apically located stratified squamous epithelium. * indicates luminal space.

Regions 2 and 4 (Figure 2.7 (a,b)) demonstrated a simple cuboidal epithelial morphology. These regions lie between the (rostrally-located) squamous and (caudally-located) columnar epithelia. The cuboidal cells were non-ciliated (Figure 2.7 (c)).

Figure 2.8 Histology of the porcine nasal transitional epithelium. * indicates luminal space.

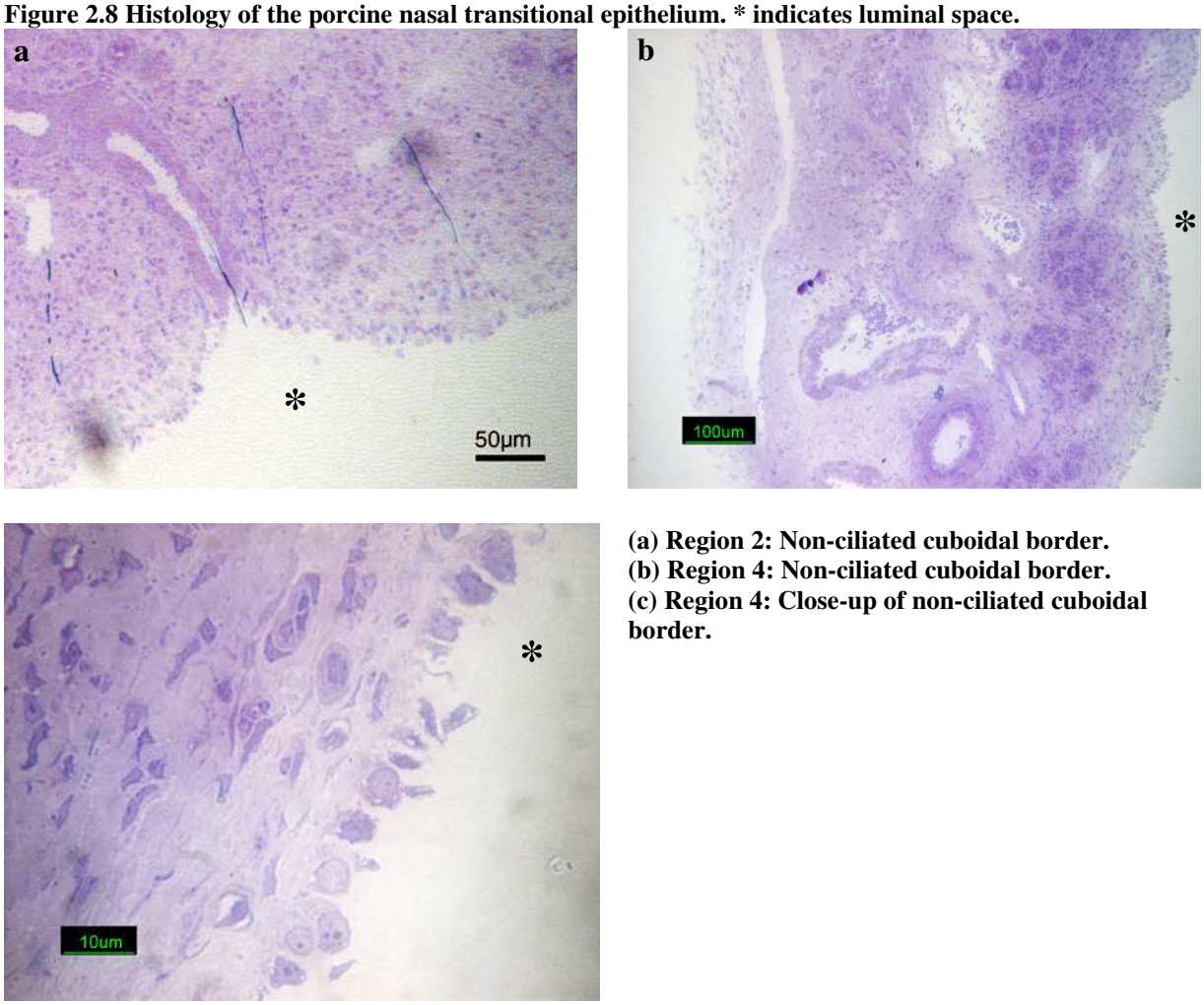

(a) Region 2: Non-ciliated cuboidal border.
(b) Region 4: Non-ciliated cuboidal border.
(c) Region 4: Close-up of non-ciliated cuboidal border.

Regions 3 and 5 (respiratory epithelium) were pseudostratified epithelium containing columnar cells in the apical cell layer (Figure 2.9 (b,d)). The columnar cells were both ciliated and non-ciliated (Figure 2.9 (b)). They had oval-shaped nuclei that were located in the middle third of the cells. Basal cells were rounder and darker stained than the columnar cells. They were located next to the basement membrane. The underlying *lamina propria* contained many more capillaries than in Region 2 (Figure 2.9 (a,c)).

Figure 2.9 Histology of the caudally-located porcine pseudostratified columnar epithelium (respiratory epithelium).

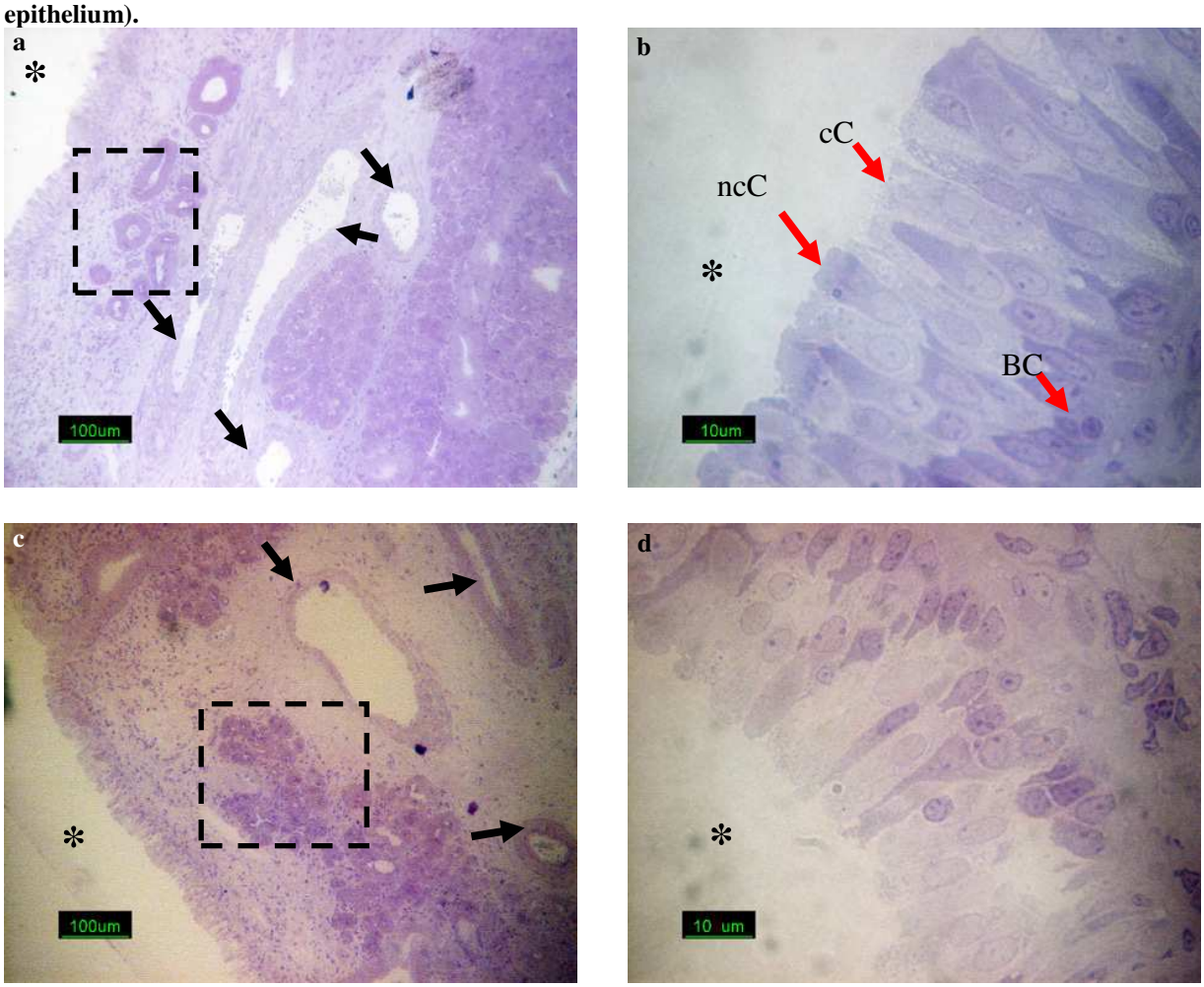

(a) Region 3: (a) Columnar border with blood vessels present in the *lamina propria* (arrows). The *lamina propria* also contained many glands (boxed). (b) Region 3: Close up of border. Presence of (ciliated [cC] and non-ciliated [ncC]) columnar cells and basal cells [BC]. (c) Region 5: Pseudostratified columnar with same gross morphology as Region 3. Blood vessels present in the *lamina propria* (arrows). The *lamina propria* also contained many glands (boxed). (d) Region 5: Close up of pseudostratified columnar epithelium. * indicates luminal space.

Olfactory epithelium was found in Region 6 (Figure 2.2) covering the dorsal turbinate. Olfactory epithelium had similar morphology to the pseudostratified columnar epithelia found in Regions 3 and 5. In addition to Regions 3 and 5, olfactory epithelium also presented olfactory neurones (Figure 2.11) in the apical layer and *filia olfactoria* (Figure 2.12) in the *lamina propria*. These were its main distinguishing features.

Figure 2.10 Region 6 (Olfactory Epithelium). Columnar border with fewer blood vessels (arrow) present in the *lamina propria* than Regions 3 and 5. * indicates luminal space. Dash lined box shows *filia olfactoria* (magnified in Figure 2.12). Solid line box magnified in Figure 2.11

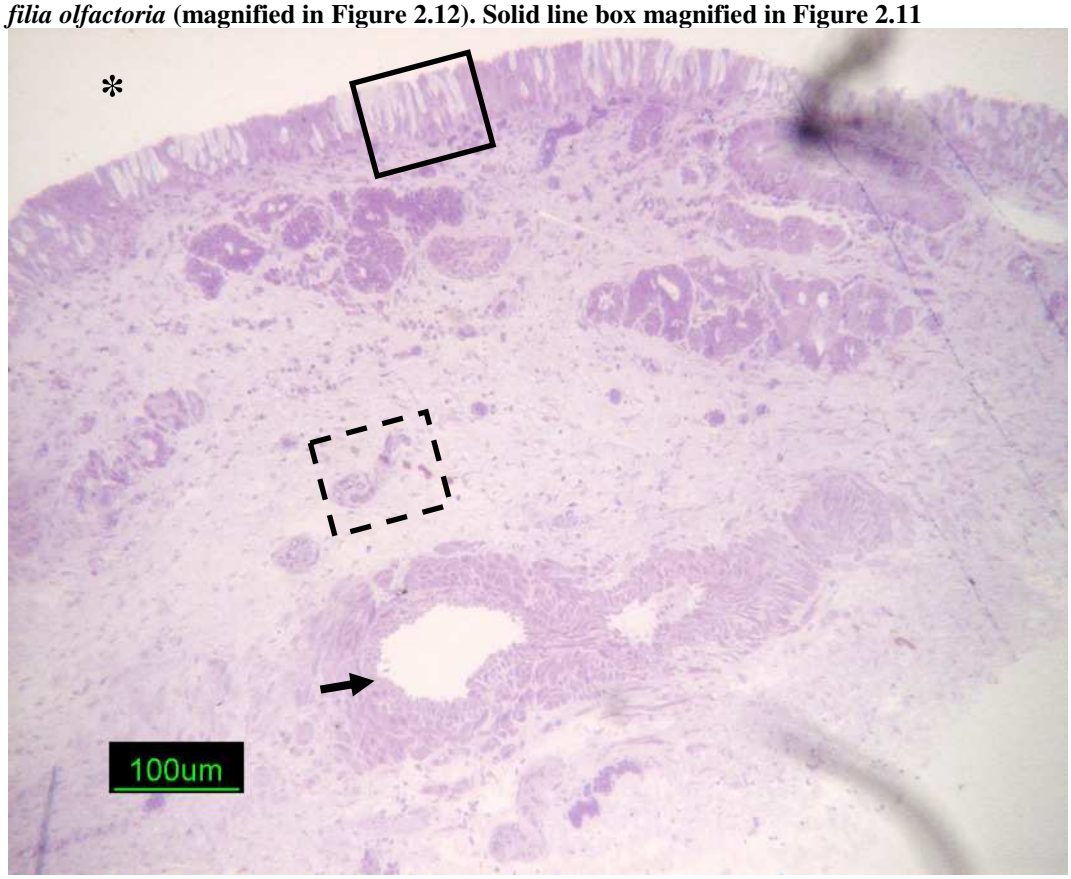

The olfactory epithelium contained ciliated pseudostratified columnar epithelium (Figure 2.11). Olfactory knobs are a feature of the apical terminus of the olfactory axons. They are highlighted by the dash lined box in Figure 2.11. Sustentacular cells (SC) are non-neuronal columnar cells in the olfactory epithelium. Basal cells similar to those found in respiratory pseudostratified columnar epithelium (Regions 3 and 5) are also highlighted.

Figure 2.11 Region 6 (Olfactory Epithelium). Cilia are clearly visible from the sustentacular cells (SC). Olfactory knobs are also seen (dashed box). BC Basal cell. * indicates luminal space.

Filia olfactory are also a key distinguishing feature of the olfactory epithelium (Figure 2.12). *Filia olfactoria* are neuronal bundles, containing neural cells (dashed box), found in the *lamina propria* underlying the olfactory epithelium. They are ensheathed with Schwann cell processes that maintain their electrical conductivity (arrow). The *filia olfactoria* traverse the cribiform plate and terminate in olfactory bulbs in the CNS.

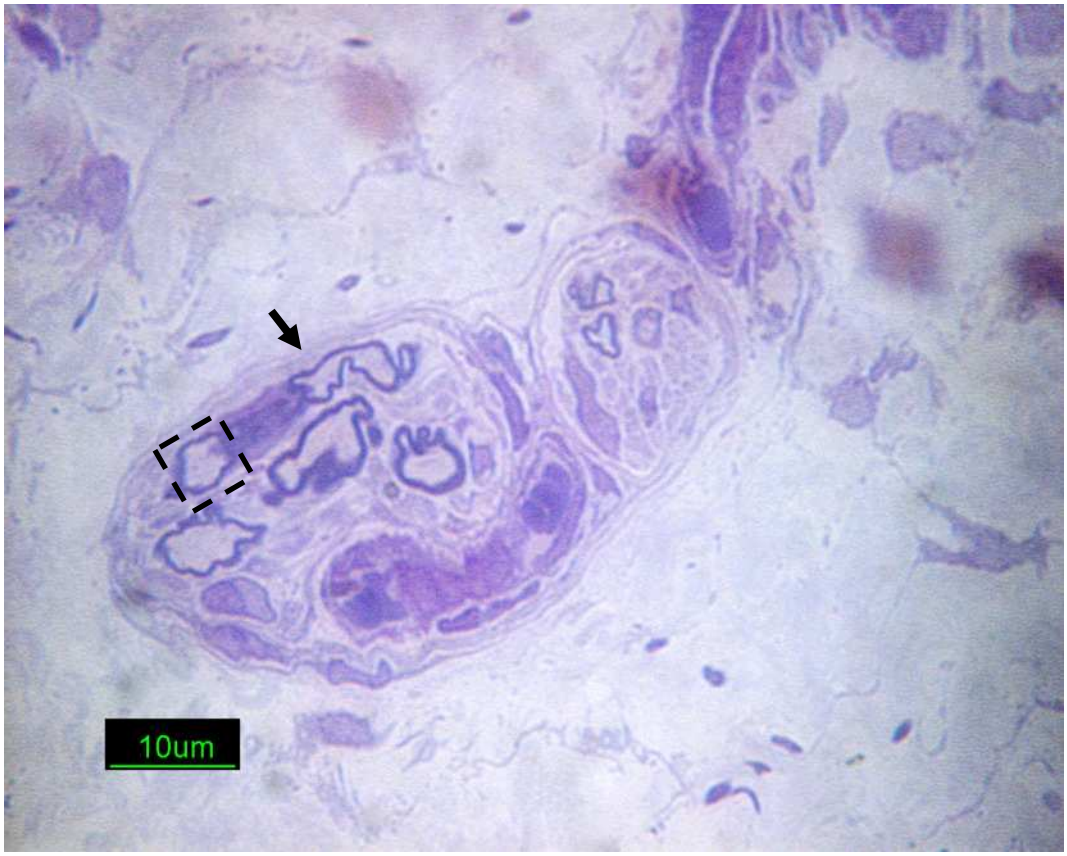

Figure 2.12 Region 6 (Olfactory Epithelium). *Filia olfactoria* magnified. Individual neuronal processes can be identified (dashed box). Schwann cell bundle can be identified (arrow).

At the subcellular level, the greatest proportion of mitochondria appeared at the apical surface of the epithelial cells. Figure 2.13 shows an example from the olfactory epithelium.

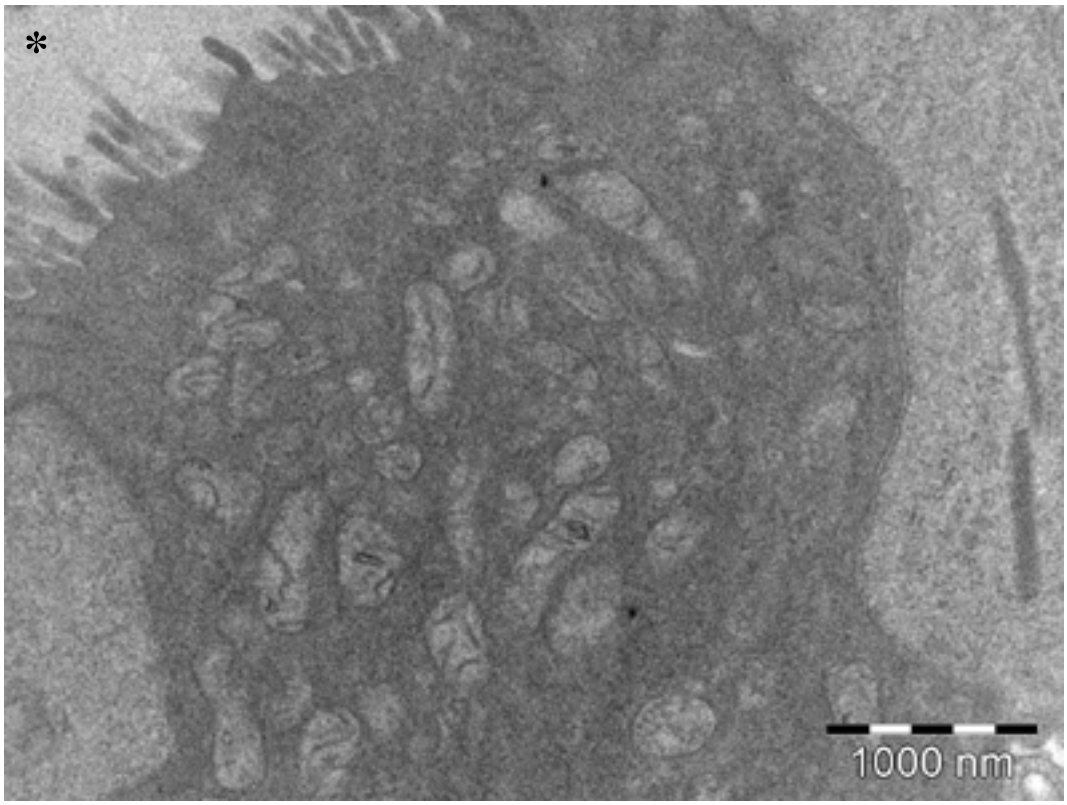

Figure 2.13 Mitochondria at luminal surface of pseudostratified columnar cells in olfactory epithelium (Region 6). * indicates luminal space.

The different epithelia found in the nasal cavity of a six month old pig are summarised in Figure 2.14.

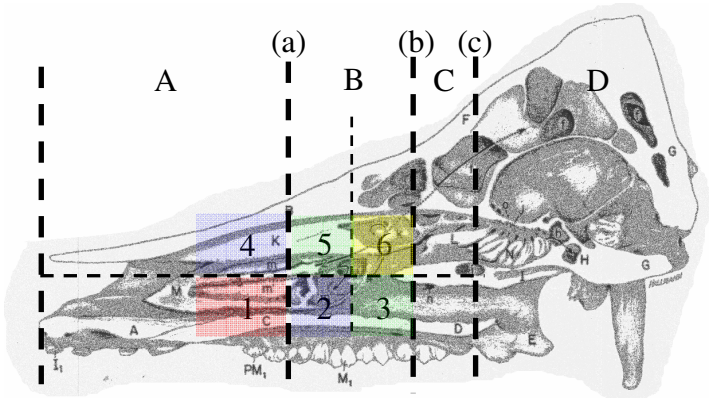

Figure 2.14 Summary of types of epithelia found in the porcine nasal cavity Adapted from (Getty 1975). Epithelium was retrieved from six different areas as shown (labelled 1-6).
<u>Green highlight</u> – pseudostratified columnar epithelium (regions 3 and 5). Respiratory epithelium.
<u>Blue highlight</u> - cuboidal cells (Regions 2 and 4).
<u>Red highlight</u> – keratinised stratified squamous epithelium (Region 1).
<u>Yellow highlight</u> - Region 6. Olfactory epithelium.

2.3.2 Effect of Different Buffers and Sodium Azide on Olfactory Epithelium

Table 2.3 summarises the post-equilibration (30-150minutes Table 2.1) R_m, PD and I_{sc} data for the 0.5mM citrate and SNS buffering conditions. Data captured within 30 minutes of tissue mounting for the electrophysiological data were assumed to be unrepresentative of stable bioelectrical conditions (although in reality this may not be true Table 2.4). The mean, standard deviation and statistical significances were calculated for each buffering system, with and without exposure to sodium azide, for all three electrophysiological measurements.

The following two observations were made. First, for SNS buffer, the addition of sodium azide to the olfactory epithelium statistically changed R_m and PD values ($p<0.05$ ANOVA) from $58.6\pm12.7\Omega cm^2$ and $-0.8\pm0.2mV$ to $8.2\pm3.0\Omega cm^2$ and $0.7\pm0.4mV$, respectively. However, similar observations could not be made for citrate buffer where no significant differences were observed. I_{sc} values were not statistically different ($p<0.05$ ANOVA).

Second, there was no statistical difference between the R_m value for SNS buffer ($58.6.3\pm12.7\Omega cm^2$) and citrate buffer ($78.8\pm40.2\Omega cm^2$) (mean±s.d.). However, there were statistical differences for PD ($-0.8\pm0.2mV$ [SNS] compared to $-0.1\pm0.1mV$ [citrate]) and I_{sc} values ($13.3\pm1.5mV$ [SNS] compared to $1.0\pm0.2mV$ [citrate]). This suggested that the citrate buffer statistically reduced the metabolic activity of the olfactory epithelia but the amount of tight junction opening remained unchanged.

Table 2.3 Post-equilibration R_m, PD and I_{sc} data summary for porcine olfactory epithelia that were mounted on the vertical Franz diffusion cell and exposed to either SNS or Citrate buffers, with and without sodium azide.

	R_m (Ωcm2)	*PD (mV)*	*I_{sc}(μA/cm2)*
SNS Buffer	58.6±12.7[a]	-0.8±0.2[a,b]	13.3±1.5[b]
SNS Buffer + azide	8.2±3.0[a]	0.7±0.4[a]	-107.0±73.0
Citrate buffer	78.8±40.2	-0.1±0.1[b]	1.0±0.2[b]
Citrate buffer + azide	11.5±2.7	1.5±0.9	-134.0±74.8

[a] Statistical difference (p<0.05) between SNS buffer and SNS buffer+azide data
[b] Statistical difference (p<0.05) between SNS buffer and citrate buffer data
Statistical test: One way ANOVA with Games-Howell *post hoc* test
(mean±s.d. deviation; n=3)

Figure 2.15 shows the Alamar Blue™ viability values for: (a) freshly excised porcine olfactory epithelia on arrival to the laboratory, and (b) olfactory epithelia that had been used for experiments in the vertical Franz diffusion chambers. The graph shows values for samples exposed to either SNS or citrate buffers (with and without added sodium azide).

A number of observations were made. First, sodium azide significantly reduced the viability of the diffusion chamber mounted epithelia exposed to SNS (10528±676 to 3260±487, mean±s.d., P<0.01 ANOVA) but not 0.5mM citrate buffered samples (p>0.05, ANOVA). However, sodium azide did statistically reduce Alamar Blue™ viability scores for 0.5mM citrate buffered olfactory epithelia (pH6.0) when compared to freshly excised citrate buffered samples (p<0.05, ANOVA). It was expected that the sodium azide would reduce the metabolic rate of cells in the epithelium since it reversibly blocks the same metabolic pathway (in the mitochondrial electron transport

chain) as that required by the conversion of the (Alamar Blue™ reagent) resazurin to resorufin (Seifalian et al 2001).

Nonetheless, even though a high concentration of the metabolic inhibitor (300mM) was used it was observed that sodium azide did not completely block the metabolism of the cells. The apparent residual viability could be a result of background levels of REDOX reactions, such as those involved in anaerobic respiratory pathways, that are also able to convert Alamar Blue™ to its fluorescent form (Seifalian et al 2001; AbD Serotec Ltd 2004).

Second, the type of buffer system had an effect on viability for azide-free samples. Alamar Blue™ measured viability was significantly reduced for 0.5mM citrate buffered (pH6.0) olfactory epithelium (9870±570) compared to SNS buffered (pH7.4) samples (6690±870) (for freshly dissected tissues in the absence sodium azide) ($p<0.05$, ANOVA, n=3) (Figure 2.15). This data shows that pH had a significant effect on viability.

Third, the diffusion chamber experiment did not have a significant effect on viability of the tissue. The mean viability values for freshly excised samples compared to samples that were subjected to the diffusion chamber experiment were not significantly different ($p>0.05$, ANOVA) for the SNS (9870±570 [freshly dissected samples] compared to 10530±390 [diffusion chamber loaded samples]) or citrate (6690±870[freshly dissected samples] compared to 5760± 280 [diffusion chamber loaded samples]) buffered epithelia.

Overall, Table 2.3 and Figure 2.15 highlight three important conclusions; first, sodium azide significantly affected the viability of the epithelia for all SNS buffered but not all the citrate buffered samples. Therefore, it could not be confirmed by these methods that the 0.5mM citrate buffered samples (pH6.0) were alive after the diffusion cell experiment. Second, a change in the buffering system from SNS (pH7.4) to 0.5mM citrate (pH6.0) buffer significantly affected the viability of the olfactory epithelia. Third, the mounting of the epithelia to the diffusion chamber did not have a direct effect on the viability of the samples.

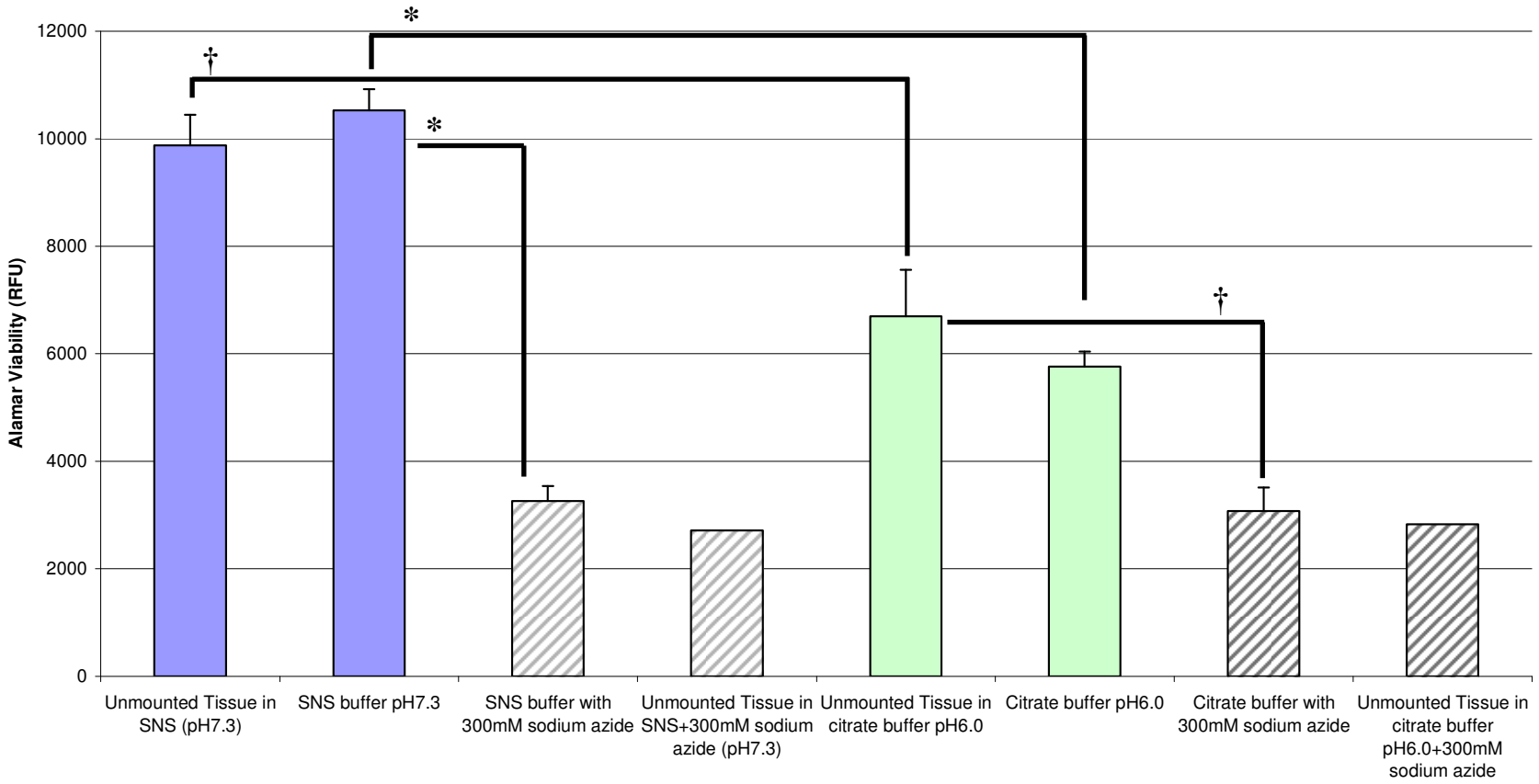

Figure 2.15 Alamar Blue™ Viability Data for porcine olfactory epithelia tested for fresh samples and samples that were dismounted from the diffusion chamber apparatus, with and without addition of azide (mean±standard error; n=8,3,3,1,5,3,3,2 [from left to right]). * Significant difference (p≤0.01), † Significant difference (p≤0.05); One way ANOVA with Bonferroni *post hoc* test.

The second conclusion, made from electrophysiology and Alamar Blue™ analysis, of the viability effects of the buffering solution on the olfactory epithelium is supported by the following morphological observations made under bright field microscopy. Figure 2.16 and Figure 2.17 demonstrate the condition of the olfactory epithelium after exposure to the diffusion chamber conditions (without the presence of particles) in the different buffering conditions. The SNS buffered epithelia appeared to have similar morphology to the fresh samples (see Figure 2.10 to Figure 2.12). However, there were minor changes to the pH6.0 citrate buffer samples such as the condition of the cilia which were not as prominent, subcellular components appeared less clear, and the shape of the olfactory knob had changed (dashed box Figure 2.17). These findings were noted when evaluating the effect of nanoparticles on the olfactory epithelia exposed to 0.5mM citrate buffer pH6.0 (Chapter 4).

Nevertheless, for both conditions the gross morphologies of these tissues were similar to the fresh sample represented in Figure 2.11. Hence, columnar cells were intact with basal cells aligned above the basement membrane and cilia were visible (solid line boxes Figure 2.16 and Figure 2.17). Therefore, from a morphological perspective (and to a lesser extent from Alamar Blue™ data) the olfactory epithelia buffered with SNS or citrate systems were deemed suitable for use with the diffusion chamber apparatus.

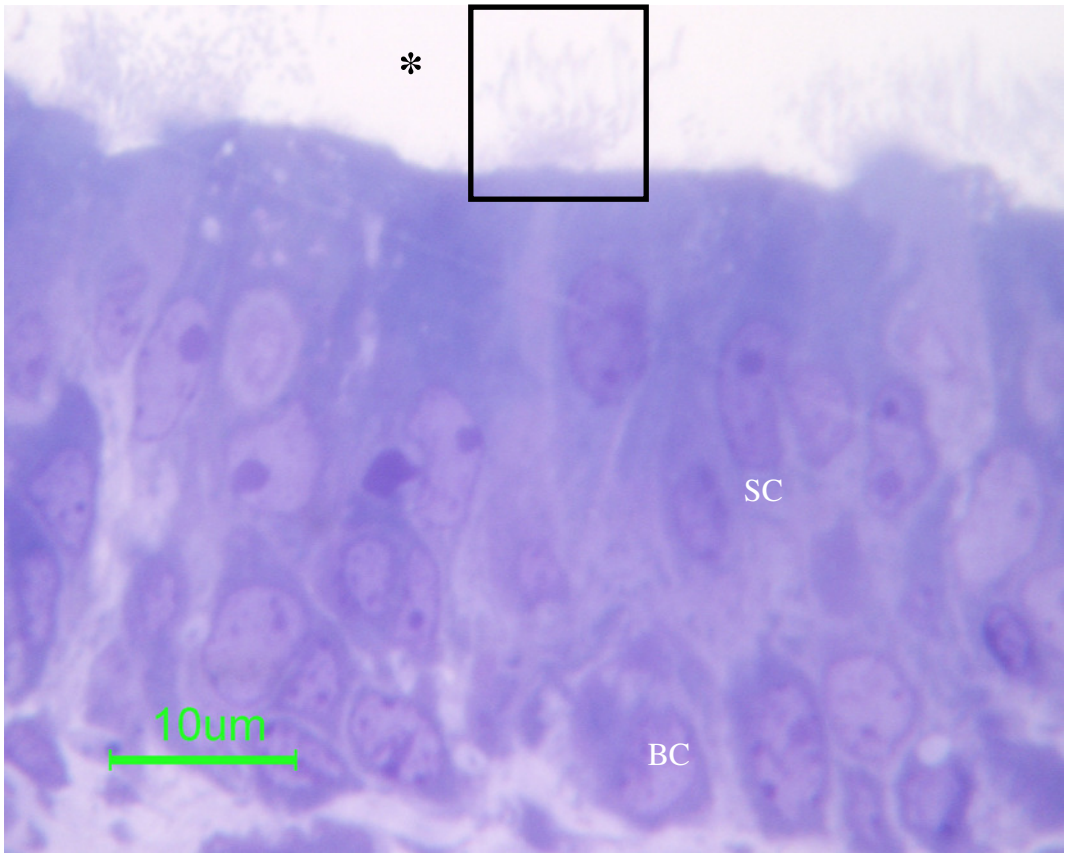

Figure 2.16 Morphology of olfactory porcine olfactory epithelium after dismounting the tissue from the diffusion chamber apparatus. The tissue was exposed to SNS buffer pH7.4 for 150 minutes. Cilia highlighted in solid lined box. BC Basal Cell. SC Sustentacular cell. * indicates luminal space.

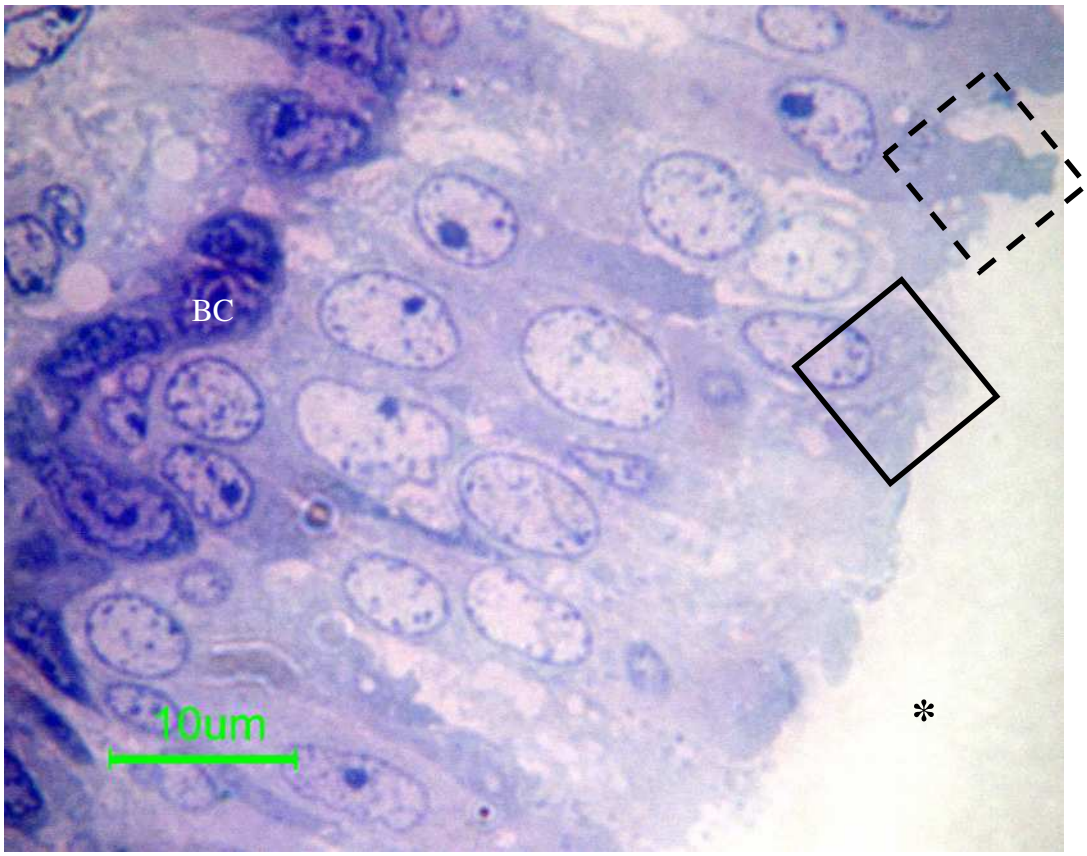

Figure 2.17 Morphology of olfactory porcine olfactory epithelium after 150 minutes exposure to citrate buffer pH6.0 in the diffusion chamber apparatus. Olfactory knob highlighted in dashed box. Vesicles appeared in the diffusion chamber exposed samples (solid and dashed boxes). BC Basal Cell. SC Sustentacular cell. * indicates luminal space.

2.3.3 Assessment of Equilibration Period

The stability of the electrophysiological readings were tested by comparing the mean values of R_m, PD and I_{sc} between 0-30 minutes and 120-150 minutes after mounting of the olfactory epithelium onto the diffusion chamber apparatus. Both the affects of sodium azide and buffer type were considered (Table 2.4).

For azide-free samples, PD and I_{sc} values remained reasonably constant over the time period measured for both buffering conditions. For citrate buffer, there was no statistical change for R_m between the two time periods. For SNS buffer, however, R_m significantly increased with time ($p<0.05$ paired t-test) from approximately 40 to 65Ωcm^2 (Table 2.4).

For azide-exposed samples corresponding R_m, PD and I_{sc} values remained constant for all buffering conditions . The results are summarised in Table 2.4.

Table 2.4 Summary of electrophysiological measurements (mean±s.d).

	R_m (Ωcm^2)	PD (mV)	I_{sc}($\mu A/cm^2$)
SNS (0-30min)	41.0±12.6*	-0.2±0.6	2.2±14.9
SNS (120-150min)	65.4±12.5*	-0.9±0.2	14.5±2.5
SNS+Azide (0-30min)	8.5±2.3	-0.3±0.6	47.5±84.1
SNS+Azide (120-150min)	7.6±3.4	0.7±0.4	-125.4±88.5
Citrate (0-30min)	62.6±26.8	0.4±0.1	-7.7±4.6
Citrate (120-150min)	80.5±43.9	-0.1±0.1	0.2±0.9
Citrate+Azide (0-30min)	9.5±4.5	1.6±1.1	-162.3±105.5
Citrate+Azide (120-150min)	12.2±1.7	1.7±1.1	-137.9±83.1

Both azide-free and azide-containing SNS and citrate buffered olfactory epithelia were tested for significant changes between two time periods: 0-30minutes and 120-150minutes. Statistical tests were performed between the two corresponding time periods to check for changes during the experiments. (n=3). * Significant difference (paired t-test) ($p<0.05$).

In summary, R_m for SNS buffer was the only parameter that changed during the experiments (Table 2.4). Otherwise R_m, PD and I_{sc} did not significantly change during the course of the measurements. Therefore, the epithelia which were mounted in the vertical Franz diffusion cell were considered to be bioelectrically stable during the course of the experiments. Hence, the 30 minute equilibration period was considered suitable for this system.

2.3.4 Comparison of Olfactory and Respiratory Tissue Metabolism

Table 2.5 summarises the Alamar Blue™ assay results for olfactory and respiratory epithelia; 6890±1602 and 8887±1752, respectively. Respiratory epithelium was more

metabolically active than olfactory epithelium ($p<0.05$; unpaired t-test; n=7). The variability was proportionally high with respect to the mean; RSD 23% and 20% for olfactory and respiratory epithelia, respectively. Therefore, a larger sample number is likely to improve the significance level.

Table 2.5 Comparison of metabolic rate between olfactory and respiratory nasal epithelia.

Date	*Olfactory RFU (Mean±s.d.)*	*Respiratory RFU (Mean±s.d.)*
21/11/2006	7040±885 (n=6)	9363±2236 (n=6)
23/11/2006	8018±2077 (n=6)	
28/11/2006	7496±1450 (n=3)	7003±924 (n=6)
30/11/2006	8801±1174 (n=4)	11286±2675 (n=7)
05/12/2006	6098±661 (n=3)	7524±556 (n=3)
06/12/2006	6960±258 (n=3)	
07/12/2006		9622±2504 (n=3)
12/12/2006	3817±462 (n=3)	6910±2748 (n=3)
13/12/2006		10497±5226 (n=6)
	6890±1602* (n=7)	**8887±1752* (n=7)**

*** Statistical difference ($p<0.05$; unpaired t-test; n=7)**

2.3.5 Correction Effect of Alamar Blue™ Values with DNA Content

Alamar Blue™ values (RFU) for 10 olfactory epithelia (each from a different animal) were corrected for their DNA content using the Hoechst DNA quantification method. A scatter diagram of DNA content against Alamar Blue™ values (RFU) was plotted (Figure 2.18). It was expected that a strong positive relationship would exist between the variables since it is logical that the metabolic activity of the tissue would depend on total amount of the tissue.

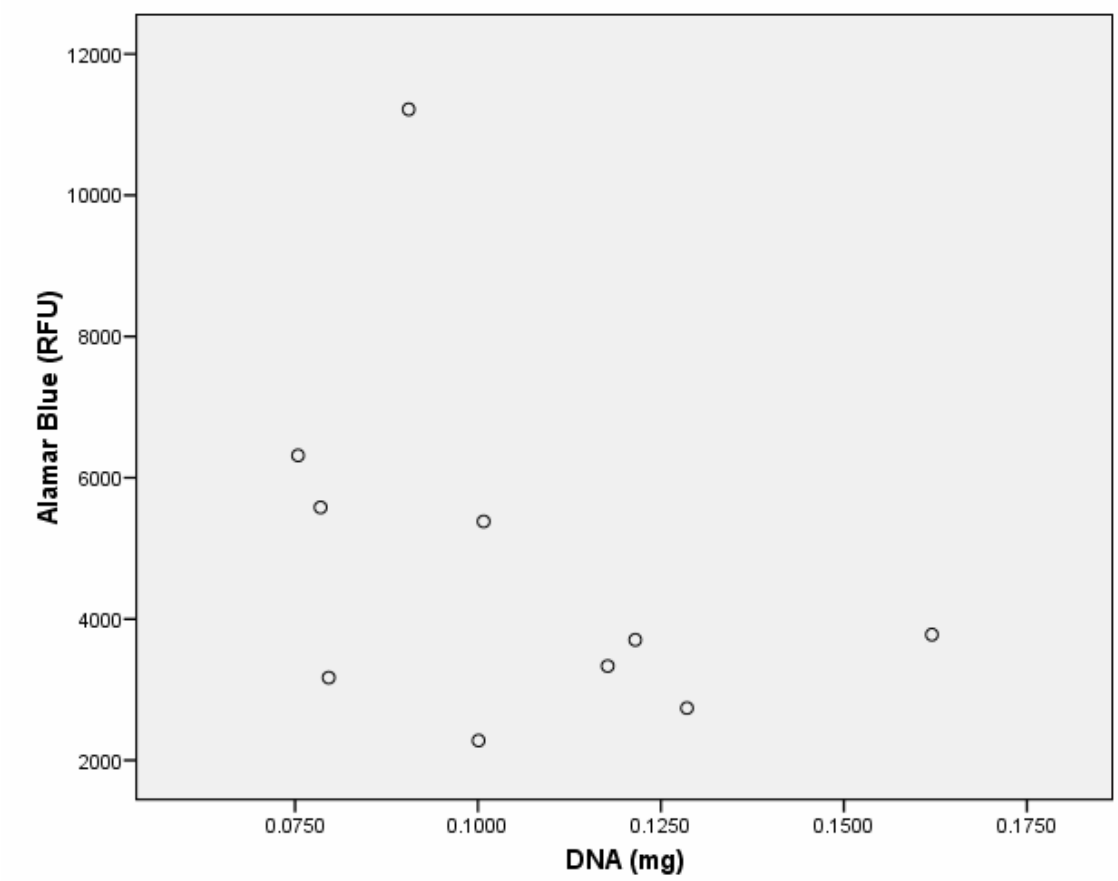

Figure 2.18 Scatter diagram showing the correlation between Alamar Blue™ viability measurements and the corresponding DNA content values.

The Spearman's Rank correlation coefficient was calculated as -0.430. There was no significant correlation between core size and Alamar Blue™ viability measurements ($p>0.05$; Spearman's Rank correlation test; $n=10$).

In addition, the variability of Alamar Blue™ data increased when the correction with DNA content was calculated. On average %RSD increased from 14% before correction to 27% after correction. It was expected that the variability would reduce, not increase, after the correction for amount of tissue per sample. Consequently, correction of Alamar Blue™ viability by DNA content was abandoned.

The DNA content per epithelial sample was derived using a DNA standard curve. Figure 2.19 shows an example of a DNA standard curve obtained using the Hoechst assay. The correlation is positive and linear. Four replicate plots were constructed in this way and all demonstrated a Pearson correlation coefficient of 0.9794 or higher. Therefore, all calibration plots were acceptable for analytical practice. The mean±s.d. Pearson correlation coefficient for these plots was 0.9887±0.008 (n=4). For good practice, however, a new calibration plot was constructed each time the DNA content of samples was measured.

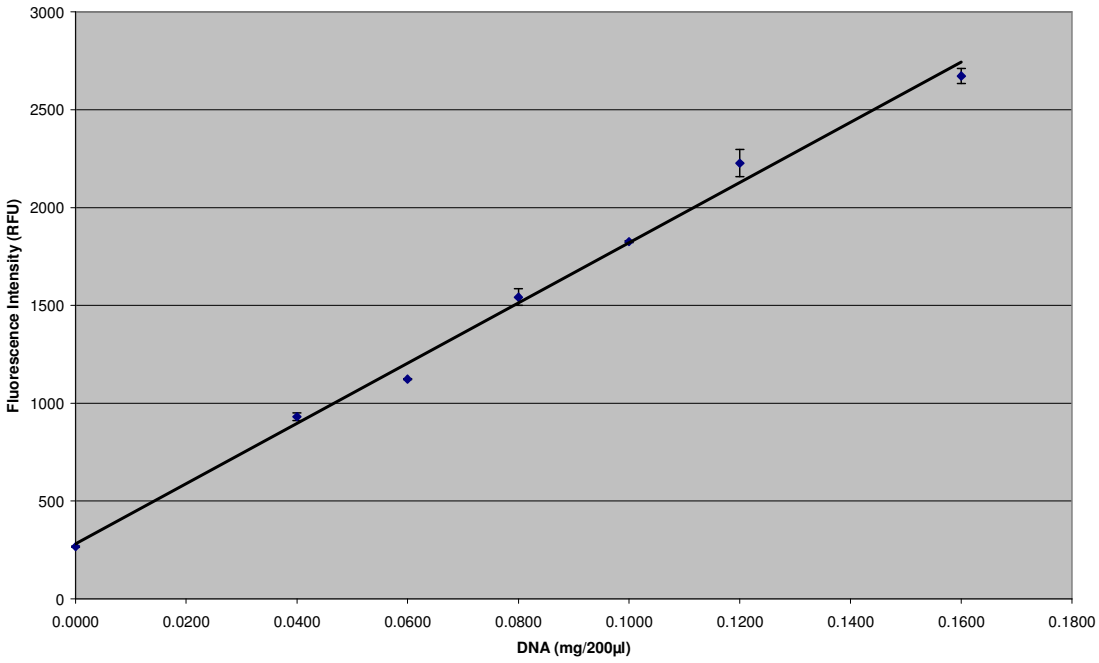

Figure 2.19 An example of a DNA standard curve using the Hoechst DNA quantification assay. A positive linear correlation was observed. The Pearson correlation coefficient for this plot was 0.9970. Individual values represent mean±standard error of mean (n=3).

2.4 DISCUSSION

The aim of this first section of investigations was to describe the method validation of the vertical Franz diffusion cell for its use with porcine olfactory epithelium in the investigation of direct N-B drug delivery of nanoparticles. Hence, it was necessary to prove that the experimental procedures had no effect on the tissue with respect to viability and cellular morphology.

The following objectives were defined in order to achieve this aim: first, an excision protocol was established to ensure that the diffusion chamber mounted epithelium was indeed olfactory; second, an assessment procedure of tissue viability was developed to ensure that the mounted tissue was alive during the experiments; and third, the morphological appearance of the olfactory epithelium before and after exposure to the experimental conditions was assessed (in absence of nanoparticles applied to the apical surface). In addition, the metabolic rate of olfactory and respiratory epithelia were compared which may help to gain a better quantitative understanding of active processes in the nasal epithelia and its speculative impact on drug delivery.

2.4.1 The Histology of the Porcine Nasal Epithelium

The morphology of the epithelium was different in various zones of the porcine nasal cavity. The transitory nature of the porcine epithelium (Adams 1990) is, in fact, common throughout the animal kingdom; goats (Kahwa & Purton 1996), rats ((Popp & Martin 1984)) bonnet monkey (Harkema et al 1987) and koalas (Kratzing 1984) and humans (Mygind 1979) have this feature.

The specific pattern of change from one epithelium type to the next was also common. In the work presented here, the porcine nasal epithelium changed from keratinised

stratified squamous at the nasal vestibule, to cuboidal and then pseudostratified columnar in the caudal direction. Indeed, these specific changes in epithelium types were remarkably similar to the Bonnet Monkey (Harkema et al 1987) which demonstrated that the gross morphology of the nasal epithelia are similar between mammalian species.

Nevertheless, a few notable differences were observed between that found here and previously in the literature. For example, Adams (1990) did not find the keratinised version of the stratified squamous epithelium in the rostral portion of the nasal cavity. The keratinised version was, however, found in goats (Kahwa & Purton 1996). The physiological function of keratinised stratified squamous epithelium is thought to protect the underlying cells from dehydration and mechanical insults. This would seem logical from the position of the epithelium at the nasal vestibule. The tissue here would be at most risk of damage from particulates upon inhalation and loss of water externally upon exhalation.

The epithelium changed from stratified squamous to non-ciliated cuboidal in the caudal direction. The physiological function of nasal cuboidal cells remains speculative. They may be involved in antigen presenting, osmotic balancing and/or detoxification (Adams 1990).

The epithelium finally changes again to pseudostratified columnar epithelium which was 30-40µm in height (Figure 2.9). Both ciliated and non-ciliated columnar cells were found in the current study. Previously, however, only the non-ciliated type has been observed in pigs (Adams 1990). It was noted that the *lamina propria* underlying this

area (Region 5 Figure 2.2) had the highest level of vascularisation. This has been observed previously in the literature (MartineauDoize & Caya 1996). From a drug delivery perspective, Region 5 is therefore a suitable epithelium for drug transport to the systemic circulation. Indeed, it has since been used in this capacity within our research group (to be published).

Moreover, Adams found that epithelial characteristics of piglets were similar regardless of age (1-70 days old) (Adams 1990). To my knowledge, no detailed study of porcine nasal mucosa has been carried out on 6 month old pigs to date. Therefore, this is the first description of such work and extends the same conclusion over the first six months of a pig's life.

Olfactory epithelium was found in Region 6 covering the caudal region of the dorsal turbinate (Figures 2.2, 2.10 and 2.11). It was characterised by a ciliated columnar epithelium (40-50µm in height). It has been suggested that the columnar cells in the olfactory epithelium are taller (60-80µm) than the respiratory type (~25µm) (Jansson 2004). However, the distinction in epithelial cell layer height in the olfactory and respiratory epithelia was less pronounced in the animals used in this study.

Finally, olfactory tissue is characterised for having *filia olfactoria* in the *lamina propria* (Figure 2.12) and olfactory knobs on the apical terminus of the olfactory axons (Figure 2.11). These features are not present in respiratory mucosa since it does not contain axons. Moreover, toluidine blue was a suitable choice of monochromatic stain since it enabled clear distinction of *filia olfactoria* and olfactory knobs from other morphological features.

In general, the pattern of epithelia found in the porcine nasal cavity conformed to that found previously in pigs (Adams 1990; MartineauDoize & Caya 1996). Modest variations in morphology may have resulted from sampling of the epithelia from slightly different locations from within the nasal cavity compared to the literature. However, it would be time consuming to exhaustively characterise the nasal cavity in this way therefore this work was not done.

2.4.2 Tissue Viability: The Effect of pH Buffers and Sodium Azide

The results presented here have shown that the excised tissue could be kept alive for approximately 4 hours after excision. During this period the epithelia were transported on ice for ~1 hour and mounted on the diffusion chamber apparatus for 2½ hours. Nasal epithelia have previously been used in similar diffusion chamber experiments in a number of different species. Viability can be maintained for 8 hours in sheep (Wheatley et al 1988), 10 hours in rabbits (Bechgaard et al 1992), 4 hours in cattle (Bechgaard et al 1992) and 8 hours in pigs (Wadell et al 1999). Therefore, the excised tissues used here were within the accepted viability timeframes.

The studies described in the literature were performed at 37°C unlike in the current work which was carried out at 29°C. Cremaschi *et al.* performed their diffusion chamber studies at 27°C in order to improve the tissue survival time (Cremaschi et al 1996). Hence, since the present experiments were conducted at a lower temperature, it was anticipated that the tissues buffered at 29°C would have a longer survival time than that described previously.

R_m, PD, I_{sc} and Alamar Blue™ assay measurements were performed in order to examine the viability of the epithelia in detail. R_m provides a measure of membrane 'leakiness.' R_m was measured to be 58.6±12.7Ωcm^2 for SNS and 78.8±40.2Ωcm^2 for citrate buffers. There is a lack of electrophysiological data available in the literature for olfactory mucosa; therefore, these values were compared to respiratory epithelium. Hence, the R_m data conformed with those found previously (Table 2.6): 75.0±28.0Ωcm^2 (porcine respiratory epithelium, 37°C (Osth et al 2002a)), ~40Ωcm^2 (rabbit respiratory epithelium, 37°C (Kubo et al 1994)), and ~70Ωcm^2 (rabbit respiratory epithelium, 37°C (Bechgaard et al 1992)). Moreover, the temperature maintained during the experiment does not appear to affect R_m, 52.1±5.6Ωcm^2 (27°C, rabbit respiratory epithelium (Cremaschi et al 1991)).

Table 2.6 Literature values (mean±s.d.) for electrophysiological parameters of nasal tissues that were mounted to diffusion cells for different animal species and at different temperatures.

Reference	*R_m ($\Omega.cm^2$)*	*PD (mV)*	*I_{sc}($\mu A/cm^2$)*	*Comment*
(Osth et al 2002a)	75.0±28.0	-4.5±3.4	58.6±28.8	37°C, porcine respiratory epithelium
(Cremaschi et al 1991)	52.1±5.6	-3.4±0.5[a]	65.0±6.7	27°C, rabbit respiratory epithelium
(Kubo et al 1994)	~40	~-5 [a]	100-120	37°C, rabbit respiratory epithelium
(Bechgaard et al 1992)	~70	-6.4±1.5 [a]	92±13	37°C, rabbit respiratory epithelium

[a] Quoted as positive values in literature because positive electrode was placed on the serosal side of the epithelium.

Nasal epithelia are regarded as a 'leaky,' i.e. have a lower permeability than other biomembranes and therefore is regarded as a potential drug delivery membrane (Lehr 2002). For example, the permeation of a paracellularly transported molecule THA (9-amino-1,2,3,4-tetrahydroacridine) was compared across different mucosae of the domestic pig. The study showed that nasal epithelium had a significantly enhanced

THA permeation rate ($p<0.05$) compared to all other biomembranes tested (sublingual, buccal, rectal, duodenum, jejunum and ileum) (Gore et al 1998).

PD, I_{sc} and Alamar Blue™ data showed that tissue viability was statistically lowered when 0.5mM citrate buffered (pH6.0) olfactory epithelium samples were compared to SNS buffered samples (Table 2.3 and Figure 2.15). Pujara *et al.* studied the effects of buffer types on protein release from the nasal mucosa of rat intranasal perfusion studies using a LDH assay (Pujara et al 1995). According to these authors protein release is positively associated with cellular damage and therefore is indicative of tight junction integrity. Phosphate and adipic acid buffers (70mM) at pH 4.75 were found to contribute least to protein release and were not significantly different to saline perfusion levels (negative control). Acetate buffer (70mM) was the most damaging which (in the authors' opinion) probably was due to phospholipid partitioning ability of the unionised (acetic acid) entity. Further, there was no apparent tissue damage resulting from 30 minute nasal perfusion with citrate or phosphate buffers. The authors suggested that there was 'an intrinsic factor unique to [each] buffer species which was responsible for any [minimal] damage to the nasal mucosa.'

Pujara *et al.* (1995) also found damage to nasal epithelium from acetate buffer in the concentration range 70mM to 210mM. This damage was proportional to the concentration of acetate ions. The unionised acetic acid molecules were thought to interfere with the phospholipid membrane function. But no such trend or mechanism was detailed for citrate or phosphate buffers (Pujara et al 1995). Moreover, the concentrations of buffering ions used in this experiment were much higher than those used in the present work (SNS buffer 1.5 mM NaH_2PO_4, 0.83 mM $NaHPO_4$ and 15 mM

$NaHCO_3$; 0.5mM citrate buffer). Therefore, buffer concentrations used here were thought to have negligible effect on tight junction integrity.

The similarity between R_m values for citrate (pH6.0) and SNS (phosphate-based; pH7.4) buffers suggested that extent of tissue damage was not correlated with pH. In support of this, Maitani *et al.* (1997) found that levels of tissue damage (expressed in terms of protein release) were the same between saline solutions adjusted to pH5.2 or pH7.4 after placing rabbit nasal tissue into a diffusion chamber apparatus. This concurred with results by Pujara *et al*. (1995) who found no differences in tissue damage over the pH range 3-10.

In contrast, Maitani *et al.* (1997) in the same study found that reducing pH from 7.4 to 5.2 significantly increased ($p<0.05$ Student's t-test) movement of Lucifer Yellow (a hydrophilic paracellular marker) across the nasal epithelium of male Japanese White rabbits. The authors did not give an explanation for this. Thus, phosphate buffer (SNS pH7.4) may preserve tight junction integrity better than citrate buffered (pH6.0) samples but no such statistical differences were observed in this investigation (Table 2.3). This could have been due to high data variability or low sample numbers.

There were differences, however, in the morphology of the samples after 150 minute exposure in the diffusion chambers (Figure 2.16 and Figure 2.17). The morphology of the cells from the citrate buffered olfactory samples was worse than that of SNS samples. This indicated that either the viability or the integrity of the olfactory epithelium was affected by the citrate buffer.

In support of this, significant differences were found between PD and I_{sc} for these two buffering systems ($p<0.05$, ANOVA, Table 2.3). When these data were compared with the data obtained for Alamar Blue™ enzymatic assay for viability it was found that samples exposed to SNS buffer were more metabolically active than those exposed to citrate buffer. This was evident both with and without the use of the diffusion chamber apparatus ($p<0.01$, ANOVA, Figure 2.15). Therefore, although no tissue damage was observed by a reduction in R_m, a reduction in metabolic activity (PD, I_{sc} and Alamar Blue™ values) was observed.

With regards to tissue viability it can be concluded, through PD, I_{sc} and Alamar Blue™ data, that metabolism was reduced by citrate (pH6.0) compared to SNS (pH7.4) buffer. Indeed, the cellular morphology of the SNS buffered samples (compared to citrate buffered ones) was more akin to the freshly excised olfactory epithelium (Figure 2.11, Figure 2.16 and Figure 2.17) which supports this conclusion. As discussed, this effect was unlikely to be a consequence of the different species of buffering ions, the concentration of buffering ions, or mechanical damage to the mucosa. Therefore, pH remained as the likely cause for this observation.

The possibility that pH reduction from pH7.4 to pH6.0 may have affected nasal tissue viability is also implied in the literature. For example, baseline pH levels of nasal mucosa in eight human volunteers (four with allergic rhinitis) have been found to be 7.04-7.70 (physiologically neutral) (Shusterman & Avila 2003). After an application of carbon dioxide the mucous pH transiently reduced before rising again to baseline levels. This would suggest that pH 7.04-7.70 is a preferable environment for the epithelial cells underlying the mucous layer compared to a lower pH environment. The homeostatic

mechanism for this was thought to involve bicarbonate ions and carbonic anhydrase enzyme similar to that found in the gastric mucosa (Allen & Flemstrom 2005).

The exact pH environment of the nasal mucus, however, is controversial since there is some evidence to suggest that it is lower. Washington *et al.* (2000) placed a pH electrode (composition of electrode unspecified) 3cm posteriorly from the nasal vestibule on the floor of the nasal cavity. They found that the mean pH was 6.27 (+0.13/-0.18) (n=12) (the standard deviation was not evenly spread due to conversion of $[H^+]$ to pH). The pH range, however, of these values varied considerably (5.20-8.00).

Similarly, McShane *et al.* (2003) used monocrystalline antimony catheter pH electrodes to measure the pH of the nasal floor 4-5cm from the nasal vestibule. Healthy volunteers had a pH 6.7±0.13 (n=6). Overall, there is considerable inter-study variation between pH measurements of nasal mucosa amongst healthy human subjects.

Cystic fibrosis patients, who have characteristically thicker mucus due to a reduced sol layer and therefore poor mucociliary clearance, had an even lower nasal pH (6.2±0.1; n=6) (McShane et al 2003). However, the pH difference between healthy and cystic fibrosis patients was not observed with gold combined pH-glass electrodes. It was not understood why the composition of the electrodes produced different results.

In contrast, nasal mucosal pH of patients with rhinitis was 7.2-8.3 (Fabricant 1941). Rhinitis is characterised by an over production of serous secretions from the epithelial cells that form the mucosal sol layer.

The observations of over- and under-production of sol layer in pathological states suggests that a pH gradient exists between nasal gel layer (pH5.5-6.5) and sol layer (pH7.4) i.e. pH measurements were low (pH 6.2±0.1) when sol layer was underproduced (cystic fibrosis) and pH was high (pH 7.2-8.3) when sol layer was overproduced (rhinitis).

If a mucosal pH gradient did exist then the single pH measurements described above would be unrepresentative of the pH conditions at the epithelial cell surface. The pH electrode tips used in these studies (~3mm diameter) were larger than the thickness of the whole mucous layer (~9µm, gel layer and sol layer combined). This could explain the differences in nasal pH measurements that were found between the studies described above.

Indeed, pH gradients have been observed previously in the rat gastric mucosa model *in vivo* (Phillipson et al 2002). In this study, male Sprague-Dawley rat gastric mucosae were exposed to 1.2cm^2 in a mucosal chamber. The pH of the sol layer (described as 'adherent mucus' by the authors) at the epithelial surface was measured using fine microelectrodes (tip diameter 1-3µm). The mucosal surface was exposed to 0.9% NaCl which was maintained at 37°C. After 10 minutes the 0.9% NaCl was replaced with acid (HCl, pH 1). The pH of the sol layer was measured as 7.03±0.09 whilst acid secretion was stimulated with *i.v.* pentagastrin (40µg.kg^{-1}h^{-1}). Pentagastrin is a pentapeptide drug that stimulates parietal cells in the stomach mucosa to secrete HCl into the gastric lumen. This experiment was repeated after removal of the gel layer (described in the report as 'loosely adherent mucus'). Removal of the gel layer did not to statistically reduce the pH in the sol layer (6.82±0.19). It was therefore concluded that the gel layer

was not important for the maintenance of the pH gradient. In addition, the experiment was also repeated with removal of gel layer and luminal exposure to 0.5mM DIDS (4,4'-diisothiocyano-stilbene-2,2'-disulphonate), a pharmacological inhibitor of apical Cl^- /HCO_3^- ion channels. In these conditions, sol layer pH was reduced to 1.37±0.21; therefore, it was concluded that a bicarbonate buffering mechanism was required for maintenance of physiologically neutral sol layer pH.

In a different study, the same gastric mucosa model showed that rats given *i.v.* HCO_3^- (5mmol.kg^{-1}.h^{-1}) produced a higher epithelial cell surface pH (pH ~5) compared to control rats (no HCO_3^- given, pH ~1.6) (Synnerstad et al 2001). This provided more evidence that HCO_3^- from the blood is involved in maintenance of the mucosal layer pH gradient. (For further reading, the nature of the gastric mucosal pH gradient can be found in greater detail elsewhere (Allen & Flemstrom 2005)).

In the current work, viability of excised nasal tissue was higher at pH7.4 than at pH6.0. Olfactory epithelia exposed to 0.5mM pH6.0 citrate buffer, which contained no HCO_3^- ions, showed reduced PD, I_{sc} and Alamar Blue™ viability scores. Therefore, it could be interpreted from this data that the nasal epithelial cells may not have been able to maintain pH7.4 in the sol layer.

Gastric mucosa acidity (~pH1) in the lumen is produced by the release of HCl from the parietal cells. In the nasal cavity the pH gradient is more likely to be derived from solubilisation of expired carbon dioxide in the nasal mucus. Carbonic acid is weaker than HCl therefore it is expected that a shallower pH gradient exists in the nasal cavity.

The effect of metabolic blocker, sodium azide, on the viability of olfactory epithelia was also assessed in these investigations. Sodium azide statistically reduced viability for the SNS buffered olfactory epithelium as measured by R_m, PD and Alamar Blue™ (but not I_{sc}) scores (R_m and PD $p<0.05$, ANOVA, Table 2.3; Alamar Blue™ $p<0.01$, ANOVA, Figure 2.15). However, similar statistical changes were not observed for citrate buffered samples ($p>0.05$, ANOVA). A reduction in metabolism, as observed by these methods, was expected since sodium azide is a broad metabolic inhibitor that affects electron transport chain production of ATP. The lack of significance for I_{sc} values was probably due to variability of data. Citrate buffered olfactory epithelium that had been mounted onto the diffusion chamber was not effected by sodium azide. It was suggested that the reduction in pH from 7.4 to 6.0 between the different buffering systems caused an overall reduction in cellular viability in the olfactory epithelium; thus, addition of metabolic blocker did not cause significant changes to the viability of the tissue.

However, it could not be concluded that the olfactory epithelium was killed by the citrate buffer. Citrate pH6.0 buffered unmounted samples had statistically higher Alamar Blue™ viability scores than citrate-buffered azide-exposed olfactory epithelium after dismounting from the diffusion cell apparatus ($p<0.05$, ANOVA, Figure 2.15).

2.4.3 The Bioelectrical Equilibration Period for Porcine Olfactory Epithelium

There were no statistical changes in PD or I_{sc} values over a 150 minute period in either SNS or citrate buffer (Table 2.4). In addition, R_m values remained constant for citrate buffered olfactory epithelia. This would suggest that equilibration occurred within 30 minutes. Tissues were dismounted from the diffusion chamber apparatus within 4 hours of slaughter. Longer validation of tissue survival time was not practical due to the total

time taken per experiment. For these reasons an equilibration period of 30 minutes was chosen.

R_m values increased with statistical significance for SNS buffered samples between 0-30 minutes and 120-150 minutes ($p<0.05$ paired t-test). This would suggest, in fact, that more time was required for equilibration since R_m values had not settled to reach a steady state. However, no other parameter required more time to a steady state (Table 2.4). Thus in conclusion, a 30 minute equilibration period was deemed sufficient for the diffusion chamber experiments.

Alternatively, it could be considered that the samples might not have equilibrated within the 150 minutes of this experiment and that significant differences could have been found if longer time periods were allowed. This, however, is unlikely since equilibration periods of greater than 120 minutes have not been necessary previously (either at 37°C or 27°C [Table 2.7]).

Indeed, a range of equilibration periods between 30-120 minutes and temperature conditions have been used in the past (Table 2.7). A 30 minute equilibration period has been used for porcine, bovine and rabbit nasal epithelia experiments at both 27°C and 37°C and for respiratory or olfactory epithelia (Cremaschi et al 1996; Schmidt et al 2000; Wadell et al 2003; Kandimalla & Donovan 2005b, a).

So, although equilibration periods up to 120 minutes have been used previously (Bechgaard et al 1992; Kubo et al 1994; Maitani et al 1997; Osth et al 2002a; Osth et al

2002b; Jansson 2004), these longer periods did not seem to be necessary and were impractical to undertake for the current work.

Table 2.7 Equilibrium periods and experimental temperatures for diffusion chamber studies with various nasal epithelia.

Equilibration Period (minutes)	*Experimental Conditions*	*Reference*
30	Bovine respiratory epithelium[a] (37°C)	(Schmidt et al 2000) [a]
30	Bovine olfactory epithelium[a] (37°C)	(Kandimalla & Donovan 2005b) [a]
30	Porcine respiratory epithelium (37°C)	(Wadell et al 2003)
30	Rabbit respiratory epithelium (27°C)	(Cremaschi et al 1996)
30-60	Bovine and porcine olfactory mucosa (37°C)	(Jansson 2004)
60	Porcine respiratory epithelium (37°C)	(Osth 2002; Osth et al 2002a; Osth et al 2002b)
60	Rabbit respiratory epithelium (37°C)	(Bechgaard et al 1992; Maitani et al 1997)
120	Rabbit respiratory nasal mucosa (37°C)	(Kubo et al 1994)

[a] **Electrophysiological data unavailable.**

2.4.4 Comparison of Olfactory and Respiratory Tissue Metabolism

Tissue viability data was examined in terms of R_m, PD, I_{sc} and Alamar Blue™ for porcine olfactory epithelium. In addition the Alamar Blue™ measurements were performed on freshly excised respiratory epithelia which were dissected from Region 5 of the pig nasal cavity (Figure 2.2).

R_m and PD values for porcine olfactory epithelia in SNS buffer (29°C) are reported here as 58.6±12.7Ωcm^2 and -0.8±0.2mV. Previously, Jansson (2004) had found similar figures for porcine olfactory epithelium in the same buffer at 37°C (45±9Ωcm^2 and -1±0.5mV [values approximated from graphical data]. This is the only example of

electrophysiological data for olfactory epithelium in the literature known to date. In addition, it is possible to speculate that the temperature difference did not have a considerable effect on the values. Nevertheless, passive and active transport of ions would presumably increase with temperature. Therefore, an explanation for the indifferent affect of temperature on the electrophysiology of the nasal epithelial tissues remains unclear. But this insensitivity of temperature on R_m has also been noted within the literature (Table 2.6).

The PD (-0.8±0.2mV [SNS], -0.1±0.1mV [citrate buffer]) and I_{sc} (-13.3±1.5μA/cm^2 [SNS], 1.0±0.2μA/cm^2 [citrate buffer]) values, however, are low compared to those for nasal respiratory epithelia from various species (Table 2.6). Rabbits had a PD of ~-5mV (Kubo et al 1994) and -6.4±1.5mV (Bechgaard et al 1992) at 37°C. The value decreased to -3.4±0.5mV when the temperature was reduced to 27°C (Cremaschi et al 1991). PD for porcine epithelia at 37°C agreed with the rabbit species but were more variable, -4.5±3.4mV (Osth et al 2002a). Also, in general, lower PD values corresponded with higher I_{sc} measurements (Table 2.6).

Hence, R_m (which measures passive transport of ions across the epithelium) agrees with previous data but PD and I_{sc} (which both measure active transport of ions across the epithelium) were lower. This would imply that the olfactory epithelium used in these studies were less metabolically active than the respiratory nasal tissues (Table 2.6). This can be explained by understanding the electrophysiological method used.

An innate resting membrane potential (PD) is generated by the active transport of ions across the epithelium. The magnitude of PD depends on a combination of two factors;

(a) the rate of ion-transport across the epithelium and (b) the 'leakiness' of the epithelium. As rate of ion transport across the epithelium increases then the PD will also increase since, by definition, the imbalance of ions across the epithelium generates the PD. If the epithelium is very 'leaky' then the imbalanced ions are able to passively transport back down the electrochemical gradient that is formed. This is essentially a naturally occurring short-circuit which has the effect of nullifying the PD. Therefore, PD is theoretically a function of tight junction integrity (R_m) and transport rate of ions across the epithelium (Lehr 2002).

Thus, the 'leaky' nature of the nasal epithelia and/or their inability to overcome the resultant short-circuit may have lead to the low observed PD and I_{sc} values. Since olfactory and respiratory R_m values are similar, then 'leakiness' of these epithelia are also likely to be the same. Therefore, the metabolic rate is likely to be different between these epithelia.

(I_{sc} is described as the externally applied current needed to extinguish the PD. Hence, PD and I_{sc} are physiologically linked and so the previous discussion may be extended to I_{sc} as well as the given example for PD).

The difference between viability scores of olfactory and respiratory epithelia was confirmed by assessment of the tissue viability by Alamar Blue™ assay (Table 2.5). Hence, olfactory and respiratory epithelia cores were extracted from pigs and assayed by Alamar Blue™, as described in 2.2.6 Comparison of Olfactory and Respiratory Tissue Metabolism. The metabolic activity of the respiratory epithelium (8887±1752 RFU) was significantly higher than that for olfactory epithelium (6890±1602 RFU)

($p<0.05$, unpaired t-test, n=7). It was not likely that the differences for the Alamar Blue™ were a result of differences between thickness of the respiratory and olfactory epithelia in these samples (2.4.5 Hoechst Assay). Therefore, this result strongly supports the conclusions obtained from the differences in electrophysiological parameters.

The reason for the difference in metabolic rate between the respiratory and olfactory epithelium were not investigated in this study. However, physiologically specialised functions of the respiratory epithelium, such as antigen sampling or generating ciliary motion, could explain the observed difference.

The difference between the metabolic activity of the olfactory and respiratory epithelia found in the nasal cavity of pigs is an important finding that may have wider implications regarding the treatment of exogenous materials (e.g. nanoparticles and drug molecules) by nasal epithelia. For example, it could mean that greater active transport of nanoparticles occurs into the respiratory epithelium compared to olfactory epithelium; this would increase the transport of nanoparticles across the respiratory epithelium compared to olfactory tissue. Alternatively, it could mean that drug molecules (or biodegradable nanoparticles) may be actively degraded at a slower rate at the olfactory epithelium and therefore this may have the potential to increase drug transport across this epithelium compared to respiratory tissue. The relationship between nasal epithelia and exogenously applied materials may also vary depending on the properties of the exogenous material. However, this relationship between drug transport and metabolic activity of the epithelium remains speculative and requires further investigation.

2.4.5 Hoechst Assay

When correcting the Alamar Blue™ data for amount of tissue per sample, it was expected that the variability would reduce since the metabolic activity of each cell in the epithelium was assumed to be equivalent (2.3.5 Correction Effect of Alamar Blue™ Values with DNA Content); however, variability was found to increase.

The reasons for this are unclear but it may be that a subset of cells (most probably located near the apical surface) was the most metabolically active in the epithelium and therefore contributed heavily to the Alamar Blue™ measurements. These cells may, for example, be responsible for the production of mucus or active movement of substances into or out of the luminal space. Thus, the overall metabolic activity of the epithelium may actually be determined by the activity of these cells and not the thickness of the membrane. This hypothesis is strengthened by the finding that there are proportionally more mitochondria located at the apical surface than elsewhere in the epithelium (Figure 2.13). This mitochondrial zone has also been reported elsewhere (Matulionis & Parks 1973). Consequently, correction of Alamar Blue™ viability by DNA content was abandoned.

2.4.6 Assessment Methods for Epithelial Viability / Metabolic Rate

The bioelectrical characterisation of membranes as described in this chapter is the best known (and probably only) example of a real time method to assess cellular activity in epithelia. Nevertheless, limitations of the method have been noted previously. For example, it can only measure one aspect of cellular metabolism – transport of ions across the epithelium. Measurement of this data is inherently variable, particularly, when the epithelia under investigation are ‘leaky’. Nasal epithelia are more ‘leaky’ than many other epithelia (2.4.2 Tissue Viability: The Effect of pH Buffers and Sodium

Azide); thus confidence levels of no more than 95% were achieved in this work for evaluating statisitcal differences for these measurements.

Furthermore, it is possible that subjecting the delicate biological membranes to unnatural electrical currents (during closed circuit conditions) may affect its condition (Cremaschi et al 1991). Cremaschi used open circuit conditions (no applied current) at 27±1°C to establish tissue viability in rabbits. The effect of externally applied currents, however, is likely to be negligible due to the short duration and small currents applied to the membranes with this procedure.

Nevertheless, alternative methods have been used previously to monitor viability. These tests, like Alamar Blue™, use enzymatic activity as a marker for cell viability/cytotoxicity. For example, Trypan Blue has been widely used to detect damaged or dead cells. The dye is taken up by non-viable cells but excluded by live ones. The method is particularly important for cells suspensions where the proportion of viable cells can quickly and easily be counted within the population by light microscopy. It is, however, less practical to use with intact epithelia and there are concerns with its accuracy and ability to penetrate the epithelium (Jones & Senft 1985).

Further, a double staining method using calcein AM ester (an acetoxymethyl ester of calcein) and ethidium homodimer has been utilised for viability assessment of (bovine olfactory) epithelium (Schmidt et al 2000; Kandimalla & Donovan 2005b, a). The first dye is a non-fluorescent precursor that is quickly metabolised by viable cells to green fluorescent calcein by esterase enzymes. The second dye enters non-viable cells and binds with DNA to form a red fluorescent signal. The signals can be observed by

fluorescent microscopes. This bimodal system is thought to be more accurate than Trypan Blue and viability can be assessed up to one week after original sample preparation. But, like Trypan Blue, it may be difficult to accurately quantify viability for intact epithelia due to the presence of mucus and other extracellular components of the tissue.

The conversion of a soluble yellow tetrazolium salt (MTT) to the insoluble blue form MTT formazan by viable cells containing succinic dehydrogenase uses a similar principle. It has also been widely used for cell cultures and monolayers. It can be adapted for membrane layers (Imamura et al 1994). The process, however, has the added step of dissolving the insoluble MTT formazan in dimethyl sulfoxide which can increase data variability.

Alternatively, lactate dehydrogenase (LDH) assay is a similar assay that is based on the reduction of a different tetrazolium salt (INT). INT is converted in an enzymatic reaction to formazan. This time formazan is a water-soluble product and exhibits an absorption maximum at 492 nm. Higher UV absorption relates to more LDH activity which is symptomatic of tissue damage or cell death.

Both MTT and LDH assay, however, can only measure cell toxicity; hence, differences between viability of different epithelia can not be assessed. Therefore, the inherent differences in overall metabolic activity, which were observed for respiratory and olfactory tissues in the work presented here, may not be observed by MTT and LDH assays.

In contrast to the above methods, Alamar Blue™ was quick, simple and easily quantifiable since both reagent and product were water soluble. Data variability was low compared to electrophysiological methods and statistical confidence levels of above 99% are reported here. Also, viability differences between olfactory and respiratory were observed, a conclusion that could not be possible by biochemical cytotoxicity assays as explained previously.

A combination of the electrophysiological method and Alamar Blue™ has the advantage of providing an overall description of viability that each individually can not. Hence, the assessment of viability by Alamar Blue™, particularly in combination with electrophysiological methods (which has not previously been described in the relevant literature to date) could prove to be a powerful method to assess the viability of excised epithelia.

2.4.7 Viability Acceptance Criteria for Porcine Olfactory Epithelium

Data variability for diffusion chamber studies could be due to species/population differences, specific site of excision, thickness of the isolated mucosa, and/or buffer conditions (temperature, pH, oxygenation and composition). These variables need to be controlled in order to identify any differences between samples. Some factors are more important than others, since for example, it has been shown in this study that pH (2.3.2 Effect of Different Buffers and Sodium Azide on Olfactory Epithelium) significantly affected tissue viability whereas the thickness of the isolated epithelium had little effect (2.3.5 Correction Effect of Alamar Blue™ Values with DNA Content).

Therefore, different acceptance criteria need to be assessed for each system used. Hence, the R_m, PD, I_{sc} and Alamar Blue™ data that are presented in this chapter will be

used to statistically compare the viability of epithelia used for nanoparticle transport studies in Chapter 4.

2.5 CONCLUSIONS

A protocol for the extraction of porcine nasal epithelia was developed and the location of olfactory epithelium was confirmed. The olfactory region was found at the caudal portion of the porcine nasal cavity (Figure 2.2). A circular piece (~2cm^2) of olfactory epithelium, which was large enough for the diffusion chamber experiments, was extracted from the epithelium lining the dorsal nasal turbinate.

In terms of tissue viability, Alamar Blue™ viability showed that the diffusion chamber experiment did not have a statistical affect ($p>0.05$, ANOVA, Figure 2.15) on the metabolic activity of the olfactory tissue when compared to samples that had not been mounted on the apparatus. Furthermore, the histological examination of the SNS buffered olfactory epithelia showed that the tissues did not change considerably when they were dismounted from the diffusion cells compared to unmounted samples.

Also, it was found that the nature of the buffering system had significant effects on the viability of the porcine olfactory epithelium. PD ($p<0.05$, ANOVA, Table 2.3), I_{sc} ($p<0.05$, ANOVA, Table 2.3) and Alamar Blue™ ($p<0.01$, ANOVA, Figure 2.15) viabilities were significantly greater for diffusion cell mounted epithelia buffered in SNS compared to those buffered in 0.5 mM citrate buffer (pH6.0). After comparison with the literature it was concluded that pH was the major contributing factor in this respect.

Further, a metabolic blocker, sodium azide, statistically reduced viability for the SNS buffered olfactory epithelium as measured by R_m, PD and Alamar Blue™ (but not I_{sc}) scores (R_m and PD $p<0.05$, ANOVA, Table 2.3; Alamar Blue™ $p<0.01$, ANOVA, Figure 2.15). However, similar statistical changes were not observed for citrate buffered samples ($p>0.05$, ANOVA). It was interpreted from this, and observations of a slight morphological deterioration to the citrate buffered olfactory tissues (Figure 2.17), that the citrate buffer may have completely reduced the viability of the olfactory epithelium. However, sodium azide did statistically reduce the Alamar Blue™ viability score of citrate buffered olfactory epithelium compared to (azide-free) unmounted tissues (Figure 2.15). Therefore, the citrate buffered samples were presumed to have statistically reduced the viability of the olfactory epithelium but not to have killed it completely.

A novel methodology was developed to find a suitable bioelectrical equilibration period for the porcine olfactory epithelium. A 30 minute equilibration period was acceptable for both SNS and citrate buffers since, except in one instance, statistical changes were not observed between the initial and final R_m, PD and I_{sc} measurements ($p<0.05$, paired Student's t-test). A 30 minute equilibration was in agreement with previous studies of nasal respiratory epithelium.

Alamar Blue™ viability for olfactory epithelium was statistically reduced compared to respiratory epithelium ($p<0.05$, unpaired Student's t-test, Table 2.5). This was confirmed by a comparison of the electrophysiological data for olfactory epithelium obtained here with that for respiratory data found in the literature (2.4.4 Comparison of Olfactory and Respiratory Tissue Metabolism). It was hypothesised that a greater

metabolic rate was required by the respiratory epithelium in order to maintain specialised functions such as ciliary beating for mucociliary clearance. From a direct N-B drug delivery perspective this may be either beneficial (by allowing slower drug degradation in the olfactory mucosa or slower efflux of drug from apical cells) or detrimental (by allowing slower uptake of drug into the olfactory epithelial cells); however, this has yet to be substantiated experimentally.

Adjustment of the Alamar Blue™ viability scores for the thickness of the epithelium was found to be ineffective at reducing data variability (Figure 2.18). It was thought that this was due to a greater metabolic activity in the apical region of the membrane. This hypothesis was strengthened by the observation that a greater proportion of mitochondria were present at the luminal surface of the olfactory epithelial cells (Figure 2.13).

In summary, the aims of this chapter were achieved sufficiently to allow both SNS (pH7.4) and 0.5mM citrate (pH6.0) buffered olfactory epithelia, which were dissected from a particular location of the porcine nasal epithelium, to be used to evaluate the transmucosal transport of nanoparticles in the vertical Franz diffusion cell (Chapter 4).

3. DEVELOPMENT OF SURFACE MODIFIED NANOPARTICLES

3.1 INTRODUCTION

The vertical Franz diffusion cell and mouse *in vivo* models (Chapter 4) were used to evaluate the permeation of nanoparticles across the olfactory epithelium. Polystyrene (PS) nanoparticles were surface modified with different materials. Therefore, changes in nanoparticle transport patterns across the epithelium could be directly attributable to different surface characteristics.

A naturally occurring polysaccharide (chitosan) and a non-ionic surfactant (polysorbate 80) were chosen for surface coating (Chapter 1). The aim of this Chapter is to explain the formulation development of 20nm, 100nm and 200nm diameter chitosan-coated (C-PS) and polysorbate 80-coated polystyrene (P80-PS) nanoparticles. Serum proteins from Foetal Calf Serum (FCS), which may interact with the olfactory epithelium to induce receptor-mediated uptake (Chapter 1), were also adsorbed onto the P80-PS formulations (P80-FCS-PS). The development methods of these colloidal systems are described here.

The aim of this Chapter was met by: (i) changing the aqueous phase ionic strength and pH conditions to investigate the experimental conditions that were required to increase the adsorption of chitosan onto PS nanoparticles; (ii) determining the minimum concentration of bulk phase polysorbate 80 required to enable maximum adsorption of polysorbate 80 to the PS surface; and (iii) determining the existence of FCS serum protein adsorption to P80-PS nanoparticle.

3.2 MATERIALS AND METHODS

3.2.1 Materials

Carboxylate-modified polystyrene nanoparticles (FluoSpheres™) were purchased from Molecular Probes (Paisley, UK) with nominal sizes of 20nm, 100nm and 200nm. Tween™ 80 (polysorbate 80) was purchased from Sigma (Gillingham, UK). FCS was purchased from Sigma Aldrich (Ayrshire, UK). Chitosan (143kDa, 89% DA) was kindly donated by Bioneer (Hørsholm, Denmark). All other reagents were obtained as detailed in Chapter 2.

3.2.2 FluoSpheres™

FluoSpheres™ are carboxylate-modified polystyrene (PS) nanoparticles with a narrow particle size distribution. They contained a fluorescent dye that is not readily released from the particles.

The narrow particle size distribution enabled tight control of particle numbers applied to the tissue. Also, the effect of nanoparticle size on transport through the epithelium could be examined by using different sized nanoparticles. The incorporated fluorescent dye allowed quantification of particle transport across the olfactory membrane using spectroflurometry as well as visualisation of particles in cross-sections of the olfactory membrane using fluorescence based microscopy techniques (Chapter 4). The images could then be used to qualitatively assess the appearance of nanoparticles within the membrane.

3.2.3 Nanoparticle Physicochemical Characterisation

Nanoparticle suspensions were characterised for nanoparticle diameter and zeta potential (ζ potential). Below is a brief introduction of the techniques and how the measurements were taken. It is beyond the scope of this work to give a detailed account of the methods. However, the reader is directed elsewhere for such discussions: Washington (Washington 1992) for particle sizing and Hunter (Hunter 1981) for ζ potential measurements.

3.2.3.1 Particle size distribution

The Dynamic Light Scattering (DLS) (Model 802, Viscotek, Worcestershire, UK) instrument was used to determine particle diameter. DLS measures the scattering pattern of polarised (laser) light and processes this through an algorithm based on the Rayleigh Theory. Such calculations were performed by the OMNISize 2.0 Software (Viscotek, Worcestershire, UK).

The DLS reports particle size as moment-mean mass diameter which is given in this work. It is equal to the diameter of the sphere that has same mass as a given particle. It is an appropriate measure of particle diameter since the bare particles are already spherical and entirely made of polystyrene. For the coated systems, the mathematical algorithm assumes that there is negligible coating material on the particles in comparison to the mass of the particles themselves i.e. it assumes that nanoparticle are entirely composed of PS. This assumption is acceptable, particularly, with the larger particle systems where the relative proportion of PS compared to adsorbent is greater.

Particles size measurements were performed in the appropriate formulation buffer at 25°C with the laser strength set to 2.5/10. The sample concentration was adjusted with the appropriate buffer so that instrument detected ~300kCounts/sec. According to the instrument manufacturer, this represented the optimum quantity of light scatter required for accurate measurements. An average of thirty (3 second) measurements was made for each sample. Particle diameter is reported as the mean±polydispersity index (PdI).

$$PdI = \frac{\sigma^2}{Z_D^2}$$

Where:

σ = standard deviation of particles

Z_D = mean particle diameter

Samples with PdI<0.04 are termed monomodal.

3.2.3.2 Measurement of ζ potential

ζ potential readings were measured using (ZetaSizer 2000, Malvern, Malvern, UK) at 25°C. The sample concentration was adjusted with the appropriate formulation buffer so that instrument detected ~300kCounts/sec. According to the instrument manufacturer, this represented the optimum quantity of light scatter required for accurate measurements. An average of five measurements was made for each sample. ζ potential is reported as the mean±standard deviation of these measurements.

3.2.4 Preparation of Chitosan-coated Nanoparticles

3.2.4.1 Varying pH conditions for adsorption (100nm C-PS)

Chitosan was adsorbed on the 100nm PS nanoparticles at pH 3.0, 4.0 and 5.0. First, 4mg chitosan was dissolved in 5.0ml 0.5M HCl. Then, the pH was adjusted as required with (2M and 0.1M) NaOH. The 0.5mg/ml solution was finally made up to 8.0ml with water. This did not affect the overall pH of the solution. 100nm PS were diluted from stock

suspension to 0.04% w/v and pH adjusted as required. 3.5ml of the particle suspension was pipetted into 3.5ml chitosan solution. The mixture was then slowly stirred overnight in the dark. Preparation of chitosan-free control samples followed the same procedure but without chitosan.

Excess chitosan was not removed from the bulk solution since it is required for the stability of the particle suspension as explained elsewhere (3.4.1.2 Effect of Excess Chitosan in Suspension).

3.2.4.2 Evaluating the Effect of Adjusting Aqueous Phase Ionic Strength

A number of alterations were made to the initial formulation conditions (3.2.4.1 Varying pH conditions for adsorption (100nm C-PS)). First, the formulation was changed by adding a small concentration of citric acid (0.5mM) to both particles and chitosan solution in order to stabilise the pH at 4.5 by creating a pH buffer with addition of NaOH. Hence, it was thought that better control of pH conditions would enable more predictable adsorption behaviour of chitosan to PS surface and therefore allow reproducible C-PS ζ potential and particle size measurements.

Second, the initial formulation attempt allowed overnight adsorption of chitosan to PS. This was changed to one hour since there is evidence to show that coating chitosan onto polylactic acid (PLA) 500nm diameter nanoparticles only required 10 minutes (Munier et al 2005). It was expected that chitosan coating to PS would behave similarly to PLA.

Third, chitosan powder was initially dissolved in aqueous HCl. During the early formulation attempts (3.2.4.1 Varying pH conditions for adsorption (100nm C-PS)) the majority of counter-ions (Na^+ and Cl^-) were generated during the neutralisation reaction

between excess 0.5M HCl with (2M or 0.1M) NaOH after chitosan was dissolved. It was therefore proposed that a less concentrated acid (0.1M HCl) would produce less excess HCl and therefore fewer counterions during pH adjustment.

The presence of a high concentration of counterions in solution reduces the likelihood of electrostatic interaction between the polycation and anionic particle surface (Bauer et al 1998). Counterions can therefore have the ability to interfere with the adsorption of chitosan to the particle surface by shielding the charges on both the particles and the chitosan. In fact, chitosan is not soluble at high salt concentrations (equivalent to 1M HCl) due to this shielding (or salting out) effect (Rinaudo et al 1999). This experiment was designed to reduce the total concentration of ions during the chitosan adsorption to PS.

Hence, 3.5mg chitosan was dissolved in 5.0ml 0.1M HCl. Then, the pH was adjusted as required with NaOH. The 0.5mg/ml solution was finally made up to 7.0ml with water. 100nm PS particles were diluted from stock suspension as required with 0.5mM citrate buffer (pH4.5). 3.5ml of the particle suspension was pipetted into 3.5ml chitosan solution. After one hour some of the suspension was pH readjusted to 6.0 and supplemented with $MgCl_2$ 0.492mM, KCl 4.56mM, $CaCl_2$ 1.2mM and D-glucose 10mM. NaCl was also supplemented to 122mM after calculating the amount produced from the neutralisation of HCl with NaOH to form the final physiological buffer. Chitosan-free samples followed the same procedure but without chitosan. The suspensions were characterised by particle sizing (DLS) and measuring ζ potential. Samples were performed in triplicate.

3.2.5 Preparation of 100nm and 200nm P80-PS

Polysorbate 80 was adsorbed onto the polystyrene particles in Simulated Nasal Solution (SNS) and in ratios similar to those suggested in the literature (Kronberg et al 1990; Tangboriboonrat et al 2003). First, a stock solution of polysorbate 80 (642µg/ml) was diluted with SNS to the required concentration for formulation. Then the PS suspension (0.08%w/v [200nm] and 0.05324%w/v [100nm]) was pipetted into this solution in a 1:1 ratio whilst agitating to allow homogenisation. The mixture was rested at room temperature for 30 minutes to allow adsorption of the surfactant to the polystyrene surface. Thereafter, particles size and ζ potential measurements were performed as described in Section 3.2.3 Nanoparticle Physicochemical Characterisation. The particle size was measured for coated, uncoated particles and for 321µg/ml polysorbate 80 solution alone.

3.2.6 Preparation of 20nm P80-PS

An estimated adsorption plateau could not be measured for 20nm nanoparticles (at these particle concentrations) due to the accuracy limits of the ζ potential instrument used. Therefore, the polysorbate 80 concentration required to coat 20nm PS was calculated from the adsorption plateau concentration of polysorbate 80 and relative surface area of 200nm PS. Hence:

$$C_{20} = 5 \times C_{200} \times \frac{S_{20}}{S_{200}}$$

Where:

C_{20}= estimated polysorbate 80 concentration required for coating of 20nm PS (µg/ml)

C_{200}= polysorbate 80 concentration required for coating of 200nm PS (134µg/ml)

S_{20}= Relative Surface Area of 20nm particles ($3.69 \times 10^{-2} m^2$/ml)

S_{200}= Relative Surface Area of 200nm particles ($1.16 \times 10^{-2} m^2$/ml)

Particles were prepared as described previously (3.2.5 Preparation of 100nm and 200nm P80-PS). Particle concentration was 0.02% w/v and polysorbate 80 concentration was 2140µg/ml. It was thought, based on the adsorption plateaus of the 200nm P80-PS particles, that this concentration would achieve maximum adsorption of the surfactant on the particles. This concentration of polysorbate was equivalent to 5 times that needed to achieve ζ potential adsorption plateau for 200nm particles.

The particle size was also measured for coated, uncoated particles and for 2140µg/ml polysorbate 80 solution alone.

3.2.7 Preparation of P80-FCS-PS

Serum proteins from FCS were adsorbed onto the P80-PS in order to investigate the potential of these proteins to enhance selectivity of uptake into olfactory cells.

For formulation, P80-PS were prepared as detailed above (Section 3.2.5 Preparation of 100nm and 200nm P80-PS). The coated particle suspension was pipetted into the required concentration of FCS in a 1:1 ratio and allowed to rest for 30 minutes for adsorption to take place. All vessels containing FCS were pre-coated with excess FCS and washed thoroughly. This prevented the adsorption of FCS to the vessel walls during formulation steps (Section 3.2.8 Preventing FCS Adsorption to Vessels during Formulation).

The particle size and ζ potential of the suspensions were measured as before (3.2.3 Nanoparticle Physicochemical Characterisation). In addition, the protein content of the

supernatant (after centrifugation of the particles) was measured using a Bradford's assay. The procedure is described below.

First, the formulated samples were centrifuged at 18,000 rpm for 90 minutes which was sufficient to sediment all the particles. The concentration of the FCS in the supernatent was determined by Bradford's protein assay. The Bradford's Protein Assay was performed by adding 0.75ml of supernatant to 0.75ml of Bradford's reagent. This was allowed to rest at room temperature for 15minutes. Samples were prepared in triplicate and assayed for absorbance by UV spectroscopy at 590nm and 450nm. The procedure was repeated without particles in order to produce a calibration plot.

In addition, initial data suggested that polysorbate 80 interfered with the results from the Bradford's Assay. Therefore, a control experiment was also preformed to determine the effect of polysorbate 80 on Bradford Assay. This was done by performing the Bradford Assay on solutions containing varying concentrations of polysorbate 80.

3.2.8 Preventing FCS Adsorption to Vessels during Formulation

Loss of FCS from the formulation due to adsorption to container walls could be misinterpreted as adsorption to particles. Therefore, it was necessary to determine extent of FCS adsorption onto the formulation vessels (glass vials and Eppendorf tubes).

There were three parts to the experiment; first, three vessels were filled with 1.5ml 92µg/ml FCS in SNS; second, three vessels 1.5ml 92µg/ml FCS that had been pre-incubated with 10%v/v FCS at 37ºC overnight. Pre-coated vessels were thoroughly washed to remove all excess FCS prior to use; third, three vessels were filled with 1.5ml

FCS-free samples. The same performed on glass vials to investigate the adsorption onto glass as well as plastic. The vials, however, could not be centrifuged.

The effect of centrifugation was also investigated for these samples since it was necessary to investigate whether FCS sedimented from the solution. A summary of the samples is listed in Table 3.1.

Table 3.1 Summary of samples used during the investigation of FCS adsorption to formulation container vessels

Sample	*Description*
Sample A	FCS (glass vial)
Sample B	FCS (eppendorf)
Sample C	FCS (eppendorf) + centrifuge
Sample D	FCS (FCS pre-treated eppendorf)
Sample E	FCS + centrifuge (FCS pre-treated eppendorf)
Sample F	SNS (glass vial)
Sample G	SNS (eppendorf)
Sample H	SNS (eppendorf) + centrifuge
Sample I	SNS (FCS pre-treated eppendorf)
Sample J	SNS + centrifuge (FCS pre-treated eppendorf)

Thereafter, Bradford's assay was performed on solutions taken from each vessel to determine loss of FCS from the solutions (3.2.7 Preparation of P80-FCS-PS).

3.3 RESULTS

In this section the results are presented in order of the chapter objectives. Hence, (i) aqueous phase ionic strength and pH conditions were altered to investigate the experimental conditions that were required to improve the adsorption of chitosan onto PS nanoparticles; (ii) the minimum concentration of bulk phase polysorbate 80 was determined to enable maximum adsorption of polysorbate 80 to the PS surface; (iii) attempts were made to establish the existence of FCS serum protein adsorption to P80-PS nanoparticle.

3.3.1 Formulation Development of C-PS Nanoparticles

3.3.1.1 Varying pH conditions for Adsorption

It was observed that the pH of each suspension was different after overnight stirring. This was attributed to the lack of pH buffering ions in the colloids. Therefore, overnight control of formulation pH was difficult with water alone. The results shown in Table 3.2 therefore report both intended experimental pH conditions and the actual pH after overnight stirring.

Table 3.2 shows the relationship between pH, ζ potential and particle diameter of 100nm PS and 100nm C-PS. For uncoated samples ζ potential reduced as pH increased. Particle diameter did not change with pH. The 100nm PS sample showed a negligible ζ potential at pH3.15 of 0.0±4.8mV whereas the sample at pH6.66 had a ζ potential of -63.8mV. The low ζ potential at pH3.15 was thought to be an artefact of the alternating current that was applied across the charge stabilised colloid in order to measure its ζ potential. Currents applied across (electrically stabilised) colloids may destabilise them by neutralising the charges on the colloidal substrate by either donating electrons or removing electrons from the charged surface groups into the bulk phase.

The ζ potential measurement artefact was characterised by a gradual increase in ζ potential from -7.8mV to +5.2mV during the 5 consecutive measurements of the same sample. Therefore, the first measurement, -7.8mV, was thought to be the most reliable reading for this sample and this was used in further discussion. A similar artefact was observed for the 100nm PS sample at pH4.01 as well.

A different trend was observed for C-PS. Here, as formulation pH was increased from pH4.56 to 5.02. ζ potential of the particles remained relatively constant in the range +39.1mV to +41.5mV. Repeated sample readings demonstrated that these ζ potential measurements were not markedly different. Concomitantly, particle size dramatically increased from 113nm to 182nm over the pH range 3.80 to 5.02. ζ potential measurements were not possible for particles at pH2.96 since the particles had aggregated and the suspension had visibly destabilised.

Table 3.2 The relationship between formulation pH, ζ potential and particle size during adsorption of chitosan to 100nm PS.

Chitosan present?	pH of sample after overnight stirring	Intended formulation pH	Diameter (nm) mean(±PdI)	ζ potential (mV) mean(±s.d.)
100nm PS	3.15	3.0	117±0.029	0.0±4.8[b] (-7.8mV)
100nm PS	4.01	4.0	106±0.047	-3.0±35.1[b] (-44.0mV)
100nm PS	4.56	4.0	104±0.049	
100nm PS	5.91	4.0	106±0.030	-63.6±1.9
100nm PS	6.66	5.0	106±0.044	-63.8±1.2
100nm C-PS	2.96	3.0	Visibly aggregated	Not possible[a]
100nm C-PS	3.80	4.0	113±0.076	
100nm C-PS	4.56	4.0	117±0.109	+39.1±0.7
100nm C-PS	4.89	5.0	153±0.056	+39.8±1.1
100nm C-PS	5.02	4.0	182±0.044	+41.5±1.2

For DLS the mean(±PdI) of thirty (3 second) readings were calculated. For ζ potential the mean(±s.d.) of 5 readings were calculated. [a] Due to colloidal instability. [b] Colloid destabilised during consecutive measurements of ζ potential (first measurement of 5 quoted in parenthesis).

3.3.1.2 Evaluating the Effect of Adjusting Aqueous Phase Ionic Strength

Table 3.3 shows the physicochemical characteristics of 20nm, 100nm and 200nm C-PS before (pH4.5) and after (pH6.0) supplementation with salts and glucose. Full physicochemical characterisation was not always performed due to time constraints. However, the following three observations were made; first, pH affected particle size and ζ potential as observed previously (Table 3.2). Hence, when pH was increased from

4.22 to 6.50 for 100nm C-PS, particle size increased from 105nm to 267nm and ζ potential values reduced from +41.6mV to +15.9mV.

Second, it was shown that supplementing the 100nm C-PS (and not changing pH) did not alter its size or ζ potential (Table 3.3). The particle diameter and ζ potential values for one sample were 106nm and +42.4±1.4mV before supplementation and 105nm and +41.6±1.2mV after supplementation. In addition, the narrow intra-sample spread of ζ potential data (given by the standard deviations [n=5]) showed that these ζ potential measurements had similar ζ potentials.

Finally, adsorption of chitosan was not detectable by particle sizing for 100nm C-PS. The mean particle size of three different samples was 108±6nm and 111±5nm for uncoated and coated samples, respectively (mean±standard deviation).

The particle sizing method showed a larger increase between uncoated and coated 20nm particles than for 100nm particles. The mean particle diameter of three different samples was 31±3nm and 48±7nm, for uncoated and coated samples, respectively (mean±s.d.). Hence, the thickness of the adsorbed chitosan layer for 20nm particles was ([48-31]/[111-108])=5.7 times larger than that for the 100nm particles. ζ potential measurements for 20nm particle may have given more detail of the adsorption behaviour of chitosan onto 20nm PS. However, the ζ potential measuring instrument could not detect sufficient scattering of light to undertake a reliable reading for these samples.

Table 3.3 Physicochemical characteristics of 20nm, 100nm and 200nm C-PS particles before and after addition of supplement.

Sample	Before Supplement pH	Particle Diameter (nm±PdI)	Zeta potential (mV) mean(±s.d.)	After Supplement pH	Particle Diameter (nm±PdI)	Zeta potential (mV) mean(±s.d.)
20nm C-PS [a]	4.53	48±0.060	-	5.95	141±0.155	-
20nm C-PS [a]	4.31	54±0.500	-	5.92	161±0.010	-
20nm C-PS [a]	4.41	41±0.031	-	6.46	138±0.358	-
20nm PS [a]	4.55	29±0.034	-			-
20nm PS [a]	4.52	30±0.027	-			-
20nm PS [a]	4.54	35±0.071	-			-
100nm C-PS[b]	4.33	106±0.077	+42.4±1.4	4.22[b]	105±0.035	+41.6±1.2
100nm C-PS	4.47	116±0.090		5.92	163±0.080	+30.1±2.0
100nm C-PS	4.41	112±0.084	+40.4±0.8	6.50	267±0.150	+15.9±0.7
100nm PS	4.40	114±0.050	-7.0±1.6	4.21	119±0.015	+8.0±2.1
100nm PS	4.55	104±0.039	-43.7±1.5			
100nm PS	4.54	105±0.030	-42.1±2.9	6.53	111±0.030	
200nm C-PS	4.53	197±0.019	+44.7±0.6	5.95	276±0.058	+23.2±1.6
200nm C-PS	4.46	200±0.055	+40.6±0.4	6.49	196±0.021	+13.6±1.6
200nm PS	4.68	191±0.022	-61.1±1.1			
200nm PS	4.60	202±0.034	-63.7±6.6	6.51	171±0.023	

For DLS the mean(±s.d.) of thirty (3 second) readings were plotted. For ζ potential the mean(±s.d.) of 5 readings were calculated. Measurement of ζ potential 20nm was not possible due to the detection limit of measuring instrument. [a] 20nm C-PS particles were statistically larger than the uncoated versions (P<0.05 unpaired t-test). [b] pH was not adjusted to 6.0 after supplementation for this sample.

3.3.2 100nm and 200nm P80-PS

The adsorption of polysorbate 80 to PS nanoparticles was investigated by adding 100nm and 200nm diameter nanoparticles to polysorbate 80 in SNS. Figure 3.1 and Figure 3.2 show that the particle size did not change noticeably for either 100nm or 200nm PS particles as polysorbate 80 was increased. As more surfactant was added the ζ potential of the 100nm particles reduced from -38mV to -20mV (Figure 3.1). Initially, small additions of surfactant screened the particle surface charge and therefore caused large reductions in ζ potential. As more surfactant was added the ζ potential reached a plateau at -20mV. At this stage it is possible that no further polysorbate 80 could adsorb since it had become saturated on the particle surface. This, however, was not confirmed as the adsorption isotherm was not determined. Figure 3.2 showed that 200nm particles demonstrated the same adsorption behaviour between -41mV and -25mV.

The adsorption plateau was estimated from the least polysorbate 80 concentration required to reach the ζ potential plateau. Adsorption plateau was estimated as 9.8mg/m^2 (3.84x10^{-4}mol/g) and 23.1mg/m^2 (5.11x10^{-4}mol/g) for 100nm and 200nm particles respectively by using the following equations:

$$EstimatedAdsorption(mg/m^2) = \frac{[Polysorbate80](mg/ml)}{ParticleSurfaceArea(m^2/ml)}$$

or

$$EstimatedAdsorption(mol/g) = \frac{[Polysorbate80](mol/ml)}{[ParticleConcentration](g/ml)}$$

The adsorption plateau value for 200nm P80-PS was used to calculate the P80 concentration required to coat 20nm PS with polysorbate 80 (3.2.6 Preparation of 20nm P80-PS).

These values for estimated adsorption are relatively high compared to the literature (3.4.2.3 Estimated Adsorption of Polysorbate 80 to FluoSpheres™). Also, up to ~2.4 times more polysorbate 80 adsorbed to 200nm particles than 100nm particles. According to the manufacturer, the charge densities of the different particles were not the same; 100nm particles had a 1.71×10^{-2}carboxylate groups/$Å^2$ whereas 200nm particles had 5.90×10^{-2}carboxylate groups/$Å^2$. Hence, the difference between the values may have been due to the different surface charges of the core particles.

Also, micelles may influence the particle size distribution hence the presence of micelles in the polysorbate 80 solution was investigated. No micelles were detected by DLS in polysorbate 80 solution alone (2140µg/ml).

The CMC (Critical Micellar Concentration) for polysorbate 80 in HBSS buffer (pH7.4) at 25°C has been measured at 65.5µg/ml (50µM) (Nerurkar et al 1997). In fact, the diameter of polysorbate 80 micelles has been measured in 50mM phosphate buffer (pH~7) as ~20nm (Simoes et al 2005).

The concentration of polysorbate 80 in this sample was 321µg/ml. In theory, micelles should have been detected at these levels but it was likely that they did not scatter enough light for the DLS detection under the current experimental conditions. However, micelles were indirectly detected when 20nm PS nanoparticles were coated with

polysorbate 80 as discussed later (3.4.2.1 Thickness of Adsorption Layer). Indeed, micelles have been measured by this equipment in the laboratory before. It is likely that the polysorbate 80 micelles would be detected by increasing the laser strength. It was therefore concluded that these particle size measurements were not considerably affected by the presence of micelles.

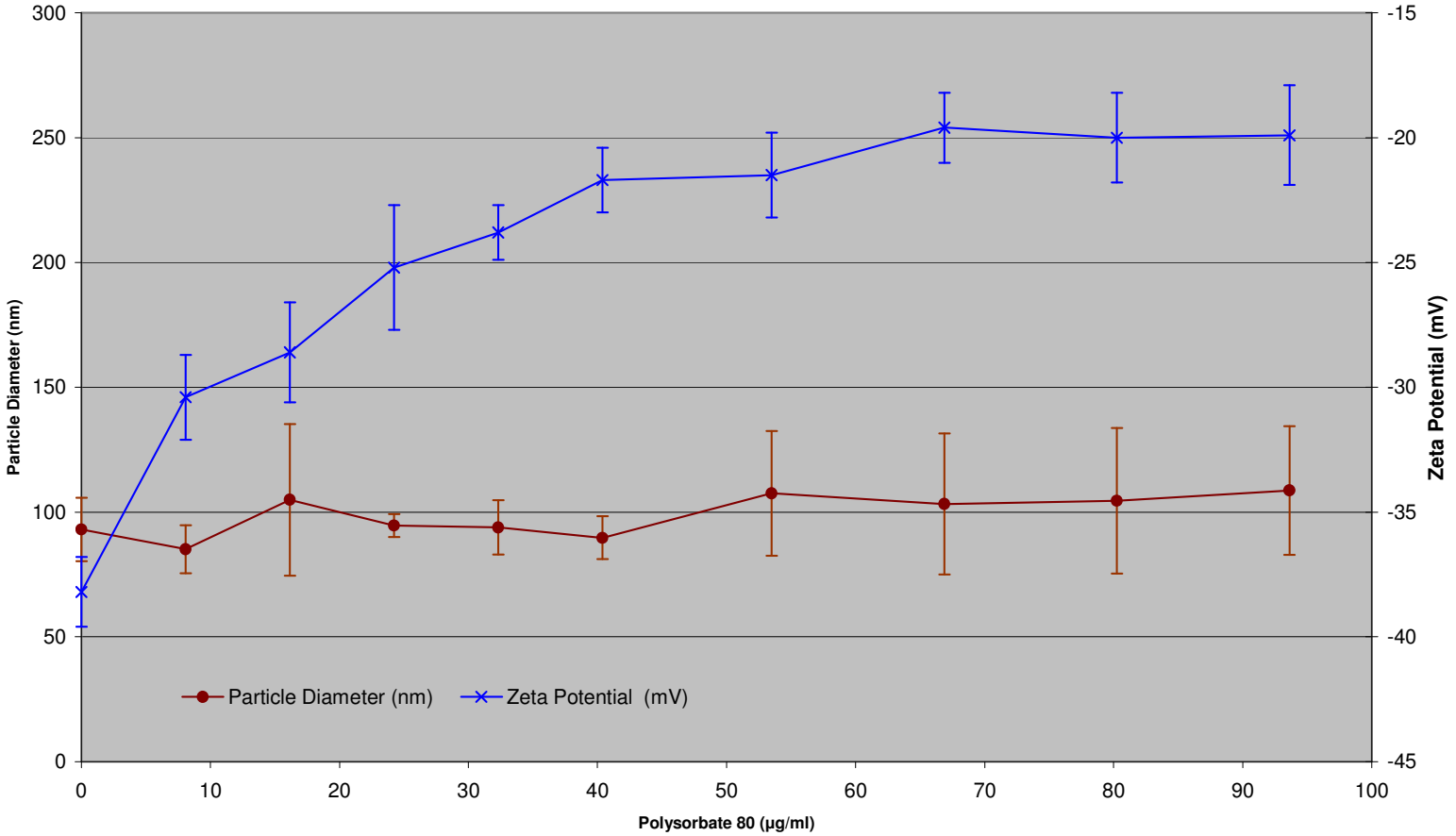

Figure 3.1 ζ potential and particle size measurements of 100nm P80-PS. Measurements were performed in SNS buffer (pH7.4) as described in Section 3.2.5 Preparation of 100nm and 200nm P80-PS. For DLS the mean(±s.d.) of thirty (3 second) readings were plotted. For ζ potential the mean(±s.d.) of 5 readings were plotted.

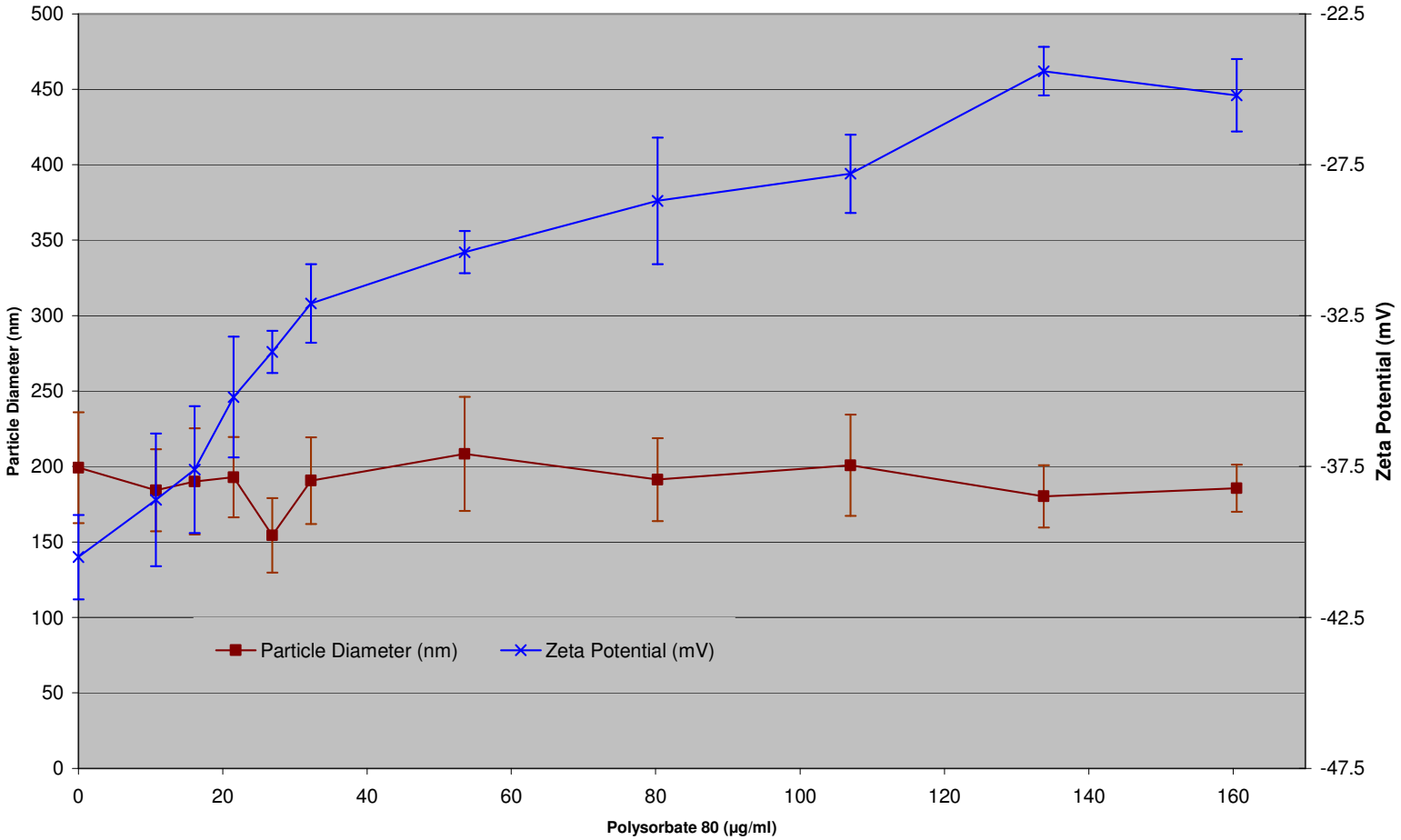

Figure 3.2 ζ potential and particle size measurements of 200nm P80-PS. Measurements were performed in SNS buffer (pH7.4) as described in Section 3.2.5 Preparation of 100nm and 200nm P80-PS. For DLS the mean(±s.d.) of thirty (3 second) readings were plotted. For ζ potential the mean(±s.d.) of 5 readings were plotted.

3.3.3 20nm P80-PS

Zeta potential measurements were not possible in the case of 20nm particles due to their small size and the limitations of the instrument used.

Particle diameter was measured at 31nm and 33nm for coated and uncoated particles, respectively. Analysis of the particle size distribution for each sample (Figure 3.3) showed that there was little difference between them.

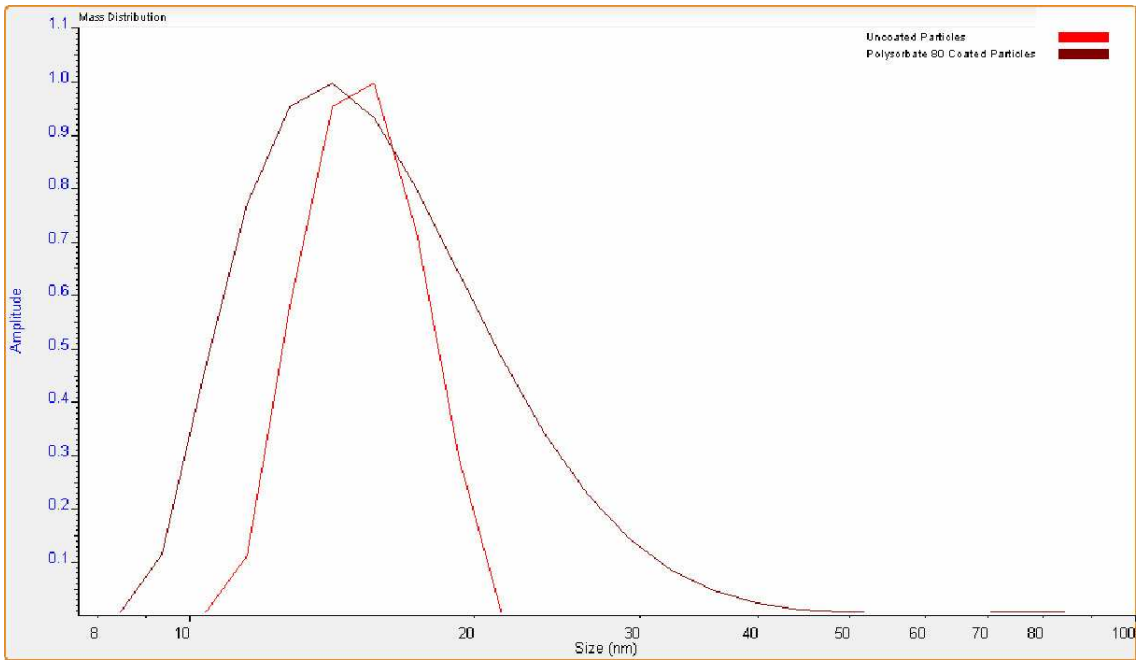

Figure 3.3 Radius mass distributions of 20nm FluoSpheres (red line) and 20nm FluoSpheres with Polysorbate 80 (brown line).

The mean particle size in the sample has reduced after adding polysorbate 80 (Figure 3.3). The dispersity of the coated particles has also increased. These facts are consistent with the detection of micelles in the colloid which are smaller than the PS nanoparticles. However, micelles were not detected in solution alone.

3.3.4 P80-FCS-PS

3.3.4.1 Zeta potential and Particle Size

Figure 3.4 shows the effect of adding FCS to 100nm P80-PS on the ζ potential and particle size measurements. ζ potential and the particle size did not change as higher concentrations of FCS were applied to the bulk phase. Average ζ potentials remained constant in the region of -15mV. Average particle diameter was ~110nm. Neither measurement showed any trend. If FCS had adsorbed onto the particle surface then it was not detectable by either of these methods.

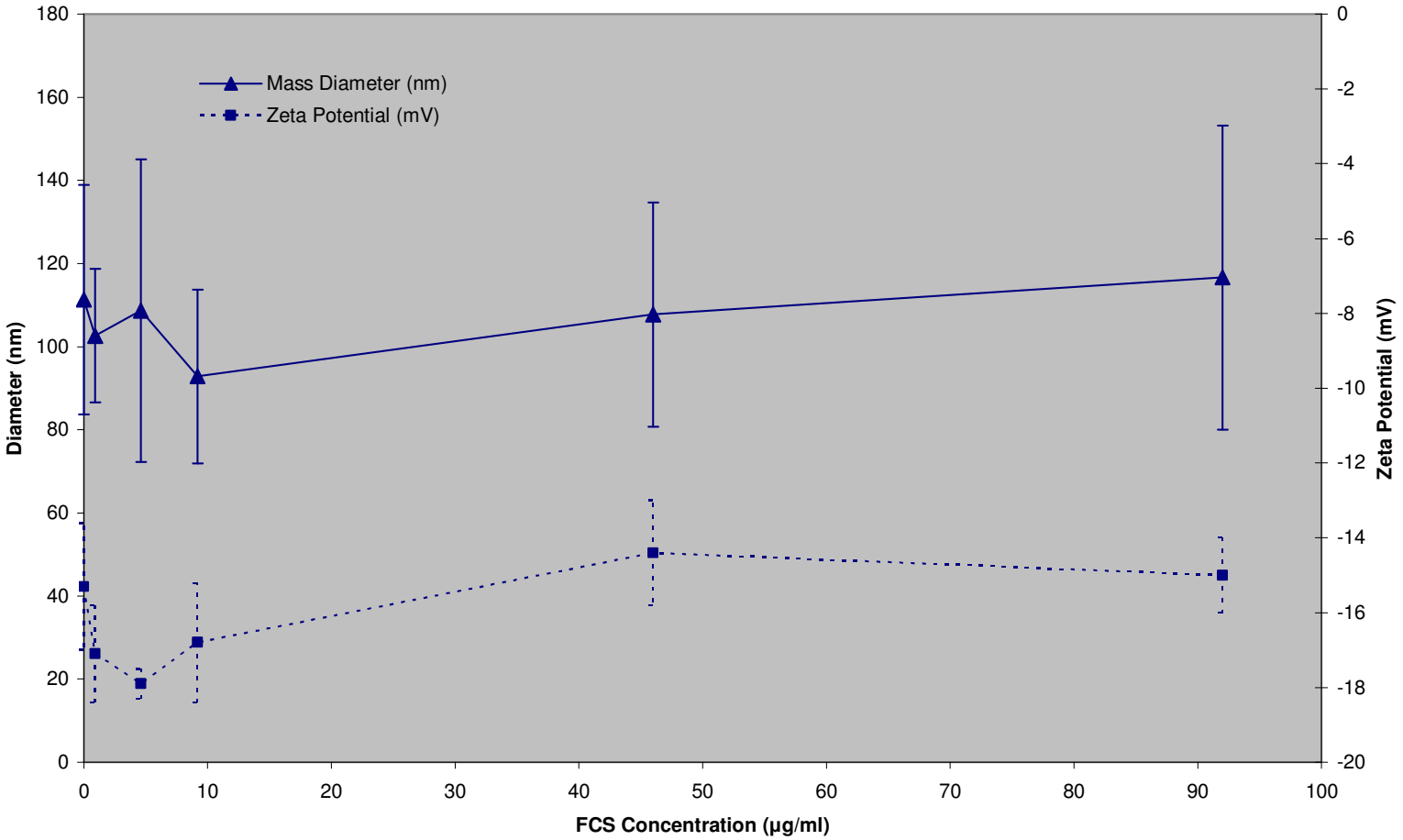

Figure 3.4 Zeta potential and particle size measurements of 100nm P80-FCS-PS. Measurements were performed in SNS buffer as described in Section 3.2.5 Preparation of 100nm and 200nm P80-PS. For DLS the mean(±s.d.) of thirty (3 second) readings were plotted. For ζ potential the mean(±s.d.) of 5 readings were plotted.

3.3.4.2 Bradford's Protein Assay

The particle size and ζ potential data was inconclusive therefore further clarification of FCS serum protein adsorption to PS was necessary (3.3.4.1 Zeta potential and Particle Size). An alternative method to determine FCS adsorption was used whereby the P80-FCS-PS nanoparticles were prepared and centrifuged. It was expected that some FCS proteins would not adsorb to the P80-PS. The excess protein that remained in the supernatant after particle sedimentation was quantified using the Bradford Assay.

Figure 3.5 shows findings from the Bradford Assay for the 100nm P80-PS and control solutions of polysorbate 80; both series contained increasing concentrations of FCS. The Bradford's reagent absorbed more UV light as more FCS was added to the P80-PS suspensions (or polysorbate 80 solutions). This indicated that the Bradford's Assay could detect increasing amounts of protein at these concentrations.

When examining the two curves, however, it appeared that the test samples (with particles [Figure 3.5 solid line curve]) contained protein levels that were indistinguishable from the control samples due to high data variability. Therefore, it could not be said that serum proteins from FCS had adsorbed onto the particles. Hence, construction of an adsorption isotherm was abandoned.

Also, it was observed that FCS-free samples (blank samples) showed absorbance of 0.12±0.003 and 0.08±0.01 for polysorbate 80 solution and P80-FCS-PS, respectively. Hence, it was suspected that polysorbate 80 was interacting with the Bradford's Assay. Therefore, a calibration plot was constructed to evaluate the effect of polysorbate 80 on the Bradford's Assay. Figure 3.6 shows Bradford's reagent absorbed more UV light as

the concentration of P80 increased. Hence, polysorbate 80 did react with Bradford's reagent at these concentrations.

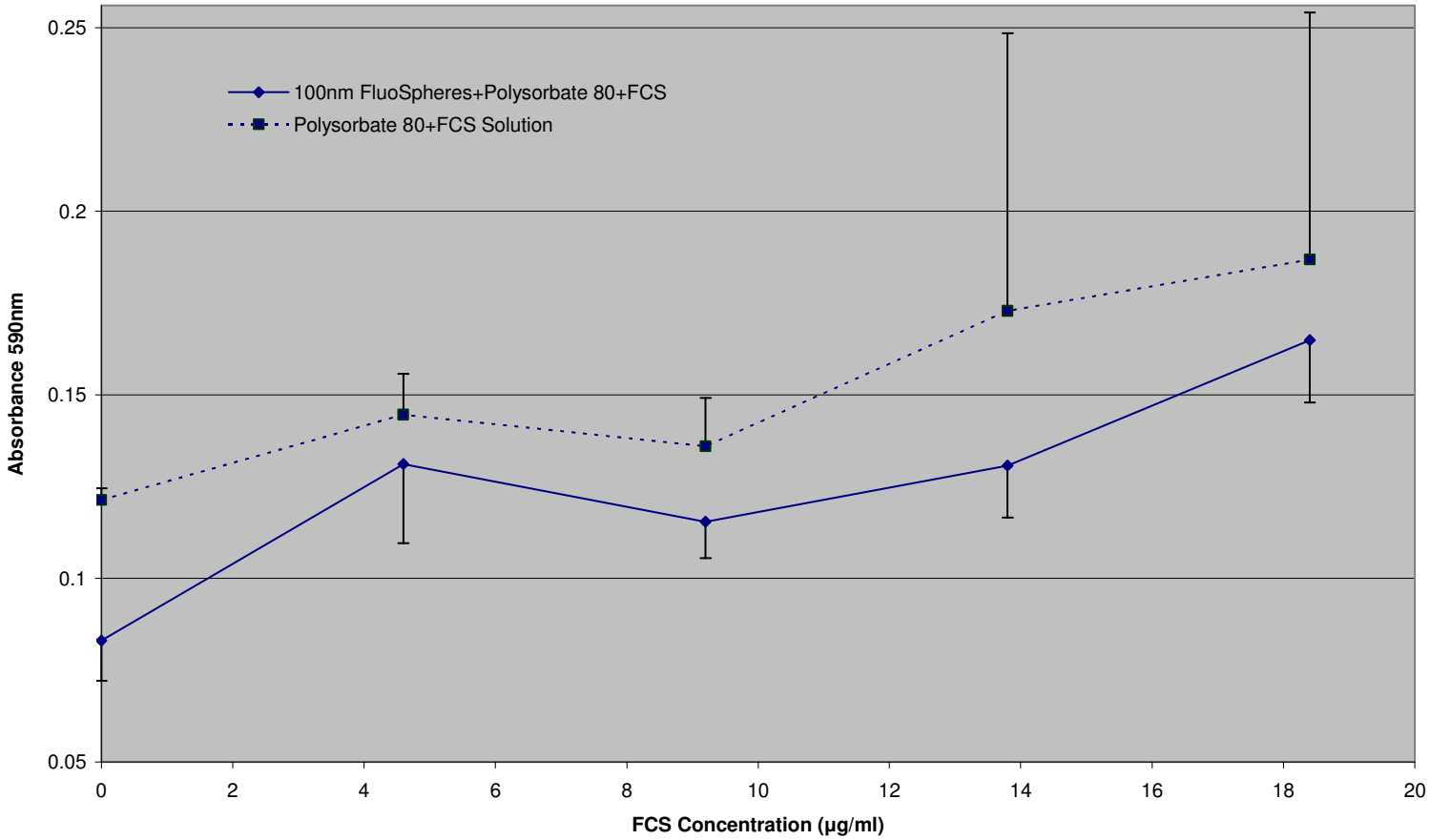

Figure 3.5 Absorbance values from centrifuged particle suspensions using Bradford's Reagent. Solid line: 100nm P80-FCS-PS with varying amounts of FCS. Broken line: solutions of polysorbate 80 with varying amounts of FCS.

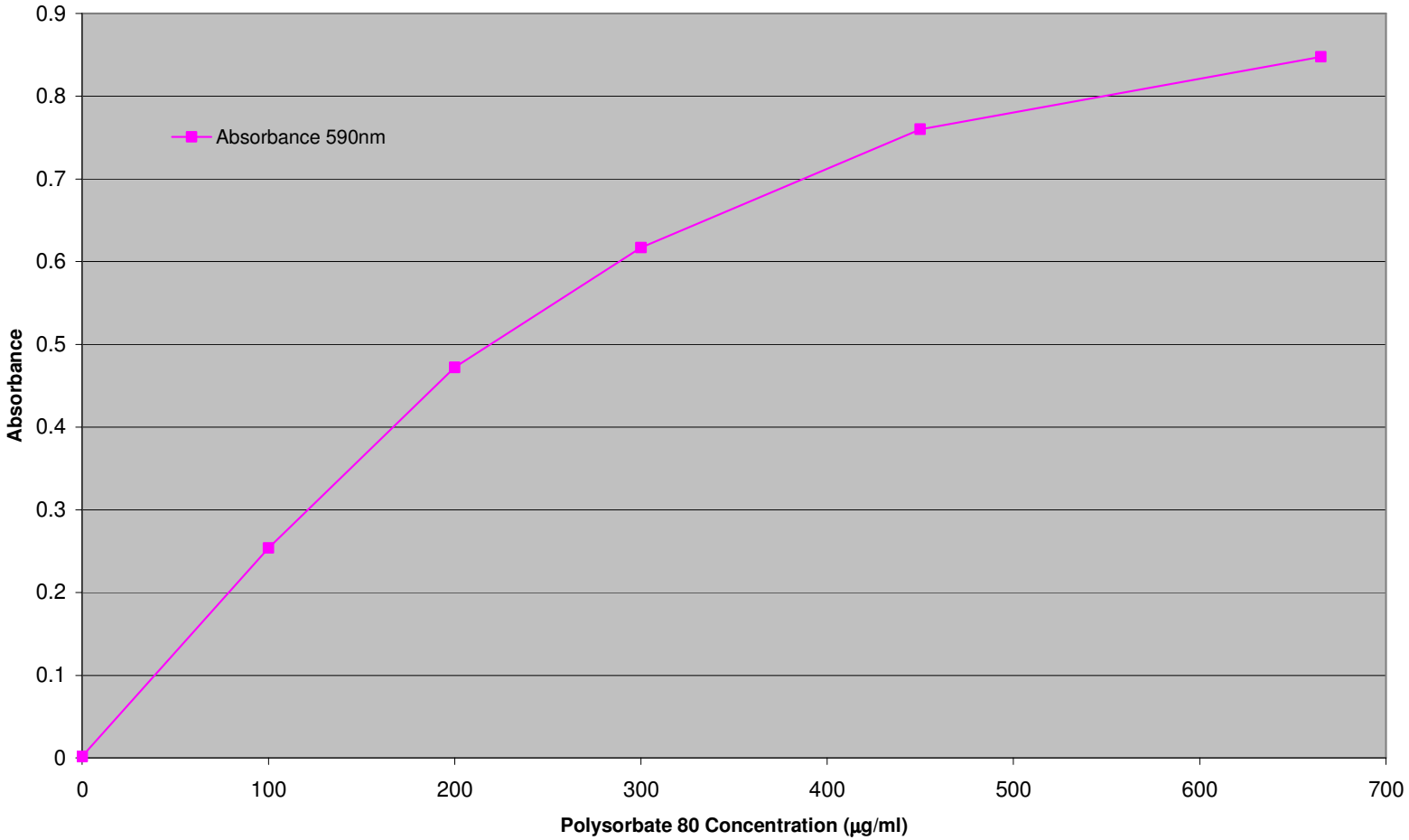

Figure 3.6 The effect of polysorbate 80 on Bradford's Assay

3.3.4.3 FCS Adsorption to Glass- and Plastic- ware

Background levels of absorbance were found for samples that contained no initial FCS (Samples F-J Figure 3.7). All samples that contained FCS showed higher absorbance. Therefore, protein was detected in the samples that contained FCS.

Samples D and E contained the greatest amount of residual FCS in the solution compared to samples A, B and C. This showed that saturation of the adsorption sites on the inner walls of the Eppendorf tubes with FCS pre-treatment prevented further adsorption of FCS from the sample.

Also, there was little difference between Samples D and E which showed that FCS was not sedimented after centrifugation from solution.

Hence, containers were pre-incubated with FCS for future studies of FCS adsorption onto P80-PS nanoparticles.

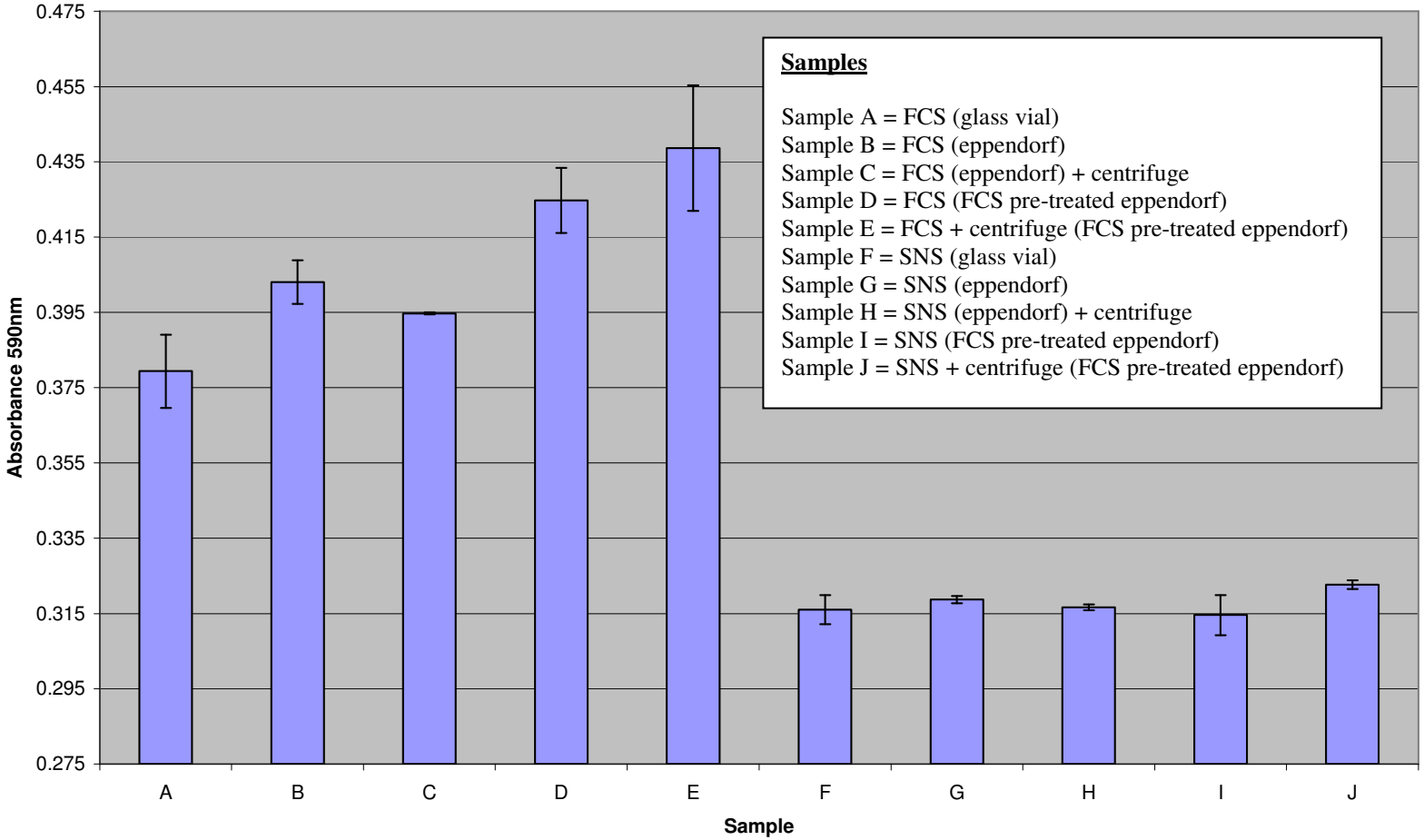

Figure 3.7 Qualitative assessment of FCS adsorption to surfaces of glass vials and Eppendorf tubes that were used during formulation of Polysorbate 80-coated FCS Surface Carrier Nanoparticles.

3.4 DISCUSSION

The aim of this Chapter was to develop colloidal nanoparticle systems that could be used to investigate the effect of nanoparticle diameter and surface character in nasal transport studies (Chapter 4). A naturally occurring polysaccharide (chitosan) and a non-ionic surfactant (polysorbate 80) were chosen for surface coating (Chapter 1). An attempt was also made to adsorb serum proteins onto the P80-PS formulations from FCS. The adsorbed serum proteins may interact with the olfactory epithelium to induce receptor-mediated uptake (Chapter 1).

The aim of this Chapter was met by: (i) changing the aqueous phase ionic strength and pH conditions to investigate the experimental conditions that were required to improve the adsorption of chitosan onto PS nanoparticles; (ii) determine the minimum concentration of bulk phase polysorbate 80 required to enable maximum adsorption of polysorbate 80 to the PS surface; and (iii) determine the existence of FCS serum protein adsorption to P80-PS nanoparticle.

3.4.1 Interactions between FluoSphere™ Surfaces and Chitosan

The application of chitosan onto the PS surface was based on the degree of ionisation of the of the amine groups on the macromolecule which is governed by the acidity of the $-NH_3^+$ group (pK_a ~6.3) (Darder et al 2003).

The solubility of chitosan is a major obstacle since surface modification of the PS is best achieved when chitosan is in solution. Variable factors that influence chitosan solubility in aqueous conditions are ionic concentration of the bulk phase (ionic strength) and pH.

Previously, there have been attempts by others to fix the positive charge on the chitosan by methylating the glucosamine residues. The methylated product, trimethylchitosan, is aqueous soluble to pH 9 (Kotze et al 1998). Trimethylchitosan does not show toxicity in short term studies (<8 hours) but it is toxic to cells in the longer term (Mao et al 2007). Therefore, chitosan was not modified in the current work.

Without methylation, chitosan is not soluble above pH6.5 or in high ionic strength solutions (Li et al 2006; An & Dultz 2007). Temperature, degree of N-group acetylation and distribution of acetyl groups along the chain are also known as solubility factors (Rinaudo 2006). The pH and ionic strength of the aqueous phase were variables and the other factors were controlled factors in the work presented here.

3.4.1.1 Effect of pH on Chitosan Adsorption

Chitosan is soluble at acidic pH due to protonation of the glucosamine residues. For a highly deacetylated chitosan (~90%) at least 50% of N-groups need to be protonated to dissolve it in aqueous conditions (Rinaudo et al 1999). Therefore, solubility increases as pH reduces.

In contrast, carboxylated PS nanoparticles have a pK_a of ~2.5 (Norris & Sinko 1997) therefore the carboxylate groups protonate at low pH. When a certain number of carboxyl groups are deionised the attractive hydrophobic-hydrophobic interactions overcome the negative-negative charge repulsion forces between particles. The polystyrene particles will thus agglomerate below pH 2.5.

Consequently a suitable pH was required for the chitosan-coating of carboxylated PS nanoparticles. An appropriate pH condition was one that allowed both a stable particle suspension and suitable chitosan protonation for adsorption.

One of the objectives of this Chapter was to find the optimal pH conditions for adsorption of chitosan from the bulk phase onto the PS surface. Uncoated particles showed little difference in particle size over the pH range 3.15-6.70 since the PS was suitably charged to enable electrostatic stabilisation of the particles at this pH. This was reflected in the ζ potential measurements over this range which was -7.8mV to -63.8mV (Table 3.2).

In contrast, the ζ potential of the chitosan-coated system was positively charged owing to the charged glucosamine units that were not interacting with the surface carboxylate groups (An & Dultz 2007). The charge (~+40mV) was enough to form a stable suspension by electrostatic repulsion.

In addition, for these particles, a range of chitosan coating thicknesses were observed from 3.5nm (pH3.80) to 38nm (pH5.02). The particle size observations can be related to either of two hypotheses. First, the widely accepted 'loop-train-tail' theory of polycationic adsorption to anionic surfaces (Breen 1999); and second, an alternative hypothesis which suggests that the adsorption layer of chitosan could grow as a result of better chitosan segment-segment interactions at low protonation (Darder et al 2003; An & Dultz 2007).

According to the first explanation, as pH increased, chitosan segment-segment interactions were more favourable as increasing numbers of glucosamine groups became deprotonated on the chitosan molecule. In addition, segment-water interactions also became less favourable as the charge neutralised along the polyelectrolyte. Concurrently, the number of strong electrostatic anchor points decreased and some segments were replaced by adsorbing ions from the bulk solution. In total, this lead to longer loops, a more flexible chitosan backbone, shorter trains and shorter tails; therefore the coating layer may have become more compact and more extended from the surface (Figure 3.8).

Indeed, direct measurements of fluorescently labelled chitosan adsorption onto DOPC (1,2-Dioleoyl-sn-glycero-3-phosphocholine) liposomes showed that more chitosan was adsorbed onto the liposomes at pH6.0 compared to pH3.4 (Quemeneur et al 2007).

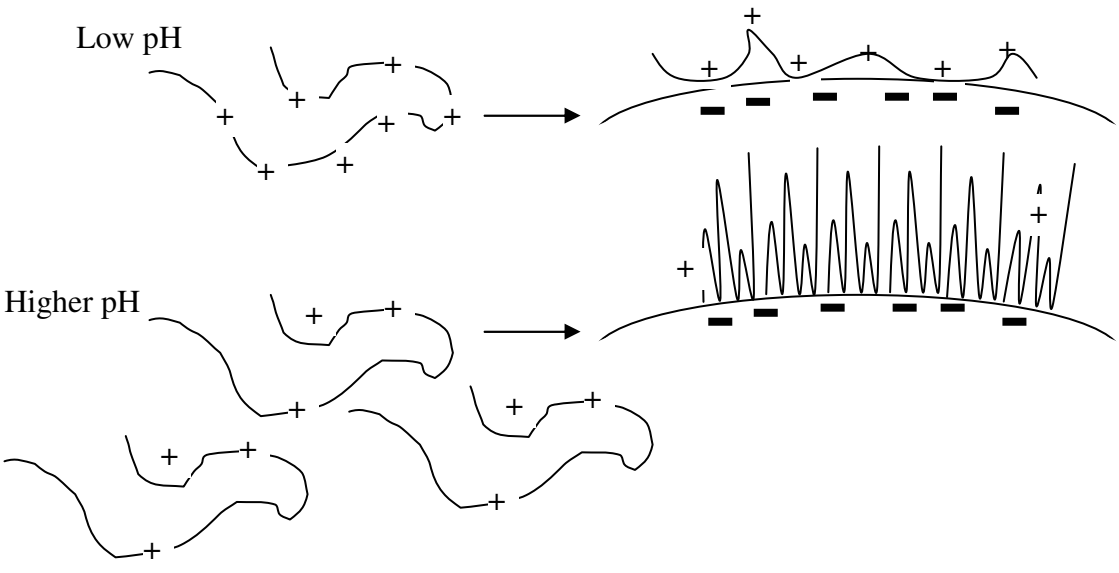

Figure 3.8 Schematic describing the influence of pH on adsorption of chitosan to PS according to the loop-train-tail hypothesis.

In addition, the distance between glucosamine monomer units within chitosan was computationally calculated as 9.839Å. The theoretical length of a single linear chitosan molecule of 143kDa is 6047.0Å (604.7nm). Therefore, if one chitosan molecule forms one loop (with negligible trains and no tails) then it would have only two anchor points and a maximum layer thickness of 302.4nm.

Since single carboxylate and charged glucosamine units interact in 1:1 ratio (both monovalent charges), it can be said that the number of anchor points (Anch) (charged glucosamine units interacting with carboxylate groups) and chitosan layer thickness can be related by the following equation:

$$LayerThickness(nm) = \frac{604.7nm}{Anch}$$

Thus, a 38nm coat would require 16 anchor points and a 3.5nm coat would require 173 anchor points; hence there would be (173/16=) 10.9 times more anchor points at pH5.02 than pH3.80.

In theory, however, there are $10^{(5.02-3.80)} = 16.6$ times more charged glucosamine units at pH5.02 compared to pH3.80. Therefore, the number of anchor points was less than the theoretical maximum (i.e. coated layer should have been thinner). The difference could be attributed to: i) presence of tails which were not accounted for in the calculation; ii) steric hindrance of anchorage (from other chitosan molecules) (An & Dultz 2007); or, iii) >1 electrostatic interactions per anchorage (long trains) (Quemeneur et al 2007). In addition, it has been shown previously that not all surface groups are electrostatically coupled by charged glucosamine units. Quemeneur *et al.* found up to 40% of charged groups on the chitosan molecule were involved in electrostatic surface interaction to

DOPC liposomes (Quemeneur et al 2008). This could also account for low anchorage. There was, nevertheless, an increase similar to what was expected.

The second hypothesis that could explain the existence of larger particles at lower pH is one where chitosan forms double or triple layers around the particles (Darder et al 2003; An & Dultz 2007). The authors of these studies did not offer and explanation for the mechanism of chitosan layer formation around negatively charged particles. However, (in my interpretation) the chitosan became less protonated as the pH was changed from 4.5 to 6.0. The reduced chitosan protonation (as well as the addition of electrolytes into the suspension to create the physiological buffer conditions) meant that the numbers of positive charges on the chitosan had reduced or the positive charged $-NH_3^+$ units were shielded. This favoured chitosan segment-segment (hydrophobic-hydrophobic) interactions (Philippova et al 2001). Therefore, the chitosan from solution could aggregate around the particle to form double and possibly triple layers. This explanation, however, remains questionable as discussed later (3.4.1.4 Chitosan Adsorption and Surface Curvature).

3.4.1.2 Effect of Excess Chitosan in Suspension

Excess chitosan was not removed from the bulk solution since it is required for the stability of the particle suspension (Brooking et al 2001). The requirement for excess polycation in solution to provide stabilisation can be explained thus; the increased competition for particle surface adsorption sites when chitosan is in excess could lead to the formation of longer loops and tails and therefore to a greater steric stabilisation component (Bauer et al 1998). To confirm this for the C-PS system, physicochemical analysis of a series of samples with increasing concentrations of chitosan would be

necessary. This work, however, was not undertaken since it was deemed to be beyond the scope of this project.

3.4.1.3 Chitosan Adsorption and pH Control

Since thickness of the chitosan coating was dependent on the pH of the aqueous phase. Small pH increments had marked affect on coating layer thickness (Table 3.2 and 3.4.1.1 Effect of pH on Chitosan Adsorption). Therefore, tight control of the aqueous phase pH with use of pH buffer was required.

A citrate buffer was chosen for this purpose. It was more suitable than SNS (phosphate) buffer which was previously employed in Chapter 2. Phosphate buffer (pK_a 7.2) is not optimal for use at pH4.5 since the ability of a buffer to stabilise pH is optimal within 1 pH scale of its pK_a. Citrate buffer (pK_a 4.76, 6.40) was therefore chosen for future experiments with chitosan (Table 3.4).

Table 3.4 pKa values for different buffers at 25ºC. Buffers are most effective when required buffer pH is ±1pH scale of one of the pKa values.

Buffer	*pK_a (at 25ºC)*
Citrate	3.13 (pK_a 1) 4.76 (pK_a 2) 6.40 (pK_a 3)
Phosphate	2.15 (pK_a 1) 7.20 (pK_a 2) 12.33 (pK_a 3)

The key advantage of citrate buffer is that they it can stabilise pH at both 4.5 and 6.0 since it has three pK_a values resulting from different protonable carboxylate groups. Therefore, the same buffer can be used for the absorption of chitosan at pH4.5 as well as undertaking transport studies at the more physiologically acceptable pH6.0.

3.4.1.4 Chitosan Adsorption and Surface Curvature

DLS showed that coating layer thickness was measurable for 20nm and 100nm particles, whereas, it was undetectable for 200nm particles ([pH4.5] chitosan 98% ionised). As the particles became smaller the size of the coating layer became thicker.

It is widely accepted that chitosan adsorbs with a flatter conformation at higher protonation due to: (i) greater opportunity to form electrostatic coupling with a negatively charged surface; and (ii) the increased rigidity of the chitosan backbone from intra-molecular charge repulsion reduces the ability of chitosan to form loops (3.4.1.1 Effect of pH on Chitosan Adsorption and (Claesson & Ninham 1992; Breen 1999; Mazeau et al 2000; Quemeneur et al 2008)).

The particle curvature was increased when the core PS particle diameter was changed from 200nm to 100nm. However, this increase in curvature was not sufficient to increase the thickness of the adsorption layer to a great extent. Some loops may have formed due to electrostatic anchorage of the chitosan molecule to the PS surface (Figure 3.9) though this was probably minimal due to the rigidity of the chitosan molecule as discussed above.

When particle diameter was reduced further to 20nm, the curvature of the particle was increased sufficiently for the chitosan adsorption behaviour to change. Hence, for 20nm diameter PS nanoparticles particles the long tails may interact with other particles to form compact floc structures that were limited in size by the length of the polycation ((Breen 1999)and Figure 3.9). These small flocculates could explain why there was such a large increase in particle size with the 20nm particles.

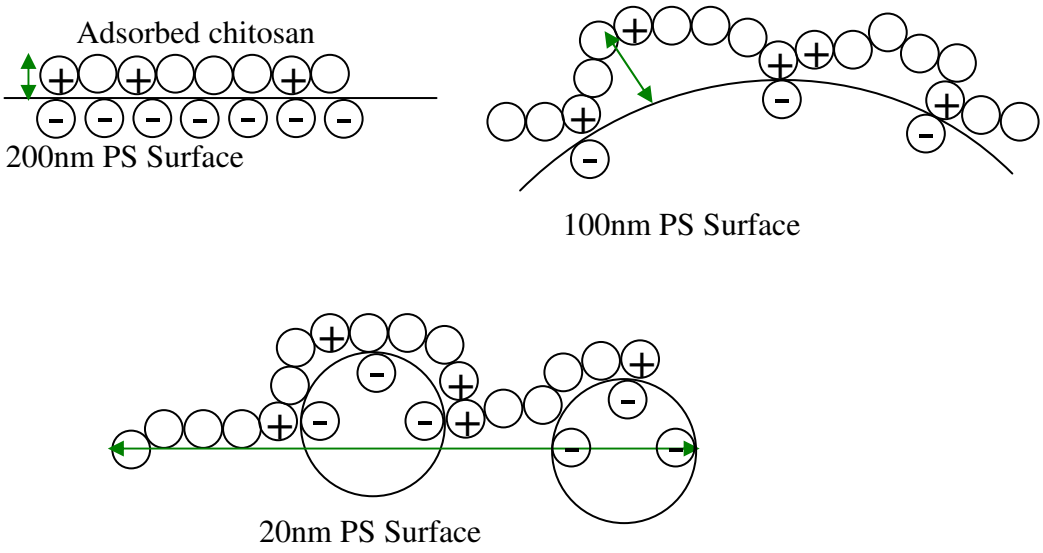

Figure 3.9 Theoretical representation of adsorption of chitosan to varying sizes of PS nanoparticles. Smaller particles had larger curvature but less charge density. Arrows indicate relative coating layer thickness.

In addition, according to the manufacturer of the PS particles, the charge density of the particles increased from 0.0171carboxylate groups/Å^2 for 20nm particles, to 0.0363carboxylate groups/Å^2 for 100nm particles, and 0.0590carboxylate groups/Å^2 for 200nm particles. This provided greater opportunity for adsorption onto the larger particles and therefore increasing anchorage for the larger particles. This could also have contributed to increasing chitosan anchorage and therefore reducing the chitosan layer thickness on the larger particles.

Regarding surface charge density of the PS and formation of chitosan layers around the particle - it would be expected that more chitosan would aggregate in layers around the larger, highly charged 200nm particles than the lesser charged 20nm particles. However, this was not observed so the observation that 20nm particles formed the largest coating layer seems incompatible with the chitosan layering hypothesis (3.4.1.1 Effect of pH on Chitosan Adsorption).

Hence, it was likely that tail and loop lengths increased as the particle diameter reduced to 20nm which was interpreted as either: i) a thicker particle coating layer; or ii) (for 20nm particles) the formation of small flocculates with a discrete size determined by the MW of the chitosan (Table 3.3 and Figure 3.9).

3.4.1.5 Chitosan Adsorption and Aqueous Phase Ionic Strength

Once particles were chitosan-coated the suspensions were supplemented with the remaining salts and glucose to form a physiologically acceptable buffer which was necessary for olfactory tissue survival in the nasal transport studies (Chapter 4).

It was inferred from Table 3.3 that the bulk solution pH had a stronger influence on adsorbed layer thickness than addition of salts and glucose. The three 100nm C-PS samples helped to make the distinction. One sample (Table 3.3(c)) was kept at pH4.5 and supplemented. This sample showed that chitosan layer thickness did not increase after the supplementing. On the other hand, the other two 100nm C-PS samples showed a size increase when pH was increased to 6.0 and supplements were added.

This related well with current understanding; for example, Philippova *et al.* (2001) found that 250μg/ml chitosan solution did not aggregate in acetate buffer (0.3M CH_3COOH/0.2M CH_3COONa) pH4.58. If aggregation of chitosan molecules was observed in this study then it could be said that nanoparticles with adsorbed chitosan would also aggregate. At pH4.58 the chitosan was 98% ionised and the ionic strength of this buffer was 200mM (Philippova et al 2001). The ionic strength used in Phillipova's study was higher than that of the citrate buffer used in this work after supplementation (122mM). Therefore, ionic shielding of charges on the chitosan was not expected to cause aggregation of the particles after supplementation in the current work.

Hence, it was important to control the aqueous environment during the adsorption process itself in order to control the adsorption process for reproducibility. Ionic strength and low pH are important factors (Henriksen et al 1997). Henriksen *et al.* (1997) found that high cationic charge on the chitosan (low pH) and low ionic shielding of the cationic and surface charges produced many anchorage points per chitosan molecule for chitosan adsorption to liposomes. Indeed, an ionic strength as low as 10mM was seen to increase the diameter of the chitosan-coated liposomes. This indicated that that a much lower ionic strength condition would be necessary for chitosan adsorption. Hence, a low concentration of citrate buffer 0.5mM and low pH conditions (pH4.5) were used to control the initial adsorption step.

3.4.1.6 Other factors Influencing Chitosan Adsorption to Surfaces

A biphasic adsorption of chitosan to the PS surface could also be possible. Such an adsorption behaviour has been demonstrated on clay mineral montmorillonite at 25°C (An & Dultz 2007). For this material, there was an initial fast electrostatic adsorption within 30 minutes followed by a slower adsorption which was thought to be driven by a rearrangement of chitosan segments by Brownian motion at the surface of the clay material. The slow rearrangement continued until optimal conformation of the chitosan molecules were achieved with respect to intra- and inter- molecular forces between chitosan molecules and the particles surface and chitosan molecules between themselves. An & Dultz (2007) thought that this rearrangement uncovered previously uncoupled adsorption sites. Hence, the longer range attractive force between bulk phase chitosan and uncovered surface charge compared to adsorption sites sterically hindered

by uncharged chitosan molecule segments may then drive the adsorption of more chitosan.

For montmorillonite the secondary phase did not stabilise until approximately 80 hours after initial adsorption (An & Dultz 2007). Most measurements in the current work were taken after 1 hour of the initial adsorption; therefore, incomplete chitosan rearrangement could have contributed to some variation in the data presented here.

3.4.2 Interactions between FluoSphere™ Surfaces and Polysorbate 80

Polysorbate 80 has been primarily used in drug delivery as a surfactant coating for nanoparticles across the blood-brain endothelium (Chapter 1). It is regarded as safe as a formulation excipient and, unlike chitosan, adsorbs to surfaces with minimal manipulation of the bulk phase (Kreuter 2001).

Little is known, however, about the interaction between polysorbate 80 and polystyrene in aqueous conditions. For example, no adsorption isotherm information is available. Nevertheless, since the surfactant is non-ionic, it was anticipated that the adsorption process would be driven by hydrophobic interactions between the PS surface and the oleic acid residue of the polysorbate 80. Therefore (unlike with chitosan) electrostatic shielding of the polysorbate 80 by salts and pH conditions of the aqueous phase were less important variables to control.

The main formulation problem was to limit the excess amount of polysorbate 80 in the bulk solution after adsorption to the polystyrene. Excess surfactant could have interfered with nanoparticle transport, or lack thereof, through the olfactory epithelium during transport studies. For example, the polysorbate 80 may interact with the

phospholipid membrane (possibly by membrane solubilisation) and allow the nanoparticles to pass into cells by a route that may not be possible with less excess surfactant. With little excess surfactant these effects are less likely to occur and thus a greater certainty of interpretation can be placed on other mechanisms of nanoparticle transport into the epithelium. The following section discusses the extent of polysorbate 80 adsorption onto PS and the factors that influence the adsorption behaviour.

3.4.2.1 Thickness of Adsorption Layer

The adsorption behaviour of polysorbate 80 onto PS was characterised by particle size analysis (light scattering) and ζ potential measurements.

Particle size was unable to clearly indicate the presence of the adsorbed layer. It is likely that the surfactant layer was very thin since it has a relatively small molecular weight (MW 1310). Nevertheless, the adsorption layer thickness of polysorbate 80 to polystyrene particles has been measured previously as 2.9nm by PCS (Muller et al 1992). This value, however, was larger than theoretical predictions of coating layer thickness as discussed below.

For instance, it is widely held through investigations of a variety of PEG-containing surfactants on polystyrene nanoparticles, that coating layer thickness increases with PEG chain length (Stuart et al 1984; Li et al 1994; Wijmans et al 1994). In fact, a previous study has correlated the thickness of the adsorbed layer to the chain length of PEG units in each copolymer molecule (Illum et al 1987). It can be estimated from such analysis that polysorbate 80, a 20 PEG unit copolymer with an average PEG chain length of 7 PEG units, should have an adsorbed layer thickness of ~0.875nm.

It was also found that the hydrodynamic layer thickness was related to twice the radius of gyration for each copolymer (Stolnik et al 1997). The radius of gyration is defined as a length representing the distance between the point about which rotation of a body occurs (the axis of rotation) and the point at which the body mass is distributed at its maximum effect. Information about the radius of gyration, however, is not available for polysorbate 80. But a relationship exists between PEG chain length and radius of gyration. Therefore, a value for radius of gyration can be estimated from the homopolymers containing the same amount chain length of PEG monomer units (Li et al 1994). Hence, twice radius of gyration for a PEG homopolymer with chain length of 7 units is ~1nm which is in good agreement with Illum *et al* (1987).

Finally, a mathematical model based on the DLVO theory has estimated that Triton X-100 (a 10-mer PEG copolymer; MW647) would produce adsorption layer of 0.8nm (Romero-Cano et al 1998).

Nevertheless, the diameter of the 20nm PS nanoparticles appeared to reduce by ~2nm after addition of polysorbate 80 to the colloid (Figure 3.3). The dispersity of the 20nm P80-PS nanoparticles also increased compared to 20nm PS. These facts are consistent with the detection of polysorbate 80 micelles in the colloidal mixture. Indeed, it would be expected that micelles did appear in the mixture since the CMC (Critical Micellar Concentration) for polysorbate 80 in HBSS buffer (pH7.4) at 25°C has been measured at 65.5µg/ml (50µM) (Nerurkar et al 1997). Also, the diameter of polysorbate 80 micelles has been measured in 50mM phosphate buffer (pH~7) as ~20nm (Simoes et al

2005) which is consistent with the findings made here since these micelles are smaller than the [nominal] 20nm PS nanoparticles.

Hence, it was not possible to determine the thickness (or even existence) of the polysorbate 80 layer on the 20nm P80-PS nanoparticles using DLS. It was also difficult to make this distinction for 100nm and 200nm P80-PS (Figure 3.1 and Figure 3.2). Therefore, a firm conclusion regarding polysorbate adsorption layer thickness could not be made.

3.4.2.2 The Influence of Adsorption on ζ Potential

There was decrease in ζ potential from -38mV (uncoated) to -20mV (fully coated) for 100nm particles and similarly from -41mV and -25mV for 200nm particles (Figure 3.1and Figure 3.2). Values for ζ potential reduced as more copolymer was applied to the particle surface as a consequence of shear plane movement away from the particle surface. Thus, the coating layer protected part of the diffuse layer against displacement by shear as more surfactant was applied. For small surfactants, however, the distance that the shear plane can move away from the surface is limited by the size of the surfactant molecule. Therefore, since polysorbate 80 has a small chain length, a residual negative ζ potential remained after maximum adsorption was reached for polysorbate 80 to PS particles (adsorption plateau Figure 3.1 and Figure 3.2).

Furthermore, the differences in ζ potential for uncoated particles were probably due to the differences in their inherent surface charge densities. According to the manufacturer, the charge densities for the different particles were 1.71×10^{-2}carboxylate groups/$Å^2$ for 100nm particles and 5.90×10^{-2}carboxylate groups/$Å^2$ for 200nm particles. Therefore, the

larger particles had a greater initial surface charge which was measured as a larger ζ potential.

3.4.2.3 Estimated Adsorption of Polysorbate 80 to FluoSpheres™

The estimated adsorption values were 3.84×10^{-4}mol/g and 5.11×10^{-4}mol/g for 100nm and 200nm particles, respectively. These estimates were unrealistically high in relation to adsorption of other low molecular weight non-ionic surfactants to polystyrene surfaces. For example, Triton X-100 (a 10-mer PEG copolymer) and hepta-ethylene glycol mono-*n*-dodecyl ether (a 7-mer PEG copolymer) had specific adsorption values of 1.0×10^{-5}mol/g and 1.3×10^{-5}mol/g, respectively, for ~150nm PS particles. These values are up to 50 times lower than those estimated by ζ potential here (Zhao & Brown 1996).

The high values found here were probably due to the indirect method of obtaining maximal adsorption values through ζ potential measurements. It was assumed in the calculations for estimated adsorption that all polymer molecules in solution had adsorbed to the particle surface. However, some polymer may have remained in solution since the adsorption process is governed by thermodynamic equilibria. Therefore, the values obtained through ζ potential measurements were likely to be high.

3.4.3 Adsorption of FCS to 100nm P80-PS

FCS is a complex mixture of plasma proteins and other biological molecules. FCS contains components such as ApoE which, if adsorbed to particle surfaces, can promote interaction of the particle with cells (Kreuter 2001). The presence of polysorbate 80 on the particles modifies the adsorption pattern of serum proteins so that the particle

surface becomes enriched with Apo E (Muller et al 1992; Goppert & Muller 2005). This serum protein adsorption modifying behaviour of polysorbate 80 was consistent with PBCA, PMMA and solid lipid nanoparticle colloidal substrates; therefore, it was thought that PS nanoparticles would also demonstrate the same effect. ζ potential, particle sizing and the Bradford Protein Assay were used to detect the presence of adsorbed protein to the particle surface.

Figure 3.4 shows there was no trend in ζ potential or the particle size when FCS was added to 100nm P80-PS (Figure 3.1). Neither parameter showed any trends. If FCS had adsorbed onto the particle surface then it was not detectable by either of these methods. It was unclear why the ζ potential did not change as expected since changes in ζ potential have been demonstrated with serum adsorption to other PEG-containing surfactant coated PS systems (Illum et al 1987). An increase of sampling numbers could have made the findings more conclusive.

Alternatively, FCS proteins may not have adsorbed whatsoever. This is, however, unlikely since a variety of plasma proteins have previously been identified to adsorb onto both uncoated polystyrene particles and polystyrene particles coated with PEG containing surfactants (Luck et al 1997; Stolnik et al 2001).

Further clarification was necessary since the particle size and ζ potential data was inconclusive. An attempt was made to detect the protein directly with use of Bradford's protein assay (Zor & Seliger 1996). This method has previously been shown to detect levels of 0.2μg/ml Bovine Serum Albumin. The lowest concentration of FCS used to

coat particles here was 4.6µg/ml. Therefore, this assay was deemed suitable to evaluate FCS adsorption to the particles as described here.

Figure 3.5 shows that more protein was detected as more FCS was added to the particle suspensions. On average there always appeared to be more FCS remaining in supernatants of the control solutions that contained no particles. But it was difficult to detect whether FCS was adsorbed onto the particles due to the variability of the data. Since the use of Bradford's Assay at these levels has previously been reported (Zor & Seliger 1996) it may have been that this was a limitation of the accuracy of the spectrophotometer.

However, it was more likely that the proportion of serum protein that adsorbed from the FCS to the nanoparticle surface may have been below the detectable range of the Bradford's Assay. In fact, Apo E is only thought to constitute 0.005%w/v (46µg/ml) of total FCS content (Goppert & Muller 2005). On this basis, the concentration of Apo E at the lowest dilution was 0.92ng/ml. Therefore, the loss of Apo E from FCS may not have been detected by Bradford's assay at the lowest FCS dilution used for formulation.

In addition, the polysorbate 80 had also reacted with the Bradford's Assay. Figure 3.5 demonstrates this since there was a difference in absorbance values between samples that contained no FCS. The relationship was confirmed when absorbance correlated with increasing concentrations of polysorbate 80 in solution (Figure 3.6). This was not expected since the manufacturer's literature for Bradford's Reagent states that concentrations of polysorbate 80 below 663µg/ml should not interfere with the results obtained by Bradford's reagent (Sigma-Aldrich 2005). The concentration of polysorbate

80 used during the FCS adsorption study was below this threshold (107µg/ml). The interaction of polysorbate 80 and Bradford's reagent at these low levels could, therefore, have resulted from the cumulative effects of buffer components and surfactant. Future studies could use an alternative method, such as 2D electrophoresis, as used previously (Blunk et al 1993; Luck et al 1998). However, there was not enough time remaining to undertake these studies.

3.5 CONCLUSIONS

PS particle of varying sizes were coated with either chitosan (143kDa, 89% deacetylated) or polysorbate 80 (1310MW). Chitosan has mucoadhesive properties and polysorbate 80 has previously been shown to improve particle delivery to the brain. Both are deemed as biologically safe materials for use in this respect.

For chitosan adsorption to PS, the pH and ionic strength can markedly affect the final diameter of the coated particle. Therefore, controlling these factors during adsorption was important. A low ionic strength citrate buffer (0.5mM) allowed control of pH at 4.5 and at 6.0 which corresponded to the adsorption and supplementing steps during formulation, respectively.

In general, the thickness of the chitosan coating layer increased with increasing pH. This was attributed to the deprotonation of glucosamine units on the chitosan at higher pH and the subsequent decoupling of glucosamine-carboxylate electrostatic bonds between the chitosan and the particle surface. An alternative hypothesis was also considered that suggested a layered chitosan structure around the core PS particle. This arrangement, however, was deemed less likely to occur since the 200nm diameter particles had a greater surface charge and a thinner chitosan adsorption layer compared to 200nm particles.

Also, the surface curvature of the particle may have been an important factor for chitosan adsorption behaviour since the coating layer thickness increased with smaller particles. This could have resulted from the inability of the chitosan molecules to form

loops and trains due to the high rigidity of the chitosan backbone particularly when highly charged at low pH. This could even have lead to multiple particle anchorage onto a single chitosan molecule which could have been detected as flocculates with a size defined by the length of the chitosan molecule.

The inherent particle surface charge density, however, was less for smaller sized particles and so the thicker coat could merely have been a result of less opportunity for chitosan-particle interactions. Therefore the effect of particle size on chitosan adsorption behaviour remains unclear.

In the P80-PS colloidal system ζ potential values became smaller as more polysorbate 80 was added to the particles. This was a consequence of shear plane movement away from the particle surface as more non-ionic surfactant was adsorbed.

The adsorption of polysorbate 80 to PS was estimated by ζ potential for 100nm and 200nm particles as 9.8mg/m^2 and 23.1mg/m^2, respectively. But these values were up to x50 higher than what was expected from the literature which was probably due to the indirect nature of ζ potential as a measure of adsorption.

Unlike with chitosan, however, particle size changes were not reliably detected for the P80-PS colloid. This was probably a result of the small size of the surfactant in comparison to the chitosan molecule. A greater sample number may have improved the variability of the measurements.

Finally, FCS was used to overcoat the P80-PS. The presence of FCS was hypothesised to improve selective uptake of particles into olfactory neurones due to the presence of binding ligands such as Apo E. The FCS adsorption to P80-PS could not be confirmed using a variety of methods (including ζ potential, particle sizing and [Bradford's] protein assay). The literature, however, was consistent in stating that serum proteins do adsorb onto PEG-containing surfactant-coated PS nanoparticles. Therefore, it was thought that a low degree of FCS serum proteins were adsorbed to the P80-PS particles. Future confirmation could come from the use of 2D gel electrophoresis.

The PS, C-PS, P80-PS and FCS-P80-PS nanoparticle colloidal systems were applied to olfactory epithelia *in vitro* and *in vivo* as described in Chapter 4.

4. DIRECT NOSE-TO-BRAIN NANOPARTICLE TRANSPORT STUDIES

4.1 INTRODUCTION

A number of studies have demonstrated the ability of small molecular weight drugs, peptides and nanoparticles to appear in the olfactory system after intranasal administration (Chapter 1). The aim of this chapter is to investigate the fundamental mechanism involved in the transport of nanoparticles into the olfactory system in both the *in vitro* porcine (Chapter 2) and *in vivo* murine animal models. The possible toxic effects of the nanoparticles on the olfactory epithelia were also investigated. A number of colloidal formulations, which differed in nanoparticle diameter and surface characteristics, were developed for application to these models (Chapter 3).

Two types of biological models were used to undertake this investigation. First, an *in vitro* approach was adapted using porcine olfactory epithelium mounted onto the vertical Franz diffusion cell. This *in vitro* model allows a detailed investigation of: (i) the time-related movement of nanoparticles across the olfactory epithelium; and (ii) interaction between the test formulation and mounted tissue. In addition, it permits strict control of physiological conditions such as pH, temperature and oxygenation. These conditions may affect the viability of the olfactory epithelium and/or stability of the colloids applied to the system.

The second adapted approach used a mouse *in vivo* model. In this investigation nanoparticle test formulations were placed directly into the nasal cavity of mice. The olfactory system was later histologically examined to determine the location of the applied nanoparticles. Advantages of using *in vivo* models compared to the vertical

Franz diffusion chamber were that: (i) transport of particles beyond the olfactory epithelium could be evaluated; (ii) the model handled the formulation in a more realistic way (e.g. formulation can clear away from the nasal cavity or formulation may not be accessible to different regions of the nasal cavity); (iii) the movement of particles in the olfactory system could be evaluated over longer periods; and (iv) the procedure was simpler (e.g. the animal is alive during the experiments therefore it is not necessary to measure the viability of the tissue).

4.2 TRANSPORT STUDY USING THE FRANZ DIFFUSION CELL

The aim of this study was to use fluorescence microscopy and fluorescence spectroscopy to compare the ability of nanoparticles, of different sizes and surface characteristics, to transport through excised olfactory epithelia in the nasal cavity using the *in vitro* vertical Franz diffusion cell model. For this investigation the procedures for measuring tissue viability (R_m, PD, I_{sc} and Alamar Blue™ tests) and dissection method to extract the olfactory epithelium from pigs are described in Chapter 2.

4.2.1 Materials and Methods

4.2.1.1 Materials

Bright Cryo-M-Bed cryomountant was obtained from Bright Instrument Co. Ltd. Huntingdon, UK. Glycerol jelly mounting medium was prepared (by dissolving 10g gelatine [Sigma, Gillingham, UK] in 60ml water and 70ml glycerol [Sigma, Gillingham, UK]) and stored at 2-8°C. All other materials were sourced and prepared as described in Chapters 2 and 3.

4.2.1.2 Transport Study Protocol

Domestic pigs (*circa* 6 months old) were slaughtered by exsanguination, the olfactory epithelium dissected, transported on ice in cold buffer (either SNS (pH7.4) or 0.5mM citrate (pH6.0) buffer depending on the test formulation requirements) and loaded onto the diffusion chamber apparatus within approximately one hour *post mortem*.

After a 30 minute electrophysiological equilibration period (during which R_m, PD and I_{sc} measurements were taken) a suitable volume of the nanoparticle-containing test formulation was placed into the donor chamber to create a suspension containing $4.55x10^{10}$particles/ml.

Thereafter, 200µl aliquots were withdrawn from the receiver side every 10 minutes (for 90 minutes) into a 96 well microtitre plate. The receiver chamber sample volume was replaced with the appropriate pre-warmed and pre-oxygenated buffer. The aliquots were later quantified for nanoparticles using fluorescence.

Finally, R_m, PD and I_{sc} measurements were taken for another 30 minute before dismounting the tissue. Three 3mm diameter circular pieces of epithelium were cut out from the dismounted tissue using a cork borer. Thereafter, the Alamar Blue™ viability test was immediately performed on these circular pieces of tissue.

For test formulations, two different types of FluoSpheres™ were used for the three different colloidal systems in this study. PS and C-PS nanoparticles contained a yellow-green fluorescent dye with excitation and emission (Ex/Em) maxima of 505nm and 515nm (505/515), respectively. P80-PS nanoparticles encapsulated a red fluorescent dye Ex/Em 580/605. The change of core particles was made to improve the visualisation of

the nanoparticles in the tissue samples. Red fluorescent nanoparticles were easier to distinguish from the natural autofluorescent background signal in fluorescent images since, unlike the yellow-green nanoparticles, they did not fluoresce in the same spectral region. According to the manufacturer's batch specifications the differences between size and surface characteristics of the red and yellow-green nanoparticles were considered negligible. Therefore, the different core particle composition was considered not to have influenced the ability of the nanoparticles to transport through the tissue in any measurable way.

Finally, in order to investigate the effects of chitosan or polysorbate 80 in the absence of nanoparticles, control samples of chitosan solution (125µg/ml) in 0.5mM citrate buffer (pH6.0) or polysorbate 80 solution (137.5µg/ml) in SNS buffer (pH7.4) were investigated in the same way as described above.

The concentration of each of these control solutions was approximately the highest theoretical concentration of chitosan or polysorbate 80 to which the olfactory epithelia was exposed during the nanoparticle transport studies. For example, 20nm P80-PS was formulated with 2140µg/ml polysorbate 80. After dilution of the 20nm P80-PS formulation for the transport study the actual concentration of polysorbate 80 in the donor side of diffusion chamber was 6.4µg/ml (Table 4.1). Hence, the highest concentration of either chitosan or polysorbate 80 found in the nanoparticle transport studies was equivalent to that found in the 200nm C-PS or 200nm P80-PS samples since they required the least dilution (Table 4.1).

Table 4.1 Concentration of formulated particles and resultant concentrations of chitosan or polysorbate 80 in donor chambers during transport studies

Nominal Particle Diameter (nm)	*Formulated Concentration (particles/ml)*	*Donor Chamber Chitosan Content*	*Donor Chamber Polysorbate 80 Content*
Control solutions		125µg/ml (0.87µM)*	137.5µg/ml (105µM)†
20	$1.51x10^{13}$	0.75µg/ml (0.005µM)	6.4µg/ml (4.9µM)
100	$2.91x10^{11}$	39.1µg/ml (0.27µM)	8.4µg/ml (6.4µM)
200	$9.59x10^{10}$	119µg/ml (0.83µM)*	127.4µg/ml (97mM)†

***,† concentration of control solutions was approximately equal to the highest concentration of either chitosan or polysorbate 80 in the other samples**

4.2.1.3 Test Formulations

20nm, 100nm or 200nm PS nanoparticles (surface modified with either chitosan (pH6.0) or polysorbate 80 (pH7.4) (Chapter 3)) were used in the transport studies. Uncoated versions were also investigated inorder to compare the effect of the surface coatings. SNS buffer and 0.5mM pH6.0 citrate buffer were used as control solutions, with and without 300mM sodium azide, to compare the effects of each of these solutions on the tissue. In addition, 100nm C-PS nanoparticles were also formulated at pH4.5 in order to investigate the relationship between pH and mucoadhesion in relation to the C-PS system.

Procurement of pigs was halted nationally by the British Government during part of this study due to an outbreak of foot-and-mouth disease in animals. Therefore, P80-FCS-PS nanoparticles could not be investigated using the diffusion chamber model.

4.2.1.4 Spectrofluorometry

The 200µL aliquots, taken during the transport study from the receiver chamber, were analysed for nanoparticles using a spectrofluorometer. Yellow-green or red fluorescent

nanoparticles were detected at Ex/Em 485/530 (FL600FA, Labtech Int. Ltd., Ringmer, UK) or 530/590 (FluoroSkan Ascent, Thermo, Stone, UK), respectively. The concentration of particles (particles/ml) in each aliquot was calculated by using a standard curve.

To construct a standard curve the concentration of particles per ml was calculated by using the following equation (Bangs 1984) :

Number of nanoparticles/ml = $\frac{6C \times 10^{12}}{\pi \rho \varphi^3}$

Where:

C = concentration of suspended nanoparticles (g/ml)

φ= diameter of nanoparticles (μm)

ρ = density of polymer (g/ml) [1.05g/ml for polystyrene]

Serial dilutions were made and the fluorescence value (RFU) for each triplicate standard was measured. The mean and standard deviation for each concentration was calculated. The limit of detection was derived (as shown in Figure 4.1). Samples that had a signal less than this value were assumed to contain no particles.

The limit of detection was used to exclude samples that gave readings which were indistinguishable from blank values (buffer alone) to a confidence level of 99.85% (i.e. within 3 standard deviations of the mean blank value assuming that the error about the blank samples is random and normally distributed) (Miller 1993).

Limit of detection was determined by adding the 3 standard deviations to the mean blank value and then deriving the corresponding particles/ml using the standard curve (Figure 4.1).

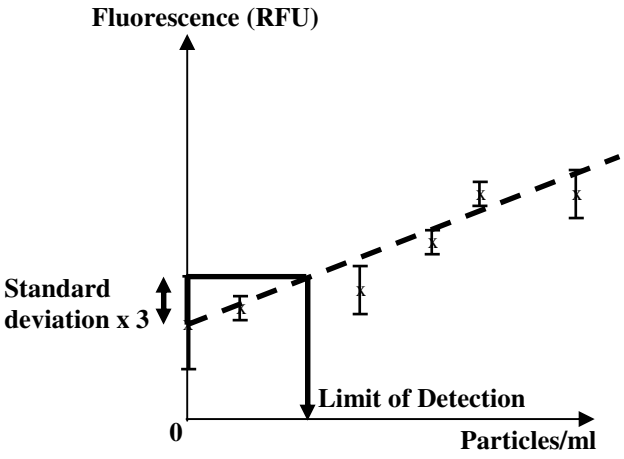

Figure 4.1 Determination of the Limit of Detection

4.2.1.5 Histological Sample Preparation

Two small pieces (approx. 4mm^2) of olfactory epithelium were cut from the dismounted tissue from the Franz diffusion cell after termination of the experiment using a scalpel knife. One sample was immediately placed into 3% glutaraldehyde in 0.1M cacodylate buffer for at least 48 hours and subsequently processed for light microscopy as previously described (2.2.7 Preparation of Tissue Samples for Microscopy).

The second sample was frozen by submerging it into isopentane which was supercooled using liquid nitrogen. This is a standard histological technique called 'snap freezing' (Bancroft & Stevens 1999). Isopentane is used for this purpose since it is hydrophobic and quickly permeates the biological tissue to freeze it. Liquid nitrogen could also be used but its boiling point is lower and it is less hydrophobic. Therefore, without cryoprotection techniques (4.3.1.5 Histological and Imaging Procedures), the inner core

of the tissue may not freeze instantaneously with the outer parts and hence this may lead to distortions in the morphology of the tissue. These samples were then stored at -80°C until required for cryo-sectioning.

For cryosectioning, snap-frozen samples were held in perpendicular alignment in relation to a cork disc. The embedding compound, Cryo-M-bed™, was applied onto the top and quickly frozen by dripping supercooled isopentane over the whole assembly. This froze the tissue sample in the correct orientation with respect to the cork disk.

The embedded sample was then sliced into 10μm sections using a cryostat (B3889, Bright Instrument Co. Ltd. Huntingdon, UK). These slices were placed on poly-L-lysine pre-coated microscope slides and allowed to melt and air dry. Air drying allowed the sample to fix onto the microscope slide.

A coverslip was then mounted using a standard histological glycerol-based mounting medium (Bancroft & Stevens 1999). The medium had low refractive index (1.42) which had the advantage of allowing better visibility of unstained structures in the tissue sample. It was also aqueous-based and therefore, unlike organic solvent-based alternatives, did not leach away the fluorescent dye from within the particles. After applying the coverslip with glycerol jelly the slide was left on a warm (40ºC) hotplate for about 30 minutes; this allowed the medium soak into the section. It was then removed to a cool place to set. Care was taken to avoid bubbles trapped under the coverslip.

Imaging of histological sections was performed using a Labophot 2 fluorescent microscope (Nikon UK Ltd, Kingston Upon Thames, UK) mounted with a high-resolution DXM1200 camera (Nikon UK Ltd, Kingston Upon Thames, UK) and bandpass filter cubes for DAPI, FITC and TRITC (Nikon UK Ltd, Kingston Upon Thames, UK). Images were acquired using Nikon ACT software (Nikon UK Ltd, Kingston Upon Thames, UK).

4.2.1.6 Statistical Analysis

Results are presented as means±standard error. A one-way analysis of variance (ANOVA) with a *post hoc* test was used to compare either 0.5mM citrate (pH6.0) or SNS (pH7.4) buffered samples to samples exposed to test formulations. A Bonferroni *post hoc* test was performed on groups with equal variances and a Games-Howell *post-hoc* test was performed on groups with unequal variances. A value of $p<0.05$ was considered statistically significant.

4.2.2 Results

This section describes the findings of the vertical Franz diffusion cell study. Fluorescence microscopy and spectroscopy were used to view excised porcine olfactory epithelia after application of test formulations. In addition, histology, electrophysiology and a fluorescence-based cellular metabolism assay (Alamar Blue™) were used to investigate the effect of the different nanoparticle formulations on the morphology and viability of the olfactory epithelia samples, respectively.

In relation to the study objectives and to demonstrate the differences (or lack thereof) in the results the data are grouped by surface modifications (PS, C-PS, P80-PS) or particle diameter (20nm, 100nm, 200nm).

4.2.2.1 The Influence of Particle Surface Modifications on Particle Transport

No transport was detected to the receiver chamber for any of the nine nanoparticle formulations. However, losses of nanoparticles were detected from the donor chamber after the transport study compared to the initial concentrations; this was calculated as a percentage loss (Table 4.2). Only a negligible (0.9±3.0%) number of particles were lost from the donor chamber for PS nanoparticles. A slightly greater loss was seen for the P80-PS nanoparticles (4.2±6.3%) compared to PS but this difference was not significant ($p>0.05$ ANOVA). In pH6.0, C-PS showed significantly higher losses from the donor side compared uncoated particles (10.6±3.2%; $p\leq0.05$ ANOVA). This loss was even greater when were applied in pH4.5 buffer (39.9±4.6%; $p\leq0.01$ ANOVA). At pH4.5 chitosan has a higher degree of charged glucosamine units. This showed that a lowering of the pH in the bulk phase changed the degree of interaction of the adsorbed chitosan layer (on the PS nanoparticle) with the olfactory mucosa.

Table 4.2 Percentage loss of particles from donor chamber during transport study with surface modified and unmodified PS

Test Formulation	*% (Mean±Standard Error)*
Uncoated Particles pH7.4 (n=12)	0.9±3.0
Polysorbate 80-coated particles pH7.4 (n=9)	4.2±6.3
Chitosan-coated Particles pH6.0 (n=11)	10.6±3.2[a]
Chitosan-coated Particles pH4.5 (n=4)	39.9±4.6[b]

Statistically significant compared to uncoated particles (ANOVA with Bonfferoni *post hoc* test [a] $p<0.05$, [b] $p<0.01$)

The loss of nanoparticles from the donor chamber, however, did not result in the appearance of nanoparticles in the receiver chamber as mentioned above. Therefore, a histological evaluation of the olfactory tissue was conducted with the aim to assess

whether the nanoparticles that were lost from the donor chamber were associated with the tissue or had penetrated into the tissue.

Figure 4.2(a,b) shows fluorescent microscopy images of PS (green), P80-PS (red) and associated with porcine olfactory epithelium prepared after transport studies. Images were slightly overexposed in order to view the location of the particles in relation to the autofluorescence signal from the olfactory tissue. The images seem to correlate with the quantitative losses of particles from the donor chambers since, in general, more fluorescence was seen interacting with the olfactory mucosa when a greater number of particles were lost from the donor chamber (Table 4.2 and Figure 4.2).

Uncoated particles showed little association with the olfactory tissue (Figure 4.2). The location of the PS at the apical edge of the mucosa suggested that they were trapped in the overlying mucus and did not penetrate into the cells.

A greater number of 100nm P80-PS nanoparticles were observed in the olfactory mucosa after a transport study than 200nm PS. It was not possible to conclude whether the particles had penetrated into the cells. The location of these particles could show that they were trapped in the overlaying mucus layer.

For 200nm C-PS in pH6.0 buffer, the bright field image shows that the particles can become highly associated with the luminal surface of the olfactory mucosa (Figure 4.2c). This high level of association was, however, not uniform throughout the whole epithelial surface. Again, it was difficult to assess if particles had penetrated into the cells. Unfortunately, direct comparisons between 100nm diameter particles with

different surface modifications were not possible since many of the transport study epithelia were lost during the protocol development stage for producing the fluorescence microscopy images.

In future, staining of cell membranes and/or nuclei could clarify the exact position of the nanoparticles in relation to the epithelial cell and overlying mucus.

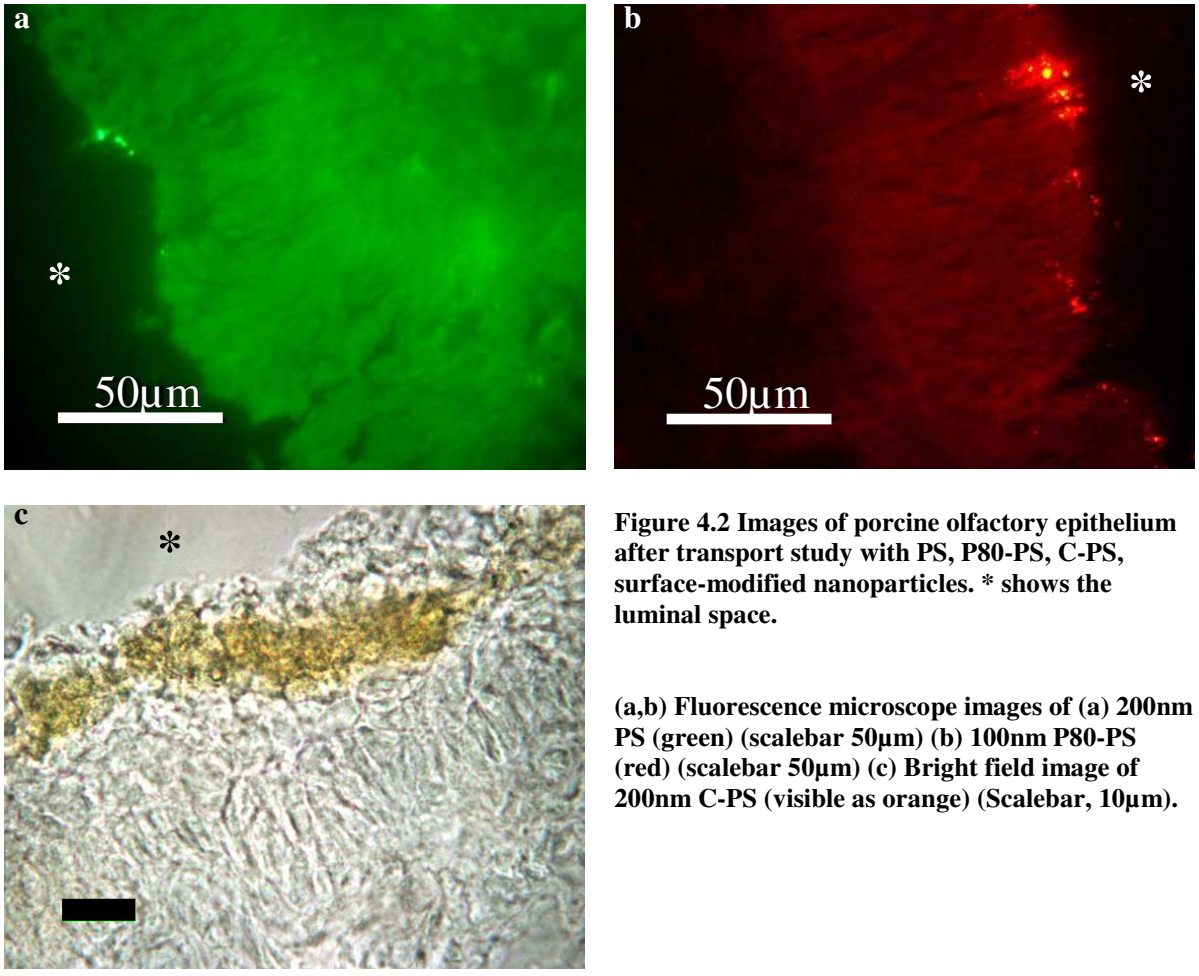

Figure 4.2 Images of porcine olfactory epithelium after transport study with PS, P80-PS, C-PS, surface-modified nanoparticles. * shows the luminal space.

(a,b) Fluorescence microscope images of (a) 200nm PS (green) (scalebar 50µm) (b) 100nm P80-PS (red) (scalebar 50µm) (c) Bright field image of 200nm C-PS (visible as orange) (Scalebar, 10µm).

Investigations were carried out using R_m, PD, I_{sc} and Alamar Blue™ tests to evaluate whether nanoparticles applied to the olfactory epithelium affected the viability of the epithelium itself. Quantitative data from these tests were collected and statistically analysed for changes compared to the control samples which were exposed to either

SNS (pH7.4) or 0.5mM citrate (pH6.0) buffers without nanoparticles. Bright field microscopy was also used to evaluate the condition of the olfactory epithelium after use in the vertical Franz diffusion cell (Figure 4.3). In addition, similar information was gathered to evaluate the effect of polysorbate 80 (105µM) and chitosan (0.87µM) solutions on olfactory epithelium compared to the SNS or citrate buffered control samples.

In the analysis below, only the surface effect of 100nm diameter nanoparticles are presented since they were the smallest nanoparticles that could be observed by fluorescence microscopy. Also, these particles were the smallest that were shown to directly interact with the olfactory epithelial cell and *in vivo* studies had shown that fewer 200nm nanoparticles were absorbed into the olfactory epithelium than 100nm particles (4.3.2.2 The Influence of Particle Surface Modifications on Particle Transport). Thus, 100nm nanoparticle had more potential to affect the viability of the epithelium than the 200nm nanoparticles; hence, data for 20nm and 200nm nanoparticles are not presented here.

Table 4.3 shows that R_m, PD and Alamar Blue™ measurements of olfactory epithelia exposed to SNS containing 300mM sodium azide were statistically different to samples that were exposed to only SNS buffer without sodium azide ($p<0.05$ ANOVA). I_{sc} measurements of the same epithelia were not found to be statistically different, due to the variability within the samples. Nevertheless, the mean values were markedly different for the different groups of olfactory epithelia that were exposed to varying conditions; $-107\pm42\mu A/cm^2$ for SNS with sodium azide compared to $+13\pm1\mu A/cm^2$ SNS without sodium azide, $+14\pm4\mu A/cm^2$ for polysorbate 80 in SNS, $+1\pm7\mu A/cm^2$ for

100nm PS, and +5±1μA/cm^2 for 100nm P80-PS. Overall sodium azide was considered to have significantly reduced the metabolism of the cells in the SNS buffered olfactory epithelium (2.4.2 Tissue Viability: The Effect of pH Buffers and Sodium Azide).

R_m, PD and I_{sc} values for polysorbate 80 (105μM) in SNS were not significantly different compared to the SNS buffer control. Alamar Blue™ data, however, were significantly lower ($p<0.05$ ANOVA). It is difficult to conclude from these contradicting results whether polysorbate 80 had any effect on the olfactory epithelium in these studies. However, when the images of olfactory epithelium that had been exposed to polysorbate 80 were compared to those that were exposed to only SNS buffer, it can be concluded that some morphological changes resulted from the application of the surfactant on the mucosa (Figure 4.3b). It can be concluded that 105μM polysorbate 80 in SNS did change the metabolic activity and morphology of the cells which was detected as a significant fall in Alamar Blue™ values and visible changes to the epithelium, respectively.

Changes to epithelial viability were not observed by any of the four viability scores for 100nm PS. This was expected since (carboxylated) PS particles should not be toxic to cells at these concentrations (Xia et al 2006). Surface modification of the 100nm PS with polysorbate 80 did not significantly reduce the viability of the samples (except for I_{sc} values) compared to the SNS buffered controls (Table 4.3) ($p<0.05$ ANOVA). However, the bright field image of 100nm P80-PS exposed olfactory epithelia (Figure 4.3c) showed little damage compared to the samples buffering in SNS alone (Figure 4.3a). Therefore, overall the P80-PS nanoparticles did not affect the viability of the olfactory epithelia.

For citrate buffer, only I_{sc} measurements for 0.5mM citrate buffer containing 300mM sodium azide (pH6.0) were statistically different to corresponding SNS values ($p<0.05$ ANOVA). R_m, PD and Alamar Blue™ measurements of the citrate buffered epithelia were not found to be statistically different. In fact, when the citrate buffer exposed epithelial were observed under light microscopy (Figure 4.3d), the apical cells in the epithelial appeared to be damaged compared to the SNS buffered olfactory epithelia (Figure 4.3a). For example, cilia appeared to be shorter and the olfactory knob (boxed) appeared disfigured compared to their usual distinctive shape (Figure 4.3d). Therefore, sodium azide was not considered to have significantly reduced the metabolism of the cells in the olfactory epithelium because the major reduction in metabolic activity was thought to have been a consequence of the 0.5mM citrate buffer itself (2.4.2 Tissue Viability: The Effect of pH Buffers and Sodium Azide).

Damage to the olfactory epithelium was made worse by the addition of 0.87µM chitosan solution (Figure 4.3e) to the citrate buffer. Under bright field, not only had the cells lost their cilia but chitosan had physically damaged cell integrity as well (Figure 4.3e).

Finally, 100nm C-PS even further deteriorated the condition of the olfactory epithelia compared to those samples exposed to chitosan solution in citrate buffer (Figure 4.3f). The 100nm C-PS exposed epithelia had damaged cell integrity to the point that the epithelium was no longer recognisable as pseudostratified columnar. Again, there was no significant difference in R_m, PD, I_{sc} and Alamar Blue™ values between 100nm C-PS and 0.5mM citrate buffer exposed olfactory epithelia.

Table 4.3 The effect of nanoparticle surface modification on R_m, PD, I_{sc} and Alamar Blue™ viability measurements using porcine olfactory epithelia during vertical Franz diffusion cell transport studies

Test Formulation	R_m (Ωcm^2)	PD (mV)	I_{sc}($\mu A/cm^2$)	Alamar Blue™ (RFU)
SNS Buffer pH7.4	59±7	-0.8±0.1	+13±1	10530±390
SNS Buffer pH7.4+azide	8±2[a]	+0.7±0.2[b]	-107±42	3260±280[a]
Polysorbate 80 in SNS	69±8	-0.9±0.3	+14±4	6910±870[a]
100nm PS	79±5	-0.0±0.5	+1±7	10490±880
100nm P80-PS	44±11	-0.2±0.1	+5±1[b]	8200±750

Test Formulation	R_m (Ωcm^2)	PD (mV)	I_{sc}($\mu A/cm^2$)	Alamar Blue™ (RFU)
Citrate Buffer pH6.0	79±23	-0.1±0.0	+1±0	5760±280
Citrate Buffer pH6.0+azide	11±2	+1.5±0.5	-134±43[c]	3080±440
Chitosan Solution	68±28	+1.0±0.9	-9±7	6200±660
100nm C-PS	45±14	-0.2±0.2	+9±8	6850±880

Mean±Standard error (n=3). [a] Significantly different (p<0.05) compared to SNS buffer (pH7.4) (ANOVA Bonferroni *post hoc* test, n=3), [b] Significantly different (p<0.05) compared to SNS buffer (pH7.4) (ANOVA Games-Howell *post hoc* test, n=3), [c] Significantly different (p<0.05) compared to 0.5mM citrate buffer (pH6.0) (ANOVA Bonferroni *post hoc* test, n=3).

Figure 4.3 The effect of nanoparticle surface modification on epithelial morphology using porcine olfactory epithelia during vertical Franz diffusion cell transport studies

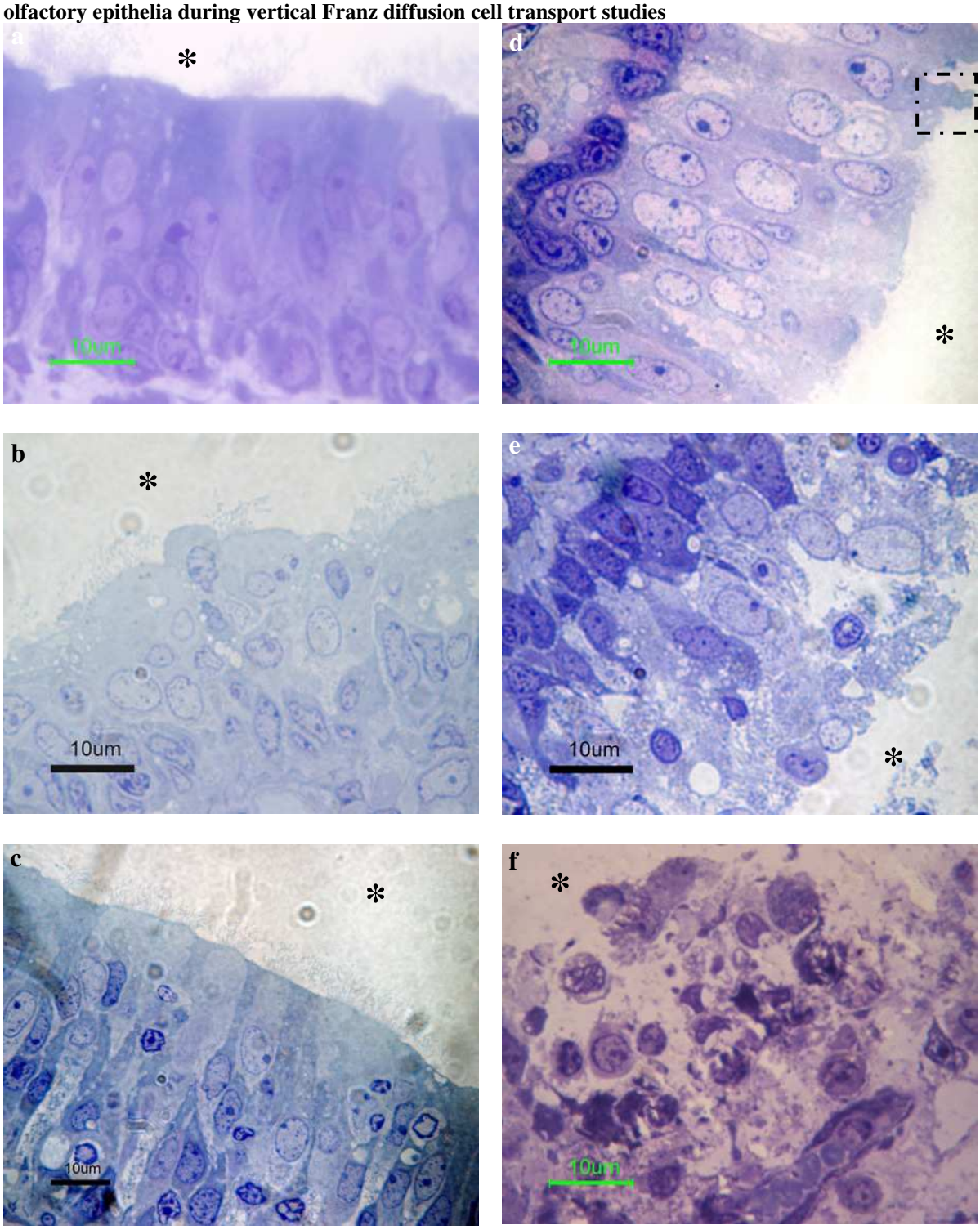

(a) SNS Buffer pH7.4 (b) Polysorbate 80 (105µM) in SNS buffer (c) 100nm P80-PS (d) 0.5mM citrate buffer pH6.0, olfactory knob boxed (e) Chitosan.HCl solution (0.87µM) (f) 100nm C-PS. * shows the luminal space.

4.2.2.2 The Influence of Particle Diameter on Particle Transport

No transport of 20nm, 100nm or 200nm C-PS nanoparticles to the receiver chamber was detected for any of the nanoparticle test formulations.

In the analysis below only the C-PS system is presented since chitosan modification showed the greatest toxicity to the porcine olfactory epithelia (Figure 4.3). These particles also demonstrated the clearest size-related damage to olfactory epithelium.

For each of the three formulations a mean loss of 8-12% of nanoparticles from the donor chamber was detected after the transport study compared to initial concentration (Table 4.4). However, no significant differences were observed between the groups of different sized nanoparticles ($p>0.05$ ANOVA). This possibly showed that particle surface modification with either chitosan or polysorbate 80 had a greater effect on the interaction of the nanoparticles with the olfactory mucosa than particle diameter in these samples, because statistical differences in percentage donor chamber particle losses were shown by surface modifying the nanoparticles (Table 4.2).

Alternatively, it was more difficult to evaluate the exact losses of particles from the donor chamber as the particle size was reduced. This may have lead to the greater degree of standard error that was observed with the smaller particles (Table 4.4), which consequently resulted in a lack of significance between the groups. Hence, proportionally more particles may have been lost from the donor chamber as particle size reduced but it was not detectable due to the accuracy limits of the fluorimeter that was employed.

Table 4.4 Percentage loss of 20nm, 100nm and 200nm C-PS nanoparticles from donor chamber during transport studies

Test Formulation	*% (Mean±Standard Error)*	*Total Donor Chamber Chitosan Content*
20nm C-PS (n=3)	12±9	0.005µM
100nm C-PS (n=4)	12±7	0.27µM
200nm C-PS (n=4)	8±3	0.83µM

No statistically differences were observed between the groups (p>0.05 ANOVA)

A morphological examination of the olfactory epithelia after exposure to the different sized C-PS, however, revealed that the 20nm diameter nanoparticles may have caused considerable more damage than either the 100nm or 200nm C-PS (Figure 4.4). The relationship between olfactory tissue damage and particle diameter showed that more damage was observed with smaller particles. For example, 200nm C-PS changed the appearance of the pseudostratified columnar cells to become less regular in shape and removed completely the appearance of cilia. 100nm C-PS damaged cell integrity of the tissue further so that the nuclei remained as the only subcellular features that could be distinguished by light microscopy. 20nm C-PS deteriorated the epithelial cells further so that even the nuclei very not visible.

Particle diameter was implicated as the main factor causing this damage, though, another uncontrolled variable in this experiment was the donor chamber chitosan concentration. Some chitosan remained in solution during the transport studies because an excess of chitosan was used during the surface modification process. The exact concentration of excess chitosan that was free in solution was not determined; but, knowledge of the initial chitosan concentration during formulation (1.74µM) was used to calculate the total chitosan in the donor chamber for each C-PS formulation (Table 4.4). By this analysis excess chitosan was unlikely to have been the cause of the

epithelial damage since the larger particle formulations contained greater concentrations of total chitosan in the system but showed least epithelial damage (Figure 4.4).

Figure 4.4 Condition of porcine olfactory epithelium after Franz diffusion cell transport studies with 20nm, 100nm, 200nm C-PS. * shows the luminal space.

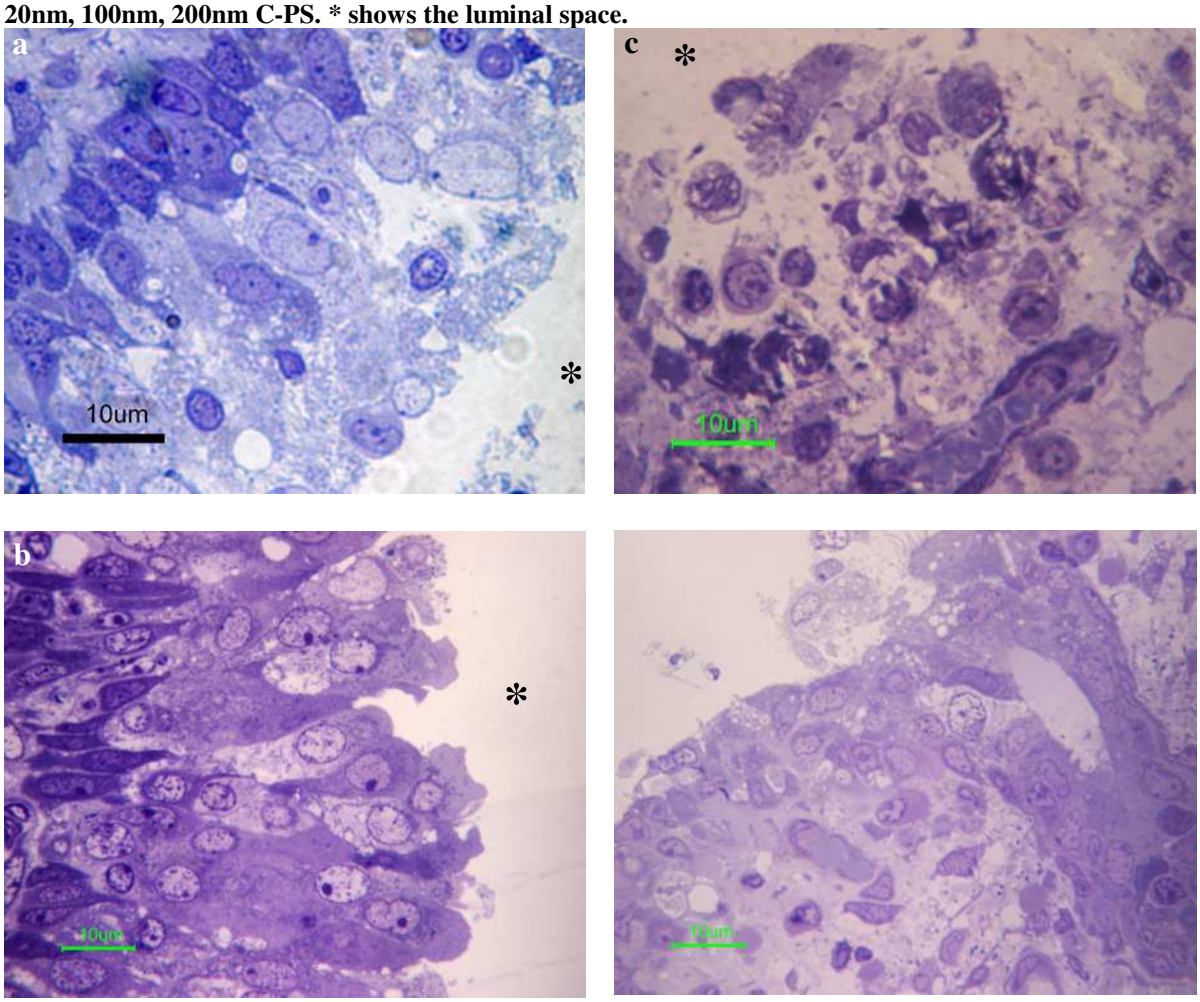

(a) Chitosan solution in citrate buffer (0.87µM) (b) 200nm C-PS (c) 100nm C-PS (d) 20nm C-PS

R_m, PD or I_{sc} and Alamar Blue™ measurements for olfactory epithelia that were exposed to 20nm, 100nm or 200nm C-PS again showed no significant difference compared to the citrate buffered epithelia ($p>0.05$ ANOVA) (Table 4.5). This was in line with the morphological observation above and earlier results that showed that the 0.5mM citrate buffer pH6.0 reduced the viability of the porcine olfactory epithelia during the vertical Franz diffusion chamber studies.

Table 4.5 The effect of 20nm, 100nm and 200nm diameter C-PS nanoparticles on R_m, PD, I_{sc} and Alamar Blue™ viability measurements using porcine olfactory epithelia during vertical Franz diffusion cell transport studies

	R_m (Ωcm^2)	*PD (mV)*	*I_{sc}($\mu A/cm^2$)*	*Alamar Blue™ (RFU)*
Citrate Buffer pH6.0	79±23	-0.1±0.0	+1±0	5760±280
20nm chitosan-coated	37±7	+0.2±0.4	-11±15	4960±410
100nm chitosan-coated	45±14	-0.2±0.2	+9±8	6850±880
200nm chitosan-coated	65±16	+0.3±0.4	-3±6	8090±1380

No statistically differences were observed between particle exposed epithelia and citrate buffered groups (p>0.05 ANOVA). Mean±Standard error (n=3).

4.3 TRANSPORT STUDY USING THE *IN VIVO* MOUSE MODEL

The objective for this study was to use fluorescence microscopy and stereological techniques to compare the abilities of nanoparticles, of different sizes and different surface characteristics, to transport through the olfactory or non-olfactory epithelia in the nasal cavity of the *in vivo* mouse model.

The different formulations used in this study were 100nm or 200nm PS nanoparticles which were surface modified with either chitosan or polysorbate 80/FCS. Uncoated 100nm particles were also used in the experiment in order to compare the effect of the surface coatings.

4.3.1 Materials and Methods

4.3.1.1 Materials

Histological samples were mounted onto microscope slide using Prolong Gold DAPI (Invitrogen A/S, Taastrup, Denmark). All other materials were sourced and prepared as described in Chapter 3.

4.3.1.2 Animals

Male inbred mice (C57BL/6JBom) (Taconic, Lille Skensved, Denmark) approximately 10 weeks old were used (body weight of 23-25g). The mice, in groups of 3-5, were housed in microisolators (filter top cages, Tecniplast, Italy) under pathogen-free conditions with a 12-hour light / 12-hour dark schedule and fed autoclaved standard chow (Altromin #1324, Lage, Germany) and water *ad libitum* throughout the experiment. The Danish Experimental Animal Inspectorate approved the experimental protocol and all the animal experiments were performed according to the ethical standards required by the local Guidelines.

The animals were inbred and provided with a standardised environment and diet to reduce data variability (Gizurarson 1990). In addition, the anatomy of the scrolled turbinates and morphology of the different nasal epithelia in the mouse are similar to most other mammals including pigs and humans.

4.3.1.3 Intranasal Administration

Prior to dosing, animals were anesthetised with isoflurane in air (3.75% v/v Forene™, Abbott Laboratories, UK) and maintained to effect. Mice were handled in a supine position to allow better contact of the formulation with the nasal epithelia during dosing (Gizurarson 1990). 15µl of the test formulation containing 4.55×10^{10}particles/ml was instilled by pipette into each naris. Mice were then placed on their sides until they woke up approximately 1-2 minutes later. The procedure was repeated every ~24 hours with freshly prepared samples for two further days. Animals were deeply anaesthetized (isoflurane) and killed on day 4 by cardiac perfusion fixation with 4% formalin in PBS. Then the head was removed and placed in the same fixative for 48 hours. Thereafter,

they were stored (for no longer than 6 weeks) in PBS buffer with 0.02% sodium azide until ready for cryosectioning.

4.3.1.4 Test formulations

In total, 6 groups of two animals were dosed intranasally with 30µl of test formulation as follows: (Group 1) 0.5mM Citrate buffer pH6.0, (Group 2) 100nm C-PS, (Group 3) 200nm C-PS, (Group 4) 100nm P80-FCS-PS, (Group 5) 200nm P80-FCS-PS, or (Group 6) 100nm PS. The formulations were made as previously described (Chapter 3) and diluted to $4.55x10^{10}$particles/ml using citrate buffer (Groups 1-3) or SNS buffer (Groups 4-6) before intranasal instillation.

Not all formulations that were developed in Chapter 3 were used here due to limitations of time and availability of animals. P80-FCS-PS formulations were preferred to P80-PS formulations since it was considered that FCS adsorbed to P80-PS could improve uptake of nanoparticles into the epithelial cells. 20nm nanoparticle formulations were not investigated here since it was not clear from the *in vitro* work whether these particles could be seen by fluorescence microscopy. The citrate buffer was chosen as a non-particulate control since damage to the epithelia due to the buffer alone could be evaluated. It was expected that the citrate buffer had a greater potential to show such damage compared to SNS buffer due to the conclusions drawn from the Franz diffusion chamber experiments (Chapter 2). In addition, SNS buffer has not shown to cause mucosal damage previously in rats (Jansson 2004) therefore a control experiment with SNS buffer alone was deemed less important than the citrate buffer.

4.3.1.5 Histological and Imaging Procedures

First the skin was removed from the skull taking care not to break the nose. Excess water was blotted off and then the sample was weighed and placed overnight into a beaker under slow stirring with EDTA in PBS buffer 0.25M pH 7.4. The skulls were subsequently blotted, weighed and returned into the decalcifying buffer each day until decalcification endpoint was reached. The decalcification was reached when skulls no longer lost weight but started to regain it. This marked the end of decalcification and start of water absorption into the tissue. Skulls were briefly washed and placed in sucrose solution for cryoprotection.

The skulls were cryoprotected by placing them in 30%w/v sucrose for 48 hours. They were then mounted onto metal discs with a layer of cryomountant (TissueTek, Sakura Finetek). Then more cryomountant was used to cover the entire skull. The whole assembly was subsequently frozen directly with liquid nitrogen.

Cryosections were cut to 5µm thickness at -20°C. At the first appearance of olfactory bulbs three sections for every 250µm were cut and placed on microscope slides until the olfactory bulbs were no longer visible. Sections were placed on microscope slides and allowed to fix by warming and drying at room temperature. Sections were then coverslip-mounted with Prolong Gold DAPI which incorporated a nuclear stain. Finally, the location of the particles along the entire olfactory system was determined using fluorescence microscopy as described below.

Imaging was performed in an inverted Axiovert 200M fluorescent microscope (Zeiss, Germany) mounted with a high-resolution CoolSnap HQ CCD camera (Photometrics,

USA) and bandpass filter cubes for GFP, Cy3 and DAPI (Chroma Technology, USA). Images were acquired using MetaMorph software (Molecular Devices, USA).

4.3.1.6 Estimating Tissue Particle Numbers

Fluorescence microscopy was used to count fluorescently labelled red particles in the histological sections. An autofluorescent signal from the epithelium was used to locate and identify the tissue during particles counting.

The method for estimating the number of particles in the tissue for each type of nasal epithelium was adapted from the stereological estimation method described by Nyengaard (Nyengaard 1999). Briefly, an unbiased sampling frame was used together with random tessellation in order to eliminate duplicate counting of particles. The random tessellation was controlled by a computer-aided stereology tool (CAST software; Visiopharm, Hørsholm, Denmark). Particles were counted manually therefore only particles that were associated with the olfactory or non-olfactory epithelium were included in the count. However, at the low magnification used (x4) to view the whole sample, it was not possible to conclude if the apically located nanoparticles were positioned extracellularly or intracellularly. But nanoparticles associated with mucus that was detached from the epithelium lining were not included (e.g. Figure 4.6b). The square sampling frame (30,000µm^2) was moved randomly by the software programme with a step length of 500µmx500µm in (x,y) coordinates. The total sampling area per histological section was 12% of the total sample surface. A total of 7-8 sections per animal were analysed in this way. The number of particles per unit area was calculated by dividing the number of particles in either olfactory or non-olfactory epithelium by the area of the sample.

Histological sections were analysed for particle numbers in an upright fluorescent microscope (Olympus BX51, Tokyo, Japan) with a GFP/dsRed filter (Chroma Technology, USA), a mounted digital camera (Olympus DP-70) and a motorized stage (Prior Scientific) in conjunction with CAST software (Visiopharm, Copenhagen, Denmark).

The appearance of olfactory epithelium was confirmed, by comparing samples with images from a histological reference (Geneser 1990) and using local knowledge within the stereological laboratory, to ensure that the correct regional distinctions between the non-olfactory and olfactory epithelia were made.

Statistical analysis of the data was not possible due to low sample numbers (only two mice were used per test formulation).

4.3.2 Results

In this section Figure 4.5 to Figure 4.6 show fluorescent microscope images of the murine nasal epithelia taken from the mice which were intranasally administered one of the six test formulations. The histological images are grouped, in relation to the chapter objectives, to demonstrate the differences (or lack of) between: (i) condition of buffer-control and nanoparticle-exposed epithelia; (ii) transport of 100nm and 200nm diameter particles; and (iii) transport of surface modified nanoparticles (C-PS and P80-FCS-PS) across olfactory or non-olfactory epithelia.

4.3.2.1 Condition of Epithelia after Exposure to Citrate Buffer

Autofluorescence (green) from the epithelia samples was detected by fluorescence microscopy to show the morphology of (a) olfactory and (b) non-olfactory nasal epithelia; in addition, nuclei were labelled with DAPI (blue) (Figure 4.5). In Figure 4.5(a) the apical surface of the olfactory epithelium was in tact and the borders of individual cells can be distinguished. The pseudostratified columnar cells were tall and nuclei were densely packed. An example of non-olfactory epithelium morphology is shown in Figure 4.5(b). The epithelium in this example was ciliated cuboidal. However, epithelial cells in the non-olfactory region in general were a mixture of ciliated cuboidal or ciliated pseudostratified columnar. Columnar cells in the non-olfactory region were shorter than pseudostratified columnar cells in the olfactory region. Also, nuclei (blue) were less densely packed in non-olfactory compared to olfactory epithelial cells. The mixture of epithelial morphologies in the non-olfactory regions meant that this tissue could not be described as respiratory epithelium; respiratory epithelium has pseudostratified columnar morphology (Adams 1972, Matulionis & Parks 1973 and 1.2.4 The Structure of Nasal Epithelia). The quality of both epithelia was comparable to those using light microscopy of fresh porcine olfactory epithelia (2.3.1 Morphological Features of Porcine Nasal Epithelia).

In some samples nuclei appeared in the mucus (Figure 4.6b). It was therefore concluded that cell debris was found in mucus lying on top of the epithelial cells in these samples. This is considered normal since mucus has been shown previously to contain cell debris by Khanvilkar *et al.* (2001). The content of cell debris in mucus varies from region-to-region (Sims & Horne 1997).

Figure 4.5 Fluorescent microscope images of murine nasal epithelia after treatment with citrate buffer.

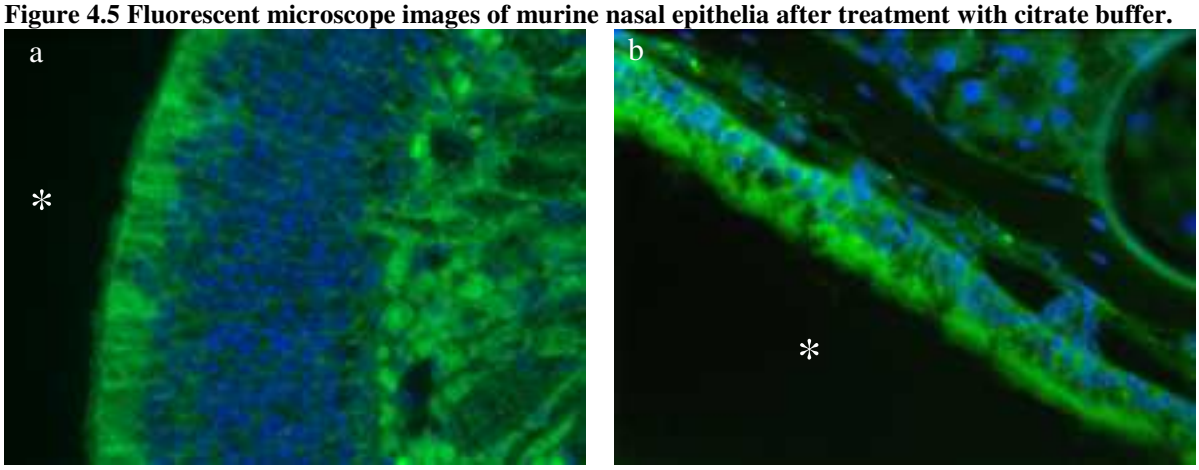

The images show the morphological differences between olfactory and non-olfactory epithelia: (a) Olfactory epithelium; (b) Non-olfactory epithelium. An autofluorescent signal (green) was used to visualise the cells. Nuclei were labelled with DAPI (blue). * marks luminal space. Magnification x40

4.3.2.2 The Influence of Particle Surface Modifications on Particle Transport

Stereological data showed that the overall particle numbers of 100nm PS associated with the mouse olfactory epithelium was 50-375particles/mm^2. 100nm PS nanoparticles were taken up into the mouse olfactory epithelium was seen by fluorescence microscopy (Figure 4.6a). Polysorbate 80-FCS modification of 100nm PS nanoparticles did not appear to change the ability of the nanoparticles to transport into the olfactory epithelium (100-300particles/mm^2) compared to bare 100nm PS particles. This was qualitatively confirmed by fluorescence microscopy (Figure 4.6a and Figure 4.7a).

Chitosan surface modification of 100nm PS (100nm C-PS), however, appeared to reduce the transport of the particles into the cells (0-60particles/mm^2) and increase association of the particles to the mucus as seen by fluorescence microscopy (Figure 4.6b) compared to both 100nm PS (50-375particles/mm^2) and 100nm P80-FCS-PS (100-300particles/mm^2) systems. This suggested that surface modification of the nanoparticles with chitosan reduced their association with the olfactory epithelia

compared to 100nm PS. However, surface modification of 100nm PS with P80/FCS did not affect epithelial distribution compared to bare 100nm PS.

Figure 4.6 Fluorescent microscope images of murine nasal epithelia after treatment with (a) 100nm PS or (b) 100nm C-PS

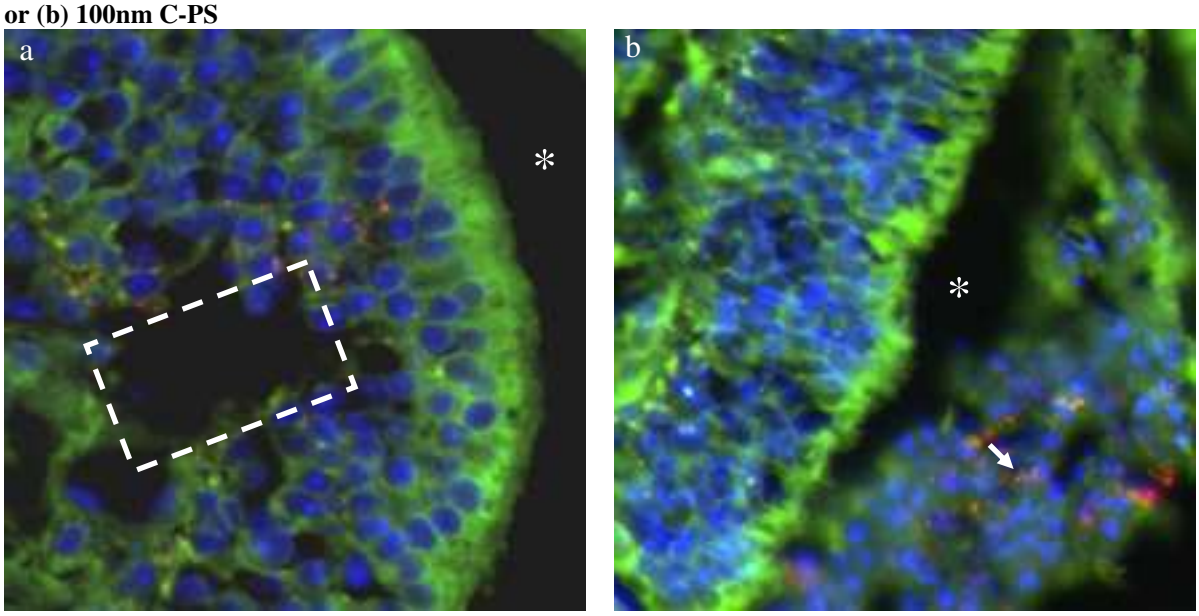

(a) 100nm PS penetrated to basement membrane of olfactory epithelium (sample contained a hole in the tissue due to a cryosectioning artefact (dashed boxed)). (b) More 100nm C-PS particles (red) associated with the mucus (arrow) and fewer 100nm C-PS particles were seen in cells. Cells were nuclear labelled with DAPI (blue). Autofluorescence (green) from olfactory epithelium. Magnification x40. * marks luminal space.

4.3.2.3 The Influence of Particle Diameter on Particle Transport

100nm and 200nm diameter P80-FCS-PS and C-PS nanoparticles were used to investigate the effect of particle size on particle transport into the olfactory epithelium. A similar comparison could not be performed for PS nanoparticles since 200nm PS was not studied in the mouse model. The transported nanoparticles were observed within epithelial cells and not between cells. An example of the transcellular transport of 100nm and 200nm P80-FCS-PS is shown in Figure 4.7(a,b).

Figure 4.7 Fluorescent microscope images of murine nasal epithelia after application of with 100nm or 200nm P80-FCS-PS

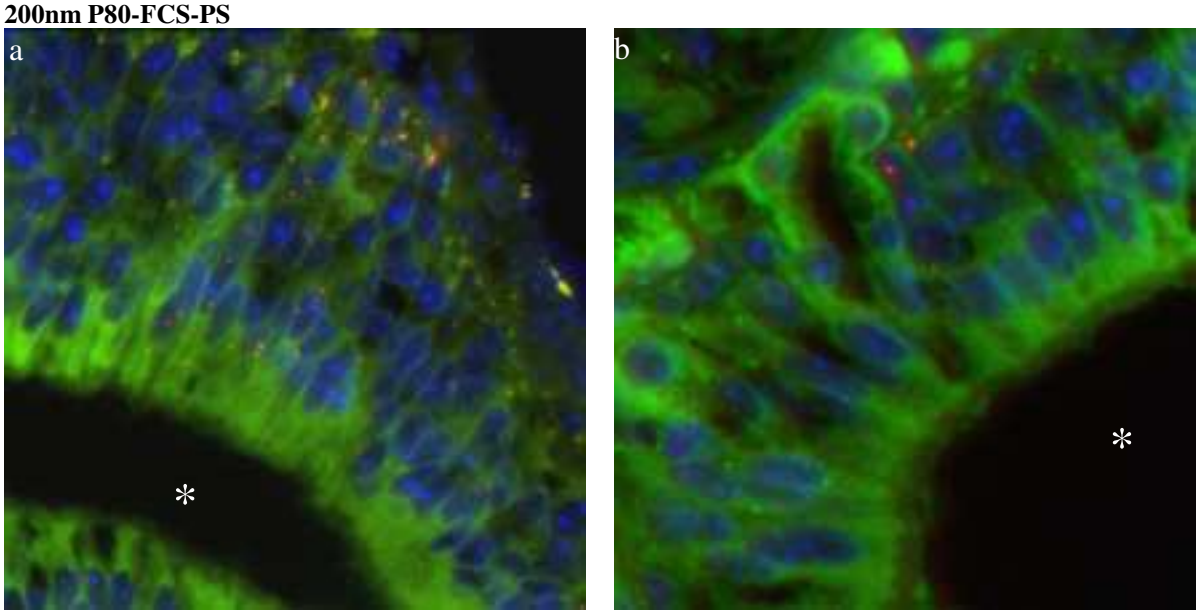

A greater number of (a) 100nm particles (red) were observed in the cells of the olfactory epithelia compared to (b) 200nm particles (red). Cells were nuclear labelled with DAPI (blue). Magnification x40.* marks luminal space.

Figure 4.7(a,b) shows a larger number of P80-FCS-PS 100nm nanoparticles were taken into the cells compared to P80-FCS-PS 200nm nanoparticles as visualised by fluorescence microscopy. This qualitative assessment was strengthened by stereological findings; hence, a greater quantity of 100nm P80-FCS-PS was associated with the murine olfactory epithelia (100-300 particles/mm^2) than 200nm diameter P80-FCS-PS

(~40 particles/mm^2) nanoparticles. The difference between 100nm and 200nm C-PS was less distinct (40-60 particles/mm^2 and 90-130 particles/mm^2, respectively). In addition, nanoparticles were not found in the olfactory bulbs of any animals (data not presented).

4.3.2.4 Affect of Olfactory and Non-Olfactory Nasal Epithelia on Particle Transport

Stereological results from the mouse model showed that particle association increased with non-olfactory epithelium compared to olfactory epithelium. A greater number of 100nm PS, 100nm C-PS and 100nm P80-FCS-PS nanoparticles were found in the non-olfactory mucosa (215 particles/mm^2, 211 particles/mm^2 and 44 particles/mm^2, respectively) compared to olfactory mucosa (101 particles/mm^2, 137 particles/mm^2 and 11 particles/mm^2, respectively).

In addition, 100nm P80-FCS-PS surface modification strategy did not result in clear preferential uptake of these nanoparticles compared to 100nm PS into either non-olfactory (211 particles/mm^2 and 215 particles/mm^2, respectively) or olfactory tissues (137 particles/mm^2 and 100 particles/mm^2, respectively).

4.4 DISCUSSION

The objective of this study was to investigate the abilities of nanoparticles with different surface characteristics and different sizes to transport into the porcine or murine olfactory epithelia using excised tissue mounted in the *in vitro* vertical Franz diffusion cell and the *in vivo* mouse models, respectively. Both models were also used to assess the extent of epithelial damage by the different nanoparticles. In addition, the *in vivo*

model was used to investigate the transport of the test nanoparticles into the non-olfactory epithelium and the olfactory epithelia.

A number of different techniques were used to assess the affect of surface coating (PS, C-PS and P80-FCS-PS nanoparticles) and particle diameter (100nm and 200nm) on the transport of these particles into the nasal epithelium. The techniques used were: (i) histological imaging of epithelial samples, (ii) stereological and spectroscopic assessment of nanoparticle transport, and (iii) biochemical and bioelectrical assessment of epithelial viability. The results are discussed below.

4.4.1 The Influence of Particle Surface Modifications on Particle Transport

Intranasal uptake of PS nanoparticles is commonly found in the literature, however, there have been no specific studies investigating nose-to-brain transport of polystyrene particles. Brooking *et al.* showed transmucosal transport of 100nm PS particles into the systemic circulation after *i.n.* administration in rats (Brooking et al 2001). The bioavailability was 2% after 3 hours as a proportion of the administered dose. This was attributed to passage of nanoparticles through non-olfactory epithelium via M cells to NALT for antigen sampling. However, the researchers found negligible 100nm PS in whole brain homogenate 3 hours after administration of the dose. At first it would appear that the 100nm PS did not pass into brain after *i.n.* instillation. However, better microdissection of certain brain areas (such as the olfactory bulb) may have shown a higher degree of uptake in specific areas. An investigation of brain uptake was not the main objective for their experiment therefore a microdissection of the brain was not done. It was found in the current study that 100nm and 200nm PS did not reach the brain in detectable concentrations. Hence, the data presented here agreed with the findings of Brooking *et al.* (2001).

For C-PS it was observed, from the bright field image (Figure 4.2), donor chamber losses of nanoparticles from the *in vitro* system (Table 4.2) and fluorescence microscopy in the mouse model (Figure 4.7), that more nanoparticles remained in the extracellular mucus compared to PS, P80-PS or P80-FCS-PS. This prevented C-PS progress into the underlying epithelial cells. Indeed, a similar observation was made by Campos *et al.* who found by confocal microscopy that 465nm diameter chitosan-coated poly-ε-caprolactone particles favoured retention in the superficial layers of the New Zealand rabbit nasal epithelium after *i.n.* instillation (de Campos et al 2004).

A well documented explanation for the retention of chitosan in mucus relates to the electrostatic interaction between the chitosan-coated nanoparticles and mucus (Kawashima et al 2000). It has been shown that the 100nm and 200nm C-PS have a positive charge in citrate buffer since they have a ζ potential of approximately +40mV (Chapter 3). It is also known that acidic residues (e.g. sialic acid pK_a 2.6 (Leung & Robinson 1992)) on mucus gel layer glycoproteins impart a negative charge to the mucosal surface (Mygind 1979). When the attractive forces were brought together by the application of C-PS to the mucus the C-PS nanoparticles adhered to the mucus which impeded their progress through it.

Indeed, in the diffusion chamber experiment 10.6±3.2% of the C-PS particles in the donor chamber adhered to the mucus at pH6.0 compared to 39.9±4.6% at pH4.5 during the transport study experiments (Table 4.2). Therefore, more particles adhered to the mucus when the olfactory epithelium was buffered at a lower pH. This result demonstrated that adhesion between mucus and C-PS was predominantly due to

electrostatic interactions and implies that other forces such as hydrogen bonding had a lesser affect.

Surface coating the PS nanoparticles with polysorbate 80 (P80-PS and P80-FCS-PS) did not statistically improve transport of surface modified particles into the nasal epithelial cells compared to bare PS nanoparticles. Donor chamber loss of the P80-PS particles (4.2±6.3%) was not a significantly greater than PS particles (0.9±3.0%) (Table 4.2). However, it is unclear whether more particles did penetrate the mucus in the *in vitro* model since fluorescence microscopy images of the dismounted olfactory epithelium found some areas of tissue did absorb P80-PS particles (Figure 4.2).

It was expected that a surface modification with PEG would increase transport of the nanoparticles through the olfactory mucus by increasing the hydrophilicity and reducing the negative charge of the particle compared to PS (Vila et al 2004; Lai et al 2007).

For example, Lai et al. (2007) found that conjugating 2kDa homopolymer PEG to the surface of 100nm and 200nm PS nanoparticles increased the diffusion coefficient of the particles through the cervicovaginal mucus by 20 and 381 times, respectively. However, differences in the experimental design described by Lai et al. (2007) and the current work may account for the disparity between the results from these studies. For example, in the diffusion chamber experiment the polysorbate 80 was adsorbed to the PS by hydrophobic-hydrophobic interactions whereas Lai et al. (2007) covalently bonded the PEG to the PS nanoparticles. Hence, it was less likely that the PEG molecule would disassociate from the PS surface in their study than in the diffusion chamber study. In

future, dissociation of the polysorbate 80 from the PS nanoparticles in the biological environment may be observed by fluorescently labelling the polysorbate 80.

In addition, there are 2.3 times more PEG monomer units in 2kDa PEG homopolymer than in polysorbate 80. Hence, surface modification of 100nm PS with 2kDa PEG homopolymer reduced ζ potential from -41mV to -4mV (Lai et al 2007); however, surface modification of 100nm PS with polysorbate 80 reduced ζ potential from -38mV to -20mV (Chapter 3). The greater negative charge on the P80-PS compared to 2kDa PEG-ylated PS would mean that the P80-PS would be repelled by negatively charged mucus to a greater extent than 2kDa PEG-ylated PS.

Nevertheless, the effect of nanoparticle PEG-ylation on mucosal penetration is controversial since there is also evidence in the literature that nanoparticles made from PEG-PLA (PEG 5kDa, PLA 45kDa) can reduce the mucosal penetration in cells (Behrens et al 2002). To assay the uptake of fluorescently labelled 196nm PEG-PLA nanoparticles, Behrens *et al.* (2002) lysed cells after 120 minute incubation of nanoparticles with (mucus producing) MTX cells or (non mucus producing) Caco-2 cells. A four-fold reduction of internalised nanoparticles was found for MTX cells. It was thought that PEG-chains on the nanoparticle surface inhibited interaction of the nanoparticles with cell surfaces.

Therefore, the effect of PEG surface modification is not fully understood. A number of variables may affect the ability of PEG-ylated nanoparticles to penetrate mucus and further uptake into epithelial cells; these may include PEG molecular weight,

nanoparticle core composition and/or effect of nanoparticle surface adsorbed proteins from the biological system.

In the mouse model, fluorescence microscopy images (Figure 4.6a and Figure 4.7a) showed that surface modification of PS with polysorbate 80 and FCS did not change the distribution of nanoparticles in the olfactory mucosa. Similarly, stereological data estimated that 50-375 100nm PS particles/mm^2 and 100-300 100nm P80-FCS-PS particles/mm^2 were associated with olfactory epithelium.

It was expected that polysorbate 80 would enrich the adsorption of certain serum proteins to the polysorbate 80 modified nanoparticles surface (e.g. ApoE, albumin) and reduce the adsorption of other FCS serum proteins (e.g. IgG) (Goppert & Muller 2005). Polysorbate 80 has been proven to promote the adsorption of ApoE (from human plasma) onto 230nm diameter solid lipid nanoparticles nanoparticles (Goppert & Muller 2005). Hence, the proportion of ApoE increased from 0.005%(w/v) in human plasma to 5.4%(w/v) adsorbed to solid lipid nanoparticles; the proportion of ApoE adsorbed to nanoparticles was increased further (15%w/v) when the core particle was made of poly-butyl-methacrylate.

Neuronal guidance during regeneration of neurones in the mouse olfactory epithelium is mediated by the presence of ApoE (Nathan et al 2007). However, the exact mechanism for this is not yet fully understood. It was speculated that the enrichment of Apo E to the PS nanoparticle surface would promote the uptake of P80-FCS-PS nanoparticle across the epithelial cells in the olfactory epithelium. Indeed, the improved uptake of serum exposed polysorbate 80-coated polybutylcyanoacrylate nanoparticles has been proven in

brain endothelial cells *in vitro* (Ramge et al 2002). The uptake of particles was mediated by the involvement of ApoE receptors in brain endothelial cells. This was proven *in vivo* through use of Apo E receptor knockout mice (Kreuter et al 2002). However, a number of reasons could explain the lack of improved uptake for the P80-FCS-PS nanoparticles compared to the PS nanoparticles in mice.

First, it has been shown that the pattern of serum protein adsorption can be determined by the nature of the core particle (as described above) (Goppert & Muller 2005). Therefore, the serum protein adsorption to polysorbate 80-coated PS nanoparticles may be different to polysorbate 80-coated polybutylcyanoacrylate nanoparticles. The PS core particle may reduce the concentration of ApoE adsorbed to the nanoparticle surface and therefore reduce the ability of the nanoparticles to be taken into cells by a receptor-mediated endocytic pathway. In fact, adsorption of FCS serum proteins to the P80-PS nanoparticles could not be proven by ζ potential measurements, particle sizing or Bradford's protein assay (Chapter 3). Second, the existence of ApoE receptors on the apical cell layer of the olfactory epithelium in mice has not been proven in the literature. Finally, extra time may be required for the adsorption of FCS serum proteins to P80-PS. Adsorption of the correct type or concentration of serum proteins may require longer than 30 minutes as used in the current work P80-FCS-PS formulation (Chapter 3).

Future experiments could use antibodies or lectin histochemistry to identify real receptor targets in the olfactory epithelium. This could be combined with better characterisation of ligand adsorption (e.g. 2D electrophoresis) which would prove the existence of appropriate ligands on the nanoparticle surface before application of these particles onto the olfactory epithelium.

4.4.2 The Influence of Particle Diameter on Particle Transport

Nanoparticle diameter may have affected the ability of P80-FCS-PS particles to penetrate the mucus overlying the nasal epithelial cells in the mouse model. Stereology showed that fewer 200nm P80-FCS-PS particles (~40 particles/mm^2) were associated with the olfactory and non-olfactory as compared to 100nm P80-FCS-PS particles (100-300 particles/mm^2) (Figure 4.7). It may be that, for this system, the larger 200nm particle could not penetrate the mucus to the same extent as the smaller 100nm particles and therefore had a more restricted access to the cell surface. For example, in one study, a greater number of 176nm diameter PEG-PLA nanoparticles were observed after *i.n.* instillation of the respective colloids (by confocal microscopy) in rat nasal epithelial cells than 1.5µm diameter particles (Vila et al 2004).

Similarly, the appearance of ^{125}I-labelled Tetanus Toxoid in the blood of rats after *i.n.* instillation of 200nm diameter PEG-PLA nanoparticles was significantly greater than that found for PEG-PLA 10µm diameter particles. The relationship was size dependent since more radioactivity was found in the blood as the particle size was reduced to 5µm and 1µm diameter, respectively (Vila et al 2005).

However, there does not appear to be a consensus within the literature about the ability of sub-micron diameter particles to penetrate the mucosal barrier. For example, it has been found that PS particles up to 500nm can penetrate cervical mucus (Lai et al 2007). This study, however, did not conclude that smaller particles penetrated the mucus faster. In fact, 200nm diameter particles penetrated the mucus just as quickly as 500nm diameter nanoparticles; 100nm particles progressed even slower. The authors proposed an explanation derived from size-exclusion chromatography that smaller particles can

access a greater number of pores in the heterogeneous mucosal pore structure. Therefore, the more tortuous route taken by smaller particles impedes their progress through the mucus.

This, however, does not fit well with observations made by others who show that smaller polystyrene particles permeate gastric mucin faster than larger ones (Norris & Sinko 1997) i.e. smaller particles have more freedom to move through the heterogeneously distributed porous structure.

In addition, particles did not transport to the olfactory bulbs. This may have been related to the diameter of the nanoparticle since the olfactory axons taper to a narrower width as they pass through the basement membrane. The average width of the olfactory axons in 2 month old rabbits was 200nm but many of these axons had diameters of less than 100nm (De Lorenzo 1960). Therefore, in my opinion, for reproducible transcellular transport of nanoparticle through the olfactory axons, nanoparticles should have a diameter of <100nm. Indeed, all studies to date that have demonstrated successful translocation of particles from the olfactory epithelium to olfactory bulbs have had diameters of less than 100nm (Chapter 1).

Also, through observations of toxicity to the porcine olfactory epithelium (Figure 4.4), the results presented here indirectly indicated that 20nm C-PS penetrated the mucus further in a basolateral direction than 100nm or 200nm C-PS. Hence, greater penetration of 20nm C-PS particles may have caused the greatest toxicity to the porcine olfactory epithelia, followed by 100nm C-PS, and least damage was caused by 200nm C-PS (Figure 4.4). Indeed, there is growing opinion in the literature that nanoparticles can

inherently cause greater damage to cells as their size reduces (4.4.3 Toxicological Aspects of Nanoparticle Exposure to Olfactory Epithelium). Therefore, the observed damage to the epithelia after their exposure to 20nm C-PS may be a result of either a more efficient mucosal penetration or a greater damaging capacity (or a combination of both).

4.4.3 Toxicological Aspects of Nanoparticle Exposure to Olfactory Epithelium

In general, a number of broad observations were made regarding the toxicological effects of the test formulations on the nasal epithelia: (i) chitosan solution and C-PS damaged porcine olfactory epithelium more than the other test formulations; (ii) a sized-dependent toxicity was observed for C-PS; and (iii) more chitosan-related toxicity was observed to the olfactory epithelia in the vertical Franz diffusion cell model than the *in vivo* mouse model.

Chitosan is widely accepted as a safe biological material (Schipper et al 1996). For example, Howard *et al.* (2006) intranasally administered 30µl of chitosan/siRNA nanoparticles (1mg/ml, 230nm diameter) for 5 consecutive days to EGFP (Enhanced Green Fluorescence Protein) transgenic mice. On day 6 the mice were killed and bronchioles were inspected by fluorescence microscopy for EGFP knockdown. EGFP was present in control animals (mismatched siRNA-chitosan nanoparticles) but the matched siRNA-chitosan nanoparticles showed EGFP knockdown (Howard et al 2006). This showed that the chitosan nanoparticles were not toxic to the cells *in vivo* since EGFP knockdown can only be produced in live cells. However, the researchers also found that siRNA-chitosan nanoparticles formed with large excesses of chitosan may be harmful (using MTT assay) to EGFP-H1299 (human lung cancer cell line).

It is clear, from the results presented here that application of the different test formulations changed the level of olfactory tissue damage (Figure 4.3). In general, the *in vitro* experiments showed that chitosan solution and C-PS particles were more damaging than equivalent P80-PS or PS particles. The reasons for the damaging effects of these particles on olfactory epithelium could be explained in terms of: (i) the chitosan salt form (chitosan.HCl) and the molecular weight (143kDa); and (ii) variation between results from different toxicity/viability assay; and (iii) the type of cell line or epithelium which were used in the experiments.

To expand, properties of chitosan such as molecular weight, degree of deactylation and salt form has been shown to modify the dose-dependent toxicity of the material towards cells *in vitro*. The chitosan solution (0.125mg/ml) used here had a large molecular weight (143kDa) and high degree of deactylation (89%). Increasing MW and DA% have been shown affect the viability of cells. Indeed, chitosans of molecular weight >100kDa are more toxic to Caco-2 cells than those with molecular weights <100kDa as determined by MTT assay (Carreno-Gomez & Duncan 1997). Also, Huang *et al.* found by MTT assay that the cytotoxic effect of chitosan solution to A549 (carcinomic human alveolar basal epithelial cells) was increased ~1.7-fold by increasing the %DA of chitosan from 46% to 88% (Huang et al 2004). Furthermore, chitosan.HCl could be regarded as the most cytotoxic salt form since it had the lowest IC_{50} values of 0.27±0.08mg/ml in caco-2 monolayers (compared to chitosan aspartate, chitosan glutamate and chitosan lactate) (Opanasopit et al 2007), and similarly, 0.21±0.04mg/ml in B16F10 cells (compared to chitosan hydroglutamate, chitosan hydrolactate and glycol chitosan) (Carreno-Gomez & Duncan 1997)as measured by MTT assay.

Also, Huang *et al.* found that 188nm diameter chitosan nanoparticles (MW 213kDa, DA% 88) were toxic to A549 in concentrations higher than 0.741mg/ml using MTT assay and neutral red (a dye that is endocytosed by viable cells) (Huang et al 2004). Since the chitosan was not surface loaded the concentration dependent cytotoxic effect is difficult to compare with the data presented here. Nevertheless, the specific nature of chitosan could explain the toxicity observed for chitosan solution to olfactory epithelia in the present study compared to the absence of such elsewhere.

In contrast, R_m or LDH assay scores showed no change after application of 290nm diameter chitosan.HCl (MW 100-130kDa, 80% deacetylation) nanoparticles to Caco-2 cell monolayer compared to monolayers without addition of chitosan nanoparticles (Behrens et al 2002). According to these workers, this ruled out the possibility that the chitosan nanoparticles caused cytotoxicity to the Caco-2 cells.

Dodane *et al.* did not find significant toxicity to Caco-2 cells up to 5mg/ml chitosan.HCl (MW 100-130kDa, 80% deacetylation) as assayed by Trypan Blue (Dodane et al 1999). Also, the study showed no damaging effects to Caco-2 cells of 1mg/ml chitosan by Transmission Electron Microscopy, although, changes in enlargement of endoplasmic reticulum and the appearance of large vacuoles were seen in the cells. These findings show that the assay method influences the interpretation of the toxicity threshold. Nevertheless the consensus suggests that no toxicity should have been observed in the current work since these thresholds are all above the concentration of chitosan used in the current work.

In the current work Alamar Blue™ assay and bioelectrical measurements (R_m, PD and I_{sc}) showed that 20nm, 100nm and 200nm C-PS did not significantly affect the viability of porcine olfactory epithelium compared to the 0.5mM citrate buffer control (pH6.0). This was probably because the citrate buffer reduced the viability of the epithelium before the application of the C-PS nanoparticles to the mucosal surface. However, histology did show that the mucosae were damaged after the exposure (Table 4.5). The amount of visible damage was increased with the application of smaller nanoparticles to the surface of the olfactory epithelia (Figure 4.4) when compared to the larger particles. This demonstrated that the Alamar Blue™ and bioelectrical viability measures used here may not have been able to sufficiently determine the effects of the test formulations on epithelial viability compared to standard histological evaluation.

Hence, Alamar Blue™ measured the viability of the whole tissue whereas the R_m, PD and I_{sc} data predominantly measured the function of the epithelial cell layer. Therefore, damage to the epithelial cells may not have been detected using Alamar Blue™.

On the other hand, R_m, PD and I_{sc} data are based on the integrity of the epithelial tight junctions, and the ability of the epithelial cells to generate a potential difference across the mucosa by actively transporting ions into the donor chamber against the ion concentration gradient. Therefore, in theory, this technique should produce a more accurate account of the viability of the epithelial cells compared to Alamar Blue™. However, the variability between different epithelia (i.e. the lack of precision of the results) was high using the electrophysiological technique. This meant that statistical differences between the grouped data were not found - which otherwise may have been.

Hence, histology, Alamar Blue™ and the R_m, PD and I_{sc} data were determining different aspects of viability of the epithelia. This difference could account for the inconsistency between the data from these techniques. Furthermore, the damage observed to the olfactory epithelial cells found here and the lack of toxicity of similar chitosan containing nanoparticle system elsewhere could be explained in a similar way. For instance, Huang *et al.* (2004) and Behrens *et al.* (2002) did not show the detailed histological effects of the chitosan nanoparticles in their studies therefore toxicity may have been observed by these researchers if this analysis was undertaken.

To my knowledge the toxicity of chitosan-coated nanoparticle systems to olfactory epithelium has not been reported to date. However, it has already been shown that physiological differences exist between olfactory and respiratory epithelia in pigs; hence, it was found that the metabolic rate of respiratory epithelia was greater than that of olfactory epithelia from the same animals (2.3.4 Comparison of Olfactory and Respiratory Tissue Metabolism). It is therefore reasonable to extrapolate that other physiological differences may also exist that may influence the susceptibility of olfactory epithelium to toxicity compared to non-olfactory epithelium. Indeed, a number of different cell types were used in the experiments described in the previous discussion on chitosan toxicity. The inherent variation in cellular physiology may have influenced the variation in toxicity that was observed in these experiments. Therefore, the chitosan-related toxicity to olfactory epithelium observed by bright field microscopy in Figure 4.4 may be influenced by the physiological nature of the olfactory epithelium compared to non-olfactory epithelium or *in vitro* cell lines.

In addition, there is growing evidence that the toxicity of nanoparticles to cells can increase as their diameters reduce (Oberdorster et al 2005). In the current work, it was observed in the diffusion chamber experiments that C-PS toxicity was sized-dependent (Figure 4.4). For example, in the previous discussion, the size of the chitosan nanoparticles used by Huang *et al.* (2004) and Behrens *et al.* (2002) (188nm and 290nm, respectively) were larger than the most toxic particle found in the current study (20nm and 100nm C-PS particles). Hence, this could also explain the differences between the lack of toxicity observed to cells with the larger particle used in these studies and the toxicity to olfactory epithelial cells found here after exposure to 20nm, 100nm and 200nm C-PS.

Two explanations can be given for the size-related toxic effects of nanoparticles to cells. Toxicity is thought to be related to either the high relative surface area (which is the surface area of an object proportional to its volume) associated with nanoparticles (Brown et al 2001) and/or the capability of small nanoparticles (<60nm) to access cell organelles (such as mitochondria) that larger particles may not (Xia et al 2006). The current observation of C-PS induced epithelial damage to the porcine olfactory epithelia is more easily explained by the latter explanation since the particle numbers were kept constant for all nanoparticle formulations (4.55×10^{10}particles/ml). Therefore, relative surface area increased with increasing nanoparticle diameter for these test formulations.

However, there are problems with a similar interpretation for the current data. First, no direct evidence of C-PS nanoparticles was seen in the porcine olfactory epithelium by fluorescence microscopy. This was mainly due to a lack of fluorescence microscopy

analysis which was a result of sample wastage during the method development phase to produce the images.

Second, the histological observations between the *in vitro* vertical Franz diffusion cell and the *in vivo* mouse model did not correlate well since uptake of 100nm and 200nm C-PS did not show morphological changes to the mouse olfactory epithelia (Figure 4.6). An explanation for this could be that pH6.0 was probably better controlled *in vitro* than *in vivo* (4.4.4 Comparison of *In vitro* and *In vivo* Biological Models) hence the C-PS nanoparticles would not have formed as many aggregates in the *in vitro* system which would result in better mucus penetration and more cellular uptake and therefore more cell damage.

However, this is speculation based on indirect evidence therefore the effect of nanoparticle C-PS surface modification and diameter on olfactory epithelial damage remains unclear.

To improve the accuracy of epithelial viability/cytotoxicity determinations after exposure to nanoparticles future *in vitro* studies could evaluate cellular events that are relevant in the drug delivery context. A combination intracellular calcium levels, ROS activity and lipid peroxidation indicators and improved histological analysis could give a more detailed and precise account of the cellular injury during nanoparticle uptake (Xia et al 2006).

4.4.4 Comparison of *In vitro* and *In vivo* Biological Models

The biological model may have affected the distribution of the nanoparticles in the nasal cavity. For example, results from the *in vivo* model showed that 100nm PS and 100nm P80-FCS-PS nanoparticles were found mainly inside the olfactory epithelium. In the vertical Franz diffusion, however, it was difficult to conclude whether PS or P80-PS were transported into cells or rested in the overlying mucus since these particles did not penetrate basolaterally far enough through the mucosa to make a clear distinction.

The difference between PS and P80-PS mucosal penetration could be attributed to the contact time that was allowed for particles with nasal epithelium in the different experiments. In the diffusion chamber experiments the particles were exposed to the olfactory tissue for 120 minutes. Contact time for the nanoparticles with the nasal epithelium in the mouse model was four days (although it was noted that some nanoparticles drained away from the nasal cavity after the mice recovered from anaesthesia 2 minutes post-dosing).

Also, bright field images of the porcine olfactory epithelia exposed to 0.5mM pH6.0 citrate buffer did not agree with the mouse model data. The quality of mouse olfactory and non-olfactory epithelia after exposure to 0.5mM citrate buffer pH 6.0 was comparable to those using light microscopy of fresh porcine olfactory epithelia (Figure 2.16 and Figure 4.5). These samples were therefore considered to be undamaged by the 0.5mM pH6.0 citrate buffer alone. However, the morphology of the 0.5mM pH6.0 citrate buffered olfactory tissue from the diffusion chamber experiment was damaged compared to the light microscopy of fresh porcine olfactory epithelia (Figure 2.17). The difference between the results can be explained by: (i) the inability of the citrate buffer

to maintain a pH gradient in the diffusion chamber model (Chapter 2); and (i) the difference in epithelium:buffer ratio in the two models.

To explain the first point, the viability of the olfactory epithelia in the diffusion chamber model was reduced in the pH6.0 citrate buffer. This may be explained in terms of a reduced mucosal pH gradient *in vitro* due to the lack of HCO_3^- ions in the citrate buffer (2.3.2 Effect of Different Buffers and Sodium Azide on Olfactory Epithelium and Figure 4.8). The exposure of surface epithelial cells *in vitro* to pH6.0 conditions could explain the damage observed to the cells in these epithelia. However, it is assumed that the mucosal pH gradient is maintained *in vivo* by blood born HCO_3^- ions. This could explain why reduced epithelial damage was observed *in vivo* compared to *in vitro*.

Also, pH6.0 conditions were more likely to have been maintained in the diffusion chamber since less tissue (1.0 cm^2 [*in vitro*], 2.5cm^2 [*in vivo* (Gizurarson 1990)]) was exposed to more 0.5mM citrate buffer (3.7ml [*in vitro*], 30µl [*in vivo*]) in this model. This difference may also have contributed to the increased damage to the epithelia in the diffusion chamber model.

C-PS nanoparticles were found in the mucous layer in both *in vivo* and *in vitro* models. However, more damage was observed to the epithelial cells in the diffusion chamber model than the mouse model when C-PS nanoparticles were applied. This may also be explained by the mucosal pH gradient (Figure 4.8). Hence, in the mouse model, pH of the mucus may change from pH6.0 at the gel layer surface to pH7.4 at the epithelial cell surface. Aggregation and physical entrapment of C-PS may occur in the gel layer as the colloid becomes unstable at higher pH towards to the epithelial cell surface (Figure 4.8).

In the diffusion chamber model the C-PS colloid is charge stabilised in the gel layer. Electrostatic interactions between the cationic particles and anionic gel layer may dominate. Hence, the mechanism of C-PS retention in mucus in each biological model may have been different.

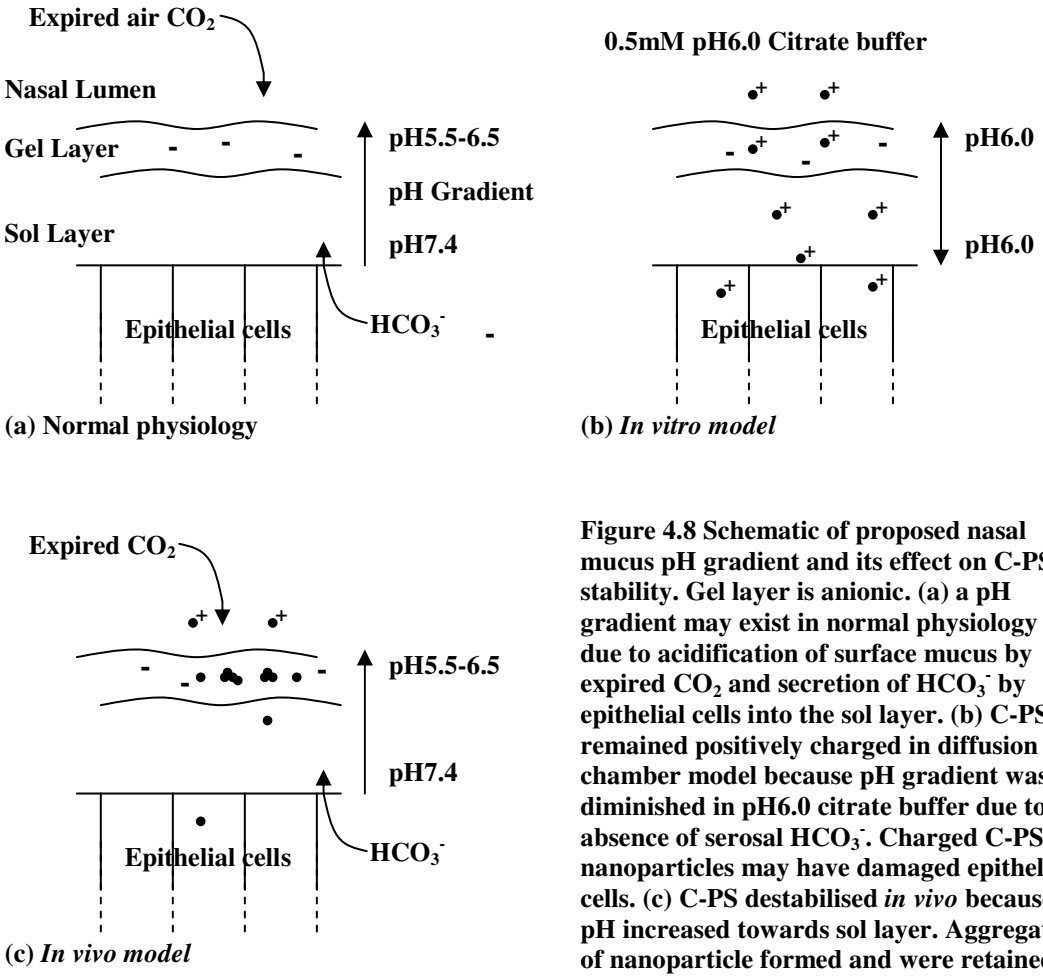

Figure 4.8 Schematic of proposed nasal mucus pH gradient and its effect on C-PS stability. Gel layer is anionic. (a) a pH gradient may exist in normal physiology due to acidification of surface mucus by expired CO_2 and secretion of HCO_3^- by epithelial cells into the sol layer. (b) C-PS remained positively charged in diffusion chamber model because pH gradient was diminished in pH6.0 citrate buffer due to absence of serosal HCO_3^-. Charged C-PS nanoparticles may have damaged epithelial cells. (c) C-PS destabilised *in vivo* because pH increased towards sol layer. Aggregates of nanoparticle formed and were retained in the porous gel layer structure.

The C-PS related epithelial damage observed by bright field microscopy could also be due to the diminished mucosal pH gradient *in vitro* (Figure 4.8). Hence, the C-PS colloid would remain stable in the sol layer and induce nanoparticle size-related damage to the epithelium as explained earlier (4.4.3 Toxicological Aspects of Nanoparticle

Exposure to Olfactory Epithelium). In the mouse model trapped C-PS aggregates in the mucous layer would prevent particles from reaching the epithelial cell surface. However, it was noted that C-PS nanoparticles were presumed to have reached the epithelial cells *in vitro* but no direct evidence of C-PS was observed in the olfactory tissues from the diffusion chamber transport studies by microscopy.

4.4.5 Particle Transport into Olfactory and Non-olfactory Epithelia

Stereological results showed there were 2.1-fold, 4.0-fold and 1.5-fold increases in the number of 100nm PS, 100nm C-PS and 100nm P80-FCS-PS nanoparticles (respectively) in the non-olfactory mucosa compared to olfactory mucosa (n=2). A well documented explanation for this is that nanoparticles are transported to a greater extent into M cells (for the function of presenting antigens to the NALT) of the non-olfactory epithelium compared to columnar epithelial cells (Ghirardelli et al 1999; Brooking et al 2001). NALT regions are not thought to exist in the olfactory epithelium. Therefore, the general increase of nanoparticle association with non-olfactory epithelium can be explained by transport into these regions. However, direct evidence for the existence of NALT and its association with nanoparticles was not investigated by microscopy in this study therefore a clear conclusion for this explanation can not be made.

100nm P80-FCS-PS surface modification strategy did not result in clear preferential uptake of these nanoparticles compared to 100nm PS into either non-olfactory or olfactory tissues. P80-FCS-PS nanoparticles were formulated with speculation that selective adsorption of certain serum proteins to P80-PS would result in preferential transport into the olfactory epithelium. Rationale for the study design and explanations

for the lack of positive outcome have been given previously (4.4.1 The Influence of Particle Surface Modifications on Particle Transport).

Future progress for olfactory selective nanoparticle formulations is likely to be made through surface modification of nanoparticles with targeting ligands that are known to react selectively with olfactory epithelium. Biorecognitive molecules such as lectins could provide the answer (Plendl & Sinowatz 1998). In fact, one successful study using *Ulex europeus* agglutinin I has already demonstrated the olfactory selectivity of lectin-conjugated nanoparticles in nasal mucosa (Gao et al 2007).

4.4.6 Implications of Study Outcomes

The outcome of this study has shown that more PS and P80-FCS-PS nanoparticles were found in nasal epithelial cells compared to C-PS. Hence, these formulations would be useful in different circumstances.

For example, C-PS nanoparticles would be useful to allow passage of surface-carried drug paracellularly through the nasal epithelia after release from the particle surface. If the release occurs over the respiratory epithelium this might result in systemic transport. However, release over olfactory epithelium could allow a direct N-B transport. If C-PS was used in this way then it would be necessary to deliver the formulation to the required epithelial locations in the nasal cavity by using drug delivery devices designed for selective deposition. Also, C-PS particles larger than 200nm may reduce mucosal penetration of the particles further and therefore avoid the damaging effects of the nanoparticles to the epithelial cells. Of course, for clinical success, the core polystyrene would eventually need to be exchanged for a biodegradeable polymer.

On the other hand, PS and P80-FCS-PS showed similar transport of particle numbers into nasal epithelial cells. Clearly, non-biodegradable polymers are not clinically useful for this type of drug delivery. As a result of this study, however, it is speculated that surface modification of biocompatible polymers with P80/FCS could produce equivalent uptake into the nasal cells to that seen here for P80-FCS-PS. Furthermore, if this strategy is successful for delivery of biodegradable nanoparticles into olfactory axons then nanoparticles containing molecules that are sensitive to the extracellular environment could eventually be delivered direct from nose-to-brain.

Indeed, the design of colloidal carriers intended to address specific delivery requirements by chitosan-coating nanoparticles for paracellular drug uptake and PEG-coating nanoparticles for transcellular uptake has also been suggested before across rabbit corneal epithelial cells (De Campos et al 2003).

4.5 CONCLUSIONS

An *in vitro* vertical Franz diffusion cell model using porcine olfactory epithelium and an *in vivo* mouse model were used to investigate the nasal transport of 20nm, 100nm and/or 200nm diameter nanoparticles with different surface modifications (PS, C-PS, P80-PS and/or P80-FCS-PS). The damaging effects of these nanoparticles to the olfactory epithelium were also reported. The *in vivo* transport of these particles were investigated through the non-olfactory and olfactory epithelia, however, particular emphasis was placed on the latter in accordance with the overall thesis aims.

First, modification of surface character changed the distribution of nanoparticles within the epithelia. C-PS caused particles to adhere to the extracellular mucus. It was thought that chitosan could be useful for deposition of drug in the extracellular mucus matrix in

order for a transport of drug via a fast paracellular route after release from the particle. In contrast, PS and P80-FCS-PS were taken into the nasal epithelial cells. In my opinion, encapsulating drugs that are sensitive to the extracellular environment into biodegradeable polymers and then overcoating with the polysorbate 80 (with or without adsorbed serum proteins) may be useful strategy for transport of drugs that are sensitive to the extracellular environment.

Second, a greater number of 100nm PS and 100nm P80-FCS-PS appeared in both types of epithelia compared to 200nm diameter equivalents. Therefore, the size of the nanoparticles was important. It was speculated that the successful translocation of the smaller particles was related to their ability to penetrate mucus more effectively than the larger ones. In the mouse model, the distinction between uptake of 100nm and 200nm C-PS particles was less pronounced than that for 100nm and 200nm P80-FCS-PS which suggested that surface character played a greater role in particle transport into the nasal epithelium compared to particle size (at these diameters) in these systems.

In addition, nanoparticles were not observed in the mice olfactory bulbs. The nanoparticles used here were possibly too large for transcellular transport after the olfactory axons narrowed in the basement membrane region in the mouse model. This agreed with *in vitro* data which showed that no particles were detectable in the receiver chamber in any of the diffusion chamber transport experiments. Therefore, it is speculated that an optimal nanoparticle size for transcellular nanoparticle transport direct from nose-to-brain would be <100nm diameter.

Also, C-PS nanoparticles caused the greatest amount of damage to the porcine olfactory epithelium compared to PS, P80-PS and P80-FCS-PS systems. The damage was likely to be a combination of: (i) the (hydrochloride) salt form and molecular weight (>100kDa) of the chitosan; (ii) the relative surface area and/or physical diameter of the nanoparticles; and (iii) depletion of the mucosal pH gradient in the *in vitro* model using pH6.0 citrate buffer.

However, C-PS size-related damage was not found in the mouse model. It was hypothesised that, unlike the *in vitro* model, the mouse model may have been able to maintain a pH gradient across the mucous layer by neutralising the acidity from the citrate buffer using blood born HCO_3^- ions. This would protect the epithelial cells by causing C-PS to aggregate in the mucus thereby preventing them from accessing the epithelial cells.

Nevertheless, if similar chitosan-coated nanoparticle systems are to be used in direct N-B drug delivery in the future then a particle diameter of >200nm is speculated to be appropriate for this system. This may enable paracellular drug delivery of small molecular weight drugs, which are insensitive to cellular efflux and degradation, to be achieved with less damage to the underlying epithelium than that found here.

Third, PS, C-PS and P80-FCS-PS nanoparticles were found in greater concentrations in the non-olfactory epithelium compared to the olfactory epithelium in the mouse model. This may be due to the transport of nanoparticles into NALT regions of the non-olfactory epithelium for antigen sampling since NALT has not been found to exist in the olfactory epithelium to date. However, this was not confirmed by co-localising NALT

and nanoparticles by fluorescence microscopy; therefore, the reason for increased association nanoparticles to non-olfactory regions remained unclear.

In conclusion, nanoparticles may be useful for drug delivery through the olfactory system. However, altering the surface character and size of the nanoparticles may lead to improved efficacy at the expense of toxicity to the biological system. Therefore, the future challenge is to design nanoparticle systems that deliver the drug payload through the appropriate pathway to the brain in a safe and efficacious manner.

To improve drug delivery to the olfactory region, promising approaches that could be used in the future relate to targeting of the olfactory epithelium through conjugation of olfactory-selective biorecognitive ligands. Such a strategy would reduce the reliance of drug delivery devices to target the olfactory epithelium through selective deposition of the nanoparticles in the olfactory region.

5. SUMMARY

5.1 FINAL CONCLUSIONS

The primary aims of the project are listed below.

(i) Design biological drug delivery models to investigate the physiological mechanisms that may allow the transport of nanoparticles directly from nose-to-brain.

(ii) Formulate a number of novel non-biodegradable nanoparticulate systems and compare their relative abilities to transport into the olfactory system.

(iii) Monitor the affect of nanoparticle exposure to the viability and morphology of olfactory epithelia.

In vitro vertical Franz diffusion chamber and *in vivo* mouse models were adapted to investigate the transport of nanoparticles via the olfactory system. A tissue extraction protocol was established by identifying the location of the olfactory epithelium in the porcine nasal cavity. The olfactory region was found at the caudal portion of the nasal cavity and extracted from the epithelium lining the dorsal nasal turbinate.

To ensure the scientific validity of the diffusion chamber studies it was necessary to prove that the experimental procedures themselves (without the addition of nanoparticles) had no effect on the mounted tissue. Therefore, viability and cellular morphology of the dissected olfactory epithelia were assessed prior to application of nanoparticles to tissues. The results showed that the diffusion chamber experiment did not visibly damage or have an affect on the metabolic activity of the olfactory tissue. However, the nature of the buffering system had significant effects on the viability of the diffusion chamber mounted olfactory epithelia. The citrate buffered samples (pH6.0)

were presumed to have reduced the viability of the olfactory epithelium by depleting the mucosal pH gradient in the epithelium but this did not kill the epithelial cells completely.

Other conclusions drawn from this work showed that; (i) metabolic activity of the olfactory epithelium was statistically reduced compared to respiratory epithelium, and (ii) normalising Alamar Blue™ data by the thickness of the epithelium did not reduce the variability of the Alamar Blue™ viability data. Overall, the diffusion chamber method validation concluded that both SNS buffered and citrate buffered porcine olfactory epithelia were suitable for nanoparticle transport studies in the vertical Franz diffusion cell.

The development of colloidal nanoparticle formulations was undertaken by surface modification of fluorescently labelled nanoparticles with chitosan, polysorbate 80 or polysorbate 80+FCS. 20nm, 100nm and 200nm diameter PS nanoparticles were surface modified with these materials. The dominant adsorption forces for chitosan and polysorbate 80 were different in each case. Chitosan adsorbed onto the carboxylated nanoparticle surface by electrostatic interactions which required careful manipulation of electrostatic charges on the surface of the nanoparticles and the chitosan molecules during formulation. Adsorption of polysorbate 80 was presumed to be driven by hydrophobic-hydrophobic interactions between the oleic acid moiety on polysorbate 80 and the surface of the PS nanoparticle. Adsorption of FCS serum proteins onto P80-PS nanoparticles was not detected by ζ potential, particle size or Bradford's protein assay. Nevertheless, the literature has consistently shown that serum protein adsorption does

occur on various polysorbate 80-coated nanoparticles. Therefore, it was presumed that serum adsorption had occurred.

The PS, C-PS, P80-PS and P80-FCS-PS nanoparticles formulations were either applied to the mucosal surface of the diffusion chamber mounted olfactory epithelia or administered intranasally in the *in vivo* mouse model.

The following observations were made: first, surface modification changed the distribution of nanoparticles within the epithelia. C-PS particles adhered to the extracellular mucus whereas PS and P80-FCS-PS were taken into the nasal epithelial cells. Stereological data showed that there was no difference between the uptake of PS and P80-FCS-PS nanoparticles in the mouse model. It was unclear whether this was due to a lack of adsorption of serum proteins to the nanoparticle surface. 2D electrophoresis may be used in the future to clarify FCS adsorption behaviour to P80-PS nanoparticles.

Second, the size of the nanoparticles was important. A greater number of 100nm PS and 100nm P80-FCS-PS appeared in mouse nasal epithelial cells compared to 200nm diameter equivalents.

Nanoparticles were not observed in the mice olfactory bulbs. This agreed with *in vitro* data which showed that no particles were detectable in the receiver chamber in any of the diffusion chamber transport experiments.

C-PS nanoparticles caused the greatest amount of damage to the porcine olfactory epithelium compared to PS, P80-PS and P80-FCS-PS systems. This may have been due

to the physicochemical character of the chitosan, the size of the C-PS nanoparticles and/or (iii) depletion of the mucosal pH gradient in the *in vitro* model using pH6.0 citrate buffer. However, similar cellular damage in the mouse model were not observed. It was hypothesised that, unlike the *in vitro* model, the mouse model may have been able to maintain a protective pH gradient across the mucous layer by neutralising the acidity from the citrate buffer using blood born HCO_3^- ions.

Third, nanoparticles were found in greater concentrations in the non-olfactory epithelium compared to the olfactory epithelium in the mouse model possibly due to the absorption of nanoparticles into non-olfactory NALT regions. However, this was not confirmed by co-localisation studies of NALT and nanoparticles by fluorescence microscopy.

5.2 SIGNIFICANCE AND FUTURE POSSIBILITIES

The outcome of this study has shown that more PS and P80-FCS-PS nanoparticle were found in nasal epithelial cells compared to C-PS. Hence, these formulations would be useful in different circumstances.

For example, C-PS nanoparticles would be useful to allow passage of surface-carried small molecular weight drugs paracellularly through the nasal epithelia after release from the particle surface. Drugs that are less sensitive to cellular efflux and degradation would be suitable candidates for this type of drug delivery. If the drug release occurs over the respiratory epithelium this might result in systemic transport. In contrast, release over olfactory epithelium could allow a direct N-B transport. However, since chitosan has no biorecognitive targeting ability, it would be necessary to deliver C-PS to

the required epithelial locations in the nasal cavity by using drug delivery devices designed for selective deposition. C-PS particles larger than 200nm may reduce mucosal penetration of the particles further and therefore avoid the damaging effects of the nanoparticles to the epithelial cells. Of course, for clinical success, the core polystyrene would eventually need to be exchanged for a biodegradeable polymer.

In contrast, PS and P80-FCS-PS showed similar uptake of particle numbers into nasal epithelial cells. Again, non-biodegradable polymers are not clinically useful for this type of drug delivery. As a result of this study, however, it is speculated that surface modification of biodegradeable polymers with P80/FCS could produce equivalent uptake into the nasal cells to that seen here for P80-FCS-PS. Furthermore, if this strategy is successful for delivery of biodegradable nanoparticles (<100nm diameter) into olfactory axons then nanoparticles containing molecules that are sensitive to the extracellular environment could eventually be delivered direct from nose-to-brain.

To improve drug targeting to the olfactory region, promising approaches that could be used in the future relate to selective targeting of olfactory epithelium through conjugation of olfactory selective biorecognitive ligands (e.g. lectins). Such a strategy would reduce the reliance of drug delivery devices to target the olfactory epithelium.

Also, olfactory epithelium had a reduced metabolic activity compared to respiratory epithelium. From a direct N-B drug delivery perspective, and depending on the drug to be delivered, this may be either detrimental (by allowing slower uptake of drug into the olfactory epithelial cells) or beneficial (by allowing slower drug degradation in the olfactory mucosa or slower efflux of drug from apical cells). However, the relationship

between epithelial metabolic activity and drug transport would need to be investigated in greater detail to establish this opinion.

Overall, nanoparticles may be useful for drug delivery through the olfactory system. However, altering the surface character and size of the nanoparticles may lead to improved efficacy at the expense of toxicity to the biological system. Therefore, the future challenge is to design nanoparticle systems that deliver the drug payload through the appropriate pathway to the brain in an efficacious and safe manner.

REFERENCES

ABD SEROTEC LTD. (2004) Alamar Blue, Technical Datasheet. AbD Serotec Ltd, Oxford

ADAMS, D. R. (1972) Olfactory and Nonolfactory Epithelia in Nasal Cavity of Mouse, Peromyscus. American Journal of Anatomy 133: 37-49

ADAMS, D. R. (1990) Epithelium Lining The Rostral Portion Of The Porcine Nasal-Mucosa. Research In Veterinary Science 49: 61-65

ADAMS, G. L., BOIES, L. R., HILGER, P. A. (1989) Boies's Fundamentals of otolaryngology a textbook of ear, nose and throat diseases. Book: pp177-95

ALLEN, A., FLEMSTROM, G. (2005) Gastroduodenal mucus bicarbonate barrier: protection against acid and pepsin. American Journal of Physiology-Cell Physiology 288: C1-C19

AN, J. H., DULTZ, S. (2007) Polycation adsorption on montmorillonite: pH and T as decisive factors for the kinetics and mode of chitosan adsorption. Clay Minerals 42: 329-339

ANDERSON, R. G. W. (1998) The caveolae membrane system. Annual Review of Biochemistry 67: 199-225

ASPDEN, T. J., MASON, J. D. T., JONES, N. S., LOWE, J., SKAUGRUD, O., ILLUM, L. (1997) Chitosan as a nasal delivery system: The effect of chitosan solutions on in vitro and in vivo mucociliary transport rates in human turbinates and volunteers. Journal of Pharmaceutical Sciences 86: 509-513

BANCROFT, J., STEVENS, A. (1999) Theory and Practice of Histological Techniques. Churchill Livingstone, London

BANGS, L. (1984) Uniform Latex Particles. Seragen Diagnostics Inc, Indianapolis, USA

BANNISTER, L. H., DODSON, H. C. (1992) Endocytic Pathways in the Olfactory and Vomeronasal Epithelia of the Mouse - Ultrastructure and Uptake of Tracers. Microscopy Research and Technique 23: 128-141

BARNETT, E. M., CASSELL, M. D., PERLMAN, S. (1993) 2 Neurotropic Viruses, Herpes-Simplex Virus Type-1 and Mouse Hepatitis-Virus, Spread Along Different Neural Pathways from the Main Olfactory-Bulb. Neuroscience 57: 1007-1025

BAUER, D., KILLMANN, E., JAEGER, W. (1998) Flocculation and stabilization of colloidal silica by the adsorption of poly-diallyl-dimethyl-ammoniumchloride (PDADMAC) and of copolymers of DADMAC with N-methyl-N-vinyl acetamide (NMVA). Colloid and Polymer Science 276: 698-708

BECHGAARD, E., GIZURARSON, S., JORGENSEN, L., LARSEN, R. (1992) The Viability of Isolated Rabbit Nasal-Mucosa in the Ussing Chamber, and the Permeability of Insulin across the Membrane. International Journal of Pharmaceutics 87: 125-132

BEHRENS, I., PENA, A. I. V., ALONSO, M. J., KISSEL, T. (2002) Comparative uptake studies of bioadhesive and non-bioadhesive nanoparticles in human intestinal cell lines and rats: The effect of mucus on particle adsorption and transport. Pharmaceutical Research 19: 1185-93

BENEDICT, C., KERN, W., SCHULTES, B., BORN, J., HALLSCHMID, M. (2008) Differential sensitivity of men and women to anorexigenic and memory-improving effects of intranasal insulin. Journal of Clinical Endocrinology & Metabolism 93: 1339-1344

BETBEDER, D., SPERANDIO, S., LATAPIE, J. P., DE NADAI, J., ETIENNE, A., ZAJAC, J. M., FRANCES, B. (2000) Biovector (TM) nanoparticles improve antinociceptive efficacy of nasal morphine. Pharmaceutical Research 17: 743-48

BLUNK, T., HOCHSTRASSER, D. F., SANCHEZ, J. C., MULLER, B. W., MULLER, R. H. (1993) Colloidal Carriers for Intravenous Drug Targeting - Plasma-Protein Adsorption Patterns on Surface-Modified Latex-Particles Evaluated by 2-Dimensional Polyacrylamide-Gel Electrophoresis. Electrophoresis 14: 1382-1387

BODIAN, D., HOWE, H. A. (1941) The Rate of Progression of Poliomyelitis Virus in Nerves. [not specified]. Johns Hopk Bull.. 1941. 69: 79-85

BOOTH, W. D., BALDWIN, B. A., POYNDER, T. M., BANNISTER, L. H., GOWER, D. B. (1981) Degeneration and Regeneration of the Olfactory Epithelium after Olfactory-Bulb Ablation in the Pig - a Morphological and Electro-Physiological Study. Quarterly Journal of Experimental Physiology and Cognate Medical Sciences 66: 533-540

BRAND, G. (2006) Olfactory/trigeminal interactions in nasal chemoreception. Neuroscience and Biobehavioral Reviews 30: 908-917

BREEN, C. (1999) The characterisation and use of polycation-exchanged bentonites. Applied Clay Science 15: 187-219

BRODBELT, A., STOODLEY, M. (2007) CSF pathways: a review. British Journal of Neurosurgery 21: 510-520

BROOKING, J., DAVIS, S. S., ILLUM, L. (2001) Transport of nanoparticles across the rat nasal mucosa. Journal of Drug Targeting 9: 267-279

BROWN, D. M., WILSON, M. R., MACNEE, W., STONE, V., DONALDSON, K. (2001) Size-dependent proinflammatory effects of ultrafine polystyrene particles: A role for surface area and oxidative stress in the enhanced activity of ultrafines. Toxicology and Applied Pharmacology 175: 191-199

BURD, G. D. (1991) Development of the Olfactory Nerve in the African Clawed Frog, Xenopus-Laevis .1. Normal Development. Journal of Comparative Neurology 304: 123-134

CARRENO-GOMEZ, B., DUNCAN, R. (1997) Evaluation of the biological properties of soluble chitosan and chitosan microspheres. International Journal Of Pharmaceutics 148: 231-40

CHARLTON, S., JONES, N. S., DAVIS, S. S., ILLUM, L. (2007) Distribution and clearance of bioadhesive formulations from the olfactory region in man: Effect of polymer type and nasal delivery device. European Journal of Pharmaceutical Sciences 30: 295-302

CHOU, K.-J., DONOVAN, M. D. (1997) Distribution of antihistamines into the CSF following intranasal delivery. Biopharmaceutics and Drug Disposition 18: 335-346

CLAESSON, P. M., NINHAM, B. W. (1992) Ph-Dependent Interactions between Adsorbed Chitosan Layers. Langmuir 8: 1406-1412

CONNER, S. D., SCHMID, S. L. (2003) Regulated portals of entry into the cell. Nature 422: 37-44

CREMASCHI, D., ROSSETTI, C., DRAGHETTI, M. T., MANZONI, C., ALIVERTI, V. (1991) Active-Transport of Polypeptides in Rabbit Nasal-Mucosa - Possible Role in the Sampling of Potential Antigens. Pflugers Archiv-European Journal of Physiology 419: 425-432

CREMASCHI, D., PORTA, C., GHIRARDELLI, R., MANZONI, C., CAREMI, I. (1996) Endocytosis inhibitors abolish the active transport of polypeptides in the mucosa of the nasal upper concha of the rabbit. Biochimica Et Biophysica Acta-Biomembranes 1280: 27-33

CROCE, C., FODIL, R., DURAND, M., SBIRLEA-APIOU, G., CAILLIBOTTE, G., PAPON, J. F., BLONDEAU, J. R., COSTE, A., ISABEY, D., LOUIS, B. (2006) In vitro experiments and numerical simulations of airflow in realistic nasal airway geometry. Annals of Biomedical Engineering 34: 997-1007

DAHLIN, M., JANSSON, B., BJORK, E. (2001) Levels of dopamine in blood and brain following nasal administration to rats. European Journal of Pharmaceutical Sciences 14: 75-80

DAHLIN, M., BERGMAN, U., JANSSON, B., BJORK, E., BRITTEBO, E. (2000) Transfer of dopamine in the olfactory pathway following nasal administration in mice. Pharmaceutical Research 17: 737-42

DARDER, M., COLILLA, M., RUIZ-HITZKY, E. (2003) Biopolymer-clay nanocomposites based on chitosan intercalated in montmorillonite. Chemistry of Materials 15: 3774-3780

DE CAMPOS, A. M., SANCHEZ, A., GREF, R., CALVO, P., ALONSO, M. J. (2003) The effect of a PEG versus a chitosan coating on the interaction of drug colloidal carriers with the ocular mucosa. European Journal of Pharmaceutical Sciences 20: 73-81

DE CAMPOS, A. M., DIEBOLD, Y., CARVALHO, E. L. S., SANCHEZ, A., ALONSO, M. J. (2004) Chitosan nanoparticles as new ocular drug delivery systems: in vitro

stability, in vivo fate, and cellular toxicity. Pharmaceutical Research 21: 803-810

DE LORENZO, A. (1960) Electron microscopy of the olfactory and gustatory pathways. Annals of otology, rhinology and laryngology 68: pp410-20

DE LORENZO, A. (1962) Olfaction and Taste. Proceedings of the First International Symposium held at the Wenner-Gren Centre Stockholm, September 1962. Wenner-Gren Centre Stockholm. Pergamon Press, pp 5-18

DE LORENZO, A. (1970) Taste and Smell in Vertebrates. J&A Churchill, London

DODANE, V., KHAN, M. A., MERWIN, J. R. (1999) Effect of chitosan on epithelial permeability and structure. International Journal of Pharmaceutics 182: 21-32

DUFES, C., OLIVIER, J. C., GAILLARD, F., GAILLARD, A., COUET, W., MULLER, J. M. (2003) Brain delivery of vasoactive intestinal peptide (VIP) following nasal administration to rats. International Journal Of Pharmaceutics 255: 87-97

EDELING, M. A., SMITH, C., OWEN, D. (2006) Life of a clathrin coat: insights from clathrin and AP structures. Nature Reviews Molecular Cell Biology 7: 32-44

EKELUND, K., OSTH, K., PAHLSTORP, C., BJORK, E., ULVENLUND, S., JOHANSSON, F. (2005) Correlation between epithelial toxicity and surfactant structure as derived from the effects of polyethyleneoxide surfactants on Caco-2 cell monolayers and pig nasal mucosa. Journal of Pharmaceutical Sciences 94: 730-744

ELDER, A., GELEIN, R., SILVA, V., FEIKERT, T., OPANASHUK, L., CARTER, J., POTTER, R., MAYNARD, A., FINKELSTEIN, J., OBERDORSTER, G. (2006) Translocation of inhaled ultrafine manganese oxide particles to the central nervous system. Environmental Health Perspectives 114: 1172-1178

FABRICANT, N. D. (1941) Significance of fhe pH of nasal secretions in situ - Further studies. Archives of Otolaryngology 34: 297-301

FECHTER, L. D., JOHNSON, D. L., LYNCH, R. A. (2002) The relationship of particle size to olfactory nerve uptake of a non-soluble form of manganese into brain. Neurotoxicology 23: 177-183

FRANSEN, N., WESTIN, U. E., NYSTROM, C., BJORK, E. (2007) The in vitro transport of dihydroergotamine across porcine nasal respiratory and. olfactory mucosa and the effect of a novel powder formulation. Journal of Drug Delivery Science and Technology 17: 267-271

FREEMAN, W., BRACEGIRDLE, B. (1976) An Advanced Atlas of Histology. p9

FREY, W. H., LIU, J., CHEN, X. Q., THORNE, R. G., FAWCETT, J. R., ALA, T. A., RAHMAN, Y. E. (1997) Delivery of I-125-NGF to the brain via the olfactory route. Drug Delivery 4: 87-92

FRICK, M., BRIGHT, N. A., RIENTO, K., BRAY, A., MERRIFIED, C., NICHOLS, B. J. (2007) Coassembly of flotillins induces formation of membrane microdomains, membrane curvature, and vesicle budding. Current Biology 17: 1151-1156

GAIDAROV, I., SANTINI, F., WARREN, R. A., KEEN, J. H. (1999) Spatial control of coated-pit dynamics in living cells. Nature Cell Biology 1: 1-7

GAO, X., CHEN, J., TAO, W., ZHU, J., ZHANG, Q., CHEN, H., JIANG, X. (2007) UEA I-bearing nanoparticles for brain delivery following intranasal administration. International Journal of Pharmaceutics 340: 207-15

GAO, X. L., TAO, W. X., LU, W., ZHANG, Q. Z., ZHANG, Y., JIANG, X. G., FU, S. K. (2006) Lectin-conjugated PEG-PLA nanoparticles: Preparation and brain delivery after intranasal administration. Biomaterials 27: 3482-3490

GARTNER, L. P., HIATT, J. L. (2000) Color atlas of histology. Lippincott Williams & Wilkins, Philadelphia, Pa.

GENESER, F. (1990) Histologi. Munksgaard, Copenhagen

GETCHELL, M. L., GETCHELL, T. V. (1992) Fine-Structural Aspects of Secretion and Extrinsic Innervation in the Olfactory Mucosa. Microscopy Research and Technique 23: 111-127

GETTY, R. (1975) Sisson and Grossman's: The Anatomy of the Domestic Animals. W.B. Saunders Company, Philadelphia

GHIRARDELLI, R., BONASORO, F., PORTA, C., CREMASCHI, D. (1999) Identification of particular epithelial areas and cells that transport polypeptide-coated nanoparticles in the nasal respiratory mucosa of the rabbit. Biochimica Et Biophysica Acta-Biomembranes 1416: 39-47

GIZURARSON, S. (1990) Animal-Models For Intranasal Drug Delivery Studies - A Review Article. Acta Pharmaceutica Nordica 2: 105-22

GIZURARSON, S., TAMURA, S., KURATA, T. (1991) Estimating Tissue Permeability And Other Bioelectrical Parameters Using Membrane Voltage And Short-Circuit Current. Chemical & Pharmaceutical Bulletin 39: 1636-7

GOPPERT, T. M., MULLER, R. H. (2005) Polysorbate-stabilized solid lipid nanoparticles as colloidal carriers for intravenous targeting of drugs to the brain: Comparison of plasma protein adsorption patterns. Journal of Drug Targeting 13: 179-187

GORE, A. V., LIANG, A. C., CHIEN, Y. W. (1998) Comparative biomembrane permeation of tacrine using Yucatan minipigs and domestic pigs as the animal model. Journal of Pharmaceutical Sciences 87: 441-447

GRAFF, C. L., POLLACK, G. M. (2003) P-glycoprotein attenuates brain uptake of substrates after nasal instillation. Pharmaceutical Research 20: 1225-30

GUMBINER, B. (1987) Structure, Biochemistry, and Assembly of Epithelial Tight Junctions. American Journal of Physiology 253: C749-C758

HARKEMA, J. R., PLOPPER, C. G., HYDE, D. M., WILSON, D. W., STGEORGE, J. A., WONG, V. J. (1987) Nonolfactory Surface Epithelium of the Nasal Cavity of the Bonnet Monkey - a Morphological and Morphometric Study of the Transitional and Respiratory Epithelium. American Journal of Anatomy 180: 266-279

HENRIKSEN, I., VAGEN, S. R., SANDE, S. A., SMISTAD, G., KARLSEN, J. (1997) Interactions between liposomes and chitosan .2. Effect of selected parameters on aggregation and leakage. International Journal of Pharmaceutics 146: 193-203

HENRIKSSON, J. T. H. (1998) Uptake of inorganic mercury in the olfactory bulbs via olfactory pathways in rats. Environmental Research. Vol. 77: 130-140

HERSEY, S. J., JACKSON, R. T. (1987) Effect of Bile-Salts on Nasal Permeability Invitro. Journal of Pharmaceutical Sciences 76: 876-879

HIRAI, S., YASHIKI, T., MATSUZAWA, T., MIMA, H. (1981) Absorption Of Drugs From The Nasal-Mucosa Of Rat. International Journal Of Pharmaceutics 7: 317

HOWARD, K. A., RAHBEK, U. L., LIU, X. D., DAMGAARD, C. K., GLUD, S. Z., ANDERSEN, M. O., HOVGAARD, M. B., SCHMITZ, A., NYENGAARD, J. R., BESENBACHER, F., KJEMS, J. (2006) RNA interference in vitro and in vivo using a chitosan/siRNA nanoparticle system. Molecular Therapy 14: 476-484

HUANG, M., KHOR, E., LIM, L. Y. (2004) Uptake and cytotoxicity of chitosan molecules and nanoparticles: Effects of molecular weight and degree of deacetylation. Pharmaceutical Research 21: 344-353

HUNTER, R. J. (1981) Zeta potential in colloid science: principles and applications. Academic Press, London

ILLUM, L. (2000) Transport of drugs from the nasal cavity to the central nervous system. European Journal Of Pharmaceutical Sciences 11: 1-18

ILLUM, L. (2004) Is nose-to-brain transport of drugs in man a reality? Journal Of Pharmacy And Pharmacology 56: 3-17

ILLUM, L., JACOBSEN, L. O., MULLER, R. H., MAK, E., DAVIS, S. S. (1987) Surface Characteristics and the Interaction of Colloidal Particles with Mouse Peritoneal-Macrophages. Biomaterials 8: 113-117

IMAMURA, H., TAKAO, S., AIKOU, T. (1994) A Modified Invasion-3-(4,5-Dimethylthiazole-2-Yl)-2,5-Diphenyltetrazolium Bromide Assay for Quantitating Tumor-Cell Invasion. Cancer Research 54: 3620-3624

JANSSON, B. (2004) Models for the Transfer of Drugs from the Nasal Cavity to the Central Nervous System. Uppsala University, Uppsala, Sweden

JONES, K. H., SENFT, J. A. (1985) An Improved Method to Determine Cell Viability by Simultaneous Staining with Fluorescein Diacetate Propidium Iodide. Journal of Histochemistry & Cytochemistry 33: 77-79

KAHWA, C. K. B., PURTON, M. (1996) Histological and histochemical study of epithelial lining of the respiratory tract in adult goats. Small Ruminant Research 20: 181-186

KALINER, M., MAROM, Z., PATOW, C., SHELHAMER, J. (1984) Human Respiratory Mucus. Journal of Allergy and Clinical Immunology 73: 318-323

KANDIMALLA, K. K., DONOVAN, M. D. (2005a) Localization and differential activity of P-glycoprotein in the bovine olfactory and nasal respiratory mucosae. Pharmaceutical Research 22: 1121-28

KANDIMALLA, K. K., DONOVAN, M. D. (2005b) Carrier mediated transport of chlorpheniramine and chlorcyclizine across bovine olfactory mucosa: Implications on nose-to-brain transport. Journal Of Pharmaceutical Sciences 94: 613-24

KAWASHIMA, Y., YAMAMOTO, H., TAKEUCHI, H., KUNO, Y. (2000) Mucoadhesive DL-lactide/glycolide copolymer nanospheres coated with chitosan to improve oral delivery of elcatonin. Pharmaceutical Development and Technology 5: 77-85

KOTZE, A. F., LUESSEN, H. L., DE LEEUW, B. J., DE BOER, B. G., VERHOEF, J. C., JUNGINGER, H. E. (1998) Comparison of the effect of different chitosan salts and N-trimethyl chitosan chloride on the permeability of intestinal epithelial cells (Caco-2). Journal of Controlled Release 51: 35-46

KRATZING, J. E. (1984) The Anatomy and Histology of the Nasal Cavity of the Koala (Phascolarctos-Cinereus). Journal of Anatomy 138: 55-65

KREUTER, J. (2001) Nanoparticulate systems for brain delivery of drugs. Advanced Drug Delivery Reviews 47: 65-81

KREUTER, J., SHAMENKOV, D., PETROV, V., RAMGE, P., CYCHUTEK, K., KOCH-BRANDT, C., ALYAUTDIN, R. (2002) Apolipoprotein-mediated transport of nanoparticle-bound drugs across the blood-brain barrier. Journal of Drug Targeting 10: 317-325

KRISHNAMOORTHY, R., MITRA, A. K. (1998) Prodrugs for nasal drug delivery. Advanced Drug Delivery Reviews 29: 135-146

KRONBERG, B., DAHLMAN, A., CARLFORS, J., KARLSSON, J., ARTURSSON, P. (1990) Preparation and Evaluation of Sterically Stabilized Liposomes - Colloidal Stability, Serum Stability, Macrophage Uptake, and Toxicity. Journal of Pharmaceutical Sciences 79: 667-671

KUBO, H., HOSOYA, K., NATSUME, H., SUGIBAYASHI, K., MORIMOTO, Y. (1994) In-Vitro Permeation of Several Model-Drugs across Rabbit Nasal-Mucosa. International Journal of Pharmaceutics 103: 27-36

KUO, C. K., HANIOKA, N., HOSHIKAWA, Y., OGURI, K., YOSHIMURA, H. (1991) Species-Difference of Site-Selective Glucuronidation of Morphine. Journal of Pharmacobio-Dynamics 14: 187-193

LAI, S. K., O'HANLON, D. E., HARROLD, S., MAN, S. T., WANG, Y. Y., CONE, R., HANES, J. (2007) Rapid transport of large polymeric nanoparticles in fresh undiluted human mucus. Proceedings of the National Academy of Sciences of the United States of America 104: 1482-1487

LAROCHELLE, R., MARTINEAUDOIZE, B. (1991) Distribution and Histochemical Characterization of Goblet Cells in the Nasal Cavity of Piglets. American Journal of Anatomy 191: 103-111

LAZARD, D., ZUPKO, K., PORIA, Y., NEF, P., LAZAROVITS, J., HORN, S., KHEN, M., LANCET, D. (1991) Odorant Signal Termination by Olfactory Udp Glucuronosyl Transferase. Nature 349: 790-793

LEHR, C. M. (2002) Cell Culture Models of Biological Barriers. Taylor & Francis Group, London

LENAERTS, V., GURNY, R. (1990) Bioadhesive Drug Delivery Systems. CRC Press, Boca Raton, USA

LEUNG, S., ROBINSON, J. (1992) Polyanionic polymers in bio-and mucoadhesive drug delivery. Polyelectrolyte gels- properties, preparations and applications (ACS Symposium Series) vol. 480.: pp.269-84.

LI, J. T., CALDWELL, K. D., RAPOPORT, N. (1994) Surface-Properties of Pluronic-Coated Polymeric Colloids. Langmuir 10: 4475-4482

LI, N., SIOUTAS, C., CHO, A., SCHMITZ, D., MISRA, C., SEMPF, J., WANG, M. Y., OBERLEY, T., FROINES, J., NEL, A. (2003) Ultrafine particulate pollutants induce oxidative stress and mitochondrial damage. Environmental Health Perspectives 111: 455-460

LI, Y. Y., CHEN, X. G., YU, L. M., WANG, S. X., SUN, G. Z., ZHOU, H. Y. (2006) Aggregation of hydrophobically modified chitosan in solution and at the air-water interface. Journal of Applied Polymer Science 102: 1968-1973

LLEDO, P. M., GHEUSI, G., VINCENT, J. D. (2005) Information processing in the mammalian olfactory system. Physiological Reviews 85: 281-317

LUCK, M., PAULKE, B. R., SCHRODER, W., BLUNK, T., MULLER, R. H. (1998) Analysis of plasma protein adsorption on polymeric nanoparticles with different surface characteristics. Journal of Biomedical Materials Research 39: 478-485

LUCK, M., SCHRODER, W., HARNISCH, S., THODE, K., BLUNK, T., PAULKE, B. R., KRESSE, M., MULLER, R. H. (1997) Identification of plasma proteins facilitated by enrichment on particulate surfaces: Analysis by two-dimensional electrophoresis and N-terminal microsequencing. Electrophoresis 18: 2961-2967

MADGE, T. (2001) White mischief : a cultural history of cocaine. Mainstream, Edinburgh

MAITANI, Y., ISHIGAKI, K., TAKAYAMA, K., NAGAI, T. (1997) In vitro nasal transport across rabbit mucosa: Effect of oxygen bubbling, pH and hypertonic pressure on

permeability of lucifer yellow, diazepam and 17 beta-estradiol. International Journal Of Pharmaceutics 146: 11-19

MAO, Z. W., MA, L., JIANG, Y., YAN, M., GAO, C. Y., SHEN, J. C. (2007) N,N,N-Trimethylchitosan chloride as a gene vector: Synthesis and application. Macromolecular Bioscience 7: 855-863

MARTINEAUDOIZE, B., CAYA, I. (1996) Ultrastructural characterization of the nasal respiratory epithelium in the piglet. Anatomical Record 246: 169-175

MATSUZAKI, O. (1995) Numbers of Olfactory Receptor-Cells and Pine Structure of Olfactory Nerves in Various Birds. Zoological Science 12: 117-123

MATULIONIS, D. H., PARKS, H. F. (1973) Ultrastructural Morphology of Normal Nasal Respiratory Epithelium of Mouse. Anatomical Record 176: 65-83

MAYOR, S., PAGANO, R. E. (2007) Pathways of clathrin-independent endocytosis. Nature Reviews Molecular Cell Biology 8: 603-612

MAZEAU, K., PEREZ, S., RINAUDO, M. (2000) Predicted influence of N-acetyl group content on the conformational extension of chitin and chitosan chains. Journal of Carbohydrate Chemistry 19: 1269-1284

MCMARTIN, C., HUTCHINSON, L. E. F., HYDE, R., PETERS, G. E. (1987) Analysis of Structural Requirements for the Absorption of Drugs and Macromolecules from the Nasal Cavity. Journal of Pharmaceutical Sciences 76: 535-540

MCSHANE, D., DAVIES, J. C., DAVIES, M. G., BUSH, A., GEDDES, D. M., ALTON, E. (2003) Airway surface pH in subjects with cystic fibrosis. European Respiratory Journal 21: 37-42

MENACHE, M. G., HANNA, L. M., GROSS, E. A., LOU, S. R., ZINREICH, S. J., LEOPOLD, D. A., JARABEK, A. M., MILLER, F. J. (1997) Upper respiratory tract surface areas and volumes of laboratory animals and humans: Considerations for dosimetry models. Journal of Toxicology and Environmental Health 50: 475-506

MERKUS, F. W. H. M., VAN DEN BERG, M. P. (2007) Can nasal drug delivery bypass the blood-brain barrier?: questioning the direct transport theory. Drugs in R & D 8: 133-144

MIACZYNSKA, M., STENMARK, H. (2008) Mechanisms and functions of endocytosis. Journal of Cell Biology 180: 7-11

MILLER, J. M. J. (1993) Statistics for Analytical Chemistry. Ellis Horwood Ltd, Chichester, UK

MILLER, M. L., ANDRINGA, A., EVANS, J. E., HASTINGS, L. (1995) Microvillar Cells of the Olfactory Epithelium - Morphology and Regeneration Following Exposure to Toxic Compounds. Brain Research 669: 1-9

MORAN, D. T., ROWLEY, J. C., JAFEK, B. W., LOVELL, M. A. (1982) The Fine-Structure Of The Olfactory Mucosa In Man. Journal Of Neurocytology 11: 721-46

MORAN, D. T., JAFEK, B. W., ELLER, P. M., ROWLEY, J. C. (1992) Ultrastructural Histopathology of Human Olfactory Dysfunction. Microscopy Research and Technique 23: 103-110

MORRISON, E. E., COSTANZO, R. M. (1990) Morphology of the human olfactory epithelium. Journal of Comparative Neurology 297: 1-13

MORRISON, E. E., COSTANZO, R. M. (1992) Morphology of Olfactory Epithelium in Humans and Other Vertebrates. Microscopy Research and Technique 23: 49-61

MULLER, R. H., WALLIS, K. H., TROSTER, S. D., KREUTER, J. (1992) Invitro Characterization of Poly (Methyl-Methacrylate) Nanoparticles and Correlation to Their Invivo Fate. Journal of Controlled Release 20: 237-246

MULLER, R. H., RUHL, D., LUCK, M., PAULKE, B. R. (1997) Influence of fluorescent labelling of polystyrene particles on phagocytic uptake, surface hydrophobicity, and plasma protein adsorption. Pharmaceutical Research 14: 18-24

MUNIER, S., MESSAI, I., DELAIR, T., VERRIER, B., ATAMAN-ONAL, Y. (2005) Cationic PLA nanoparticles for DNA delivery: Comparison of three surface polycations for DNA binding, protection and transfection properties. Colloids and Surfaces B-Biointerfaces 43: 163-173

MYGIND, N. (1979) Nasal allergy. Blackwell Scientific, Oxford [etc.]

MYGIND, N., DAHL, R. (1998) Anatomy, physiology and function of the nasal cavities in health and disease. Advanced Drug Delivery Reviews 29: 3-12

NATHAN, B. P., NANNAPANENI, S., GAIRHE, S., NWOSU, I., STRUBLE, R. G. (2007) The distribution of apolipoprotein E in mouse olfactory epithelium. Brain Research 1137: 78-83

NEL, A., XIA, T., MADLER, L., LI, N. (2006) Toxic potential of materials at the nanolevel. Science 311: 622-627

NERURKAR, M. M., HO, N. F. H., BURTON, P. S., VIDMAR, T. J., BORCHARDT, R. T. (1997) Mechanistic roles of neutral surfactants on concurrent polarized and passive membrane transport of a model peptide in Caco-2 cells. Journal of Pharmaceutical Sciences 86: 813-821

NEWMAN, S. P., STEED, K. P., HARDY, J. G., WILDING, I. R., HOOPER, G., SPARROW, R. A. (1994) The distribution of an intranasal insulin formulation in healthy volunteers: effect of different administration techniques. Journal of Pharmacy & Pharmacology 46: 657-60

NIEUWENHUYS, R., TEN DONKELAAR, H. J., NICHOLSON, C. (1998) The Central Nervous System of Vertebrates. Springer, Berlin

NORRIS, D. A., SINKO, P. J. (1997) Effect of size, surface charge, and hydrophobicity on the translocation of polystyrene microspheres through gastrointestinal mucin. Journal of Applied Polymer Science 63: 1481-1492

NYENGAARD, J. R. (1999) Stereologic methods and their application in kidney research. Journal of the American Society of Nephrology 10: 1100-1123

OBERDORSTER, E. (2004) Manufactured nanomaterials (Fullerenes, C60) induce oxidative stress in the brain of juvenile largemouth bass. Environmental Health Perspectives 112: 1058-1062

OBERDORSTER, G., OBERDORSTER, E., OBERDORSTER, J. (2005) Nanotoxicology: An emerging discipline evolving from studies of ultrafine particles. Environmental Health Perspectives 113: 823-839

OBERDORSTER, G., SHARP, Z., ATUDOREI, V., ELDER, A., GELEIN, R., KREYLING, W., COX, C. (2004) Translocation of inhaled ultrafine particles to the brain. Inhalation Toxicology 16: 437-45

OKUYAMA, S. (1997) The first attempt at radioisotopic evaluation of the integrity of the nose-brain barrier. Life Sciences 60: 1881-1884

OPANASOPIT, P., AUMKLAD, P., KOWAPRADIT, J., NGAWHIRANPAT, T., APIRAKARAMWONG, A., ROJANARATA, T. (2007) Effect of salt forms and molecular weight of chitosans on in vitro permeability enhancement in intestinal epithelial cells (Caco-2). Pharmaceutical Development and Technology 12: 447-455

OSTH, K. (2002) The Horizontal Ussing Chamber Method in Studies of Nasal Drug Delivery. Uppsala University, Uppsala

OSTH, K., GRASJO, J., BJORK, E. (2002a) A new method for drug transport studies on pig nasal mucosa using a horizontal Ussing chamber. Journal Of Pharmaceutical Sciences 91: 1259-73

OSTH, K., PAULSSON, M., BJORK, E., EDSMAN, K. (2002b) Evaluation of drug release from gels on pig nasal mucosa in a horizontal Ussing chamber. Journal Of Controlled Release 83: 377-88

PARDRIDGE, W. M. (1999) Non-invasive drug delivery to the human brain using endogenous blood-brain barrier transport systems. Pharmaceutical Science & Technology Today 2: 49-59

PERSSON, E., HENRIKSSON, J., TJALVE, H. (2003a) Uptake of cobalt from the nasal mucosa into the brain via olfactory pathways in rats. Toxicology Letters 145: 19-27

PERSSON, E., HENRIKSSON, J., TALLKVIST, J., ROULEAU, C., TJALVE, H. (2003b) Transport and subcellular distribution of intranasally administered zinc in the olfactory system of rats and pikes. Toxicology 191: 97-108

PHILIPPOVA, O. E., VOLKOV, E. V., SITNIKOVA, N. L., KHOKHLOV, A. R., DESBRIERES, J., RINAUDO, M. (2001) Two types of hydrophobic aggregates in aqueous solutions of chitosan and its hydrophobic derivative. Biomacromolecules 2: 483-490

PHILLIPS, P. P., MCCAFFREY, T. V., KERN, E. B. (1990) Measurement of Human Nasal Ciliary Motility Using Computerized Microphotometry. Otolaryngology-Head and Neck Surgery 103: 420-426

PHILLIPSON, M., ATUMA, C., HENRIKSNAS, J., HOLM, L. (2002) The importance of mucus layers and bicarbonate transport in preservation of gastric juxtamucosal pH. American Journal of Physiology-Gastrointestinal and Liver Physiology 282: G211-G219

PIETROWSKY, R., THIEMANN, A., KERN, W., FEHM, H. L., BORN, J. (1996a) A nose-brain pathway for psychotropic peptides: Evidence from a brain evoked potential study with cholecystokinin. Psychoneuroendocrinology 21: 559-572

PIETROWSKY, R., STRUBEN, C., MOLLE, M., FEHM, H. L., BORN, J. (1996b) Brain potential changes after intranasal vs intravenous administration of vasopressin: Evidence for a direct nose brain pathway for peptide effects in humans. Biological Psychiatry 39: 332-340

PLENDL, J., SINOWATZ, F. (1998) Glycobiology of the olfactory system. Acta Anatomica 161: 234-53

POPP, J. A., MARTIN, J. T. (1984) Surface-Topography and Distribution of Cell-Types in the Rat Nasal Respiratory Epithelium - Scanning Electron-Microscopic Observations. American Journal of Anatomy 169: 425-436

PROETZ, A. (1953) Applied physiology of the nose.

PUJARA, C. P., SHAO, Z. Z., DUNCAN, M. R., MITRA, A. K. (1995) Effects of Formulation Variables on Nasal Epithelial-Cell Integrity - Biochemical Evaluations. International Journal of Pharmaceutics 114: 197-203

QUEMENEUR, F., RINAUDO, M., PEPIN-DONAT, B. (2008) Influence of molecular weight and pH on adsorption of chitosan at the surface of large and giant vesicles. Biomacromolecules 9: 396-402

QUEMENEUR, F., RAMMAL, A., RINAUDO, M., PEPIN-DONAT, B. (2007) Large and giant vesicles "Decorated" with chitosan: Effects of pH, salt or glucose stress, and surface adhesion. Biomacromolecules 8: 2512-2519

RAMGE, P., UNGER, R. E., OLTROGGE, J. B., ZENKER, D., BEGLEY, D., KREUTER, J., VON BRIESEN, H. (2002) Polysorbate-80 coating enhances uptake of polybutylcyanoacrylate (PBCA)-nanoparticles by human and bovine primary brain capillary endothelial cells. European Journal of Neuroscience 12: 1931-1940

RHODIN, J. A. G. (1974) Histology a text and atlas. Oxford University Press, New York

RINAUDO, M. (2006) Chitin and chitosan: Properties and applications. Progress in Polymer Science 31: 603-632

RINAUDO, M., PAVLOV, G., DESBRIERES, J. (1999) Solubilization of chitosan in strong acid medium. International Journal of Polymer Analysis and Characterization 5: 267-276

RINPOCHE, R., KUNZANG, J. (1973) Tibetan medicine.

ROMERO-CANO, M. S., MARTIN-RODRIGUEZ, A., CHAUVETEAU, G., DE LAS NIEVES, F. J. (1998) Colloidal stabilization of polystyrene particles by adsorption of nonionic surfactant - II. Electrosteric stability studies. Journal of Colloid and Interface Science 198: 273-281

ROTHEN-RUTISHAUSER, B. M., SCHURCH, S., HAENNI, B., KAPP, N., GEHR, P. (2006) Interaction of fine particles and nanoparticles with red blood cells visualized with advanced microscopic techniques. Environmental Science & Technology 40: 4353-4359

SAKANE, T., AKIZUKI, M., YAMASHITA, S., SEZAKI, H., NADAI, T. (1994) Direct drug transport from the rat nasal cavity to the cerebrospinal fluid: The relation to the dissociation of the drug. Journal of Pharmacy and Pharmacology 46: 378-379

SAKANE, T., AKIZUKI, M., YAMASHITA, S., NADAI, T., HASHIDA, M., SEZAKI, H. (1991) The Transport Of A Drug To The Cerebrospinal Fluid Directly From The Nasal Cavity The Relation To The Lipophilicity Of The Drug. Chemical and Pharmaceutical Bulletin 39: 2456-2458

SAKANE, T., AKIZUKI, M., TAKI, Y., YAMASHITA, S., SEZAKI, H., NADAI, T. (1995) Direct drug transport from the rat nasal cavity to the cerebrospinal fluid: The relation to the molecular weight of drugs. Journal of Pharmacy and Pharmacology 47: 379-381

SCHIPPER, N. G. M., VARUM, K. M., ARTURSSON, P. (1996) Chitosans as absorption enhancers for poorly absorbable drugs .1. Influence of molecular weight and degree of acetylation on drug transport across human intestinal epithelial (Caco-2) cells. Pharmaceutical Research 13: 1686-1692

SCHMIDT, M. C., SIMMEN, D., HILBE, M., BODERKE, P., DITZINGER, G., SANDOW, J., LANG, S., RUBAS, W., MERKLE, H. P. (2000) Validation of excised bovine nasal mucosa as in vitro model to study drug transport and metabolic pathways in nasal epithelium. Journal of Pharmaceutical Sciences 89: 396-407

SEIFALIAN, A. M., SALACINSKI, H. J., PUNSHON, G., KRIJGSMAN, B., HAMILTON, G. (2001) A new technique for measuring the cell growth and metabolism of endothelial cells seeded on vascular prostheses. Journal Of Biomedical Materials Research 55: 637-44

SEMMLER, M., SEITZ, J., ERBE, F., MAYER, P., HEYDER, J., OBERDORSTER, G., KREYLING, W. G. (2004a) Long-term clearance kinetics of inhaled ultrafine insoluble iridium particles from the rat lung, including transient translocation into secondary organs. Inhalation Toxicology 16: 453-59

SEMMLER, M., SEITZ, J., ERBE, F., MAYER, P., HEYDER, J., OBERDORSTER, G., KREYLING, W. G. (2004b) Long-term clearance kinetics of inhaled ultrafine

insoluble iridium particles from the rat lung, including transient translocation into secondary organs. Inhalation Toxicology 16: 453-459

SHIN, K., FOGG, V. C., MARGOLIS, B. (2006) Tight junctions and cell polarity. Annual Review of Cell and Developmental Biology 22: 207-235

SHUSTERMAN, D., AVILA, P. C. (2003) Real-time monitoring of nasal mucosal pH during carbon dioxide stimulation: Implications for stimulus dynamics. Chemical Senses 28: 595-601

SIGMA-ALDRICH. (2005) Bradford Reagent - Technical Bulletin.

SIMOES, S. I., TAPADAS, J. M., MARQUES, C. M., CRUZ, M. E. M., MARTINS, M. B. F., CEVC, G. (2005) Permeabilisation and solubilisation of soybean phosphatidylcholine bilayer vesicles, as membrane models, by polysorbate, Tween 80. European Journal of Pharmaceutical Sciences 26: 307-317

SIMS, D. E., HORNE, M. M. (1997) Heterogeneity of the composition and thickness of tracheal mucus in rats. American Journal of Physiology-Lung Cellular and Molecular Physiology 17: L1036-L1041

SINGLA, A. K., CHAWLA, M. (2001) Chitosan: some pharmaceutical and biological aspects - an update. Journal of Pharmacy and Pharmacology 53: 1047-1067

SMITH, J., WOOD, E., DORNISH, M. (2004) Effect of chitosan on epithelial cell tight junctions. Pharmaceutical Research 21: 43-49

SMITH, J. M., DORNISH, M., WOOD, E. J. (2005) Involvement of protein kinase C in chitosan glutamate-mediated tight junction disruption. Biomaterials 26: 3269-3276

SORKIN, A. (2004) Cargo recognition during clathrin-mediated endocytosis: a team effort. Current Opinion in Cell Biology 16: 392-399

STOCKHORST, U., PIETROWSKY, R. (2004) Olfactory perception, communication, and the nose-to-brain pathway. Physiology & Behavior 83: 3-11

STOLNIK, S., FELUMB, N. C., HEALD, C. R., GARNETT, M. C., ILLUM, L., DAVIS, S. S. (1997) Adsorption behaviour and conformation of selected poly(ethylene oxide) copolymers on the surface of a model colloidal drug carrier. Colloids and Surfaces a-Physicochemical and Engineering Aspects 122: 151-159

STOLNIK, S., DAUDALI, B., ARIEN, A., WHETSTONE, J., HEALD, C. R., GARNETT, M. C., DAVIS, S. S., ILLUM, L. (2001) The effect of surface coverage and conformation of poly(ethylene oxide) (PEO) chains of poloxamer 407 on the biological fate of model colloidal drug carriers. Biochimica Et Biophysica Acta-Biomembranes 1514: 261-279

STUART, M. A. C., WAAJEN, F., COSGROVE, T., VINCENT, B., CROWLEY, T. L. (1984) Hydrodynamic Thickness of Adsorbed Polymer Layers. Macromolecules 17: 1825-1830

SUNDERMAN, F. W., JR. (2001) Nasal toxicity, carcinogenicity, and olfactory uptake of metals. Annals of Clinical & Laboratory Science 31: 3-24

SYNNERSTAD, I., JOHANSSON, M., NYLANDER, O., HOLM, L. (2001) Intraluminal acid and gastric mucosal integrity: the importance of blood-borne bicarbonate. American Journal of Physiology-Gastrointestinal and Liver Physiology 280: G121-G129

TADROS, T. F. (2005) Applied surfactants: principles and applications. Wiley-VCH, Weinheim

TANGBORIBOONRAT, P., BURANABUNYA, U., SANGRIBSUB, S. (2003) Heterocoagulation of polychloroprene on natural rubber latex particles for use in the preparation of toughened polystyrene. Journal of Applied Polymer Science 87: 9-13

THORNE, R. G., PRONK, G. J., PADMANABHAN, V., FREY, W. H. (2004) Delivery of insulin-like growth factor-I to the rat brain and spinal cord along olfactory and trigeminal pathways following intranasal administration. Neuroscience 127: 481-96

TUCKER, D. (1971) Nonolfactory responses from the nasal cavity: Jacobson‘s organ and the trigeminal system. . Springer, Heidelberg

UGWOKE, M. I., VERBEKE, N., KINGET, R. (2001) The biopharmaceutical aspects of nasal mucoadhesive drug delivery. Journal of Pharmacy and Pharmacology 53: 3-21

VAN DER BAAN, B. (2000) Ciliary function. Acta Oto-Rhino-Laryngologica Belgica. 54: 293-298

VAN ITALLIE, C. M., ANDERSON, J. M. (2006) Claudins and epithelial paracellular transport. Annual Review of Physiology 68: 403-429

VILA, A., GILL, H., MCCALLION, O., ALONSO, M. J. (2004) Transport of PLA-PEG particles across the nasal mucosa: effect of particle size and PEG coating density. Journal of Controlled Release 98: 231-244

VILA, A., SANCHEZ, A., EVORA, C., SORIANO, I., MCCALLION, O., ALONSO, M. J. (2005) PLA-PEG particles as nasal protein carriers: the influence of the particle size. International Journal of Pharmaceutics 292: 43-52

WADELL, C., BJORK, E., CAMBER, O. (1999) Nasal drug delivery - evaluation of an in vitro model using porcine nasal mucosa. European Journal of Pharmaceutical Sciences 7: 197-206

WADELL, C., BJORK, E., CAMBER, O. (2003) Permeability of porcine nasal mucosa correlated with human nasal absorption. European Journal Of Pharmaceutical Sciences 18: 47-53

WANG, B., FENG, W. Y., WANG, M., SHI, J. W., ZHANG, F., OUYANG, H., ZHAO, Y. L., CHAI, Z. F., HUANG, Y. Y., XIE, Y. N., WANG, H. F., WANG, J. (2007) Transport of intranasally instilled fine Fe2O3 particles into the brain: Micro-distribution,

chemical states, and histopathological observation. Biological Trace Element Research 118: 233-243

WASHINGTON, C. (1992) Particle size analysis in pharmaceutics and other industries: theory and practice. Ellis Harwood, New York

WESTERLING, D., PERSSON, C., HOGLUND, P. (1995) Plasma-Concentrations of Morphine, Morphine-3-Glucuronide, and Morphine-6-Glucuronide after Intravenous and Oral-Administration to Healthy-Volunteers - Relationship to Nonanalgesic Actions. Therapeutic Drug Monitoring 17: 287-301

WESTIN, U., PIRAS, E., JANSSON, B., BERGSTROM, U., DAHLIN, M., BRITTEBO, E., BJORK, E. (2005) Transfer of morphine along the olfactory pathway to the central nervous system after nasal administration to rodents. European Journal Of Pharmaceutical Sciences 24: 565

WHEATLEY, M. A., DENT, J., WHEELDON, E. B., SMITH, P. L. (1988) Nasal Drug Delivery - an Invitro Characterization of Trans-Epithelial Electrical-Properties and Fluxes in the Presence or Absence of Enhancers. Journal of Controlled Release 8: 167-177

WIJMANS, C. M., LEERMAKERS, F. A. M., FLEER, G. J. (1994) Diblock Copolymer Adsorption on Small Particles. Langmuir 10: 1331-1333

WRIGHT, N., ALISON, M. (1984) The Biology of Epithelial Cell Populations (Volume 1). Oxford University Press, Oxford

XIA, T., KOVOCHICH, M., BRANT, J., HOTZE, M., SEMPF, J., OBERLEY, T., SIOUTAS, C., YEH, J. I., WIESNER, M. R., NEL, A. E. (2006) Comparison of the abilities of ambient and manufactured nanoparticles to induce cellular toxicity according to an oxidative stress paradigm. Nano Letters 6: 1794-1807

XIANG, S. D., SCHOLZEN, A., MINIGO, G., DAVID, C., APOSTOLOPOULOS, V., MOTTRAM, P. L., PLEBANSKI, M. (2006) Pathogen recognition and development of particulate vaccines: Does size matter? Methods 40: 1-9

ZHANG, Q., JIANG, X., JIANG, W., LU, W., SU, L., SHI, Z. (2004) Preparation of nimodipine-loaded microemulsion for intranasal delivery and evaluation on the targeting efficiency to the brain. International Journal of Pharmaceutics (Kidlington) 275: 85-96

ZHANG, Q. Z., ZHA, L. S., ZHANG, Y., JIANG, W. M., LU, W., SHI, Z. Q., JIANG, X. G., FU, S. K. (2006) The brain targeting efficiency following nasally applied MPEG-PLA nanoparticles in rats. Journal of Drug Targeting 14: 281-290

ZHAO, J. X., BROWN, W. (1996) Comparative study of the adsorption of nonionic surfactants: Triton X-100 and C(12)E(7) on polystyrene latex particles using dynamic light scattering and adsorption isotherm measurements. Journal of Physical Chemistry 100: 3775-3782

ZOR, T., SELIGER, Z. (1996) Linearization of the bradford protein assay increases its sensitivity: Theoretical and experimental studies. Analytical Biochemistry 236: 302-308

APPENDIX

The following buffers were required during sample preparation, for measuring DNA content of tissues, as described in Section 2.2.5.3 Hoechst DNA Quantification.

Papain Buffer

Dibasic sodium phosphate (0.1M), cysteine HCl (0.005M) and EDTA (0.005M) were diluted with water and adjusted to pH6.5 2.0M HCl.

Preparation of Papain Solution

Papain was dissolved in papain buffer (1.06mg/ml) to produce papain solution.

Preparation of Hoechst Concentrate Solution

Saline sodium citrate buffer was diluted (1 in 20) with water. This was used to dissolve bisbenzamide (1mg/ml). 100µl aliquots of this concentrated solution were frozen (-20°C) until required.

Preparation of Hoechst Buffer

EDTA (0.01M), NaCl (0.1 M) and Trizma Base (0.01M) were diluted with water and adjusted to pH7 with 2.0M HCl.

Preparation of Hoechst working solution

Bisbenzimide (1.5µg/ml) was diluted in Hoechst buffer with 0.4 M NaCl.